

Probing Quark-Gluon Plasma with D Mesons

by

Jing Wang

Submitted to the Department of Physics
in partial fulfillment of the requirements for the degree of

Doctor of Philosophy in Physics

at the

MASSACHUSETTS INSTITUTE OF TECHNOLOGY

June 2019

© Massachusetts Institute of Technology 2019. All rights reserved.

Author
Department of Physics
May 24, 2019

Certified by
Yen-Jie Lee
Associate Professor
Thesis Supervisor

Accepted by
Nergis Mavalvala
Associate Department Head of Physics

Probing Quark-Gluon Plasma with D Mesons

by

Jing Wang

Submitted to the Department of Physics
on May 24, 2019, in partial fulfillment of the
requirements for the degree of
Doctor of Philosophy in Physics

Abstract

Heavy quarks are powerful tools for the study of the properties of the high-density QCD medium created in heavy-ion collisions as they are sensitive to the transport properties of the medium and may interact with the QCD matter differently from light quarks. As the main observables to study the medium effect, the D^0 nuclear modification factor (R_{AA}) provides insights into the flavor dependence of in-medium parton energy loss, and the D^0 azimuthal anisotropy coefficient (v_n) provides information about the degree of the thermalization of the bulk medium. Furthermore, the production of D^0 in jets is sensitive to the diffusion in the medium and the role of medium response. Using the large proton-proton and PbPb data samples at $\sqrt{s_{NN}} = 5.02$ TeV collected by the Compact Muon Solenoid (CMS) detector at the Large Hadron Collider (LHC), high precision measurements of D^0 have been performed.

Thesis Supervisor: Yen-Jie Lee

Title: Associate Professor

Acknowledgments

Life as a graduate student is not always easy, but the people who accompany me on my journey made it meaningful.

First of all, I would like to express my sincere gratitude to my adviser Professor Yen-Jie Lee, who is a talented and generous instructor and friend. He has been an inspiration to me, showing how to work as a great experimental physicist and how to help others with the best way. He saved me every time my research work got stuck, and I was so much inspired by his advice and ideas. His patience and assistance meant a lot to me and convinced me to continue with physics.

It has been a great experience to work with the intelligent people in MIT heavy ion group. I would like to thank Professor Gunther Roland and Professor Bolek Wyslouch for giving me supports on both research work and student life. Professor Wit Busza raised invaluable physics discussions which avoid me being buried by technical details. His passion for physics is truly encouraging. The time I spent with Ta-Wei and Ran was one of the most unforgettable memories over the past six years. They helped me a lot and brightened up my life inside and outside the office. I was lucky to work closely with Gian-Michele for five years, and we collaborated on most of the heavy flavor analyses. He always stayed positive and made me feel much less stressful about the challenges I was getting through. I also need to thank Michael for helping with trigger related issues in the D-jet correlation measurement. Dragos and Alex were senior students when I joined the group, and I would not have adapted so quickly to the new environment without their assistance. Austin and Chris joined the group and graduated at the same time as me, so we grew up and explored everything new together in MIT. Their advice on tracks and jets was valuable for the analyses involved in this thesis. Also, this thesis would have never been done without the help from Kaya, George, Camelia, Doga and Anna in various ways.

I would also like to thank my CMS colleague Jian for partially contributing to the work in this thesis. It was my pleasure to join CMS collaboration and work with so many great people.

I feel blessed to have Xinmei as my first friend in MIT and feel lucky to have the most kind and reliable friends in Boston from PKU, Jiahua, Zhicheng, Yinan, Zheng, Chuteng and Quntao. I spent almost all my time outside the lab with you guys, and it is amazing that we have been keeping so close to each other in such a busy life. All those happy memories will last forever. Special thanks to Fanghua for being my

irreplaceable best friend over the years. We are seven thousand miles apart from each other, but I always feel you are there with me.

I would also like to extend my deepest gratitude to my parents. Knowing you are standing right behind me made me brave. It has been a huge encouragement that you always believe in me and support every decision I made.

The last part is to my friend Dongying. It was a difficult time, and I have been through it, but I do wish you were here at this important moment of my life.

Contents

1	Introduction	27
1.1	The Big Bang: Quark Gluon Plasma	27
1.1.1	QCD Phase Diagram	27
1.1.2	Thermodynamics: Equation of State	30
1.2	The Little Bang: Heavy-ion Collisions	32
1.2.1	Initial Stage and Particle Production	32
1.2.2	Ideal Fluid and Hydrodynamics	35
1.2.3	Hard Probes	39
1.3	The Golden Probe: Heavy Quarks in Heavy-ion Collisions	40
1.3.1	Heavy Quark Dynamics in Heavy-ion Collisions	42
1.3.2	Probing QGP Properties with Heavy Flavor Leptons	48
2	CMS at LHC	55
2.1	Large Hadron Collider	55
2.2	CMS Detectors	57
2.3	Triggering	58
2.3.1	Trigger System	58
2.3.2	Minimum-Bias and Centrality Trigger	60
2.3.3	Jet Trigger	63
2.3.4	D ⁰ Trigger	65
3	Monte-Carlo Simulation	69
4	Physics Objects	73
4.1	Tracks	73
4.1.1	Tracking Algorithm	73
4.1.2	Study Track Efficiency using D meson Decays	77

4.2	Jets	78
5	$D^0 \rightarrow K\pi$ Decay Reconstruction	83
5.1	Secondary Vertex Reconstruction	83
5.2	Cut Optimization	85
5.3	Signal Extraction	89
6	Prompt D^0 Production in Heavy-ion collisions	93
6.1	Analysis Technique	93
6.1.1	Dataset and D^0 Selection	93
6.1.2	Acceptance and Efficiency Correction	94
6.1.3	b-hadron Feed-down Subtraction	95
6.2	Results	99
6.2.1	Prompt D^0 Cross-section in pp collisions	99
6.2.2	Prompt D^0 Cross-section in PbPb collisions	103
6.2.3	Prompt D^0 Nuclear Modification Factor	103
6.3	Systematic Uncertainty Study	113
7	Prompt D^0 Azimuthal Anisotropy in Heavy-ion Collisions	117
7.1	Analysis Technique	117
7.1.1	Dataset and D^0 Selection	117
7.1.2	Event Plane	118
7.1.3	v_n Determination	124
7.1.4	Acceptance and Efficiency	128
7.2	Results	129
7.2.1	Prompt $D^0 v_2$ in PbPb Collisions	129
7.2.2	Prompt $D^0 v_3$ in PbPb Collisions	134
7.3	Systematic Uncertainty Study	135
8	D^0 Jet Angular Correlation	139
8.1	Analysis Techniques	141
8.1.1	Analysis Procedure	141
8.1.2	D^0 Selection	142
8.1.3	Jet Selection and Correction	142
8.1.4	Jet Background Subtraction	146
8.2	Results	150

8.2.1	D ⁰ Radial Distribution in jets in pp and PbPb Collisions	150
8.3	Systematic Uncertainty Study .	153
9	Conclusions	157
9.1	Discussions .	157
9.2	Outlook .	167
	Bibliography	171

List of Figures

- | | | |
|-----|--|----|
| 1-1 | Measurements of the renormalized coupling constant α_s as a function of Q . Figure from Ref. [1]. | 28 |
| 1-2 | The QCD phase diagram in the scope of current knowledge in terms of temperature T and baryon number chemical potential μ_B . With help of lattice QCD calculations, the cross-over at small μ_B (yellow shadow) is well understood, while the predicted critical point to 1st order transition is under exploration. Figure from Ref. [2]. | 29 |
| 1-3 | (Left) The trace anomaly as a function of temperature under different N_τ and the continuum extrapolation; (Right) The continuum extrapolation of the renormalized pressure, energy density and entropy density as a function of temperature. The yellow vertical shadow indicates the cross-over region, and the black dash line labels the ideal gas limit (Stefan-Boltzmann limit) for the energy density; The dark solid lines in both panels correspond to the prediction of the hadron resonance gas models (HRG). Figure from Ref. [6]. | 31 |
| 1-4 | Sketch of evolution of relativistic heavy-ion collisions with proper time τ . The moment two nuclei collide is taken as $\tau = 0$. Two ultra-relativistic heavy ion approach each other with velocity close to light and cross through each other. Meanwhile, hundreds of nuclei interact, create a strongly interacting field, and generate numerous particles. During $\tau \sim 1$ fm/c, particles interact with each and force the system to equilibrium, and fluid-like matter with extremely high temperature and high density emerges. With the matter expands and temperature decreases, the free partons are fragmented into hadronizations, and these hadrons or their decay daughters are detected by detectors. Figure from [10]. | 33 |

1-5 (Left) Differential yield of $Z \rightarrow \gamma\gamma$ dN/dy divided by the expected nuclear overlap function and as a function of $\langle N_{\text{part}} \rangle$ calculated by Glauber model compared with NLO QCD calculations. Figure from Ref. [14]; (Right) Production yield of W^+ (red), W^- (blue) and W^\pm (gray) boson per binary collision as a function of $\langle N_{\text{part}} \rangle$ calculated by Glauber model compared with an NLO QCD calculation. Figure from Ref. [13].

35

1-6 (Left) Average $dN_{\text{ch}}/d\eta$ normalized by $\langle N_{\text{part}} \rangle$ as a function of $\langle N_{\text{part}} \rangle$ measured in PbPb and XeXe collisions by the CMS [17] and ALICE [18, 19, 20] Collaborations and in CuCu and AuAu collisions by the PHOBOS [21] and BRAHMS [22] Collaborations. The bands around the data points denote the systematic uncertainties. Under the same collision energy and same $\langle N_{\text{part}} \rangle$, $dN_{\text{ch}}/d\eta$ is not same between PbPb and XeXe especially in the most central events (same situation for CuCu and AuAu); (Right) Average $dN_{\text{ch}}/d\eta$ normalized by $\langle N_{\text{part}} \rangle$ and $2A$ as a function of $\langle N_{\text{part}} \rangle / 2A$, where A is the atomic number of one colliding nucleus. It clearly shows that different collision systems are consistent under this scaling at a specific collision energy. This indicates the multiparticle production in heavy-ion collisions not only depends on N_{part} but also the geometry of the nuclei. Figures from Ref. [17].

36

1-7 The 2nd (v_2 , red) and 3rd (v_3 , blue) anisotropic coefficient of charged particles as a function of p_T in multiple collision centrality ranges in PbPb collisions at $\sqrt{s_{\text{NN}}} = 5.02$ TeV [24]. The curves represent calculations made with the CUJET 3.0 [25] and the SHEE models [26]. . .

38

1-8 p_T -Integrated v_2 of charged particles as a function of centrality measured by STAR [29] in AuAu collisions at 200 GeV (rectangle) and ALICE [30] in PbPb collisions at 2.76 TeV (circle). Data is fitted using a hybrid approach VISHNU [31], providing parameter $\eta/s = 0.16$ at RHIC and $\eta/s = 0.20$ at LHC, and the curves with $\eta/s = 0.16, 0.24$ with LHC configuration is shown as reference. Monte Carlo KLN (MC-KLN) [32] Model is picked to calculate initial particle production, and the same fit using Glauber Model [33] is also performed in Ref. [27]. Figure from Ref. [27].

39

2-3 CMS L1 output rate (top) and physics stream output rate after HLT (bottom) as a function of time in Fill 7467 of Pb-Pb collisions at $\sqrt{s_{\text{NN}}} = 5$ TeV.	59
2-4 Energy in GeV after background subtraction correlated with ADC count (left) and input charge (right) studied in low pile-up pp colli- sions at $\sqrt{s} = 13$ TeV.	60
2-5 Centrality distributions for HFOR (black circles) and HFAND && HFOR selection (red circles).	61
2-6 Distribution of the sum E_{T} measured in the HF calorimeters with minimum-bias event sample divided into centrality classes.	62
2-7 Efficiency of the L1 centrality triggers in minimum-bias events trig- gered by HFAND in PbPb collisions at $\sqrt{s_{\text{NN}}} = 5.02$ TeV as a function of the offline event centrality.	62
2-8 L1 (left) and HLT (right) trigger efficiency as a function of the lead- ing offline jet p_{T} evaluated in minimum-bias pp events. The vertical lines correspond to jet p_{T} of 60 and 80 GeV/c respectively. The error function fits used to parametrise the efficiency are superimposed.	64
2-9 L1 (left) and HLT (right) trigger efficiency as a function of the leading offline jet p_{T} evaluated in minimum-bias PbPb events. The vertical lines correspond to jet p_{T} of 60, 80, and 100 GeV/c respectively. The error function fits used to parametrise the efficiency are superimposed.	64
2-10 p_{T} distributions of all jets for events triggered with different HLT paths in pp (left) and PbPb (right) collisions after prescale and trigger effi- ciency correction.	65
2-11 Flowchart for D^0 triggers utilized in pp and PbPb collisions at $\sqrt{s_{\text{NN}}} =$ 5.02 TeV with CMS.	66
2-12 D^0 HLT (right) and corresponding L1 seed (left) efficiencies versus p_{T} of leading D^0 fulfilling online D^0 selection requirements in pp collisions at $\sqrt{s_{\text{NN}}} = 5.02$ TeV.	67
2-13 D^0 HLT (middle) and corresponding L1 seed (left) efficiencies versus p_{T} of leading D^0 fulfilling online D^0 selection requirements in PbPb collisions at $\sqrt{s_{\text{NN}}} = 5.02$ TeV. Fit on the plateau region of HLT efficiency is shown in the right panel.	68

3-1	Normalized decay length (top) and secondary vertex (bottom) distributions of D^0 mesons. Red and green lines measure distributions of D^0 matching generated truth and from sideband subtraction in MC simulations. Blue lines in the upper panel present variable distributions from data with background subtraction, while the blue lines in the bottom panel show ratio of output from data over MC. Results are shown with (right) and without (left) reweighting MC simulations.	71
4-1	Tracking efficiency (left) and fake rate (right) as a function of p_T for centrality inclusive PbPb events estimated in PYTHIA +HYDJET simulations.	77
4-2	ΔM ($M_{K\pi\pi} - M_{K\pi}$ or $M_{K\pi\pi\pi} - M_{K\pi\pi\pi}$) distribution fits of 3-prong (top) and 5-prong (bottom) D^* candidates with $p_T > 5$ GeV/c (left) and $p_T > 13$ GeV/c (right) in pp collisions at 5.02 TeV.	79
4-3	(Left) Ratio of production of 5-prong and 3-prong D^* as a function of p_T thresholds in pp collision data; (Right) relative tracking efficiencies of data and MC as a function of p_T thresholds.	80
5-1	Charm quarks created in the initial hard scatterings partly fragment into D^0 meson. The fragment fraction is $f(c \rightarrow D^0) = 0.6176 \pm 0.0160$ in pp collisions [129]. D^0 mesons propagate with a relatively long displacement ($c\tau = 123.03 \pm 0.45\mu\text{m}$ [128]) and decay into K and π with branching ratio of $\text{BR}(D^0 \rightarrow K\pi) = (3.89 \pm 0.04)\%$ [128]. The charged particles K and π are detected by the trackers and are reconstructed by the scenario described in Section 4.1.	84
5-2	Distributions of D^0 cut variables $d_0/\text{Err}(d_0)$ (left) and secondary vertex probability (right) of background (blue) and signal (red) candidates at $6 < p_T < 8$ GeV/c in Pb-Pb collisions.	87
5-3	Definition of quantities applied in cut optimization. s and b are the expected number of signal yield and background counts in the signal region after the selections, which are used to calculate the significance ($s/\sqrt{s+b}$). They are estimated by selection efficiencies and the yields of signal (s') and background (b') before the selections. b' is calculated by b'_{sideband} , the number of background in sidebands.	88

5-4	Signal efficiency (blue solid line) and background efficiency (red solid line) versus signal efficiency from classification by TMVA with rectangular cuts for D^0 at $5 < p_T < 6$ GeV/c in Pb-Pb collisions.	89
5-5	Statistical significance ($s/\sqrt{s+b}$) versus signal efficiency for D^0 at $5 < p_T < 6$ GeV/c (left) and $15 < p_T < 20$ GeV/c (right) in Pb-Pb collisions.	90
5-6	Examples of D^0 candidate invariant mass distributions at $5 < p_T < 6$ GeV/c (left) and $25 < p_T < 30$ GeV/c (right) in pp (top) and Pb-Pb (bottom) collisions.	91
6-1	Efficiency ($\alpha \times \epsilon_{\text{reco}} \times \epsilon_{\text{sel}}$) as a function of p_T of prompt (red) and non-prompt (blue) D^0 in pp collisions (left) and Pb-Pb collisions in the inclusive centrality range (middle) and in most central events (0–10%) (right).	95
6-2	Diagram of prompt (left) and non-prompt (right) D^0 . Prompt component is defined by D^0 directly fragmented from charm quark, while non-prompt D^0 from b-hadron decays. Distance of Closest Approach (DCA) is defined by the distance between primary vertex and the direction of the momentum of D^0 . Non-prompt D^0 is featured by a large DCA due to the displacement of their parent b-hadrons, and therefore DCA is possibly used to distinguish the two components.	96
6-3	DCA distribution of prompt and nonprompt from MC simulations (left top) in pp collisions at $6 < p_T < 8$ GeV/c; Invariant mass distributions and sideband scales (left bottom); DCA fit of data by the MC templates smeared to achieve best χ^2 probability (middle top) and the ratio of data over fit (middle bottom); Prompt fractions by randomly varying MC and data DCA distribution according to their statistic uncertainties (right top and bottom).	97
6-4	DCA distribution of inclusive D^0 in data (black circles), of prompt D^0 (red histogram) from simulations, and of non-prompt D^0 (blue histogram) from simulations at $10 < p_T^{D^0} < 12.5$ GeV/c in pp (left) and PbPb (right) collisions. As a fitting parameter, the fraction of the red histogram implies the fraction of prompt components in data.	98

6-5 Fraction of prompt D^0 (f_{prompt}) as a function of p_T in pp events (left), PbPb events in centrality class 0 – 100% (middle), and PbPb events in centrality class 0 – 10% (right). The error bars and the boxes indicate statistic and systematic uncertainties.	98
6-6 $D^0 f_{\text{prompt}}$ versus p_T via fitting data DCA with template fixed from MC (black markers), and with template floating resolution (green markers). The two panels show results in pp (left) and PbPb (right) collisions. In the left panel, $f_{\text{prompt}}^{\text{fonll}}$ obtained based on FONLL calculation is presented by red markers. In the right panel, $f_{\text{prompt}}^{\text{fonll}}$ is displayed by color shadow. The shadow cover variation of R_{AA} measured for B^+ and non-prompt J/ψ	100
6-7 The p_T -differential production cross section of prompt D^0 mesons in pp collisions at $\sqrt{s_{\text{NN}}} = 5.02$ TeV. The vertical bars (boxes) correspond to statistical (systematic) uncertainties. The global systematic uncertainty, listed in the legend and not included in the point-to-point uncertainties, comprises the uncertainties in the integrated luminosity measurement and the D^0 meson \mathcal{B} . Results are compared to FONLL [49] (orange) and GM-VFNS [51, 52, 53] (green) calculations.	102
6-8 The p_T -differential production yields of D^0 mesons divided by the nuclear overlap functions T_{AA} for PbPb collisions in the 0–100% (red) and 0–10% (blue) centrality ranges compared to the pp cross sections (black) which is same with Figure 6-7.	104
6-9 Prompt $D^0 R_{\text{AA}}$ as a function of p_T in the centrality range 0–100% (left) and 0–10% (right). The vertical bars (boxes) correspond to statistical (systematic) uncertainties. The global systematic uncertainty, represented as a grey box at $R_{\text{AA}} = 1$, comprises the uncertainties in the integrated luminosity measurement and T_{AA} value. The prompt $D^0 R_{\text{AA}}$ values are also compared to calculations from various theoretical models [134, 135, 136, 137, 138, 139, 140, 141, 142, 143, 144].	105

6-10 (Left) Prompt D^0 nuclear modification factor R_{AA} as a function of p_T in the centrality range 0–100% (green squares) [131] compared to the R_{AA} of charged particles (red circles with yellow boxes) [34], B^\pm mesons (blue triangles) [149], nonprompt D^0 (purple crosses) and nonprompt J/ψ meson (red crosses and stars) [150] in the same centrality range at 5.02 TeV. (Right) D^0 nuclear modification factor R_{AA} as a function of p_T in the centrality range 0–10% (green squares) [131] compared to the R_{AA} of charged particles (red circles with yellow boxes) [34] in the same centrality range. The error bars (boxes) indicate statistical (systematic) uncertainties.	109
6-11 Prompt D^0 nuclear modification factor R_{AA} as a function of p_T in the centrality range 0–100% (green squares) [131] compared to the R_{AA} of prompt J/ψ meson (orange crosses and stars) [150] in the same centrality range at 5.02 TeV.	111
6-12 (Left) Prompt D^0 nuclear modification factor R_{AA} as a function of p_T in the centrality range 0–100% performed by CMS collaboration in PbPb collisions at 2.76 TeV; (Right) Prompt D^0 nuclear modification factor R_{AA} as a function of p_T in the centrality range 0–10% performed by CMS (green) and ALICE (red) [152] collaboration in PbPb collisions at 5.02 TeV, and by STAR collaboration (black) in AuAu collisions at 200 GeV [153].	112
6-13 $D^0 R_{AA}$ measured in PbPb collisions at $\sqrt{s_{NN}} = 5.02$ TeV (blue) compared with heavy-flavor muon R_{AA} measured in PbPb collisions at $\sqrt{s_{NN}} = 2.76$ TeV (black) [97] as a function p_T . R_{AA} of inclusive charged particles in PbPb collisions at $\sqrt{s_{NN}} = 2.76$ TeV (red) [44] is also presented. Figure from Ref. [97].	113
7-1 Definition of the coordinate system.	119
7-2 (Top) Event-plane angle distributions for HF^+ before (black curves) and after (red curves) flattening for harmonics $n = 2, 3, 4, 5, 6$. (Bottom) Correlations of before and after event-plane angles.	122
7-3 Event-plane angle distributions for HF^- and HF^+ before corrections (top panels), after flattening (middle panels) and after both recentering and flattening corrections are applied. The results are for the $n = 2$ harmonic.	123

7-4 (Left) Simultaneous fit to the invariant mass spectrum and $v_2^{S+B}(m_{\text{inv}})$ in the p_T interval 4–5 GeV/c in PbPb collisions in the centrality class 10–30%. (Right) Simultaneous fit to the invariant mass spectrum and $v_3^{S+B}(m_{\text{inv}})$ in the p_T interval 5–6 GeV/c in PbPb collisions in the centrality class 30–50%.	126
7-5 Prompt D^0 fraction with (blue) and without (red) for centrality 0–10% (left), 10–30% (middle) and 30–50% (right).	127
7-6 D^0 mass spectrum fit in $\Delta\phi$ bins for v_2 in p_T 5 – 6 GeV/c in PbPb collisions in the centrality range 10 – 30%.	128
7-7 Fit for v_2 on $d^2N/(dp_{\text{T}}d\Delta\phi)$ in p_T 5 – 6 GeV/c in PbPb collisions in the centrality range 10 – 30%.	129
7-8 D^0 efficiency as a function of p_T .	130
7-9 Prompt $D^0 v_2$ coefficient at midrapidity ($ y < 1$) as a function of p_T from scalar product (SP) method (red) and $\Delta\phi$ bins method (blue) in PbPb collisions in the centrality range 0–10% (left), 10–30% (middle) and 30 – 50% (right).	130
7-10 Prompt D^0 (red) and charged particle (black) v_2 coefficient at midrapidity ($ y < 1$) as a function of p_T in PbPb collisions in the centrality range 0 – 10% (left), 10 – 30% (middle) and 30 – 50% (right). The vertical bars represent statistical uncertainties, grey bands represent systematic uncertainties from nonprompt D^0 mesons and open boxes represent other systematic uncertainties. Various theoretical calculations for prompt D^0 meson v_2 coefficient [140, 146, 143, 145, 135] are also plotted for comparison.	131
7-11 Prompt D^0 (red), charged particle (black) and nonprompt J/ψ (blue) v_2 coefficient as a function of p_T in PbPb collisions. D^0 and charged particles are measured in $ y < 1$ in PbPb collisions at 5.02 TeV in the centrality range 10 – 30%, while nonprompt J/ψ is measured in $ y < 2.4$ ($1.6 < y < 2.4$ for different p_T ranges) in PbPb collisions at 2.76 TeV in the centrality range 10 – 60%.	132

8-4 Jet transverse momentum response for quark, gluon, and inclusive jets as a function of generated jet p_T in PYTHIA and in different event collision centrality intervals in PYTHIA +HYDJET after the jet energy correction for inclusive jet.	144
8-5 Averaged p_T ratio $\mu_{p_T^{\text{reco}}/p_T^{\text{gen}}}$ as a function of n_{CS} for jets with $70 < p_T^{\text{reco}} < 80$ GeV/c (black markers) for pp collisions (left) and PbPb collisions at centrality class of 0 – 30% (middle) and 30 – 100% (right). A linear fitting (blue line) and the same quantity after correction (red markers) are also shown.	145
8-6 p_T -dependence of the jet energy resolution after correction from PYTHIA (left) and from PYTHIA +HYDJET at centrality class of 0 – 30% (middle) and 30 – 100%.	146
8-7 Signal event of a genuine correlation of D-jet compared to the background events due to the presence of at least one object (jet or D^0) coming from the underlying event.	147
8-8 r distribution of D^0 with $4 < p_T^D < 20$ GeV/c in PbPb collisions before background subtraction (black), the background contributions subtracted (Purple), and the result after background subtraction (orange) with event mixing methods.	149
8-9 Genuine type of uncorrelated event that enters the η -reflection subtraction and therefore it is statistically subtracted with this procedure.	150
8-10 Distributions of D^0 mesons in jets as a function of the distance from the jet axis for jets of $p_T^{\text{jet}} > 60$ GeV/c and $ \eta^{\text{jet}} < 1.6$ measured in pp and PbPb collisions at $\sqrt{s_{\text{NN}}} = 5.02$ TeV. The measurement is performed in the $D^0 p_T^D$ range 4 – 20 GeV/c (left) and for $p_T^D > 20$ GeV/c (right). Each spectrum is normalized to its integral in the region $0 < r < 0.3$. The vertical bars (boxes) correspond to statistical (systematic) uncertainties.	151
8-11 Distributions of D^0 mesons in jets as a function of the distance from the jet axis for jets of $p_T^{\text{jet}} > 60$ GeV/c and $ \eta^{\text{jet}} < 1.6$ measured in pp and PbPb collisions at $\sqrt{s_{\text{NN}}} = 5.02$ TeV. The predictions from the PYTHIA 8 event generator are also superimposed, and in the bottom panel the ratios of the D^0 radial distributions of pp over PYTHIA 8 predictions are presented.	152

8-12 The ratios of the D^0 radial distributions of PbPb to pp in the D^0 p_T^D range $4 - 20$ GeV/c (left) and for $p_T^D > 20$ GeV/c (right).	152
9-1 D^0 nuclear modification factor R_{AA} (left) and elliptic flow coefficient v_2 (right) as a function of p_T in PbPb collisions at $\sqrt{s_{NN}} = 5.02$ TeV in the centrality class of 0–10% and 30–50% respectively from PHSD with (solid line) and without (dashed line) shadowing effects. Figure from Ref. [183].	158
9-2 Calculations of D^0 nuclear modification factor R_{AA} (up), elliptic flow v_2 (middle) and triangle flow v_3 (bottom) as a function of p_T in PbPb collisions at $\sqrt{s_{NN}} = 5.02$ TeV under different configurations; The simulations apply both energy loss model ($\alpha\Gamma_{flow}$, $\xi T^2\Gamma_{flow}$) and Langevin-based model (M&T, G&A) with two sets of parameters for both. The bands are obtained by varying decoupling temperature $120 < T_d < 160$ MeV. Figures from Ref. [184].	160
9-3 Comparison of the heavy quark dimensionless spatial diffusion coefficient at zero momentum $D_s 2\pi T$ ($p = 0$) versus temperature across multiple approaches. Figure from Ref. [186].	161
9-4 Comparison of the heavy quark dimensionless momentum diffusion coefficient at $p = 10$ GeV (\hat{q}/T^3 ($p = 10$ GeV)) versus temperature across multiple approaches. Figure from Ref. [186].	163
9-5 Langevin simulation of D^0 nuclear modification factor R_{AA} as a function of p_T in PbPb collisions at $\sqrt{s_{NN}} = 5.02$ TeV in the centrality class of 0–100% from with (solid line) and without (dashed line) the chromo-electromagnetic field fluctuations. Figure from Ref. [191].	164
9-6 Calculations of D^0 nuclear modification factor R_{AA} (up), elliptic flow v_2 (middle) and triangle flow v_3 (bottom) as a function of p_T in PbPb collisions at $\sqrt{s_{NN}} = 5.02$ TeV with solid line) and without (dashed line) coalescence hadronization on top of fragmentation taken into account. Figures from Ref. [184].	165
9-7 v_2 (top) and R_{AA} (bottom) calculated from POWLANG for D mesons and charm quark in PbPb collisions at $\sqrt{s_{NN}} = 5.02$ TeV in the centrality class of 30–50%. Two sets of transport coefficients are applied. Figure from Ref. [192].	166

9-8 (Left) Projected performance of nuclear modification factors of charged particles, D^0 , B^+ and non-prompt J/ψ in CMS in Pb-Pb collisions for $\mathcal{L}_{\text{int}} = 10 \text{ nb}^{-1}$; (Right) Projected v_2 of charged particles and D^0 with the expected statistics of minimum-bias event $\mathcal{L}_{\text{int}} = 0.2 \text{ nb}^{-1}$ compared to theoretical predictions of $D^0 v_2$	168
9-9 (Left) Normalized χ^2 as a function of spatial diffusion coefficient ($2\pi TD_s$) under different experimental precision from an Fokker-Plank transport model; (Right) Coefficient range (90% credibility region) in the phase plane of $2\pi TD_s$ vs T/T_c under different experimental precision, estimated by a model-to-data Bayesian analysis using an improved Langevin framework.	169
9-10 Projection for the radial distribution of D^0 mesons in jets as a function of the distance from the jet axis for jets of $p_T > 60 \text{ GeV}/c$ in Pb-Pb collisions divided by the distribution in pp collisions with integrated luminosity $\mathcal{L}_{\text{int}}^{\text{PbPb}} = 10 \text{ nb}^{-1}$ and $\mathcal{L}_{\text{int}}^{\text{pp}} = 650 \text{ pb}^{-1}$	170

List of Tables

1.1	Measurements of open heavy flavor decay leptons in heavy-ion collisions.	54
2.1	Summary of luminosity of collisions performed in LHC for heavy-ion physics.	56
2.2	HLT paths and corresponding L1 seeds utilized in analysis discussed in Section 8.	63
2.3	L1 jet trigger seeds for D^0 trigger paths in 2015 pp and PbPb collisions at $\sqrt{s_{\text{NN}}} = 5.02$ TeV with CMS. The strategy of trigger combinations applied in high- p_T D^0 analyses are also presented.	66
4.1	Tracking iterations employed in 2015 Pb-Pb run by CMS and their targeting tracks.	74
6.1	Track selection criteria applied in the R_{AA} analysis at low and high p_T .	94
6.2	The selection criteria on D^0 candidates in different p_T intervals applied in prompt $D^0 R_{\text{AA}}$ analysis.	94
6.3	Summary of implement configurations of theoretical models in the current market.	107
6.4	Summary of relative systematic uncertainties for R_{AA} in Pb-Pb collisions at 5.02 TeV in the centrality class of 0–100%.	115
6.5	Summary of relative systematic uncertainties for R_{AA} in Pb-Pb collisions at 5.02 TeV in the centrality class of 0–10%.	116
7.1	The selection criteria on D^0 candidates in different p_T intervals applied in prompt $D^0 v_n$ analysis.	118
7.2	Summary of systematic uncertainties for v_2 . Absolute uncertainties are assigned.	136

7.3	Summary of systematic uncertainties for v_3 . Absolute uncertainties are assigned.	137
8.1	Summary table of the optimal selections on D^0	142
8.2	Summary of relative systematic uncertainties in pp collision.	154
8.3	Summary of relative systematic uncertainties in PbPb collision.	155

Chapter 1

Introduction

1.1 The Big Bang: Quark Gluon Plasma

1.1.1 QCD Phase Diagram

Over the past decades, Quantum Chromodynamics (QCD) achieved a great success in describing the strong interactions of quarks and gluons. In the view of QCD, each quark carries one of three color charges, while gluons carry both a color charge and an anticolor charge. Although quark model works very well, no free quarks have been detected. In fact, no color-charged particle is observed as free particles. The normal states (called hadrons) are all color-neutral — mesons ($q\bar{q}'$) are bound states of quarks and antiquarks, while baryons (qqq) are made of 3 quarks. The feature that color-charged particles are always constrained to color singlet states is called color confinement. The coupling constant α_s is one of the fundamental parameters of QCD, indicating the strength of interactions. Despite the word “constant” in its name, α_s is featured by varying as a function of the energy scale of the specific interaction. In the framework of perturbative QCD (pQCD), the coupling constant can be solved from the renormalization group equation. In a process with momentum transferred of Q , to leading order, the solution is

$$\alpha_s(Q^2) = \frac{12\pi}{33 - 2n_f} \left(\ln \frac{Q^2}{\Lambda_{\text{QCD}}^2} \right)^{-1} \quad (1.1.1)$$

where n_f is the number of quark flavors considered. Λ_{QCD} is a constant from integration. Its value is determined by experiments ($\Lambda_{\text{QCD}} \simeq 200$ MeV), and it is the scale

where perturbation approximation is valid. The absolute scale of α_s is conventionally represented by its value at Z mass, $\alpha_s(M_Z^2)$. $\alpha_s(M_Z^2)$ have been determined by multiple experiments, and the world average is $\alpha_s(M_Z^2) = 0.1181 \pm 0.0011$ [1]. Looking back to Eq. (1.1.1), as the energy scale increases, the scaling constant decreases rapidly. This introduces another feature of QCD: asymptotic freedom – although it is impossible for particles carrying color to propagate freely, the strong interaction between colored particles becomes weaker as Q increases. The right panel of Figure 1-1 presents the summary of α_s measurements versus the momentum transferred Q [1]. As a parameter introduced in pQCD rather than a real physical observable, extraction of α_s is theory-dependent. In Figure 1-1, the text in parentheses indicates the order of perturbation utilized corresponding to each data point. NLO is next-to-leading order, NNLO is next-to-next-to-leading order (res. stands for resummation to next-to-leading logs), and N^3LO is next-to-NNLO. Figure 1-1 clearly shows the evidence of the decreasing α_s as the energy increases as expected.

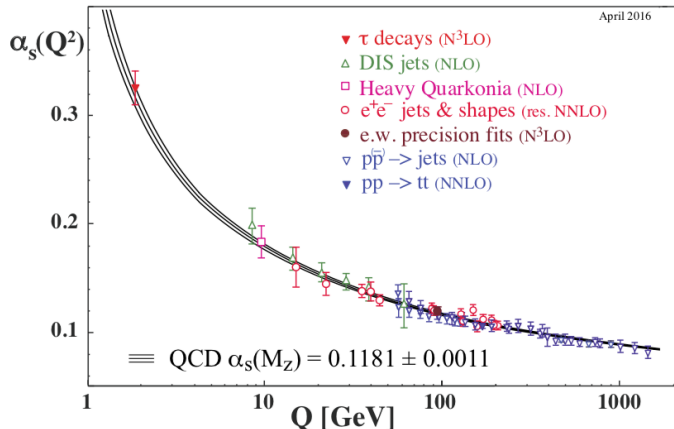


Figure 1-1: Measurements of the renormalized coupling constant α_s as a function of Q . Figure from Ref. [1].

This feature raises an interesting question: what will happen when energy density becomes extremely high? According to the prediction of QCD, different from the ordinary matter in the macroscope, the confinement of quarks and gluons in hadrons is relaxed and they are free from being bounded. This state is called quark-gluon plasma (QGP). This state is particularly interesting initially because it is believed that QGP existed in early universe. During $\sim 10^{-6}$ s after the big bang, the universe was filled with extremely hot and dense matter where quarks and gluons moved with near light velocity. The partons carried colors but were not bounded together with

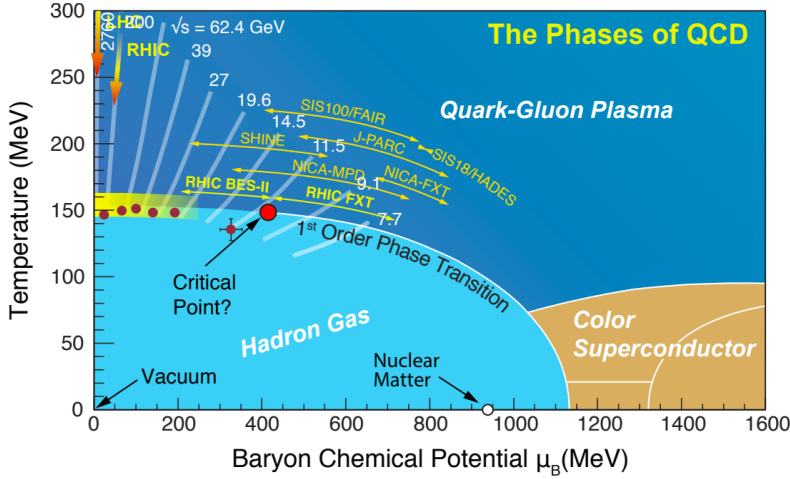


Figure 1-2: The QCD phase diagram in the scope of current knowledge in terms of temperature T and baryon number chemical potential μ_B . With help of lattice QCD calculations, the cross-over at small μ_B (yellow shadow) is well understood, while the predicted critical point to 1st order transition is under exploration. Figure from Ref. [2].

weak interaction due to the high temperature. Then the system expanded quickly, and consequently after a short time quarks and gluons were hadronized into regular hadron matter as temperature decreased rapidly.

Figure 1-2 shows the phase diagram of QCD matter in the scope of current knowledge in terms of T and μ_B , where T is the temperature of the medium and μ_B is the baryon chemical potential. QGP is located at the high temperature region. When temperature and μ_B are both relatively low, ordinary hadron gas is observed. Near $\mu_B = 0$, with temperature increasing, the deconfinement of color particles in hadron gas happens and QGP is produced. This transition is a cross-over and can be calculated with decent accuracy by lattice QCD. More details will be discussed in the following paragraphs. At $\mu_B \sim 400$ MeV, a critical point changing from cross-over to first-order phase transition is predicted. It has not been known whether such a point exists, and the experiment designed to scan low energy region like Phase 2 of the Beam Energy Scan at RHIC (BES-II) is scheduled to search this point and explore the transition in the intermediate-to-high μ_B region. Finally, in the region at low temperature with sufficiently high baryon chemical potential, the color superconductivity (CSC) is predicted [3]. CSC is characterized by a condensate of Cooper pairs formed by quarks near the Fermi surface, which is similar to the electron pairs emerging in superconductivity. This region is particularly interesting because it is believed that

CSC happens in the core of a compact star [4].

1.1.2 Thermodynamics: Equation of State

Quark gluon deconfinement predicted at high temperature may lead to a wrong impression that the particles are totally free like gas in QGP. In fact, the name plasma reveals the fact that the deconfined constituents in QGP strongly interact with their neighbors. Later we will see the nature of QGP is more like liquid instead of gas, and is described well by hydrodynamic models. Before discussing hydrodynamics, we start with the thermodynamic description of QGP — the equation of state (EoS), which is an important input of hydrodynamics. We can also extract information concerning the phase transition and the properties of QGP by EoS itself. First, the partition function is naturally introduced since the thermodynamic observables can be obtained from the partition function with the proper derivatives. For example, the pressure and the energy density are

$$p = \frac{\partial(T \ln Z)}{\partial V}, \quad \epsilon = \frac{T^2}{V} \frac{\partial \ln Z}{\partial T} \quad (1.1.2)$$

There are some other useful observables, and they are connected by the relation

$$I = \epsilon - 3p, \quad s = \frac{\epsilon + p}{T} \quad (1.1.3)$$

where the first quantity is called trace anomaly. The grand canonical partition function of QCD as an SU(3) gauge theory with fermions having mass m and chemical potential μ is

$$Z(V, \mu_f, T; g, m_f) = \int DAD\bar{\psi}D\psi e^{-S_g[A_\mu]}e^{-S_f[\bar{\psi}, \psi, A_\mu]} \quad (1.1.4)$$

where S_g and S_f are the Euclidean gauge and fermion actions respectively. After integrating over the fermion fields ψ_f , with N_f fermion flavors, Eq. (1.1.4) becomes

$$Z(T, \mu) = \int DU e^{-S_g[U]} \prod_{f=1}^{N_f} \det M(m_f, \mu, T) \quad (1.1.5)$$

where M is the Dirac operator of the fermion action selected.

Solving QCD thermodynamic equation was a difficult task for a long time, while

thanks to the improvement of computing powers, nowadays the numerical simulations on lattice [5] are employed. A typical lattice setup of a hypercubic lattice includes spatial extent N_s , temporal extent N_τ and lattice spacing a . The temperature varies by changing the lattice spacing $T = (aN_\tau)^{-1}$. Figure 1-3 presents one lattice calcula-

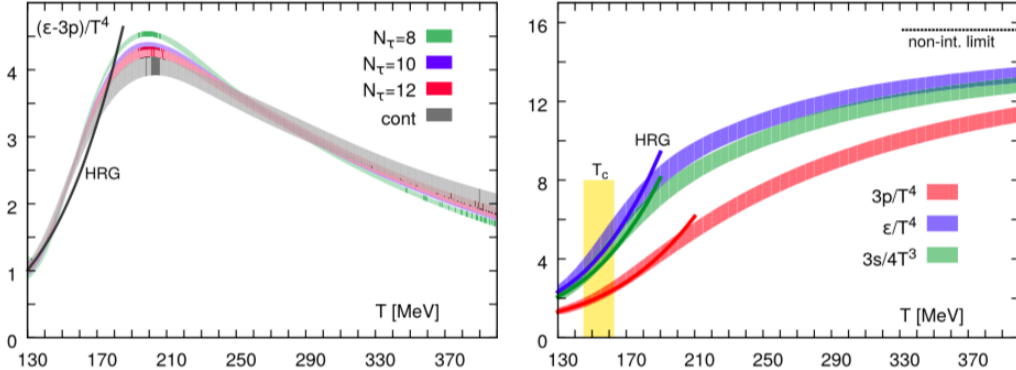


Figure 1-3: (Left) The trace anomaly as a function of temperature under different N_τ and the continuum extrapolation; (Right) The continuum extrapolation of the renormalized pressure, energy density and entropy density as a function of temperature. The yellow vertical shadow indicates the cross-over region, and the black dash line labels the ideal gas limit (Stefan-Boltzmann limit) for the energy density; The dark solid lines in both panels correspond to the prediction of the hadron resonance gas models (HRG). Figure from Ref. [6].

tion of the EoS at vanishing chemical potential in (2+1)-flavor QCD [6]. $\mu_B = 0$ is a good limit for high-energy experiments like LHC where the baryon chemical potential is negligible. This calculation picks the highly improved staggered quark (HISQ) [7] action, and “(2+1) flavor” refers to the 3 parameters — the gauge coupling $\beta = 10/g^2$, the light-quark mass $m_l = m_u = m_d$ and the heavier-quark mass m_s . Looking at the right-hand panel in Figure 1-3, in the temperature region below T_c , the thermodynamic quantities are well calculated by the hadron resonance gas models (HRG). In the yellow shadow region ($T_c = 154 \pm 9$ MeV), the energy density increases rapidly, corresponding to new degrees of freedom, which implies deconfinement of colored particles in the transition from hadron gas to QGP. The figure also indicates the transition is a continuous cross-over instead of a first-order transition. Above T_c , it is observed that the energy density of QGP is still far from the ideal gas limit (dot line in right panel) up to $T = 400$ MeV. It clearly indicates that the QGP produced in current heavy-ion experiments is far from the picture of non-interacting constituents, but strongly couple in short spatial scale. This situation will eventually converge into

the gas limit at $T \rightarrow \infty$ though. In classic plasma study, to determine whether a fluid is strongly coupled, the interaction energy is compared with the thermal energy, and this is characterized by the couple parameter Γ . In QGP, a similar parameter is introduced as $\Gamma = Cg^2/(dT)$ [8], where C is the Casimir invariant, g the strong coupling parameter, d the average distance between particles, and T the temperature. We consider the situation with $T \sim 200$ MeV and $g \simeq 2$. Using a lattice QCD calculation [9] for rough estimation, the particle density at $T \sim 200$ MeV is $\bar{n} \simeq 5T^3$ that leads to $d \simeq 1/\sqrt[3]{\bar{n}} \simeq 0.6$ fm. This brings $\Gamma \sim 10 - 20 \gg 1$ for quarks and gluons indicating strong interaction compared with thermal fluctuations.

1.2 The Little Bang: Heavy-ion Collisions

Inspired by the dense matter emerging after the Big Bang, relativistic heavy-ion collisions are used to reproduce the extreme conditions so as to study the QCD matter at extraordinary high temperature and high density. That is, two energetic heavy ions collide, and generate events with much higher multiplicity than the case in proton-proton collisions. Now heavy-ion experiments are mainly carried out in the Relativistic Heavy-Ion Collider (RHIC) at Brookhaven and the Large Hadron Collider (LHC) at CERN. RHIC collides ions like uranium, copper and gold at the center of mass energy from 7.7 GeV to 200 GeV, while LHC uses lead and xenon at TeV energy scale. They conduct heavy-ion experiments to study systems with different temperatures and sizes. Figure 1-4 illustrates the evolution of the system during relativistic heavy-ion collisions.

1.2.1 Initial Stage and Particle Production

As the name indicates, before collisions two ultra-relativistic heavy ions approach each other with velocity close to light. They look like two disks due to length contraction. Taking 5.02 TeV lead-lead (PbPb) collisions at LHC as an example, the contraction factor is $\gamma = 1/\sqrt{1-v^2} \simeq 2500$. With the two nuclei crossing through each other, collisions between the nucleons happen and a huge number of new particles are produced. At the very early time after collisions, hard processes (processes with large Q value) take place at $\tau \sim 1/Q$ due to the uncertainty principle, and high- p_T particles are created. Although these events rarely happen, those very energetic particles turn out to be good probes of QGP (called hard probes). QGP exists during

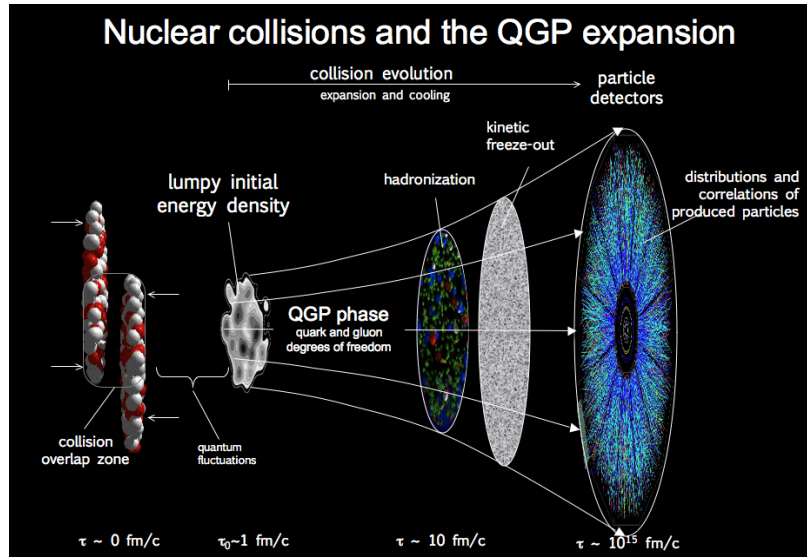


Figure 1-4: Sketch of evolution of relativistic heavy-ion collisions with proper time τ . The moment two nuclei collide is taken as $\tau = 0$. Two ultra-relativistic heavy ion approach each other with velocity close to light and cross through each other. Meanwhile, hundreds of nuclei interact, create a strongly interacting field, and generate numerous particles. During $\tau \sim 1 \text{ fm}/c$, particles interact with each and force the system to equilibrium, and fluid-like matter with extremely high temperature and high density emerges. With the matter expands and temperature decreases, the free partons are fragmented into hadronizations, and these hadrons or their decay daughters are detected by detectors. Figure from [10].

so short a time that the medium is difficult to probe by inputting probe particles. Fortunately, the hard particles are created at very beginning and thus experience the whole evolution of the system from initial scatterings to the final hadron states. They interact with the particles in QGP and are changed by the existence of the medium. Therefore we can gain knowledge of the strong interactions between colored particles and extract interesting properties of QGP by comparing their final states with the well known initial states. A straightforward idea of calculating the initial scattering cross section is to multiply the number of binary collisions with the cross section of individual proton-proton collisions. This idea is specified in the calculation procedure called Glauber Model [11]. The number of binary collisions is called N_{coll} , and a similar but different physics-meaning variable is the number of nucleons colliding with other nucleons N_{part} . Generally in the experiments, N_{coll} and N_{part} cannot be measured directly, but calculated by model and other observables. As a test of validity of Glauber Model, the production of high- p_{T} (large transverse momenta) electricweak bosons in heavy-ion collisions are measured [12, 13, 14, 15, 16], since they do not participate in strong interactions and are not affected by the medium produced. Therefore, the final state detected reflects the initial condition. Figure 1-5 shows consistency of Z , W production in PbPb collisions with pQCD calculation in different N_{part} classes calculated by Glauber model. Therefore, fortunately we have a well-defined description of the hard process which is an important input for studying thermalization in the later stages.

Sequentially softer processes ($Q \sim 1$ GeV) occur at about 0.2 fm/c, and produce a huge number of low- p_{T} new particles. The probability of these kind of processes is much higher than that of hard scatterings, so the multiplicity (total number of particles) measured in the final states is mostly determined at this stage. It has been long observed that the multiplicity is approximately proportional to N_{part} indicating the number of participating particles. However, the case is not that simple. Figure 1-6 presents the recent measurements of charged particle production in xenon-xenon collisions conducted at LHC, showing the dependence of multiplicity on N_{part} is not the same for different collision systems, but different collision systems are consistent if renormalizing the atomic number A at the same collision energy.

As mentioned previously, it is predicted that the particles in the medium created in current heavy-ion experiments (like RHIC and LHC) strongly interact with neighbour particles. An immediate corollary is that the system possibly reaches thermal

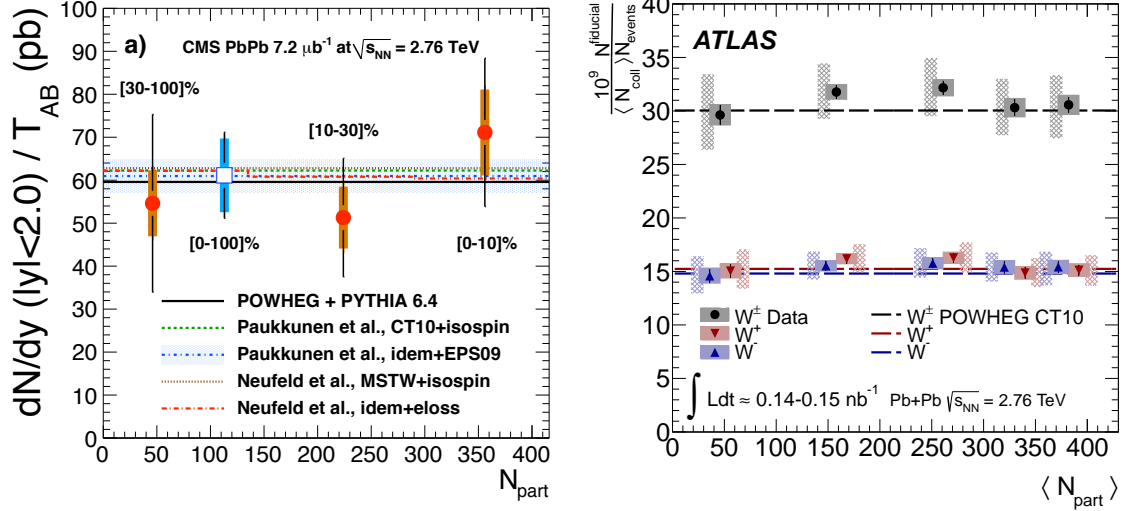


Figure 1-5: (Left) Differential yield of $Z \rightarrow \gamma\gamma$ dN/dy divided by the expected nuclear overlap function and as a function of $\langle N_{\text{part}} \rangle$ calculated by Glauber model compared with NLO QCD calculations. Figure from Ref. [14]; (Right) Production yield of W^+ (red), W^- (blue) and W^\pm (gray) boson per binary collision as a function of $\langle N_{\text{part}} \rangle$ calculated by Glauber model compared with an NLO QCD calculation. Figure from Ref. [13].

equilibrium. After collisions it takes a relatively short time $\sim 1 \text{ fm/c}$ to rapidly reach thermal equilibrium, which is impossible for weak-coupled systems. The thermalization process within this $\sim 1 \text{ fm/c}$ (called the pre-equilibrium stage) cannot be described by hydrodynamics, and is not yet completely understood. The initial energy density distributions after pre-equilibrium stage is another important input of the hydrodynamics. Although it is complicated to calculate the evolution of thermalization, the resulting average energy density can be roughly estimated and measured. In the case of Pb-Pb collisions at $\sqrt{s_{\text{NN}}} = 2.76 \text{ TeV}$, for the 5% most central collisions, the energy density per unit volume is estimated to be about 14 GeV/fm^3 at a time of $\tau_0 = 1 \text{ fm/c}$ after the collision [23].

1.2.2 Ideal Fluid and Hydrodynamics

After the pre-equilibrium stage, the QGP phase is formed and lasts a short time. During this time, the partonic matter expands and cools down. When the temperature is below the critical point as described in Section 1.1.1, the free quarks and gluons are constrained into hadron state again. This process takes $\sim 10 \text{ fm/c}$, and understanding

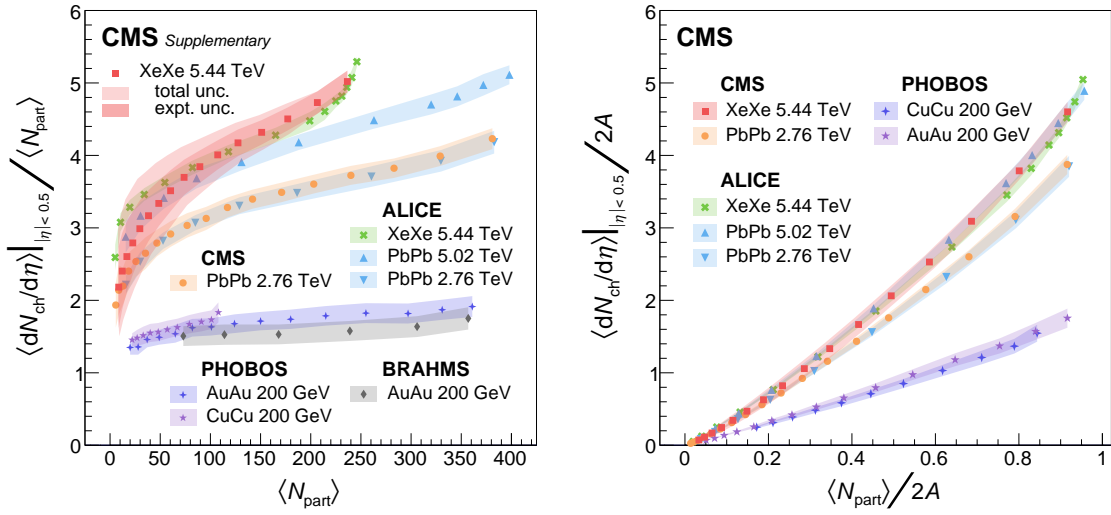


Figure 1-6: (Left) Average $dN_{ch}/d\eta$ normalized by $\langle N_{part} \rangle$ as a function of $\langle N_{part} \rangle$ measured in PbPb and XeXe collisions by the CMS [17] and ALICE [18, 19, 20] Collaborations and in CuCu and AuAu collisions by the PHOBOS [21] and BRAHMS [22] Collaborations. The bands around the data points denote the systematic uncertainties. Under the same collision energy and same $\langle N_{part} \rangle$, $dN_{ch}/d\eta$ is not same between PbPb and XeXe especially in the most central events (same situation for CuCu and AuAu); (Right) Average $dN_{ch}/d\eta$ normalized by $\langle N_{part} \rangle$ and $2A$ as a function of $\langle N_{part} \rangle / 2A$, where A is the atomic number of one colliding nucleus. It clearly shows that different collision systems are consistent under this scaling at a specific collision energy. This indicates the multiparticle production in heavy-ion collisions not only depends on N_{part} but also the geometry of the nuclei. Figures from Ref. [17].

the properties and dynamics in this short time is the most important task of heavy-ion collisions. In the experiments conducted over the past decades, many prominent phenomena have been observed, and the most striking one is probably the idea-fluid properties. Right after the initial collisions, we believe the parton spatial distribution is not isotropic. On the one hand, the wounded region overlapped by the two ions is not a sphere, but more like an “olive” geometrically. On the other hand, the two nuclei are not really two smooth balls. In microscopic scale, the nuclei are multiple nucleons, so they are actually so lumpy that the fluctuations create considerable anisotropy. If the interaction is weak, as with gas, the nucleons liberated from the nuclei move randomly. In consequence, the initial spatial anisotropy should be almost completely forgotten during propagation, and can not be detected in the detectors. In contrast, in the liquid-like case where the interaction between constitute particles is strong, the picture is totally different. The overlap part has a non-uniform density distribution and a pressure gradient consequently. Thus, the particles, especially those low-momentum particles, are driven by the collective motion (flow), and the final momentum distribution detected reflects the initial spatial anisotropy. This collective flow of soft particles has been observed in many heavy-ion measurements. The common observable quantifying this phenomenon is the Fourier coefficients in the azimuthal angle distribution (ϕ) of hadrons

$$\frac{dN}{d\phi} = A \left(1 + 2 \sum_n v_n \cos [n(\phi - \Phi_n)] \right) \quad (1.2.1)$$

Figure 1-7 shows v_2 and v_3 of charged particles as a function of p_T in different centrality classes. Centrality quantifies the degree of overlap of the two colliding nuclei, and is a variable corresponding to N_{part} . The smaller the centrality is, the larger N_{part} is, and the more two nuclei overlap. Figure 1-7 clearly presents non-zero v_2 and v_3 over a wide range of p_T , confirming the flow behavior. This is a strong argument of formation of the strong-interacting matter. In addition, on one hand observation of increasing v_2 with centrality increasing is consistent with the picture of greater initial anisotropy when two nuclei have a smaller fraction overlapping. On the other hand, the non-zero v_2 in most central events where the collision overlapping region is almost spherical confirms the important role of the fluctuation of nucleons in the nuclei. The finite v_3 is also a manifestation of the lumpy nuclei.

The early efforts on studying dynamics in heavy-ion collisions applied ideal fluid

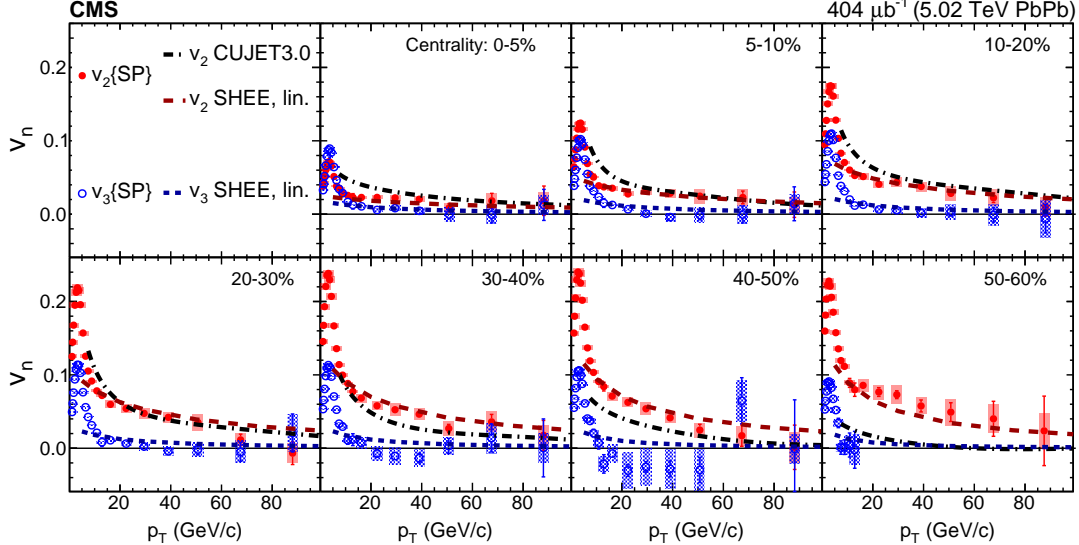


Figure 1-7: The 2nd (v_2 , red) and 3rd (v_3 , blue) anisotropic coefficient of charged particles as a function of p_T in multiple collision centrality ranges in PbPb collisions at $\sqrt{s_{NN}} = 5.02$ TeV [24]. The curves represent calculations made with the CUJET 3.0 [25] and the SHEE models [26].

hydrodynamics (zero mean-free-path limit $\lambda_{\text{mfp}} \sim 0$) on the whole evolution, which worked fairly well in central collisions [10]. This implied the feature of low viscosity, though this model failed in the more peripheral events. The variable specific viscosity η/s (ratio of shear viscosity to entropy density) is used to quantify the degree of viscosity, and Figure 1-8 presents the art of η/s determination by v_2 measurements [27]. It presents the specific viscosity $\eta/s = 0.16, 0.24$ for RHIC and LHC respectively, which is very close to the strong-coupling limits for the specific viscosity $\eta/s \simeq 1/4\pi$ established by the anti-de Sitter/conformal field theory (AdS/CFT) [28]. Comparing different η/s values, we find smaller v_2 with stronger viscosity. This shows that the small shear viscosity plays an important role in flow study, since it keeps the initial conditions from being dissipated rapidly.

Recalling the original motivation of conducting heavy-ion experiments, it is predicted that the hot and dense matter consisting of asymptotically free partons is created in heavy-ion collisions. It is a controversial topic whether this phase is indeed created, but several pieces of evidence of QGP emergence have been observed. The azimuthal anisotropy of soft hadrons described above is definitely one strong piece of evidence, and we will see several other modifications resulting from the existence of the medium.

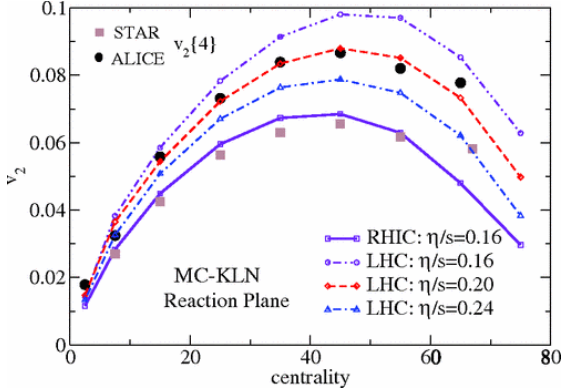


Figure 1-8: p_T -Integrated v_2 of charged particles as a function of centrality measured by STAR [29] in AuAu collisions at 200 GeV (rectangle) and ALICE [30] in PbPb collisions at 2.76 TeV (circle). Data is fitted using a hybrid approach VISHNU [31], providing parameter $\eta/s = 0.16$ at RHIC and $\eta/s = 0.20$ at LHC, and the curves with $\eta/s = 0.16, 0.24$ with LHC configuration is shown as reference. Monte Carlo KLN (MC-KLN) [32] Model is picked to calculate initial particle production, and the same fit using Glauber Model [33] is also performed in Ref. [27]. Figure from Ref. [27].

1.2.3 Hard Probes

At the very beginning of collisions (before the end of pre-equilibrium), the scatterings with large momentum transferred occur and the hardest particles are created first. In vacuum, those particles with large virtualities propagate, fragment into a bunch of hadrons with maintaining p_T known as jets. However, if the space is filled with dense matter, the hard particles interact with the partons in the medium, and thus the final hadrons seen by detectors carry information of the transport properties compared with the vacuum case. Therefore, these high- p_T particles are called hard probes. One prompt consequence of the hot and dense medium is that jets lose considerable energy in the medium (jet quenching), which can be reflected in multiple observables. First, due to energy loss, the p_T spectrum of hadrons shifts towards low- p_T direction, and consequently one observes suppression of high- p_T hadrons. This modification is typically quantified using the ratio of the particle p_T -spectrum in AA collisions to that of pp collisions, scaled by the average N_{coll} . This quantity is known as the nuclear modification factor R_{AA}

$$R_{\text{AA}}(p_T) = \frac{dN^{\text{AA}}/dp_T}{\langle N_{\text{coll}} \rangle dN^{\text{pp}}/dp_T} \quad (1.2.2)$$

where N^{AA} and N^{pp} are the particle yields in AA and pp collisions respectively. The left panel in Figure 1-9 shows R_{AA} of charged particles as a function of p_T in PbPb collisions at 5.02 TeV measured by CMS experiment [34]. It suggests a strong suppression up to a factor of 5 around $p_T = 7$ GeV/c. The shape of R_{AA} over the p_T range reflects various processes and features including parton energy loss, p_T -spectrum shape, and collective flow motion of soft particles. The same observable measured in pPb collisions [35] is also shown in the same figure ruling out effects related to the initial-state conditions of the lead nucleus, known as cold nuclear matter (CNM) effects, as a cause of the high- p_T suppression seen in PbPb collisions. Multiple measurements performed by different collision systems and experiments present similar results [36, 37, 38, 39, 40, 41, 42, 43, 44]. Second, the two jets with similar initial p_T due to momentum conservation present momentum imbalance in the final state, because they experience different path lengths inside the medium. A fraction of all events with two back-to-back jets ($\Delta\phi > 2\pi/3$) having small dijet asymmetry ratio ($A_J \equiv (p_{T,1} - p_{T,2}) / (p_{T,1} + p_{T,2}) < 0.15$) as a function of N_{part} is shown in the right panel of Figure 1-9 [45]. A significant imbalance between leading- and subleading-jets is an indication of path-length dependent energy loss of partons in the medium. Third, as mentioned earlier, the production of high- p_T electricweak bosons (i.e. photons, Z bosons, W bosons) does not participate in strong interactions and is not affected by the medium produced in heavy-ion collisions. This makes them golden references reflecting initial states. Several boson+jet correlation studies are conducted in heavy-ion collisions. Figure 1-10 displays γ -to-jet p_T ratio ($x_{j\gamma} \equiv p_T^{\text{jet}}/p_T^\gamma$) of back-to-back photon+jet pairs in PbPb and pp collisions. A prominent nuclear modification on $x_{j\gamma}$ is observed, especially in the most central events. This is consistent with the prediction considering the collision system is larger and denser in central events compared with more peripheral events.

1.3 The Golden Probe: Heavy Quarks in Heavy-ion Collisions

The hard probes mentioned in Section 1.2.3 are particularly useful because they are created in the early stage and pQCD serves to calculate the initial production due to their high momentum. Naturally one may ask what if we want to look at intermediate- p_T regime? Are there “softer” hard probes? The answer is yes – we will see how

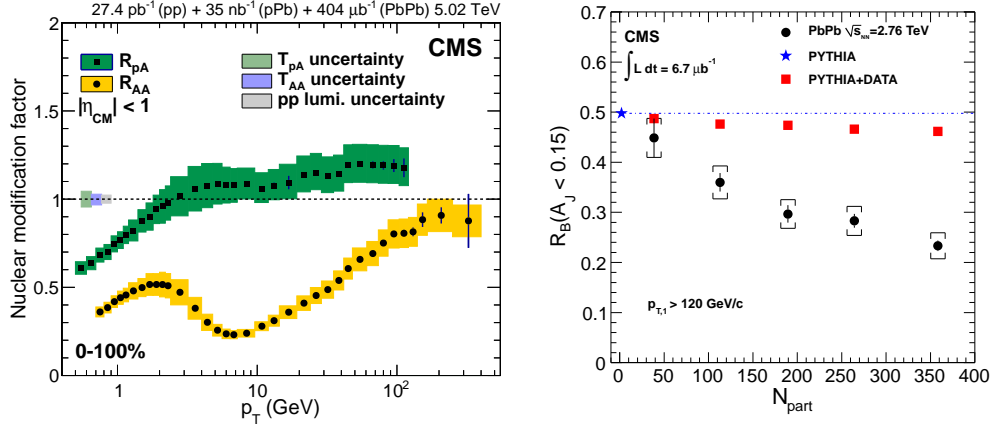


Figure 1-9: (Left) Measurements of the nuclear modification factor (R_{AA}) of charged particles as a function p_T for an inclusive centrality class for both PbPb [34] (yellow) and pPb [35] (green) collisions at 5.02 TeV performed by CMS. $R_{AA} < 1$ is observed in a wide kinematic range in PbPb collisions indicating strong suppression particles experience in the medium; (Right) Fraction of all events with a leading jet with $p_{T,1} > 120$ GeV/c for which a subleading jet with dijet asymmetry ratio $A_J \equiv (p_{T,1} - p_{T,2}) / (p_{T,1} + p_{T,2}) < 0.15$ and $\Delta\phi > 2\pi/3$ as a function of N_{part} performed by CMS experiment [45]. The black filled circles are for the PbPb data. The result for reconstructed PYTHIA dijet events (blue filled star) is plotted at $N_{part} = 2$. The red squares are for reconstruction of PYTHIA + data events.

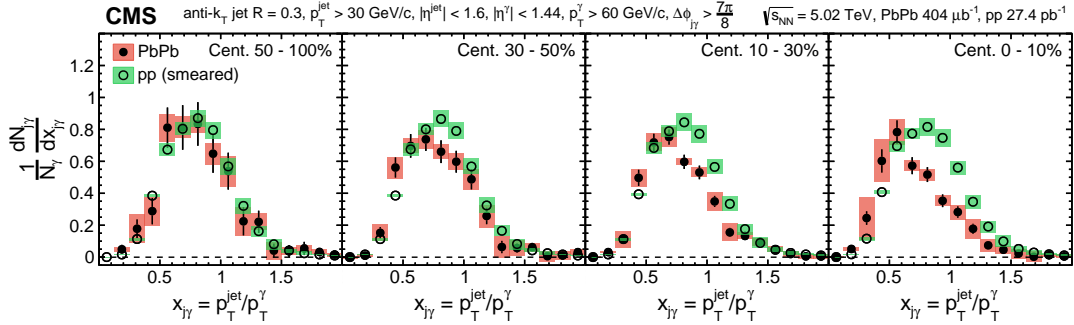


Figure 1-10: Centrality dependence of $x_{j\gamma} \equiv p_T^{\text{jet}}/p_T^\gamma$ of photon+jet pairs with $\Delta\phi > 7\pi/8$ normalized by the number of photons for PbPb (full circles) and smeared pp (open circles) accounting for resolution difference data performed by CMS [46]. In the most peripheral collisions (50%–100% centrality), the $x_{j\gamma}$ distribution agrees with the smeared pp reference data. As collisions become more central, the PbPb distributions shift towards lower $x_{j\gamma}$ and the integrals of the $x_{j\gamma}$ spectra become smaller.

heavy quarks (HQ) serve as hard probes of the hot and dense medium in this section. Quarkonia consisting of heavy quarks (charmonia or bottomonia) are called hidden heavy flavor mesons. In contrast, charmed hadrons ($c\bar{q}$ or cqq' and c.c., i.e. $C = \pm 1$) and bottom hadrons ($b\bar{q}$ or bqq' and c.c., i.e. $B = \pm 1$) are called open heavy flavor hadrons. Although studying quarkonia is important topic in heavy-ion collisions, only open heavy flavors are in the scope of this thesis.

1.3.1 Heavy Quark Dynamics in Heavy-ion Collisions

The major characteristic of heavy quarks is their large masses, $m_c \simeq 1.3 \text{ GeV}/c^2$, $m_b \simeq 5 \text{ GeV}/c^2$. The mass is considered heavy in terms of two scales, *(i)* m_Q is larger than the QCD scale ($m_Q \gg \Lambda_{\text{QCD}} \simeq 200 \text{ MeV}$); *(ii)* m_Q is larger than the typical temperature of the hot medium emerging in heavy-ion collisions ($m_Q \gg T \simeq 200 \text{ MeV}$); *(iii)* the thermalization time is delayed by a factor of $\tau \sim m_Q/T$. We will see how these features lead to different transport behaviors from light quarks and let heavy quarks be a valuable tool to study the properties of QGP.

PRODUCTION Due to the feature of $m_Q \gg T$, the thermal production of heavy quarks is significantly suppressed, that is, the heavy quarks seen in the final states mainly emerge from initial scatterings. Thus, the heavy quark production yield in different centrality classes can be obtained scaled by N_{coll} . Note modifications of parton distribution function in a nucleus (nPDF) from an isolated nucleon have to be taken into account. Figure 1-11 illustrates nuclear modifications of PDF in bound protons compared with free protons. $R_i^A(x, Q^2) = f_i^A(x, Q^2)/f_i^p(x, Q^2)$ is a scale-dependent modification factor, and i denotes parton types. Figure 1-11 indicates suppression of small- x partons in nuclei, and this is called “shadowing”. The depletion of the nuclear ratios in this region is related with the multiple scatterings of hadronic fluctuations of the virtual photon with different nucleons [48]. In addition, because HQ mass is also well above the QCD scale, it is sufficient to recruit pQCD to estimate the production cross section over the full kinematic range. This is distinct from light-quark sector at low- p_T regime. At leading order, the only processes of HQ production are gluon fusion and $q\bar{q}$ annihilation, which are displayed at the top of Figure 1-12. At next-to-leading order (NLO), processes like gluon splitting and flavor excitation are taken into account, whose Feynman diagrams are displayed at the bottom of Figure 1-12. Therefore, on one hand, measurement of heavy-flavor hadron production in pp collisions provides an important test for pQCD in low- and intermediate- p_T range.

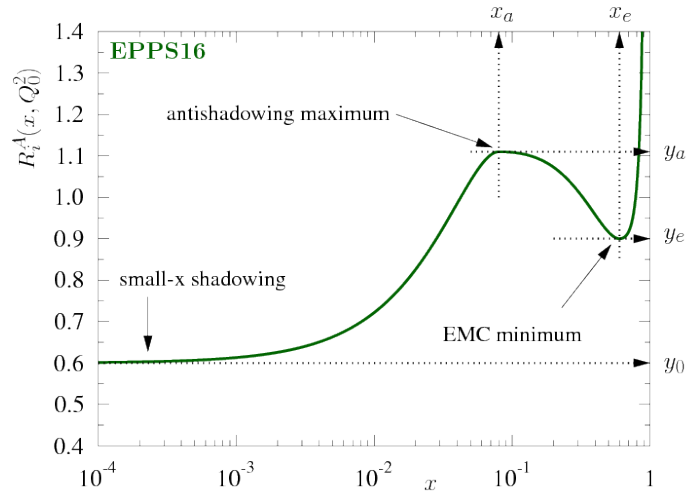


Figure 1-11: Illustration of the nuclear modification of PDF in bound protons by EPPS16. Figure from Ref. [47].

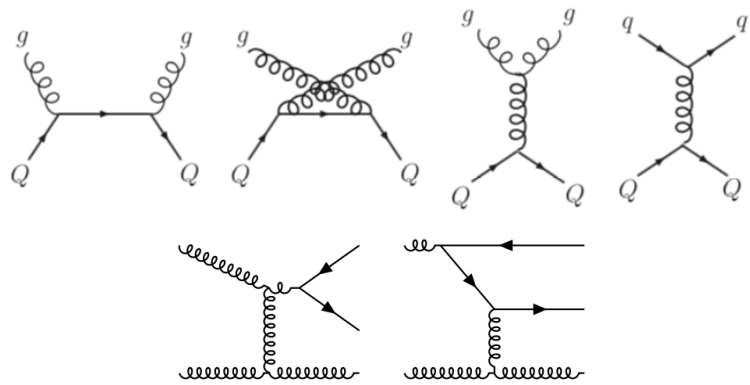


Figure 1-12: Feynman diagrams of leading order pQCD processes (top), gluon splitting (bottom left) and flavor excitation (bottom right) contributing to heavy quark productions.

On the other hand, the well-known production cross section provides a good starting point of studies of hot medium effects in heavy-ion collisions. The most popular NLO pQCD calculations on heavy quark production are Fixed Order calculations with Next-to-Leading-Log resummation (FONLL) [49, 50] and the approach using General-Mass Variable Flavour Number Scheme (GM-VFNS) [51, 52, 53]. FONLL calculates p_T -differential cross sections via a perturbative expansion in the strong coupling constant α_s to next leading order (α_s^3).

$$\begin{aligned} \frac{d\sigma}{dp_T^2} = & A(m)\alpha_s^2 + B(m)\alpha_s^3 \\ & + \left(\alpha_s^2 \sum_{i=2}^{\infty} a_i (\alpha_s \ln(\mu/m))^i + \alpha_s^3 \sum_{i=1}^{\infty} a_i (\alpha_s \ln(\mu/m))^i \right) \times G(m, p_T) \quad (1.3.1) \\ & + \mathcal{O}(\alpha_s^4) \end{aligned}$$

where $\mu \equiv \mu_R$ is the renormalization scale for α_s ($\alpha_s = \alpha_s(\mu)$). Its name stands for fixed next-to-leading order pQCD α_s^3 (FO) calculation with all-order resummation to next-to-leading log (NLL) $\alpha_s^3 \sum_{i=1}^{\infty} a_i (\alpha_s \ln(\mu/m))^i$. When p_T is small, the heavy-quark mass m is the only large scale, and thus fixed-order calculation is reliable. However, if $p_T \gg m$, then there are two different large scales, and therefore large logs $\ln(p_T/m)^i$ have to be resummed. According to Eq. (1.3.1), FONLL performs exact treatments up to α_s^3 , and potential contribution from higher order is parameterized with a factor $G(m, p_T)$. GM-VFNS exploits an approach utilized in a massless scheme (zero-mass variable-flavor number scheme (ZM-VFNS)) to absorb the large logarithmic terms into parton distribution functions and fragmentation functions. As an adoption for heavy quarks, GM-VFNS introduces quark mass effect by matching massless scheme at limit $m \rightarrow 0$.

DIFFUSION The thermal momentum of a heavy quark $\sim \sqrt{3m_Q T}$ is much larger than the typical momentum transfer from the medium $\sim T$ since $m_Q \gg T$. That means the behavior of heavy quarks can be considered as Brownian motion, and heavy quarks interact with the medium multiple times but have small momentum transfer in each interaction. In the following text, we will follow the derivation in Ref. [54] to find the conclusion that the dynamic equation in the framework of Brownian motion can be parameterized by the transport coefficients in a straightforward way. The

Boltzmann equation for the heavy quark phase-space distribution is

$$\left[\frac{\partial}{\partial t} + \frac{\mathbf{p}}{\omega_{\mathbf{p}}} \frac{\partial}{\partial \mathbf{x}} + \mathbf{F} \frac{\partial}{\partial \mathbf{p}} \right] f_Q(t, \mathbf{x}, \mathbf{p}) = C[f_Q] \quad (1.3.2)$$

where $\omega_{\mathbf{p}}$ and \mathbf{p} are the energy and three-momentum of a heavy quark respectively, \mathbf{F} is the mean-field force, and $C[f_Q]$ denotes the collision integral. Neglecting the mean-field effects and integrating on the spatial coordinate, Eq. (1.3.2) becomes

$$\frac{\partial}{\partial t} f_Q(t, \mathbf{p}) = C[f_Q] \quad (1.3.3)$$

The collision integral $C[f_Q]$ has a form of

$$C[f_Q] = \int d^3k [w(\mathbf{p} + \mathbf{k}, \mathbf{k}) f_Q(\mathbf{p} + \mathbf{k}) - w(\mathbf{p}, \mathbf{k}) f_Q(\mathbf{p})] \quad (1.3.4)$$

where $w(\mathbf{p}', \mathbf{k}')$ is the transition rate of the interaction between a heavy quark with the medium, changing the heavy quark momentum from \mathbf{p}' to $\mathbf{p}' - \mathbf{k}'$. In the limit of multiple scatterings with small momentum transfer $|\mathbf{k}| \ll |\mathbf{p}|$,

$$\begin{aligned} & w(\mathbf{p} + \mathbf{k}, \mathbf{k}) f_Q(\mathbf{p} + \mathbf{k}) - w(\mathbf{p}, \mathbf{k}) f_Q(\mathbf{p}) \\ & \simeq \mathbf{k} \frac{\partial}{\partial \mathbf{p}} [w(\mathbf{p}, \mathbf{k}) f_{Q(\mathbf{p})}] + \frac{1}{2} k_i k_j \frac{\partial^2}{\partial p_i \partial p_j} [w(\mathbf{p}, \mathbf{k}) f_{Q(\mathbf{p})}] \end{aligned} \quad (1.3.5)$$

Therefore, Eq. (1.3.2) can be parameterized as

$$\frac{\partial}{\partial t} f_Q(t, \mathbf{p}) = \frac{\partial}{\partial p_i} \left[A_i(\mathbf{p}) f_Q(t, \mathbf{p}) + \frac{\partial}{\partial p_j} (B_{ij}(\mathbf{p}) f_Q(t, \mathbf{p})) \right] \quad (1.3.6)$$

which is known as the Fokker-Planck equation. Here the two coefficients are

$$\begin{aligned} A_i(\mathbf{p}) &= \int d^3k w(\mathbf{p}, \mathbf{k}) k_i, \\ B_{ij}(\mathbf{p}) &= \frac{1}{2} \int d^3k w(\mathbf{p}, \mathbf{k}) k_i k_j \end{aligned} \quad (1.3.7)$$

In the case of local equilibrium, rotational symmetry stands in the local rest frame. Hence the coefficients can be decomposed as

$$\begin{aligned} A_i(\mathbf{p}) &= A(\mathbf{p}) p_i \\ B_{ij}(\mathbf{p}) &= B_0(\mathbf{p}) P_{ij}^{\parallel}(\mathbf{p}) + B_1(\mathbf{p}) P_{ij}^{\perp}(\mathbf{p}) \end{aligned} \quad (1.3.8)$$

where

$$P_{ij}^{\parallel}(\mathbf{p}) = \frac{p_i p_j}{\mathbf{p}^2}, \quad P_{ij}^{\perp}(\mathbf{p}) = \delta_{ij} - \frac{p_i p_j}{\mathbf{p}^2} \quad (1.3.9)$$

In a simplified case, $\gamma \equiv A(\mathbf{p})$ and $D \equiv B_0(\mathbf{p}) = B_1(\mathbf{p})$, Eq. (1.3.6) becomes

$$\frac{\partial}{\partial t} f_Q(t, \mathbf{p}) = \gamma \frac{\partial}{\partial p_i} [p_i f_Q(t, \mathbf{p})] + D \frac{\partial^2}{\partial p_i^2} [f_Q(t, \mathbf{p})] \quad (1.3.10)$$

It can be verified by the gaussian form

$$f_Q(t, \mathbf{p}) = \left(\frac{\gamma}{2\pi D} [1 - \exp(-2\gamma t)] \right)^{-3/2} \exp \left(-\frac{\gamma}{2D} \frac{[\mathbf{p} - \mathbf{p}_0 \exp(-\gamma t)]^2}{1 - \exp(-2\gamma t)} \right) \quad (1.3.11)$$

which is one solution under specific initial conditions, and hence

$$\langle \mathbf{p} \rangle = \mathbf{p}_0 \exp(-\gamma t), \quad \langle \mathbf{p}^2 \rangle - \langle \mathbf{p} \rangle^2 = \frac{3D}{\gamma} [1 - \exp(-2\gamma t)] \quad (1.3.12)$$

Now we can recognize the physical meanings of γ and D from this special solution. The inverse of the momentum-drag coefficient $\tau_Q \equiv 1/\gamma$ is the relaxation time for the average momentum to its equilibrium value, while D is the momentum-diffusion coefficient. The specific formalism of $w(\mathbf{p}, \mathbf{k})$ needs to be calculated by the cross section of the collision between a heavy quark and a light quark.

Several models are developed to solve the diffusion coefficients. To regulate an infrared divergence in the integral of the scattering matrix element, the earliest attempt introduced a Debye screening mass $m_D = gT$ in the t -channel interaction gluon propagator, cutting off scattering at large impact parameters [55]. This configuration under fixing α_s leads to a relaxation time which appears to be too long compared with experimental measurements. This has been improved in the scope of perturbative calculation by revising the Born cross section. One attempt (employed by POWLANG [56], Nantes/MC@HQ+EPOS [57, 58, 59] and BAMPS [60, 61] transport model) is matching a Hard Thermal Loop (HTL) calculation at low momentum transfer $|t|$ to pQCD calculation at large $|t|$, and introducing running strong coupling constant α_s (HTL-pQCD + running coupling constant). The former action effectively reduced Debye screening, and thus enhanced the strong coupling. Another idea is based on the quasiparticle model with infrared enhanced coupling constant, in which the heavy quarks are coupled with a bulk medium matching EoS from lQCD calculation. This approach is picked by PHSD [62, 63, 64] and CATA-

NIA [65] model. In addition, the idea of using potential to describe the interaction is borrowed from heavy quarkonia study, which allows extension to non-perturbative approaches. TAMU model [66, 67] uses the free energy from lQCD as the potential and applies the thermodynamic T -matrix formalism in calculations. Alternatively, UrQMD model [68] applies a resonance approach to take diffusion coefficient. This approach [69] introduces considerable interaction of heavy quarks with medium by assuming resonances are present in the heavy-light quark sector. This is inspired by the possible presence of bound states in the QGP for temperatures of 1-2 T_c indicated by lattice QCD calculations. A completely different model is based on anti-de Sitter/conformal field theory (AdS/CFT) [70], which models the heavy quark by the end of a moving string.

ENERGY LOSS As mentioned in Section 1.2.3, “jet quenching” has been observed for multiple hard probes. That is, when partons pass through quark gluon plasma, the interaction is reflected by numerous energy losses. In the picture of perturbative QCD, there are two distinct energy loss mechanisms of heavy quarks. One is called “collisional energy loss” via elastic scatterings of heavy quarks over the relative slow particles in the medium. The other one is called “radiative energy loss” caused by the gluon radiation of the heavy quark induced by the medium. The significance of both mechanisms varies for p_T . At low- p_T collisional contribution dominates, while radiation becomes important with energy increasing. One important reason exciting interest in heavy quark energy loss is that energy loss of a heavy-quark is predicted to differ from the case of a massless parton. On one hand, gluons with larger color charges are predicted to lose more energy than quarks. On the other hand, the distribution of gluons radiated by a parton with mass M and energy E is given by

$$dP = \frac{\alpha_S C_F}{\pi} \frac{d\omega}{\omega} \frac{d\theta^2}{\theta^2} \left(1 + \frac{\theta_0^2}{\theta^2}\right)^{-2}, \quad \theta_0 \equiv \frac{M}{E} \quad (1.3.13)$$

under small angle approximation

$$\theta \simeq \frac{k_\perp}{\omega} \quad (1.3.14)$$

The first part of Eq. (1.3.13) is the standard gluon bremsstrahlung spectrum. The second part of Eq. (1.3.13) implies that gluon radiation of heavy quarks is suppressed by their large mass. Therefore, the radiative energy loss of heavy quarks in small angle is smaller than that of light quarks, which is known as “dead cone effect” [71]. This is a kinematic consequence, while flavor dependence of energy loss becomes a

crucial test of underlying parton energy loss mechanisms, and motivates searching for mass hierarchy of energy loss. In the language of AdS/CFT, heavy quark energy loss is described by a drag force [72].

hadronization During the propagation in vacuum, the virtuality of high- p_{T} partons decreases and they become hadrons via fragmentation processes. However in the case inside QGP, hadron production can also occur via coalescence where partons combine with each other while traversing the QGP medium [73]. This process is often called “recombination”. Recombination process is studied by the ratio of baryon to meson, since the coalescence contribution to the baryon production is expected to be more significant than for mesons because of their larger number of constituent quarks.

1.3.2 Probing QGP Properties with Heavy Flavor Leptons

Open heavy flavors have been used to study hot medium effects in nucleus-nucleus collisions by RHIC and LHC over the past twenty years. The pioneering study of open heavy-flavor production in heavy-ion collisions was conducted by the PHENIX experiment at RHIC [74]. In this study, the transverse momentum spectra of single electrons from heavy-flavor hadron decays were measured in Au+Au collisions at $\sqrt{s_{\text{NN}}} = 130$ GeV. Indirect measurement of semileptonic decay children was employed in early time not surprisingly due to its (*i*) high signal-background ratio; (*ii*) low requirement on vertex resolution; (*iii*) easy and clean trigger. However, it is crucial to distinguish signal from the background contributions from non-heavy-flavor sources, and background subtraction should be treated carefully. The background of a single electron mainly includes

- Photonic electrons from Dalitz decays of light mesons (π^0 , η) and from photon conversions in the detector materials;
- Electrons from weak kaon decays (K_{e3});
- Dielectrons from decays of quarkonia and light vector mesons (ρ , ϕ , ω).

For muons, background was contributed by

- Muons from in-flight primary light hadrons (π , K);
- Muons from secondary light hadron decays inside absorbers;
- Punch-through hadrons that are misrecognized as muons in detectors.

The significance of contribution from the background sources above varies with kinematic ranges, and therefore the subtraction methods are accordingly different. Left panel of Figure 1-13 shows the yields of inclusive electrons and background electrons from various sources as a function of p_T in proton-proton collisions at 7 TeV from ALICE. In the whole p_T range, photonic electrons are dominant among all background contributions. At high transverse momentum region, contributions of electrons from particles emerging via hard scatterings (e.g. J/ψ) become significant. Also, it suggests a quite high signal purity especially for high- p_T electrons.

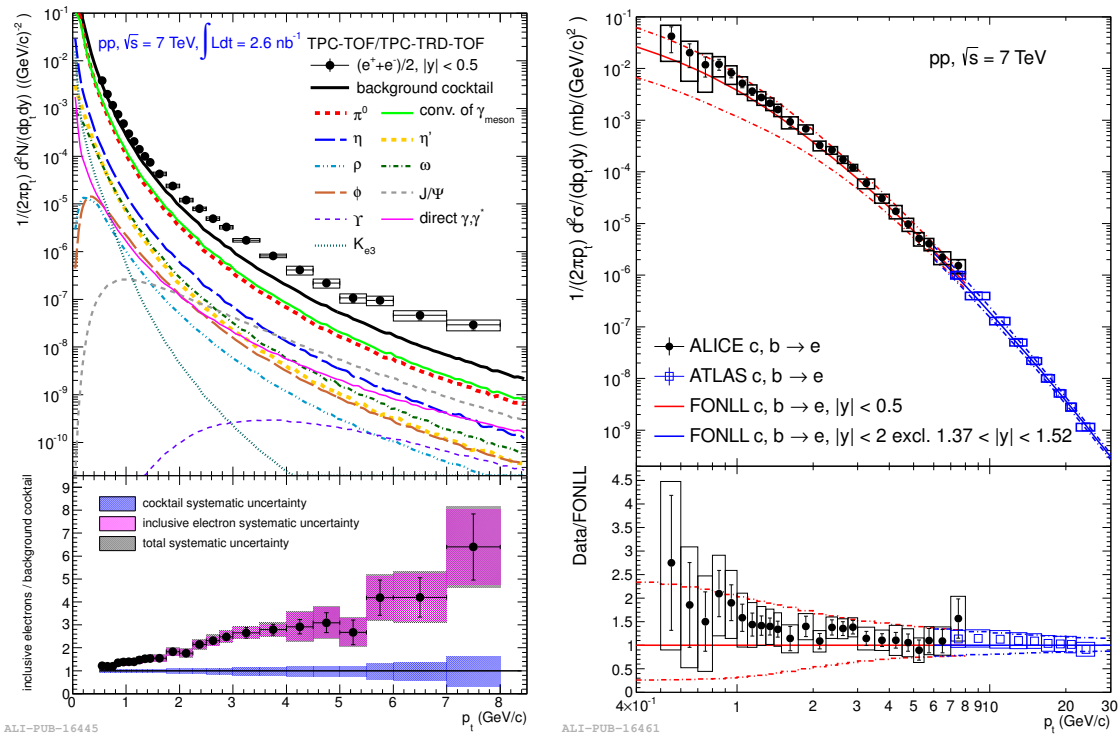


Figure 1-13: (Left) Inclusive electron yield per minimum bias pp collision as function of p_T in comparison with background electron cocktails for the TPC-TOF/TPC-TRD-TOF analysis. Lower panels show the ratio of the inclusive electron yield to the background electron cocktail [75]; (Right) Invariant differential production cross sections of electrons from heavy-flavor decays measured by ALICE [75] (black) and ATLAS [76] (blue) in pp collisions at $\sqrt{s} = 7$ TeV in $|y| < 0.5$ and $|y| < 2$ excluding $1.37 < |y| < 1.52$ respectively. The cross section and uncertainty from FONLL pQCD calculations with the same rapidity selections are shown as solid and dashed lines respectively [49]. Ratio of measurements over calculations is presented in the bottom panel.

Next, we will see what we have learned from the early measurements of heavy

flavor via semileptonic decays. In Section 1.3.1 we mentioned one of the unique characteristics of heavy quarks is that their initial cross sections can be calculated by pQCD with adequate precision. This was tested in proton-proton collisions with various energy in wide kinematic ranges by RHIC and LHC. Right panel of Figure 1-13 presents invariant differential production cross section of electrons from heavy-flavor semileptonic decays measured by ALICE [75] and ATLAS [76] in proton-proton collisions at $\sqrt{s} = 7$ TeV. They cover low- p_T ($0.5 < p_T < 8$ GeV/c) and high- p_T ($7 < p_T < 26$ GeV/c) respectively. In the whole p_T range, data measurements are consistent with FONLL calculations, while the center values of data are close to upper limits of calculations. Therefore, measurements in proton-proton collisions are satisfactory reference to study hot medium effect.

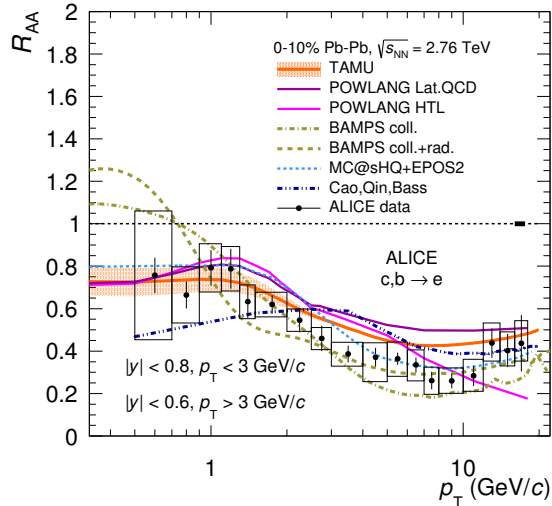


Figure 1-14: R_{AA} of electrons from semileptonic heavy-flavour hadron decays at mid-rapidity as a function of p_T in 0–10% Pb-Pb collisions at $\sqrt{s_{NN}} = 2.76$ TeV [77] compared to model calculations. Error bars (open boxes) represent the statistical (systematic) uncertainties. The normalization uncertainties are represented by the boxes at $R_{AA} = 1$.

In Figure 1-14, nuclear modification factor of electrons from semileptonic heavy-flavor hadron decays is presented as a function of p_T in Pb-Pb collisions at $\sqrt{s_{NN}} = 2.76$ TeV measured by ALICE. The results are measured in the most central events (0 – 10%). In the whole measured p_T range ($0.5 < p_T < 18$ GeV/c), R_{AA} is smaller than 1, indicating energy loss of heavy quarks in heavy-ion collisions. Heavy-flavor decaying electrons experience the strongest suppression at $7 < p_T < 10$ GeV/c with

a factor of 5, and R_{AA} increases towards low and high p_T . Despite poor precision, it also implies a ridge at $p_T \sim 1$ GeV/c which is considered result from collective flow motion of slow particles. Compared with Figure 1-9, weaker suppression of heavy-flavor decaying electrons is suggested compared with light hadrons at low p_T will R_{AA} is similar at high p_T . Also the flow ridge of heavy-flavor leptons sits at lower momentum. On the other side, flow motion was also studied via leptonic decays. Recall heavy quarks are predicted to obtain smaller elliptic flow coefficients due to their large masses. Figure 1-15 presents elliptic flow of heavy-flavour decay electrons as a function of p_T in Pb-Pb collisions at $\sqrt{s_{NN}} = 2.76$ TeV by ALICE. Heavy-flavor decay electron v_2 is significantly non-zero at low p_T that implies that heavy quarks take part in collective motions. v_2 reaches maximum value at $p_T \sim 1.5$. Measurements are compared with theoretical calculations in Figure 1-14 and Figure 1-15. We can see although the models predict the shapes, many of them underestimate the large energy loss and collective flow of heavy quarks. The measurements also trigger long lasting debates on heavy quark dynamic mechanisms and raise the challenging problem to describe heavy quark R_{AA} and v_2 simultaneously. To study the cold nuclear matter

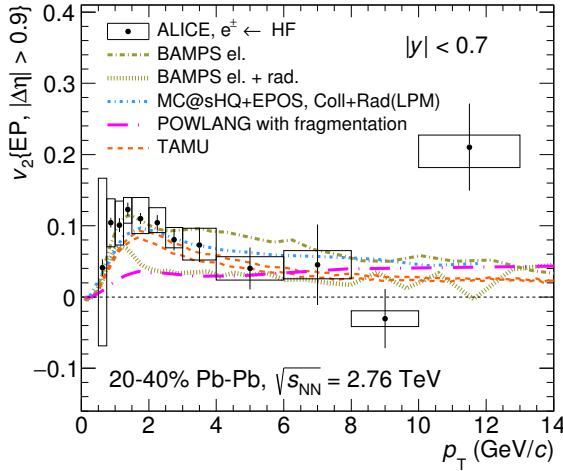


Figure 1-15: Heavy-flavour decay electron v_2 at mid-rapidity ($|y| < 0.7$) as a function of p_T in semi-central (20–40%) Pb-Pb collisions at $\sqrt{s_{NN}} = 2.76$ TeV compared to model calculations. The vertical error bars and open boxes represent the statistical and systematic uncertainties respectively.

effects, measurements are conducted also in light-heavy ion collisions in both RHIC and LHC. It is believed that quark gluon plasma is not produced in small systems, and thus it helps isolate hot medium effects from other effects e.g. shadowing in heavy-ion

collisions. Figure 1-16 shows R_{pA} of heavy-flavor electrons measured in p-Pb collisions as a function of p_{T} . It is found R_{pA} is consistent with unity within uncertainties over the p_{T} range measured, which indicates the strong suppression observed in heavy-ion collisions is not associated with cold nuclear matter effects.

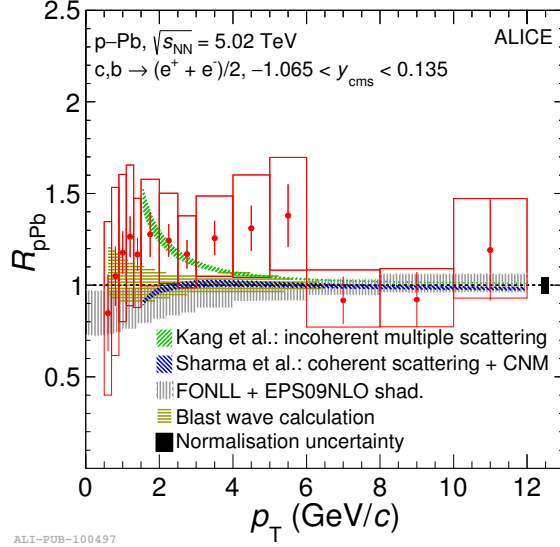


Figure 1-16: Nuclear modification factors R_{pA} of electrons from heavy-flavor hadron decays measured in p-Pb collisions at $\sqrt{s_{\text{NN}}} = 5.02$ TeV as a function of p_{T} . Results are compared with theoretical calculations [78, 79, 80, 81, 49].

Studies of heavy flavors via semileptonic decays from RHIC and LHC are summarized in Table 1.1. According to these early studies of heavy flavors by measuring their decay daughter leptons, we have obtained some preliminary knowledge about the features of motion and interactions of heavy quarks. First we see the production of single leptons from heavy flavor decay in proton-proton collisions can be calculated by pQCD with decent precision. In heavy-ion collisions, a strong suppression was observed over a wide kinematic ranges, which turns out not to be due to cold nuclear matter effects. This indicates unexpectedly significant energy loss of heavy quarks in quark gluon plasma. The shape of R_{AA} has a minimum point at $p_{\text{T}} = \mathcal{O}(1)$ GeV/c and increases towards lower and higher p_{T} . Also, non-zero elliptic flow coefficients of leptons from heavy flavor are found, which implies flow motion of heavy quarks in the medium.

Despite the success achieved by these studies, there are crucial problems. First, flavor is not distinguished in semileptonic decay studies, that is charm and beauty are not separated. It is predicted energy loss of beauty quark is smaller than charm

quark due to different mass, and we are strongly interested in the flavor dependence of parton interactions in quark gluon plasma. Second, the leptons measured are from all heavy-flavor hadrons, and it is impossible to distinguish their mother particles. Separating different hadrons is meaningful since inclusive lepton measurements convolute multiple effects apart from the interactions between heavy quarks and the medium. For example, strange heavy-flavor hadron production is sensitive to strangeness enhancement, and baryons have quite different behaviors with mesons due to hadronization mechanisms. Third, it is not trivial to derive the parton kinematics from the daughter leptons. The observables are measured in bins of p_T , while leptons of given p_T are originally from hadrons with various p_T . These problems can be resolved by fully reconstructing heavy-flavor hadrons with tracks. Improvement of detector resolutions allows to reconstruct and recognize secondary vertices, and we will see that it is possible to perform measurements over a wide kinematic range with full reconstruction in the most central heavy-ion events even with no help of particle identifications. In addition, higher precision is demanded to understand the properties of quark gluon plasma and interaction mechanisms with heavy quarks. For example,

- Can pQCD describe heavy quark production precisely?
- How initial fluctuation affects heavy quarks?
- What are the diffusion coefficients of heavy quarks in the medium?
- What are heavy-quark energy loss mechanisms, and how they contribute within different kinematic ranges?
- Is there flavor dependence of energy loss?
- What are the hadronization mechanisms of heavy quarks?

Apart from precision, also studies in wide kinematic range are required. We see in this section the measurement of heavy-flavor leptons is up to ~ 20 GeV/c in LHC, and high- p_T heavy-flavor studies are missing. In this thesis, we will see how the measurements of D^0 help understand the questions above and constrain theoretical models strongly in a wide kinematic range.

Exp.	Coll. Syst.	Obj.	Obs.	Rap.	p_T (GeV/c)	Ref.
PHENIX	Au+Au (200 GeV)	$c, b \rightarrow e$	R_{AA}	$ y < 0.35$	0.3 – 9	[82][83]
PHENIX	Au+Au (200 GeV)	$c, b \rightarrow e$	v_2	$ y < 0.35$	0.3 – 9	[82][83]
PHENIX	Cu+Cu (200 GeV)	$c, b \rightarrow \mu$	R_{AA}	$1.4 < y < 1.9$	1 – 4	[84]
STAR	Au+Au (62.4, 200 GeV)	$c, b \rightarrow e$	R_{AA}	$ y < 0.35$	1.2 – 10	[85][86]
STAR	Au+Au (39, 62.4, 200 GeV)	$c, b \rightarrow e$	v_2	$ y < 0.35$	0.2 – 7	[87][86]
ALICE	Pb+Pb (2.76 TeV)	$c, b \rightarrow e$	R_{AA}	$ y < 0.8$	0.5 – 18	[77][88]
ALICE	Pb+Pb (2.76 TeV)	$b(\rightarrow c) \rightarrow e$	R_{AA}	$ y < 0.8$	1.3 – 8	[89]
ALICE	Pb+Pb (2.76 TeV)	$c, b \rightarrow e$	v_2	$ y < 0.7$	0.5 – 13	[90]
ALICE	Pb+Pb (2.76 TeV)	$c, b \rightarrow \mu$	R_{AA}	$2.5 < y < 4$	4 – 10	[91]
ALICE	Pb+Pb (2.76 TeV)	$c, b \rightarrow \mu$	v_2	$2.5 < y < 4$	3 – 10	[92]
ALICE	Pb+Pb (5.02 TeV)	$c, b \rightarrow e$	R_{AA}	$ y < 0.8$	0.5 – 26	[93]
ALICE	Pb+Pb (5.02 TeV)	$c, b \rightarrow e$	v_2	$ y < 0.7$	1.5 – 8	[94]
ALICE	Pb+Pb (5.02 TeV)	$c, b \rightarrow \mu$	R_{AA}	$2.5 < y < 4$	3 – 20	[93]
ALICE	Xe+Xe (5.44 TeV)	$c, b \rightarrow e$	R_{AA}	$ y < 0.8$	0.2 – 6	[95]
ALICE	Xe+Xe (5.44 TeV)	$c, b \rightarrow \mu$	R_{AA}	$2.5 < y < 4$	3 – 8	[96]
ATLAS	Pb+Pb (2.76 TeV)	$c, b \rightarrow \mu$	R_{AA}	$ \eta < 1$	4 – 14	[97]
ATLAS	Pb+Pb (2.76 TeV)	$c, b \rightarrow \mu$	$v_{2,3,4}$	$ \eta < 2$	4 – 14	[97]
PHENIX	d+Au (200 GeV)	$c, b \rightarrow \mu$	R_{dA}	$1.4 < y < 2$	1 – 6	[98]
STAR	d+Au (200 GeV)	$c, b \rightarrow e$	R_{dA}	$ y < 0.35$	1.2 – 10	[85]
ALICE	p+Pb (5.02 TeV)	$c, b \rightarrow e$	R_{pA}	$ y < 0.6$	0.5 – 12	[99]
ALICE	p+Pb (5.02 TeV)	$b(\rightarrow c) \rightarrow e$	R_{pA}	$ y < 0.6$	1 – 8	[89]
ALICE	p+Pb (5.02 TeV)	$c, b \rightarrow e$	v_2	$ \eta < 0.8$	1.5 – 6	[100]
ALICE	p+Pb (5.02 TeV)	$c, b \rightarrow \mu$	R_{pA}	$2.5 < y < 4$	2 – 16	[101]

Table 1.1: Measurements of open heavy flavor decay leptons in heavy-ion collisions.

Chapter 2

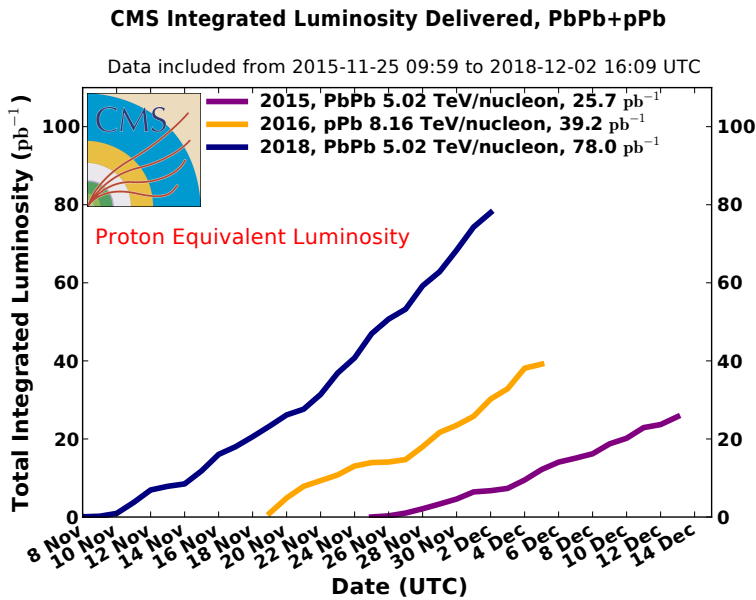
CMS at LHC

2.1 Large Hadron Collider

The Large Hadron Collider (LHC) is a large and powerful particle accelerator built by European Organization for Nuclear Research (CERN). The LHC consists of a 27-kilometer ring of superconducting magnets with a number of accelerating structures to boost the energy of the particles along the way. There are four main detectors constructed at the LHC. The Compact Muon Solenoid (CMS) [102] detector and the A Toroidal LHC ApparatuS (ATLAS) [103] detector are multi-purpose apparatuses, while the A Large Ion Collider Experiment (ALICE) [104] detector and the Large Hadron Collider beauty (LHCb) [105] detector are dedicated for heavy-ion physics and b-physics respectively. For heavy-ion physics study, LHC yielded head-on collisions of two proton beams of $\sqrt{s} = 5.02$ TeV, of two lead (Pb) ion beams of $\sqrt{s_{NN}} = 2.76$ TeV, 5.02 TeV, of one proton beam and one lead beam of $\sqrt{s_{NN}} = 5.02$ TeV, 8.16 TeV, and of two xenon (Xe) ion beams of $\sqrt{s_{NN}} = 5.44$ TeV. The energy is 25 times higher than the previous heavy-ion accelerators like RHIC. The luminosity that LHC delivered and that CMS recorded of the collisions above is listed in Table 2.1. The luminosity of proton-proton run is determined to be decent as reference of given heavy-ion runs. Figure 2-1 shows the delivered proton-equivalent luminosity versus time for Run 2 heavy-ion collisions.

Collision System		Energy	LHC Delivered	CMS Recorded
Run 1				
2011	Pb+Pb	2.76 TeV	$184 \mu\text{b}^{-1}$	$174 \mu\text{b}^{-1}$
2013	p+Pb	5.02 TeV	36.1 nb^{-1}	35.5 nb^{-1}
Run 2				
2015	p+p	5.02 TeV	28.8 pb^{-1}	28.1 pb^{-1}
2015	Pb+Pb	5.02 TeV	0.60 nb^{-1}	0.55 nb^{-1}
2016	p+Pb	5.02 TeV	0.53 nb^{-1}	0.51 nb^{-1}
2016	p+Pb	8.16 TeV	188 nb^{-1}	180 nb^{-1}
2017	Xe+Xe	5.44 TeV	$6.3 \mu\text{b}^{-1}$	$6.0 \mu\text{b}^{-1}$
2017	p+p	5.02 TeV	334 pb^{-1}	316 pb^{-1}
2018	Pb+Pb	5.02 TeV	1.80 nb^{-1}	1.77 nb^{-1}

Table 2.1: Summary of luminosity of collisions performed in LHC for heavy-ion physics.



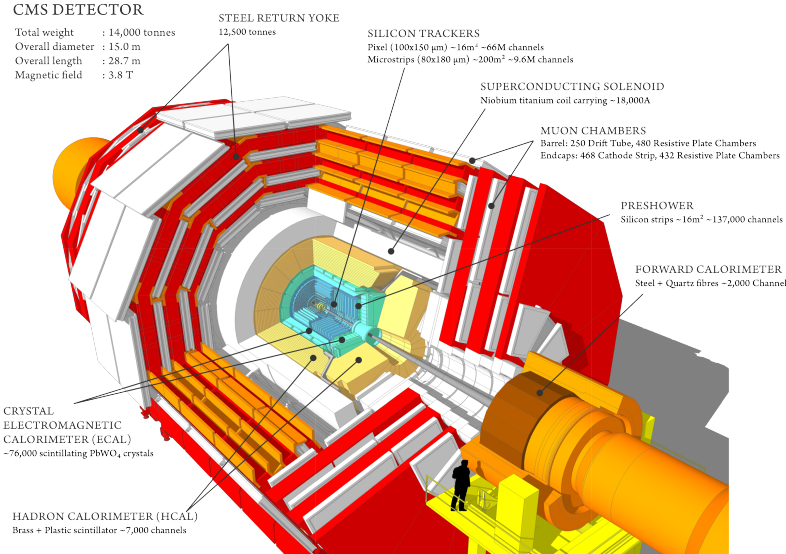


Figure 2-2: Sectional view of the CMS detector. The LHC beams travel in opposite directions along the central axis of the CMS cylinder colliding in the middle of the CMS detector. Figure from Ref. [106]

2.2 CMS Detectors

The overall layout of the CMS detector is shown in Figure 2-2. At the heart of CMS sits a 13-m-long, 6-m-inner-diameter, 4-T superconducting solenoid providing a large bending power (12 Tm) before the muon bending angle is measured by the muon system. The return field is large enough to saturate 1.5 m of iron, allowing 4 muon stations to be integrated to ensure robustness and full geometric coverage. Each muon station consists of several layers of aluminium drift tubes (DT) in the barrel region and cathode strip chambers (CSC) in the endcap region, complemented by resistive plate chambers (RPC). The bore of the magnet coil is large enough to accommodate the inner tracker and the calorimetry inside. The tracking volume is given by a cylinder of 5.8-m length and 2.6-m diameter. In order to deal with high track multiplicities, CMS employs 10 layers of silicon microstrip detectors, which provide the required granularity and precision. In addition, 3 layers of silicon pixel detectors are placed close to the interaction region to improve the measurement of the impact parameter of charged-particle tracks, as well as the position of secondary vertices. The electromagnetic calorimeter (ECAL) uses lead tungstate (PbWO₄) crystals with coverage in pseudorapidity up to $|\eta| < 3.0$. The scintillation light is detected by silicon avalanche photodiodes (APDs) in the barrel region and vacuum phototriodes

(VPTs) in the endcap region. A preshower system is installed in front of the endcap ECAL for π^0 rejection. The ECAL is surrounded by a brass/scintillator sampling hadron calorimeter (HCAL) with coverage up to $|\eta| < 3.0$. The scintillation light is converted by wavelength-shifting (WLS) fibres embedded in the scintillator tiles and channeled to photodetectors via clear fibres. This light is detected by photodetectors (hybrid photodiodes, or HPDs) that can provide gain and operate in high axial magnetic fields. This central calorimetry is complemented by a tail-catcher in the barrel region (HO) ensuring that hadronic showers are sampled with nearly 11 hadronic interaction lengths. Coverage up to a pseudorapidity of 5.0 is provided by an iron/quartz-fibre calorimeter. The Cerenkov light emitted in the quartz fibres is detected by photomultipliers. The forward calorimeters ensure full geometric coverage for the measurement of the transverse energy in the event. An even higher forward coverage is obtained with additional dedicated calorimeters (CASTOR, ZDC) and with the TOTEM tracking detectors.

2.3 Triggering

2.3.1 Trigger System

The trigger system in CMS is comprised of an Level-1 (L1) hardware trigger and an High-Level-Trigger (HLT) array of commercially available computers running high-level physics algorithms [107]. In high-energy physics experiments triggers are applied to reduce output event rates and storage on disks. Trigger design is required to collect events with high purity, that is discard events not interested as soon/much as possible. In CMS Pb-Pb run, peak luminosity is about $3 - 4 \times 10^{27} \text{ cm}^{-2} \text{ sec}^{-1}$ with peak pile-up ~ 0.004 . Taking one fill in the latest PbPb run in 2018 as example, Figure 2-3 shows the output rate after L1 and HLT decisions. L1 trigger output rate is around 20 kHz, while HLT physics stream rate of raw data into first data storage is about 7 kHz. These rates are even lower in 2015 before upgrades of the L1 trigger system. Also, the trigger algorithm need to maintain physics interesting events as much as possible. Achieving good efficiency sometimes requires complex scenario which leads to slow triggers, and therefore trigger latency also need to be taken into account. If the trigger is not fully efficient, correction need to be taken into account in analysis. This will be discussed in the following sections for specific trigger algorithm.

Four trigger algorithms are applied in the analyses discussed in this thesis –

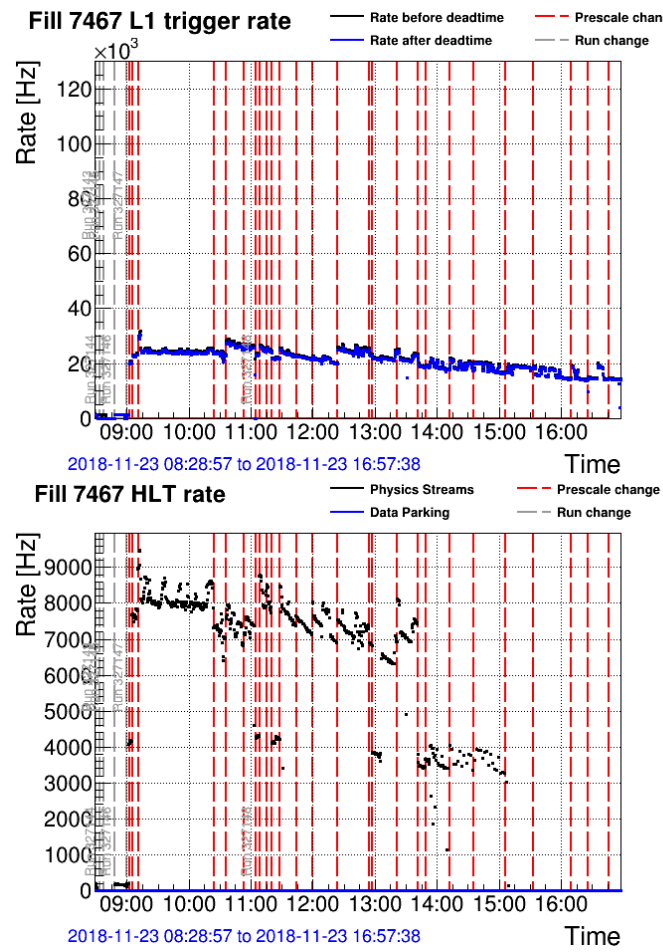


Figure 2-3: CMS L1 output rate (top) and physics stream output rate after HLT (bottom) as a function of time in Fill 7467 of Pb-Pb collisions at $\sqrt{s_{\text{NN}}} = 5 \text{ TeV}$.

minimum-bias trigger, centrality trigger, jet trigger and D⁰ trigger, and they are described in the rest sections of this chapter.

2.3.2 Minimum-Bias and Centrality Trigger

The minimum-bias trigger is required to be in coincidence with bunches colliding (BPTX) in the interaction region using coincidence in the Forward Hadronic calorimeter (HFAND). This is insured by requiring coincidence signals in BPTX and in HF above a threshold. The signal in HF is due to the energy deposit, and the energy in GeV is obtained from the ADC count in HF by converting the ADC count into fC, subtracting the pedestal and correcting for the gain of each individual channel. The threshold is assigned in unit of ADC count. Figure 2-4 shows conversion to energy in GeV from ADC count and from input charge. This requirement allows to largely sup-

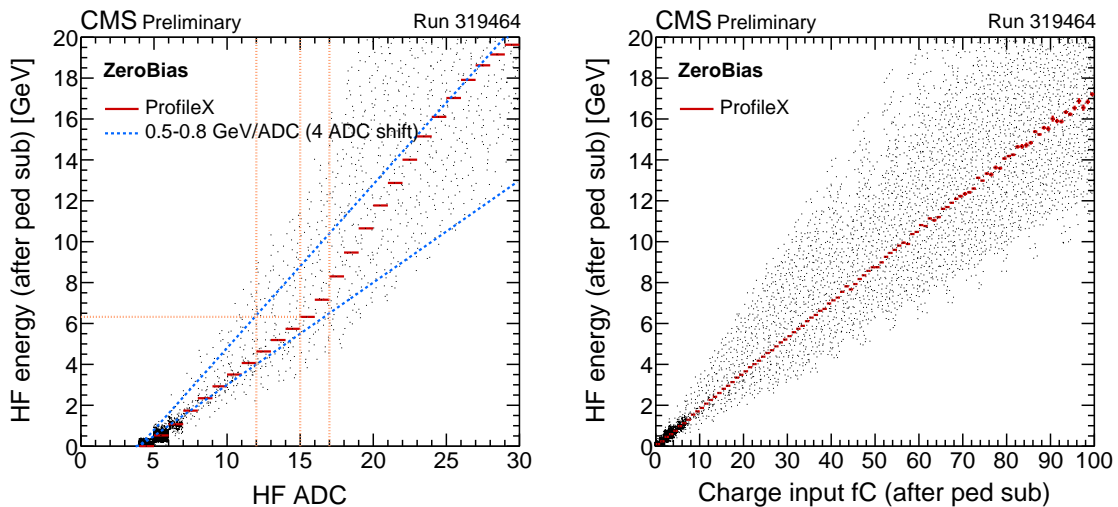


Figure 2-4: Energy in GeV after background subtraction correlated with ADC count (left) and input charge (right) studied in low pile-up pp collisions at $\sqrt{s} = 13$ TeV.

press events due to noise, cosmic rays, double-firing triggers, and beam backgrounds. The collected events are cleaned for detector noise artifacts with the use of a hadronic calorimeter noise cleaning filter, and electromagnetic calorimeter spike removal. The minimum bias trigger is fully efficient for the centrality range 0-90%. The Figure 2-5 shows the centrality distribution (in 0.5% binning) for HFAND and HFOR (signal above threshold in at least one side of HF) selections. Both selection gave a flat distribution and the ratio is consistent with one over the centrality range 0-90%. In addition, events are further selected offline by requiring at least three hits in the HF

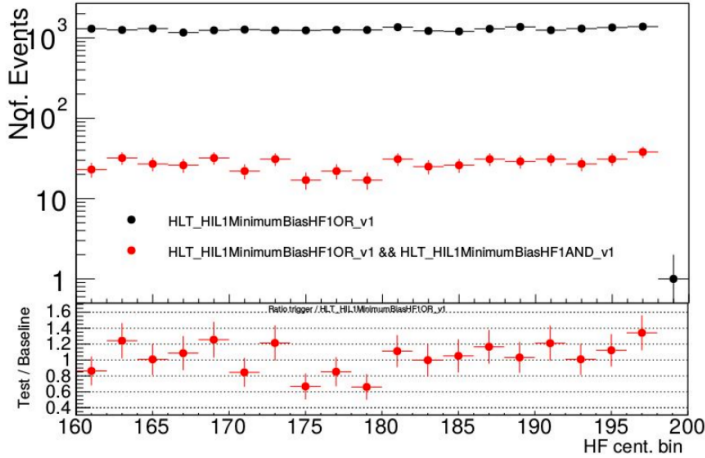


Figure 2-5: Centrality distributions for HFOR (black circles) and HFAND && HFOR selection (red circles).

calorimeters at both ends of CMS, with at least 3 GeV of energy in each cluster, and the presence of a reconstructed primary vertex containing at least two tracks. The default reconstructed primary vertex is required to be located within 15 cm of the nominal collision point along the beam axis and within a radius of 2.0 cm relative to the average vertex position in the transverse plane.

To keep low threshold hard objects coming from peripheral collisions unprescaled, an L1 trigger selecting specific centralities was designed. The trigger computes the summed transverse energy E_T measured in the HF calorimeters, and uses a Look-Up Table (LUT) to associate the sums to event centralities. The LUT was first derived from simulated events, then it was updated based on the first data. This is very similar to how centrality is defined offline which uses sums of energy deposit in HF towers. The distribution of the sum of HF E_T is shown in Figure 2-6, and the events are divided into centrality classes with percentage. Very central events (centrality equal to 0%) are characterized by a large energy deposite.

Figure 2-7 shows the turn-on curve of the L1 centrality triggers performed in 2015 PbPb collisions. As can be seen, the triggers reach their efficiency plateau by 30%, 50%, and 70%. The turn-on curves for more central events are not shown in this figure but the performance of the L1 centrality triggers are even better for more

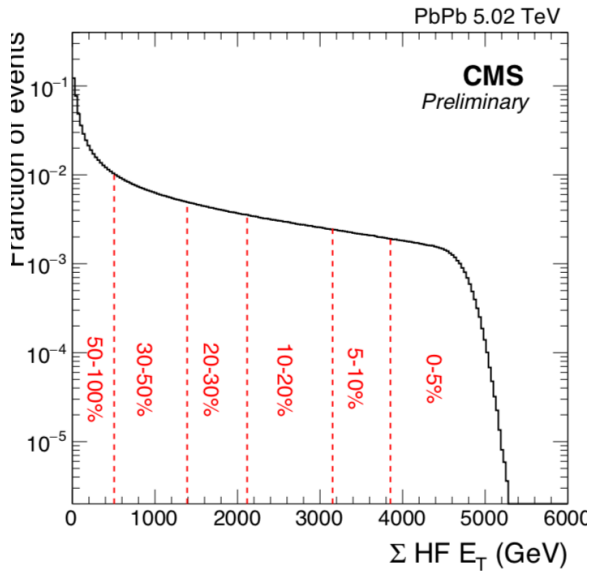


Figure 2-6: Distribution of the sum E_T measured in the HF calorimeters with minimum-bias event sample divided into centrality classes.

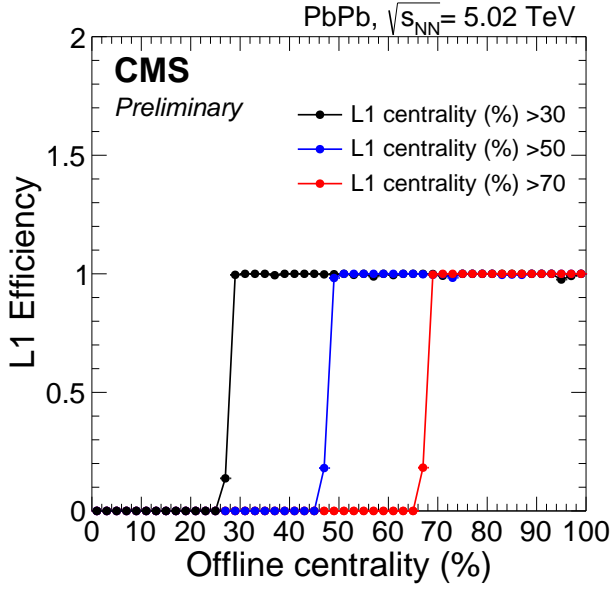


Figure 2-7: Efficiency of the L1 centrality triggers in minimum-bias events triggered by HFAND in PbPb collisions at $\sqrt{s_{NN}} = 5.02$ TeV as a function of the offline event centrality.

central events.

2.3.3 Jet Trigger

The L1 jet trigger uses transverse energy sums computed using both HCAL and ECAL in the central region ($|\eta| < 3$) or HF in the forward region ($|\eta| > 3$). The calorimeter granularity is grouped into several regions in (η, ϕ) , and a L1 jet candidate is identified if finding energy deposit in a region higher than its neighbouring 8 regions. The jet is characterized by the sum of transverse energies in the 3×3 regions where the highlighting region is at center. In heavy-ion collisions, the jets sit on top of a large underlying event backgrounds. Therefore, the jet energy is estimated by subtracting averaged energy in ϕ ring via an iterative pile-up subtraction technique similar with offline processes. In run 1, background subtraction is implemented in HLT level, while in run 2 it is realized in L1 algorithms. At the HLT, jets are reconstructed using the anti- k_T clustering algorithm with cone size $R = 0.4$. The inputs for the jet algorithm are either calorimeter towers (CaloJet), or the reconstructed particle flow objects (PFJet). HLT paths and their L1 seeds utilized in the analysis discussed in

Data	HLT Path	L1 Seed	Note
pp	HLT_AK4PFJet60Eta5p1_v1	L1_SingleJet40BptxAND	anti- k_T PFJet $p_T > 60 \text{ GeV}/c$ $ \eta < 5.1$
PbPb	HLT_HIPuAK4CaloJet60Eta5p1_v1	L1_SingleS1Jet28BptxAND	anti- k_T CaloJet $p_T > 60 \text{ GeV}/c$ $ \eta < 5.1$ PU sub

Table 2.2: HLT paths and corresponding L1 seeds utilized in analysis discussed in Section 8.

this thesis are listed in Table 2.2. It will be mentioned in Section 4.2, PF jets with resolution parameter $R = 0.3$ and $p_T > 60 \text{ GeV}/c$ are used in the analysis for both pp and PbPb collisions. In 2015 run, however, PF jet trigger is only implemented in pp collisions, so in CaloJet paths are used in analysis performed for PbPb collisions. In Figure 2-8 and Figure 2-9, the L1 and HLT trigger efficiencies of different thresholds are presented as a function of offline leading jet p_T in pp and PbPb data respectively. The efficiencies are evaluated using minimumbias events collected at the same energy. The trigger turn-on curves are fitted both in pp and PbPb with the error-function

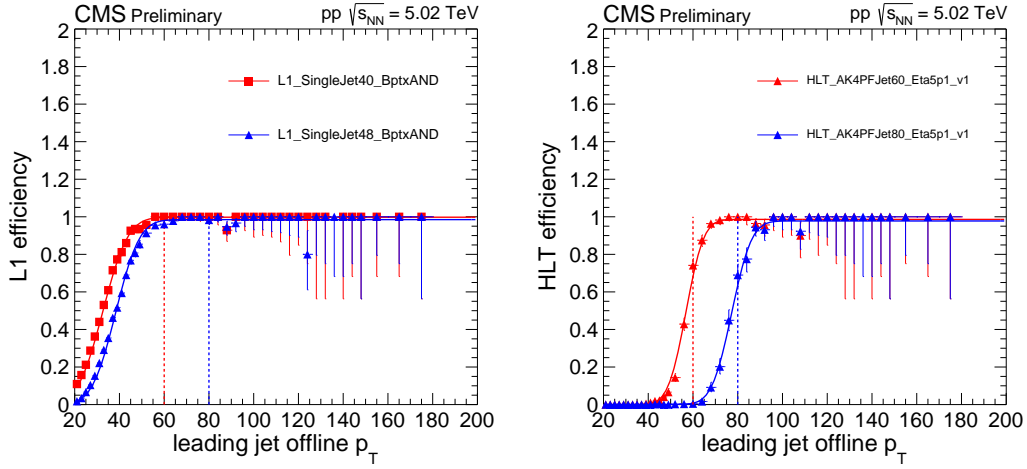


Figure 2-8: L1 (left) and HLT (right) trigger efficiency as a function of the leading offline jet p_T evaluated in minimum-bias pp events. The vertical lines correspond to jet p_T of 60 and 80 GeV/c respectively. The error function fits used to parametrise the efficiency are superimposed.

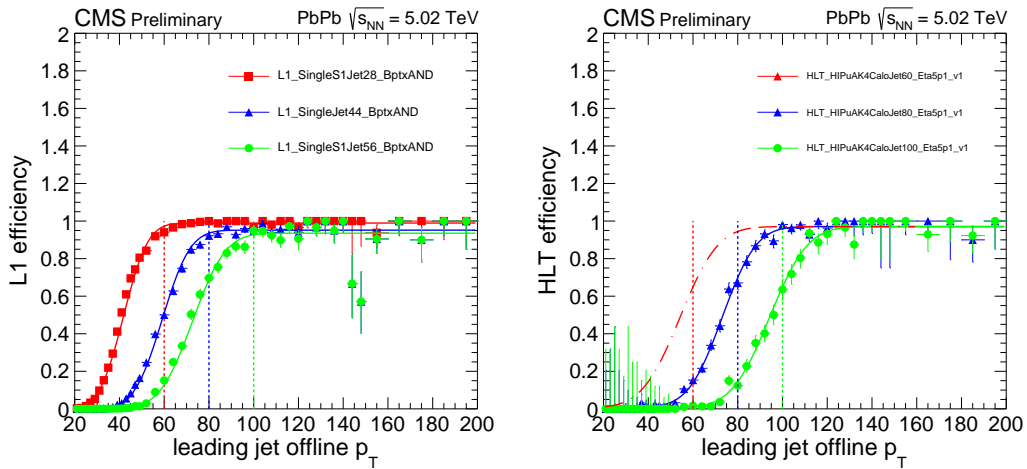


Figure 2-9: L1 (left) and HLT (right) trigger efficiency as a function of the leading offline jet p_T evaluated in minimum-bias PbPb events. The vertical lines correspond to jet p_T of 60, 80, and 100 GeV/c respectively. The error function fits used to parametrise the efficiency are superimposed.

functional form

$$f(x) = \frac{1}{2} \cdot [(1-d) \cdot a \cdot \text{erf}(bx + c) + (1+d)] \quad (2.3.1)$$

The resulting fit functions are used to weight the jet p_T spectra in order to correct the biases due to trigger selections. In Figure 2-10, the offline jet p_T distributions are presented after applying prescale correction. Spectra with and without trigger efficiency correction are superimposed to display the performance of fixing trigger biases.

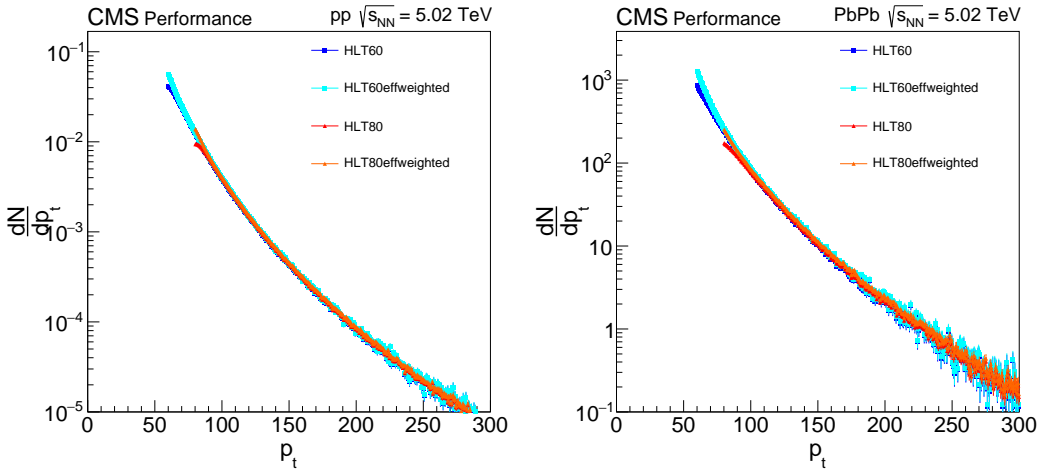


Figure 2-10: p_T distributions of all jets for events triggered with different HLT paths in pp (left) and PbPb (right) collisions after prescale and trigger efficiency correction.

2.3.4 D^0 Trigger

In order to enhance the statistics of high- p_T D^0 mesons, dedicated HLT D^0 triggers were designed for both pp and PbPb data taking. While the lower-threshold triggers had to be prescaled because of the high instantaneous luminosity of the LHC, the highest threshold trigger used in the analysis ($p_T > 60(50)$ GeV/c for PbPb (pp) data taken) was always unprescaled. Figure 2-11 sketches the workflow of D^0 triggers employed in pp and PbPb collisions with CMS detectors. Since high- p_T D^0 mesons are usually associated with jets and high energy calorimeter towers in the HCAL, HLT D^0 triggers are seeded by L1 jet triggers, which are gated with coincidence signal in BPTX requirement (both proton or lead beams are present, meaning a collision could happen) in order to lower the L1 rate. Details about Jet L1 triggers can be found in Section 2.3.3. Due to the difficulty to trigger on very low- p_T jet in PbPb collisions,

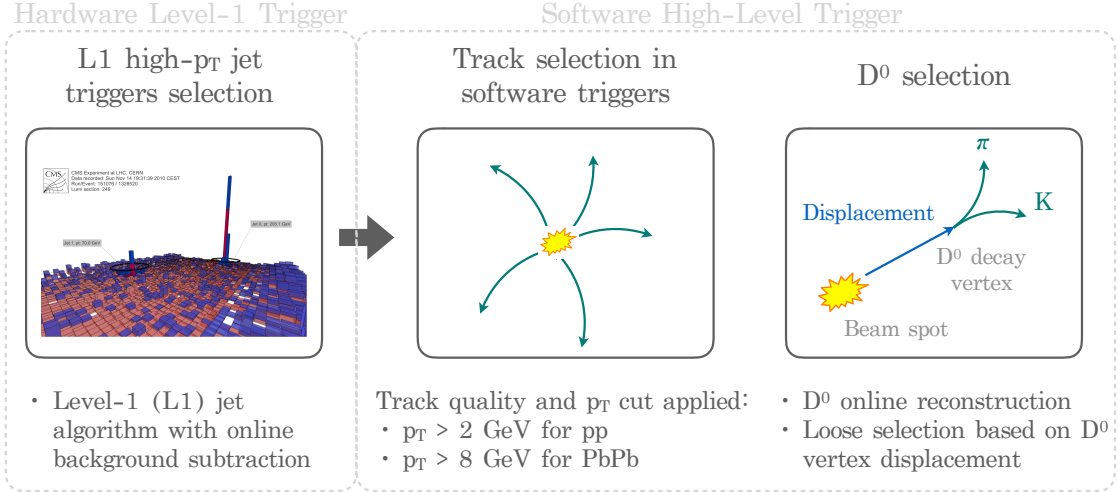


Figure 2-11: Flowchart for D⁰ triggers utilized in pp and PbPb collisions at $\sqrt{s_{\text{NN}}} = 5.02 \text{ TeV}$ with CMS.

low- p_{T} D⁰ triggers in PbPb are seeded by a minimum-bias trigger L1 seed. The L1 triggers associated with each D⁰ trigger path are shown in Table 2.3. For events

Dataset	p_{T} Interval	HLT Threshold	L1 Seed
pp	$20 < p_{\text{T}} < 40 \text{ GeV/c}$	HLT_Dmeson_Dpt15	L1_SingleJet24_BptxAND
	$40 < p_{\text{T}} < 60 \text{ GeV/c}$	HLT_Dmeson_Dpt30	L1_SingleJet40_BptxAND
	$p_{\text{T}} > 60 \text{ GeV/c}$	HLT_Dmeson_Dpt50	L1_SingleJet48_BptxAND
PbPb	$20 < p_{\text{T}} < 40 \text{ GeV/c}$	HLT_Dmeson_Dpt20	L1_MinimumBiasAND_BptxAND
	$40 < p_{\text{T}} < 60 \text{ GeV/c}$	HLT_Dmeson_Dpt40	L1_SingleJet28_BptxAND
	$p_{\text{T}} > 60 \text{ GeV/c}$	HLT_Dmeson_Dpt60	L1_SingleJet44_BptxAND

Table 2.3: L1 jet trigger seeds for D⁰ trigger paths in 2015 pp and PbPb collisions at $\sqrt{s_{\text{NN}}} = 5.02 \text{ TeV}$ with CMS. The strategy of trigger combinations applied in high- p_{T} D⁰ analyses are also presented.

in which the desired L1-seed fired, a track reconstruction routine is performed at HLT. The online track reconstruction in PbPb corresponds to the standard heavy-ion tracking sequence used in the offline analyses. The HLT track reconstruction in pp includes the first 5 offline tracking iterations instead of full iterations. The slowest step in the trigger is secondary vertex reconstruction, since it loops any pair of selected tracks. Thus further selections are applied on tracks to reduce the rate of secondary vertex. For track quality, the working point called high purity (details see Section 4.1.1) is exclusively selected and pseudorapidity is required to be $|\eta| < 2.4$. Since only high- p_{T} D⁰ are triggered, transverse momentum selection is applied to fairly

reduce the number of tracks into secondary vertex reconstruction. Selections for pp and PbPb are different due to dramatically different multiplicities – $p_T > 2 \text{ GeV}/c$ for pp and $p_T > 8 \text{ GeV}/c$ for PbPb. Additional, χ^2 normalized by number of freedom degree and number of layers fired should be smaller than 0.15. Only tracks with number of total hits $n_{\text{Hits}} > 10$ in trackers are maintained, and relative p_T error need to be smaller than 0.1 (0.3) for pp (PbPb) collisions. Once tracks are reconstructed, D^0 candidates are built at HLT by associating pairs of displaced tracks with opposite sign. To reduce the background contamination and the resulting HLT rate, a loose topological selection is also applied at HLT. The D^0 candidate are requested to have a displacement normalized by its error larger than 1 for pp collisions and cosine of pointing angle larger than 0.8. A tighter selection on displacement significance larger than 2.5 is applied in the PbPb case to suppress the fake rate of HLT decisions. The displacement was calculated online with respect to the online beam spot in order to be independent from the online primary vertex reconstruction.

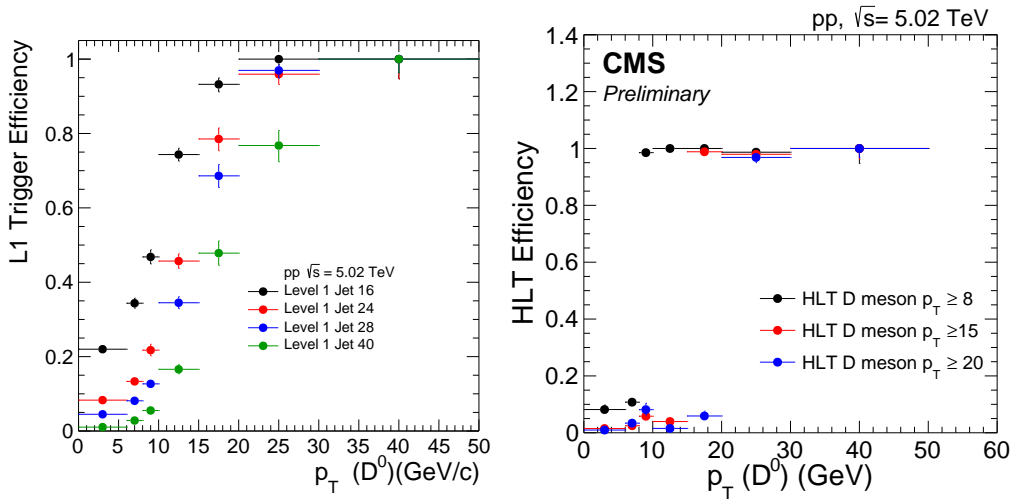


Figure 2-12: D^0 HLT (right) and corresponding L1 seed (left) efficiencies versus p_T of leading D^0 fulfilling online D^0 selection requirements in pp collisions at $\sqrt{s_{\text{NN}}} = 5.02 \text{ TeV}$.

In order to evaluate the D^0 trigger efficiency, both HLT and L1 trigger decisions for offline signal events are studied in minimum-bias triggered samples of 2-billion (150-million) events in pp (PbPb) collisions. The trigger efficiencies are defined as following. The denumerator is defined as the number of events with a leading D^0 that fullfil online D^0 selection requirements. The numerators are the number of events that in addition fire the corresponding L1 seed or HLT paths. Figure 2-12 shows the L1

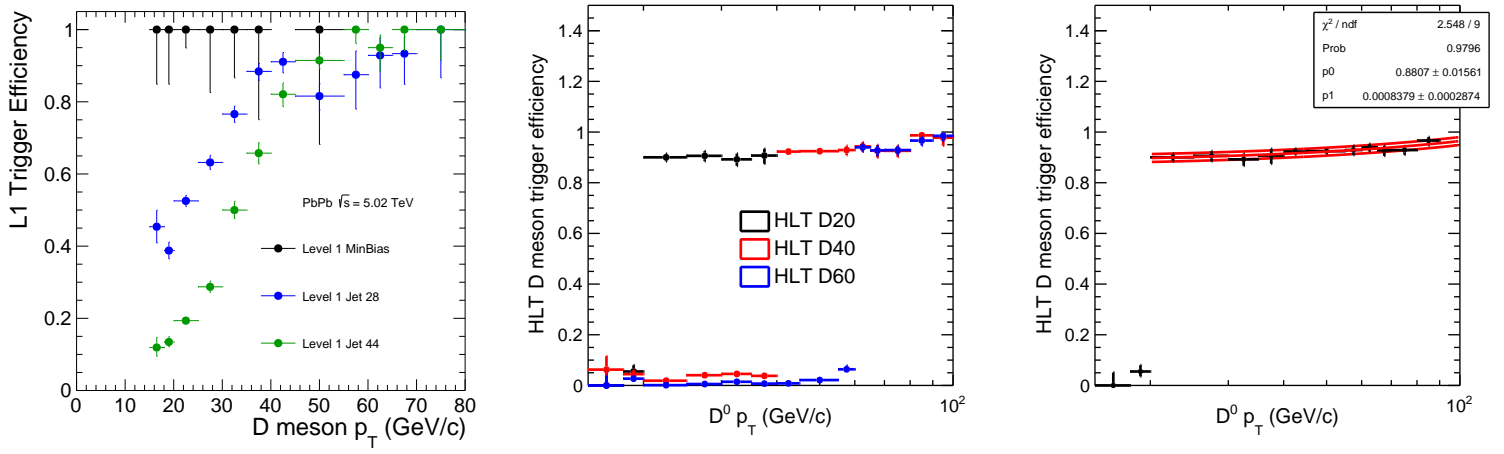


Figure 2-13: D^0 HLT (middle) and corresponding L1 seed (left) efficiencies versus p_T of leading D^0 fulfilling online D^0 selection requirements in PbPb collisions at $\sqrt{s_{NN}} = 5.02$ TeV. Fit on the plateau region of HLT efficiency is shown in the right panel.

trigger and HLT efficiencies as a function of the p_T of the leading D^0 (i.e. D^0 with the highest p_T) candidate in the event, passing online selection criteria in pp collisions. The trigger efficiency reaches 100% at high p_T . In the left (middle) panel of Figure 2-13, the L1 trigger (HLT) efficiency in PbPb are presented as a function of leading D^0 p_T . Samples recorded with different trigger paths are combined together for D^0 p_T spectrum analyses, and the strategy of p_T interval for each D^0 path (see Table 2.3) is taken into account in this study. The final turn-on curves utilized to derive the trigger efficiency correction is presented in the right panel of Figure 2-13. It is fitted with a linear function, and the systematic uncertainty on the trigger efficiency is estimated by the uncertainty on the zero-th polynomial coefficient of the fit.

Chapter 3

Monte-Carlo Simulation

Several Monte Carlo (MC) simulated event samples are generated to evaluate background components, signal efficiencies, and detector acceptance corrections. Proton-proton collision events are generated with generator PYTHIA 8 v212 [108] tune CUETP8M1 [109]. A number of hard QCD processes are implemented (HardQCD:all) based on perturbative QCD cross sections

- HardQCD:gg2gg $g g \rightarrow g g$
- HardQCD:gg2qqbar $g g \rightarrow q \bar{q}$
- HardQCD:qg2qg $q g \rightarrow q g, \bar{q} g \rightarrow \bar{q} g$
- HardQCD:qq2qq $q q' \rightarrow q q', q \bar{q}' \rightarrow q \bar{q}', \bar{q} \bar{q}' \rightarrow \bar{q} \bar{q}'$
- HardQCD:qqbar2gg $q \bar{q}' \rightarrow g g$
- HardQCD:qqbar2qqbarNew $q \bar{q} \rightarrow q' \bar{q}'$

“tune” means sets of parameters that can be adjusted to control the modeling of the properties of the underlying event events (UE). CUET stands for CMS UE tune, P8 refers to PYTHIA 8, and M is due to application of PDF from Monash tune. CUETP8M1 is tuned by fitting charged particle and p_T density to match CDF proton-antiproton data from the Tevatron at $\sqrt{s} = 0.3, 0.9, 1.96$ TeV [110] and CMS pp data from the LHC at $\sqrt{s} = 7$ TeV [111]. After production, only events with at least one D^0 with $p_T > 1$ GeV/c and $|\eta| < 2$ are retained. To obtain sufficient statistics of D^0 in the whole kinematic range up to very high p_T , samples are generated with various minimum \hat{p}_T thresholds. About 500 thousands events are generated for each \hat{p}_T bin

with boundaries of $\hat{p}_T > 0, 5, 10, 15, 30, 50, 80, 120, 170$ for both prompt (fragmented from c-quark) and nonprompt (from b-hadron decays) D^0 meson. Sequentially the D^0 mesons are forced to decay exclusively into $K\pi$ with EVTGEN 1.3.0 [112], and final-state photon radiation in the D^0 decays is simulated with PHOTOS 2.0 [113]. In EVTGEN, a dedicated package for heavy-flavor hadron decays, decay amplitudes are implemented to simulate the decay chains, including all angular and time-dependent correlations. Response of the CMS detector on the events from generator is simulated with the GEANT4 package [114]. For the PbPb MC samples, each PYTHIA 8 event is embedded into a PbPb collision event generated with HYDJET 1.8 [115], which is tuned to reproduce global event properties such as the charged-hadron p_T spectrum and particle multiplicity.

In the analysis, z -direction position of primary vertex in MC simulations is adjusted to match data. Also, the centrality distribution of PbPb MC simulations is reweighted according to the one observed in data to account for the different track reconstruction efficiency in central and peripheral events. In addition, p_T spectra of generated D^0 are reweighted according to fonll p_T shape, and comparison between the case with and without D^0 p_T shape account for systematic uncertainties from p_T shape. Acceptance and efficiency correction is deeply sensitive to simulation output, and thus validating MC simulations are crucial. Distributions of D^0 kinematic variables obtained from MC simulations are compared with that from data. To extract variable distributions of real D^0 from data, sideband subtraction procedures are applied. For a given variable, first the distributions from both signal region and sideband region are produced. Then the one from sideband region is scaled by the ratio of signal region width over sideband width. Subtracting the histogram from signal region with the rescaled histogram from sideband region, the resulting distribution should be the components contributed by real signal D^0 mesons. Figure 3-1 shows the distributions of the three-dimensional normalized decay length and the secondary vertex (definition see Section 5.2) of D^0 mesons from MC and data. The left and right columns are results with and without reweights respectively, and clearly reweighting procedures described above significantly improves.

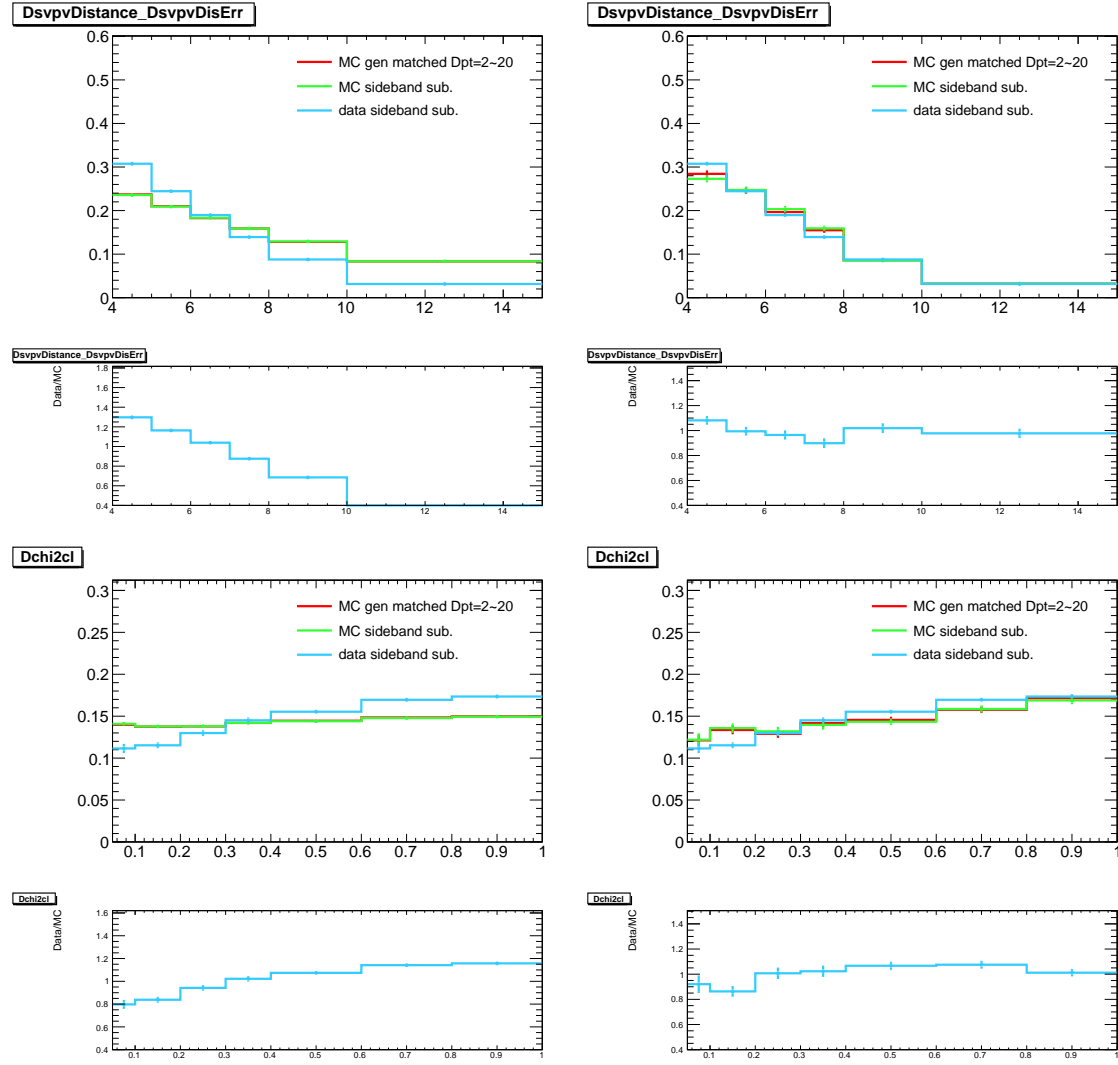


Figure 3-1: Normalized decay length (top) and secondary vertex (bottom) distributions of D^0 mesons. Red and green lines measure distributions of D^0 matching generated truth and from sideband subtraction in MC simulations. Blue lines in the upper panel present variable distributions from data with background subtraction, while the blue lines in the bottom panel show ratio of output from data over MC. Results are shown with (right) and without (left) reweighting MC simulations.

Chapter 4

Physics Objects

4.1 Tracks

4.1.1 Tracking Algorithm

The most fundamental elements to reconstruct D^0 mesons are charged particle tracks. Charged particles deposit energy in the tracker, and the signal reflect energy loss and position information. The trajectories of charged particles are bent with the strong magnetic field existing in CMS detector, and the momenta could be derived. This section will briefly introduce the general algorithms of track reconstruction employed in CMS [116], that is, to obtain estimates for the momentum and position parameters of the charged particles responsible for the hits obtained from the detectors. The first step of the reconstruction process is identifying signals from the trackers. The read-out system accepts a pixel/strip only when the channel reports a signal above some threshold to suppress noises, while the thresholds are loose enough to prevent from harming true signals. When charged particles passing a layer of the tracker, multiple neighbouring pixels/strips may detect energy deposit. Therefore, clusters are formed from adjacent pixels (side-by-side and corner-by-corner) or from neighbouring strips, and a cluster is kept if its total charges pass a threshold. The cluster position in pixels is determined by a template-based algorithm based on a large number of simulated particles traversing pixel modules, which are modeled using simulations with PIXELAV [117, 118]. The position of the hit corresponding to each cluster is determined from the charge-weighted average of its strip positions, corrected in the TIB (TOB) to account for the Lorentz drift. Reconstructing the trajectories from hits utilizes a iterative tracking process. The basic idea is that multiple iterations

are executed sequentially for tracks with different features. The initial iterations are designed for tracks that are easiest and fastest to find such as tracks with relatively high- p_T . After a iteration is finished, hits belonging to the tracks generated from this iteration are removed from the collection. Therefore, the candidate combinations of hits are dramatically reduced for reconstruction of tracks that are difficult to find. It can be imagined that reconstruction of inclusive low- p_T tracks will be extremely slow using the full hit collection especially in heavy-ion collisions. Table 4.1 reports the iterations applied in track reconstruction of 2015 Pb-Pb data by CMS. First, a iteration to quickly produce high- p_T tracks is carried out using triplet seeds. Sequentially one iteration is run to find low- p_T tracks with triplet seeds, and another iteration is implemented to recover more high- p_T tracks using more seeds. In addition, there are another two iterations to find displaced tracks that a bit far from primary vertices and to find tracks close to high- p_T jets respectively. Each iteration experiences sequent

Iteration	Targets	Seeds
initialStep	high- p_T tracks	pixel triplets
lowPtTripletStep	low- p_T tracks	pixel triplets
pixelPairStep	recover high- p_T tracks	pixel pairs
detachedTripletStep	displaced tracks	pixel triplets
jetCoreRegionalStep	tracks around high- p_T jets	pixel triplets

Table 4.1: Tracking iterations employed in 2015 Pb-Pb run by CMS and their targeting tracks.

steps of seed generation, track finding, track fitting and track selection.

SEED GENERATION Seeds are initial track candidates reconstructed using only two or three hits. Each seed includes a potential track defined by initial estimate of trajectory parameters and their uncertainties. Only pixel hits are used to construct seeds because of low occupancy and high efficiency in pixel layers. Seed collections are defined by seeding layers and tracking regions. Seeding layers control two or three layers are involved. For pixel pairs, both hits in each inner layer are used, and recognized as a seed if the trajectory parameters satisfy tracking region criteria. For pixel triplets, apart from a pair consist of two hits in inner layers, another hit in the outer layer is searched. There is a fourth inner layer constructed in CMS since phase 1 upgrade, but it is out of the scope of this thesis and thus not discussed here. Tracking regions constrains trajectory parameter ranges, including the minimum p_T , and the maximum transverse (D_{xy}) and longitudinal (D_z) distances of closest approach to

the assumed production point of the particle. With larger track region, on one hand more seeds cover more tracks. On the other hand, building more combinations leads to long computing time. Therefore, different iterations pick different seeds optimized for their target tracks. The seeds applied in each iteration is reported in Table 4.1.

TRACK FINDING Track finder is developed based on the Kalman filter method [119, 120, 121, 122]. Generally speaking, track finder starts from the seeds produced from previous step, add more hits at outer layers one-by-one and adjust trajectory parameters. To add one more layer, four steps are involved. The first step specifies the next layer by extrapolating the trajectory from current layer. The propagation is realized by utilizing a fast analytical propagator with parameters of the current track candidates and their uncertainties as input. The propagator assumes a uniform magnetic field, with which trajectory is reconstructed to a perfect helix, and therefore the procedure is speeded up. Once the layer is navigated, the second step searches the modules that may be interested in this layer. A module is considered compatible with the trajectory if the position at which the trajectory intercepts the module surface is smaller than 3 of standard deviations outside the module boundary. In this step, not only the magnetic field is accounted for, the determination of modules also estimates the effects of multiple Coulomb scattering and energy loss. Next, hits are grouped according to modules. A χ^2 test is used to check which of the hits are compatible with the extrapolated trajectory. Also a ghost hit may be added to present failure of producing a hit in the module. The last step is to update the trajectory using the original track candidates and the hits kept in the last step. So far, new candidates of tracks are produced and the parameters and their uncertainties are updated, and they are passed into the loop to add next layer. To prevent number of track candidates from increasing rapidly, only a few track candidates with best qualities are kept. The quality is estimated by the normalized χ^2 probability and the number of ghost hits. The propagation procedure to additional hits are stopped when it reaches the outlest layer, or there are too many number of ghost hits, or the p_T of track candidates is too low.

TRACK FITTING After track-finding step, a collection of candidate tracks are obtained with an estimate of trajectory parameters. However, these parameters may be biased by constraints implemented in previous steps, and therefore, a refit based on Kalman filter method is performed after all hits are known. First initial parameters are obtained by fitting on the few most inner hits that initializes the first Kalman filter.

The fit then proceeds from inner hits to outer hits while trajectory parameters are updated, and at the same time the hit position uncertainty is also re-evaluated. This is followed by a smoothing procedure and a second filter is initialized by the current parameters and their uncertainties. Then the second filter proceeds backwards from outer hits and inner hits. The track parameters associated with any of its hits can then be obtained from the weighted average of the track parameters of these two filters.

TRACK SELECTION Track reconstructed following the steps above generally include a large number of fake tracks. Therefore, additional quality selections are necessarily applied. The quality selection is quantified with output of a multivariate analysis (MVA) tool, and particularly the method utilized is called boosted decision tree (BDT). The discriminating variables involved are

- n_{Hits} : Number of hits associated with the track;
- n_{Layers} : Number of layers in which the track has an associated hit;
- $\chi^2/n_{\text{DOF}}/n_{\text{Layers}}$: Normalized χ^2 divided by number of layers;
- η : Pseudorapidity of the track;
- $D_{xy}/\sigma(D_{xy})$: Transverse distance of closest approach normalized by its uncertainty;
- $D_z/\sigma(D_z)$: Longitudinal distance of closest approach normalized by its uncertainty;
- $\sigma(p_T)/p_T$: Relative error of p_T .

MVA distinguishes real tracks from fake tracks, and translates multiple variable into a single quantity. Multiple working points according to BDT cut values are determined, since some analyses demands fake tracks as few as possible, while some analyses wish to keep higher efficiency. The analyses associated with D^0 (in fact most heavy-ion analyses) generally use quality selection called high purity, which is a relatively tight working point. The performance of track reconstruction in PbPb can be seen in Figure 4-1. Tracking efficiency is fraction of those simulated charged particles that can be associated (“matched”) with a reconstructed track, which suggests how many tracks are missing under given tracking algorithm. In D^0 analyses, the inefficiency in

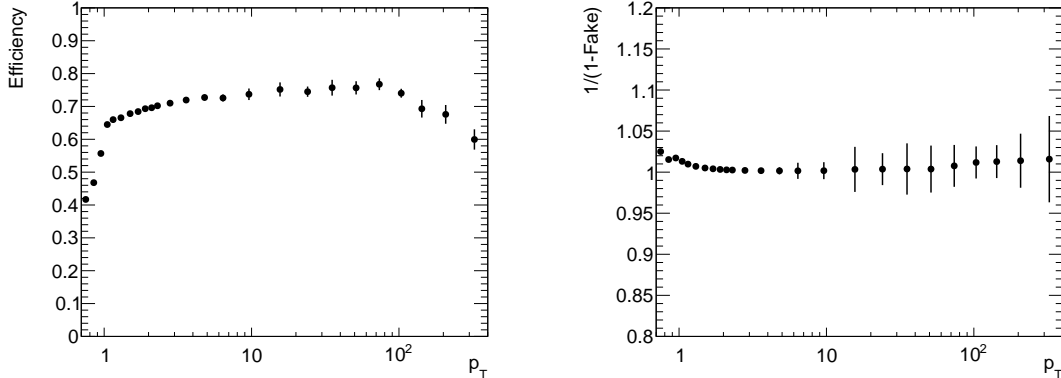


Figure 4-1: Tracking efficiency (left) and fake rate (right) as a function of p_T for centrality inclusive PbPb events estimated in PYTHIA + HYDJET simulations.

data will be corrected with simulations, and the discrepancy between data and MC is studied with D^* decays. This will be discussed in Section 4.1.2. The fake rate is defined as the fraction of reconstructed tracks that are not associated with any simulated particle, which represents the degree of track misidentification. It turns out the fake rate is low, and as D^0 signal is extracted from invariant mass, this is further suppressed with background removal.

4.1.2 Study Track Efficiency using D meson Decays

The efficiency of track reconstruction is corrected by simulation in the analysis. A data-driven method is applied to estimate the relative tracking efficiency for pions in data compared to MC by measuring the ratio of D^0 decaying to final states of four or two charged particles. This ratio is sensitive to the square of the tracking efficiency, because there are two additional charged particles in the numerator compared to the denominator. Specifically, we measure the production for decay $D^0 \rightarrow K^-\pi^+\pi^-\pi^+$ (“ $K3\pi$ ”) relative to that for decay $D^0 \rightarrow K^-\pi^+$ (“ $K\pi$ ”) in both data and MC. To increase the purity and provide a common production source, we reconstructed D^0 decays in the chain $D^{*+} \rightarrow D^0\pi^+$. After correction by simulation, the ratio

$$\mathcal{R} = \frac{N_{K3\pi}}{N_{K\pi}} \cdot \frac{\epsilon_{K\pi}}{\epsilon_{K3\pi}} \quad (4.1.1)$$

divided by the ratio of PDG branching fraction, will be proportional to the square of the ratio of pion tracking efficiencies in data and MC, that is, the relative tracking

efficiency for pions in data and MC can be estimated by

$$\frac{\epsilon(\text{data})}{\epsilon(\text{MC})} = \sqrt{\frac{\mathcal{R}}{\mathcal{R}(\text{PDG})}} \quad (4.1.2)$$

A cut optimization procedure similar with the scenario described in Section 5.2 is performed to reduce the combinatorial background of D^* candidates. Raw yields of D^* are extracted for each p_T threshold via a fitting procedure to ΔM ($M_{K\pi\pi} - M_{K\pi}$ or $M_{K\pi\pi\pi} - M_{K\pi\pi\pi}$). The fitting function consists of following components.

- double(triple) Gaussian with same mean but different width and area to describe 3-prong(5-prong) D^* signal;
- a phenomenological threshold function to describe combinatorial background:

$$f = (1 - e^{-\frac{\Delta M - \Delta m_0}{p_0}}) \left(\frac{\Delta M}{\Delta m_0} \right)^{p_1} + p_2 \left(\frac{\Delta M}{\Delta m_0} - 1 \right), \quad (4.1.3)$$

where Δm_0 is the endpoint, taken to be the pion mass;

- single Gaussian to describe the 5-prong D^* candidates with wrong track mass assignment.

Figure 4-2 shows example fits of ΔM distribution for 3-prong and 5-prong D^* in Minimum-Bias data with $p_T > 5, 13$ GeV/c. Corrected by simulation, the ratio of production of 5-prong and 3-prong D^* vs. p_T thresholds is displaced in the left panel of Figure 4-3, while the relative tracking efficiencies of data and MC result is shown in the right panel using Eq. (4.1.1) and Eq. (4.1.2). Based on this study, MC does not fully correct data tracking efficiency with a discrepancy around 4% per track, which is quoted as the systematic uncertainty from the single track reconstruction efficiency correction. Figure 4-3 also suggests the relative tracking efficiency for pions in data compared to MC does not show obvious p_T dependence within the D^* p_T range studied.

4.2 Jets

Jet reconstruction in heavy-ion collisions in CMS is performed with the anti- k_T jet algorithm that is encoded in the FastJet framework [123]. The anti- k_T jet algorithm is run over the Particle Flow (PF) objects that are reconstructed by matching

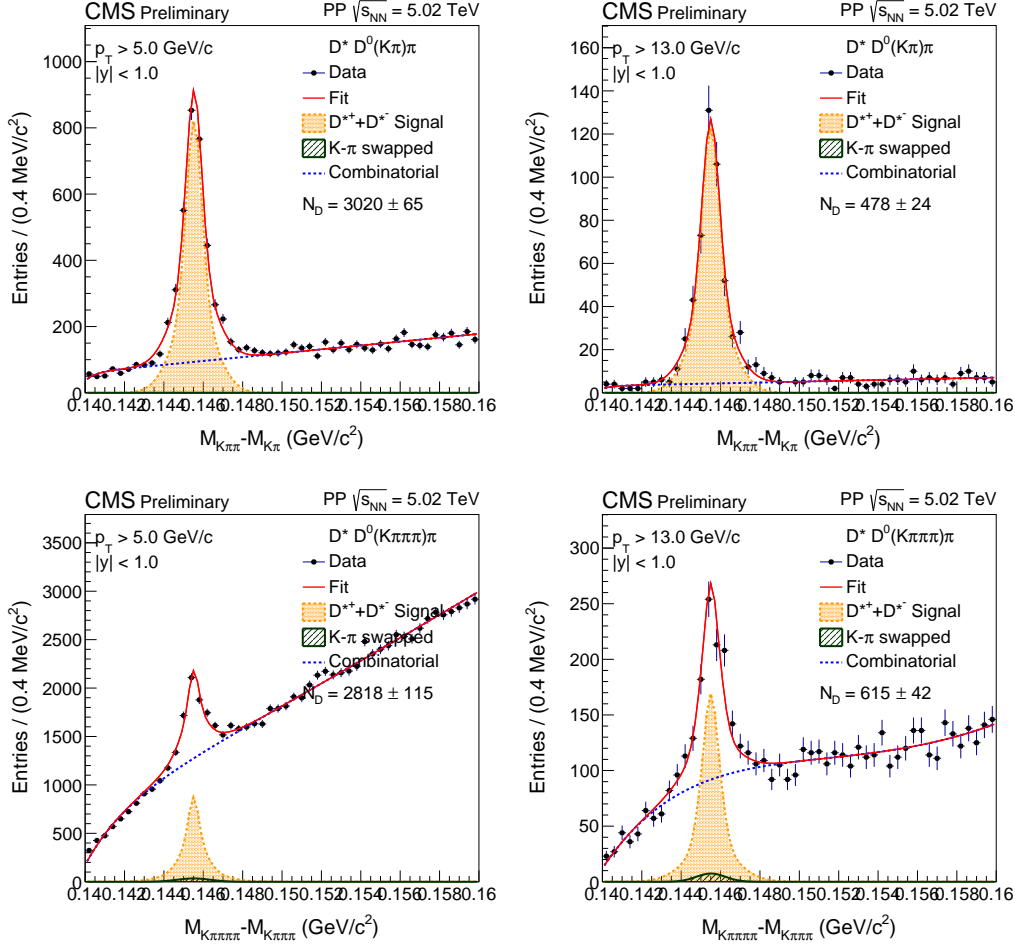


Figure 4-2: ΔM ($M_{K\pi\pi} - M_{K\pi}$ or $M_{K\pi\pi\pi} - M_{K\pi\pi\pi}$) distribution fits of 3-prong (top) and 5-prong (bottom) D^* candidates with $p_T > 5$ GeV/c (left) and $p_T > 13$ GeV/c (right) in pp collisions at 5.02 TeV.

tracks from the tracker to the calorimeters (ECAL and HCAL) and the muon chamber [124, 125]. The constitute particles consist of electrons, muons, photons, charged hadrons and neutral hadrons. Electrons are reconstructed by a combination of a track and of energy deposits in the ECAL, from the electron itself and from possible Bremsstrahlung photons radiated by the electron in the tracker material on its way to the ECAL. Muons are reconstructed and identified with very large efficiency and purity from a combination of the tracker and muon chamber information. Photons are reconstructed with great energy resolutions by ECAL. Charged and neutral hadrons deposit their energy in the hadron calorimeter (HCAL), and the charged hadrons are reconstructed combining the calorimeters and the tracker.

Although the default algorithm for pp collisions is anti- k_T with a resolution pa-

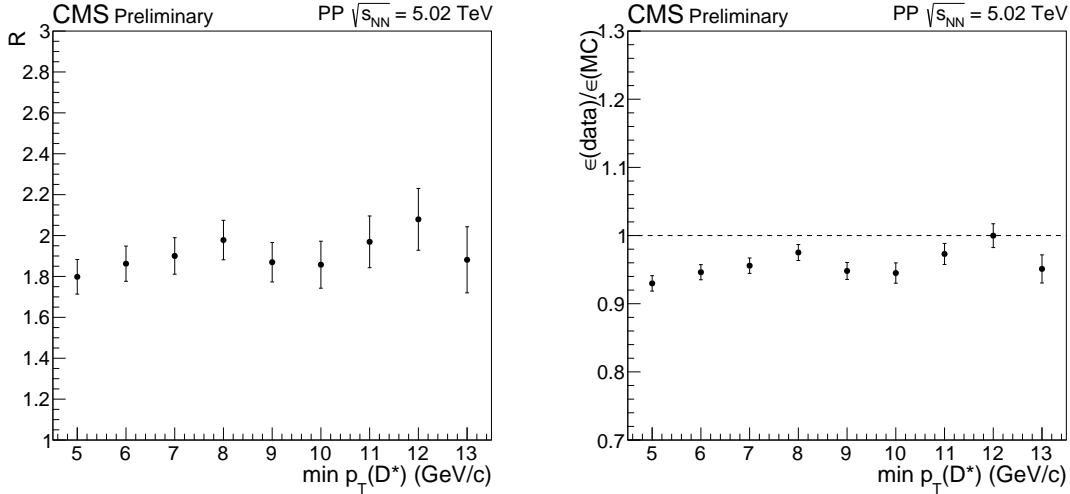


Figure 4-3: (Left) Ratio of production of 5-prong and 3-prong D^* as a function of p_T thresholds in pp collision data; (Right) relative tracking efficiencies of data and MC as a function of p_T thresholds.

rameter of $R = 0.4$, a smaller resolution parameter of $R = 0.3$ is used to minimize the effects of heavy ion background fluctuations in the analysis discussed. While it is possible to subtract the heavy-ion background with the FastJet framework using a definition of an active 4-vector area (A_{jet}), for the analysis associated with this thesis, an algorithm that is a variant of an iterative “noise/pedestal subtraction” technique is used to estimate the heavy ion background event-by-event [126, 127]. It is challenging in the jet reconstruction to understand the uncorrelated background within the selected jet cone due to the large multiplicity in the heavy-ion collisions. This uncorrelated background may worsen the jet energy resolution in the data. We try to study this background as a function of centrality, p_T , and η , the last of which is necessary given reconstruction differences in the Barrel and Endcap regions in CMS experiment. The algorithm to estimate and subtract the background energy for each jet event-by-event is a variant of an iterative “noise/pedestal subtraction” technique is Ref. [127], which is designed for discrete quantification of the energy in η and ϕ and ideal for a calorimetric measurement. To use the same subtraction code to candidates reconstructed with particle flow, which have a continuous distribution in momentum space, a calorimeter tower geometry is imposed on the PF objects. This is performed by summing up the p_T of the PF candidates that point to a fixed $\eta \times \phi$ bin that corresponds to the HCAL cell granularity, although evaluated with respect to the momentum values of candidates at the vertex, not the calorimeter surface. After this

projection, the mean value and dispersion of the energies recorded in the calorimeter cells are calculated for all rings of cells at constant pseudorapidity, η . The value of this pedestal function, $P(\eta)$, containing the information on the mean and dispersion, is then subtracted from all cells. If a cell energy comes out negative, it is set to zero. The algorithm subtracts $\langle E_{\text{cell}} \rangle + \sigma(E)$ from each cell in order to compensate for the bias caused by this elimination of negative energy. Jets are then reconstructed, using the standard anti- k_T algorithm, from the remaining non-zero particle flow objects. In a second iteration, the pedestal function is recalculated using only calorimeter cells outside the area covered by reconstructed high p_T jets ($p_T > 15 \text{ GeV}/c$). The threshold of 15 GeV/c was chosen to optimize the final extracted jet energy resolution. The cell energies are updated with the new pedestal function (again subtracting mean plus dispersion) and the jets are reconstructed once more using the updated calorimeter cells.

Chapter 5

$D^0 \rightarrow K\pi$ Decay Reconstruction

5.1 Secondary Vertex Reconstruction

The hadronic decay channels $D^0 \rightarrow K^-\pi^+$ and $\overline{D^0} \rightarrow K^+\pi^-$ are used to extract D^0 and $\overline{D^0}$ signals due to the large branching ratio $\text{BR}(D^0 \rightarrow K\pi) = (3.89 \pm 0.04)\%$ [128] and simple two-prong combination. In heavy-ion collisions, charm quarks are believed to be created mainly via the initial hard scatterings. They partly fragment into D^0 meson with fragment fraction $f(c \rightarrow D^0) = 0.6176 \pm 0.0160$ [129]. Before decay, D^0 mesons propagate with a relatively long displacement ($c\tau = 123.03 \pm 0.45\mu\text{m}$ [128]), which is crucial for suppressing combinatorial background, as seen in Section 5.2, and makes it possible to study D^0 production with the CMS detector without usage of particle identification. D^0 candidates are reconstructed by combining pairs of oppositely charged tracks with an invariant mass within $0.2 \text{ GeV}/c^2$ from the nominal D^0 mass from particle data group (PDG) [128] ($m_{D^0}^{\text{PDG}} = 1864.83 \pm 0.05 \text{ MeV}/c^2$). Figure 5-1 shows the cartoon of the production and propagation of D^0 mesons in heavy-ion collisions.

Tracks used in D^0 reconstruction are reconstructed using the scenario described in Section 4.1. For each pair of selected tracks, two D^0 candidates with opposite mass hypothesis are created by assuming that one of the particles has the mass of the pion while the other has the mass of the kaon, and vice-versa.

For each pair of selected tracks, two D^0 candidates are considered by assuming one of the particle having the mass of the pion and the kaon and vice-versa. The secondary (decay) vertex is reconstructed from the final states (daughter tracks) by using a “KinematicParticleVertexFitter” built in ROOT. Kinematic fitting is designed

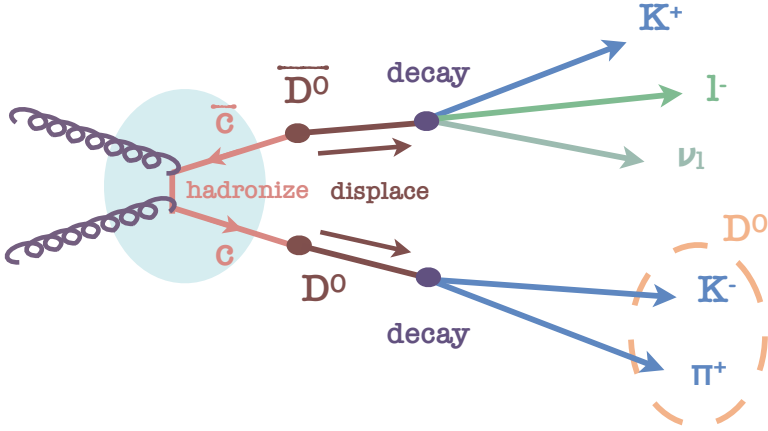


Figure 5-1: Charm quarks created in the initial hard scatterings partly fragment into D^0 meson. The fragment fraction is $f(c \rightarrow D^0) = 0.6176 \pm 0.0160$ in pp collisions [129]. D^0 mesons propagate with a relatively long displacement ($c\tau = 123.03 \pm 0.45 \mu\text{m}$ [128]) and decay into K and π with branching ratio of $\text{BR}(D^0 \rightarrow K\pi) = (3.89 \pm 0.04)\%$ [128]. The charged particles K and π are detected by the trackers and are reconstructed by the scenario described in Section 4.1.

to solve minimization problems with constraints (physics laws) introduced. The mathematical approach based on Least Mean Squared minimization (LMS) with Lagrange multiplier is implemented in the kinematic fitter described. This method allows to constrain the decay with particles having specific mass, momentum, etc. When the constraint equations are linear, the minimization problem has analytic solutions under the method of LMS with Lagrange multiplier. The main idea is actually straightforward. Consider the input reconstructed tracks, and their status can be described by a set of kinematic variables $y = \{y_1, y_2, \dots, y_n\}$ with their associated error matrices $\mathcal{V}_y = (\mathcal{V}_1, \mathcal{V}_2, \dots, \mathcal{V}_n)$. They are subject to a set of constraint equations $\mathcal{H}(y) = 0$. With LMS method, the refitted parameters (y^{ref}) are determined to minimize

$$\chi^2 = (y^{\text{ref}} - y) \mathcal{V}_y^{-1} (y^{\text{ref}} - y)^T \quad (5.1.1)$$

satisfying the constraint equations

$$\mathcal{H}(y^{\text{ref}}) = 0 \quad (5.1.2)$$

If the precision of the fit is not satisfactory, further fitting iteration can be performed. These steps are terminated when the maximum number of iterations is reached or the

precision is better than a certain criterion. For our case, $D^0 \rightarrow K^-\pi^+$ reconstruction from two tracks, the constraint condition is to require the two tracks to have a given invariant mass (D^0 mass).

In order to further reduce the combinatorial background, the D^0 candidates are selected based on three topological criteria:

- $d_0/\sigma(d_0)$: the three-dimensional (3D) decay length normalized to its uncertainty (decay length significance);
- θ_p : the pointing angle defined as the angle between the total momentum vector of the tracks and the vector connecting the primary and the secondary vertices;
- Vertex probability: the χ^2 probability, divided by the number of degrees of freedom, of the D^0 vertex fit.

The selection is optimized in each p_T bin using a multivariate technique [130] in order to maximize the statistical significance of the D^0 meson signals. We will discuss more details about cut optimization in Section 5.2.

5.2 Cut Optimization

The goal of the optimization procedure is to maximize the statistical significance of the signals while keeping reasonably high signal efficiencies. TMVA (Toolkit for Multivariate Data Analysis with ROOT) [130] is used to discriminate signal D^0 from the data sample mixed with background candidates. To separate signal from background rectangular cuts on discriminating variables are applied. It is the simplest classifier in TMVA training, and is least likely to result in over train compared with more complex algorithm. Implied by its name, rectangular cuts method assumes that the signal is clustered and one minimum and one maximum requirement on each variable is sufficient to discriminate signal and background. The cut optimization analysis proceeds by first building binary search trees for signal and background. For each variable, statistical properties like mean, root-mean-squared (RMS), variable ranges are computed to guide the search for optimal cuts. Cut optimization requires an estimator that quantifies the goodness of a given cut ensemble. Maximizing this estimator minimizes (maximizes) the background efficiency ϵ_B for each signal efficiency ϵ_S . The previous quantity is often represented by background rejection $r_B \equiv 1 - \epsilon_B$ as well.

Several fitters could be applied by rectangular cuts: Monte-Carlo sampling, Genetic Algorithm, and Simulated Annealing. Monte-Carlo sampling (CutsMC), the most straightforward one, randomly samples the fit parameters and choose the parameters that optimizes the estimator. For rectangular cuts, each sample corresponds to a point in the (ϵ_S, r_B) . The sampling distribution is uniform or Gaussian within the parameter limits. Genetic Algorithm (CutsGA) is a technique to find approximate solution of optimization. It applies processes that are modeled in biological evolution – selections, inheritance, mutation, “sexual recombination”. First, a initialized group of solutions are created. Each individual is created by randomly setting the parameters on variables. For each individual fitness function is calculated to evaluate goodness. It is largely determined by the difference of the best found background rejection and the one valued by the current individual. Individuals are decided to be stored or abandoned according to its fitness function, and only the surviving individuals produce next generation. The next generation keeps same number of individuals, and the new individuals are produced via copy, mutation and recombination. Mutation means changing some values of parameters of some individuals randomly with a Gaussian distribution function. The evaluation, selection and reproduction processes are repeated until a maximum number of cycles set or an individual satisfies a maximum-fitness criterion. Simulated Annealing (CutsSA) is inspired by the process of metal annealing that occurs in condensed matter physics. When first heating and then slowly cooling down a metal its atoms move towards a state of lowest energy, while for sudden cooling the atoms tend to freeze in intermediate states higher energy. For infinitesimal annealing activity the system will always converge in its global energy minimum. Rectangular cut optimization using Genetic Algorithm and Simulated Annealing achieves similar performance, and the analyses described in this thesis applies Simulated Annealing fitter.

Reconstructed candidates which can be matched to generated particles in MC are used as signal sample during training in TMVA, while the reconstructed candidates of data inside sideband $0.1 < |m_{D^0} - m_{D^0}^{\text{PDG}}| < 0.15 \text{ GeV}/c^2$ is used as background sample. An identical loose pre-selections are applied on both signal and background samples to speed up the training process. Figure 5-2 shows the distributions of the cut variables of signal and background candidates at $6 < p_T < 8 \text{ GeV}/c$ in Pb-Pb collisions. According to the figure, we found the decay length significance distribution and the secondary vertex probability of signal is larger than that of background. This

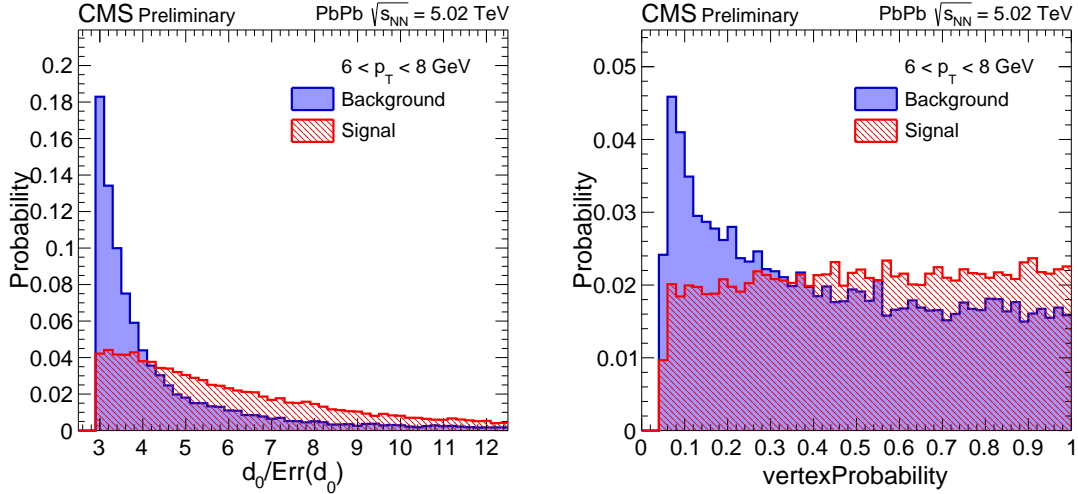


Figure 5-2: Distributions of D^0 cut variables $d_0/\text{Err}(d_0)$ (left) and secondary vertex probability (right) of background (blue) and signal (red) candidates at $6 < p_T < 8 \text{ GeV}/c$ in Pb-Pb collisions.

suggests that these two variables have discrimination power for signal and background. In TMVA classification process, input samples are split into training sample and testing sample. The previous part is used to distinguish signal and background, while the latter part validates the training result and performs over-train test.

The optimal cut values are defined as the one maximizing the statistical significance $s/\sqrt{s+b}$. s is the expected number of signal yield after the selections, and b is the expected number of background counts in the signal region, where signal region is defined as $|m_{D^0} - m_{D^0}^{\text{PDG}}| < 2\sigma$. σ is the width of D^0 signal mass in MC. s and b are estimated by the procedures below

- $s = s' \times \epsilon_S$, where s' is the number of D^0 signal in data before optimal cuts, and ϵ_S (signal cut efficiency) is the ratio of D^0 signal number after optimal cuts over that before optimal cuts. This efficiency can be read out directly from TMVA at each working point. $s' = s'' \times (\text{pre-selection efficiency})$ where s'' is the number of D^0 signal before pre-selections, which is estimated by FONLL calculation and preliminary R_{AA} . The pre-selection efficiency is the ratio of (reconstructed D^0 signal after pre-selection in MC) over (generated candidate number in MC).
- $b = b' \times \epsilon_B$, where b' is the number of background in signal region in data before cuts, and ϵ_B (background cut efficiency) is the ratio of background after optimal cuts over that before optimal cuts. This efficiency can be read out

directly from TMVA at each working point. $b' = b'_{\text{sideband}} \times (w_{\text{signal region}}/w_{\text{sideband}})$ where $w_{\text{signal region}}$ and w_{sideband} are the width of signal region and the width of sideband.

Figure 5-3 illustrated the definition of all quantities mentioned.

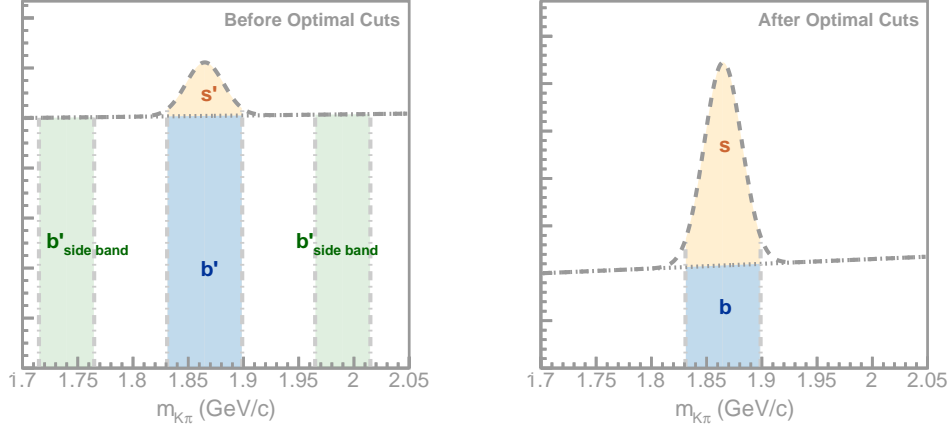


Figure 5-3: Definition of quantities applied in cut optimization. s and b are the expected number of signal yield and background counts in the signal region after the selections, which are used to calculate the significance ($s/\sqrt{s+b}$). They are estimated by selection efficiencies and the yields of signal (s') and background (b') before the selections. b' is calculated by b'_{sideband} , the number of background in sidebands.

The optimization of cuts performed by TMVA maximizes the background rejection at given signal efficiency. Scanning over signal efficiencies from 0 to 1, each working point corresponds to a specific background efficiency. This relationship is presented in Figure 5-4. The more different signal and background efficiencies are, the better performance of signal-background separation is. the significance ($s/\sqrt{s+b}$) as a function of signal efficiency can be found, which is presented in Figure 5-5. Therefore, TMVA simplifies a multiple variable problems into a one-dimension problem. According to Figure 5-5, we find the optimal working point (corresponding to maximum significance) at $5 - 6$ GeV/c has smaller signal efficiency compared with $15 - 20$ GeV/c. This is reasonable considering the fact that combinatorial background level is higher at lower p_T , and therefore, a tighter selection is necessary to reduce combinatorial background and achieve the maximum significance.

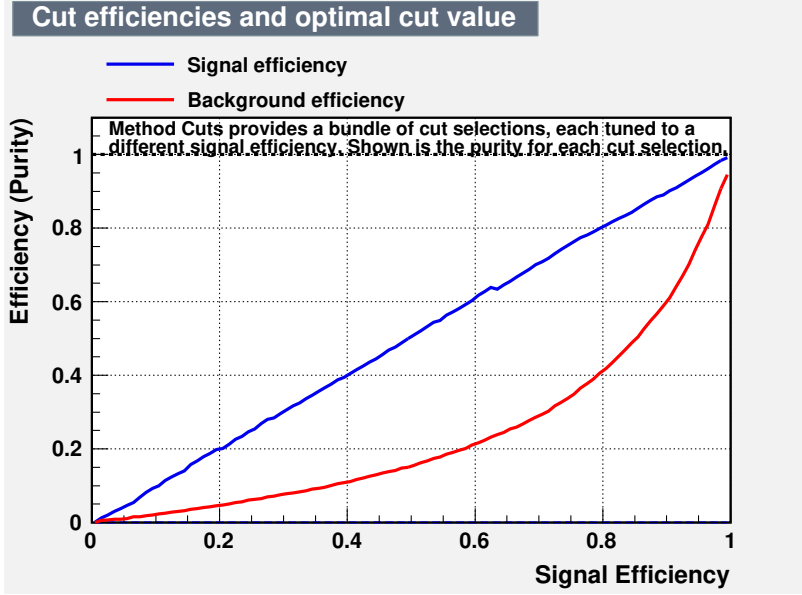


Figure 5-4: Signal efficiency (blue solid line) and background efficiency (red solid line) versus signal efficiency from classification by TMVA with rectangular cuts for D^0 at $5 < p_T < 6$ GeV/c in Pb-Pb collisions.

5.3 Signal Extraction

Invariant mass distributions with reasonable significance are obtained in all p_T bins after the cut optimization procedure discussed above. The D^0 meson yields in each p_T interval are extracted with a binned maximum-likelihood fit to the invariant mass distributions in the range $1.7 < m_{\pi K} < 2.0$ GeV/c 2 . Several examples of D^0 candidate invariant mass distributions are shown in Figure 5-6 for pp (top) and Pb-Pb (bottom) collisions.

The combinatorial background, originating from random pairs of tracks not produced by a D^0 meson decay, is modeled by a third-order polynomial. For combinatorial background, unlike-sign pairs and like-sign pairs have pretty similar mass spectrum shape (slightly different, but good enough for background shape check), so like-sign track pairs passing all D^0 cuts are used to check combinatorial background shape. The signal shape was found to be best modeled over the entire p_T range measured by two Gaussian functions with the same mean but different widths. An additional Gaussian function is used to describe the invariant mass shape of D^0 candidates with incorrect mass assignment from the exchange of the pion and kaon designations. The widths of the Gaussian functions that describe the D^0 signal shape

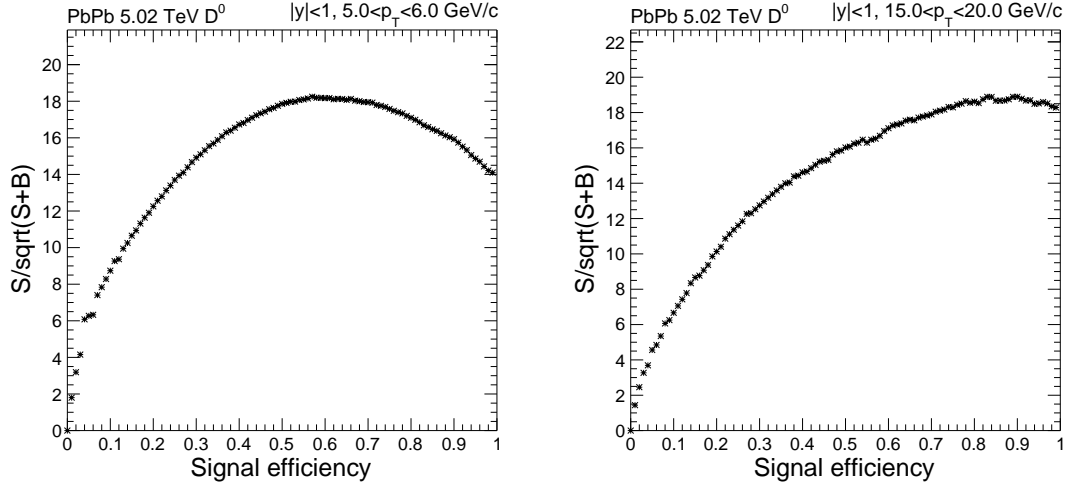


Figure 5-5: Statistical significance ($s/\sqrt{s+b}$) versus signal efficiency for D^0 at $5 < p_T < 6$ GeV/c (left) and $15 < p_T < 20$ GeV/c (right) in Pb-Pb collisions.

and the shape of the D^0 candidates with swapped mass assignment are described by the values extracted from simulation and a free parameter in the fit. The parameter is employed to cover the potential different resolution in data and simulations. The ratio between the yields of the signal and of the D^0 candidates with swapped mass assignments is fixed to the value extracted from simulation.

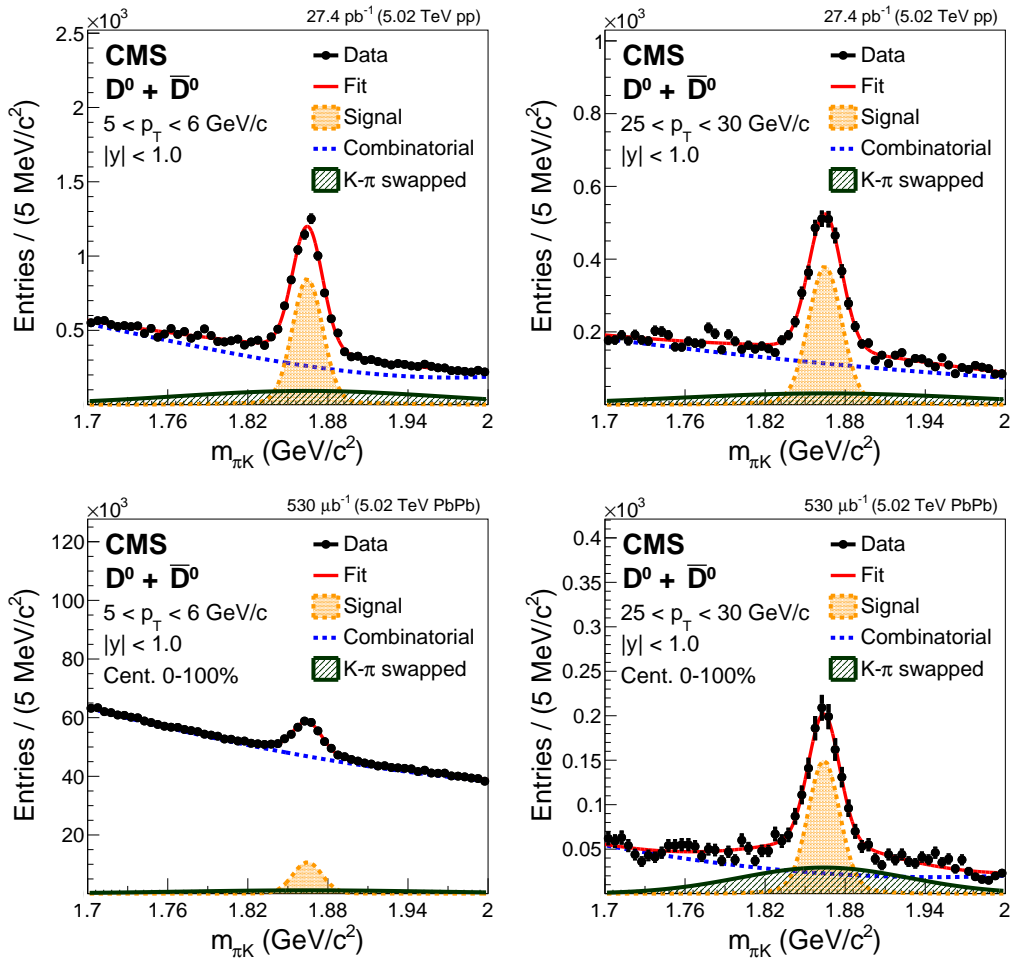


Figure 5-6: Examples of D^0 candidate invariant mass distributions at $5 < p_T < 6 \text{ GeV}/c$ (left) and $25 < p_T < 30 \text{ GeV}/c$ (right) in pp (top) and Pb-Pb (bottom) collisions.

Chapter 6

Prompt D^0 Production in Heavy-ion collisions

In this chapter, the measurement of production of prompt D^0 mesons in pp and PbPb collisions at 5.02 TeV with the CMS detector is discussed. Section 6.1 describes analysis techniques employed in this analysis. The production cross section and yields of prompt D^0 in pp and PbPb collisions are displayed in Section 6.2.1 and Section 6.2.2, and the nuclear modification factor (R_{AA}) is discussed for two centrality intervals: in the inclusive sample (0 – 100%) and in one corresponding to the most overlapping 10% of the collisions in Section 6.2.3. In addition, study of systematical uncertainties is briefly discussed in Section 6.3. This work is based on the paper Ref. [131].

6.1 Analysis Technique

6.1.1 Dataset and D^0 Selection

The pp (PbPb) dataset used for this analysis corresponds to an integrated luminosity of 27.4 pb^{-1} ($530 \mu\text{b}^{-1}$). The D^0 meson production is measured from p_T of 2 up to 20 GeV/c using large samples of minimum-bias events ($\simeq 2.5$ billion pp events and $\simeq 300$ million PbPb events). For D^0 above 20 GeV/c, the HLT designed to identify online events with a D^0 candidate that is described in Section 2.3.4 is employed. D^0 candidates are reconstructed following the scenario described in Section 5.1. Tracks used in D^0 reconstruction in this analysis are required to fulfill the kinematic selections described in Table 6.1. The table presents the track selection applied in the pp and PbPb analysis at low p_T ($p_T < 20$ GeV/c with the MB sample) and high p_T

($p_T > 20$ GeV/c with the triggered sample). The tighter selection on the single track p_T applied in the high- p_T PbPb analysis (8.5 GeV/c) is justified by the presence of a 8 GeV/c selection in the HLT tracking. The D^0 mesons are required to be within $|y| < 1$, optimized in conjunction to the track pseudorapidity selection to give the best signal to background ratio over the whole range of $D^0 p_T$ studied. To suppress

	pp (low p_T)	pp (high p_T)	PbPb (low p_T)	PbPb (high p_T)	
Track quality	highpurity	highpurity	highpurity	highpurity	
$ \eta $	< 1.5	< 1.5	< 1.5	< 1.5	
p_T (GeV/c)	> 1.0	> 2.0	> 1.0	> 8.5	
σ_{p_T}/p_T	< 0.3	< 0.1	< 0.3	< 0.3	

Table 6.1: Track selection criteria applied in the R_{AA} analysis at low and high p_T .

combinatorial backgrounds, cut optimization described in Section 5.2 is performed, and the final cut values are reported in Table 6.2. The definitions of each variable can be found in Section 5.1.

	p_T	θ_p	$d_0/\sigma(d_0)$	Vertex Probability	
	$2 < p_T < 3$ GeV/c	< 0.12	> 4.62	> 0.161	
	$3 < p_T < 4$ GeV/c	< 0.12	> 4.80	> 0.197	
	$3 < p_T < 5$ GeV/c	< 0.12	> 4.63	> 0.141	
	$5 < p_T < 6$ GeV/c	< 0.12	> 4.53	> 0.172	
	$6 < p_T < 8$ GeV/c	< 0.12	> 4.09	> 0.120	
	$8 < p_T < 10$ GeV/c	< 0.12	> 4.02	> 0.098	
	$10 < p_T < 12.5$ GeV/c	< 0.12	> 3.66	> 0.099	
	$12.5 < p_T < 15$ GeV/c	< 0.12	> 3.70	> 0.084	
	$15 < p_T < 20$ GeV/c	< 0.12	> 3.53	> 0.047	
	> 20 GeV/c	< 0.12	> 3.50	> 0.050	

Table 6.2: The selection criteria on D^0 candidates in different p_T intervals applied in prompt $D^0 R_{AA}$ analysis.

6.1.2 Acceptance and Efficiency Correction

As described in Section 6.1.1, selections on kinematic variables are applied to suppress combinatorial background and lead to discrepancy of signal at the same time. In addition, track reconstruction described in Section 4.1 and secondary vertex reconstruction described in Section 5.1 are not fully efficient either. To cover these effects, acceptance and efficiency studies are performed with PYTHIA sample for pp

and PYTHIA+HYDJET sample for Pb-Pb. The acceptance factor α is defined as the fraction of D^0 mesons generated in $|y| < 1$ that have both daughters that fulfill the single track acceptance selections (single track p_T and η selection). The reconstruction efficiency ϵ_{reco} is defined as the fraction of D^0 mesons generated in $|y| < 1$ that have both daughters which are reconstructed in the acceptance region and fulfill the track selection criteria. The selection efficiency (ϵ_{sel}) is defined as the fraction of reconstructed D^0 candidates with reconstructed and selected tracks that fulfill the D^0 selection criteria. The details concerning simulations are described in Section 3.

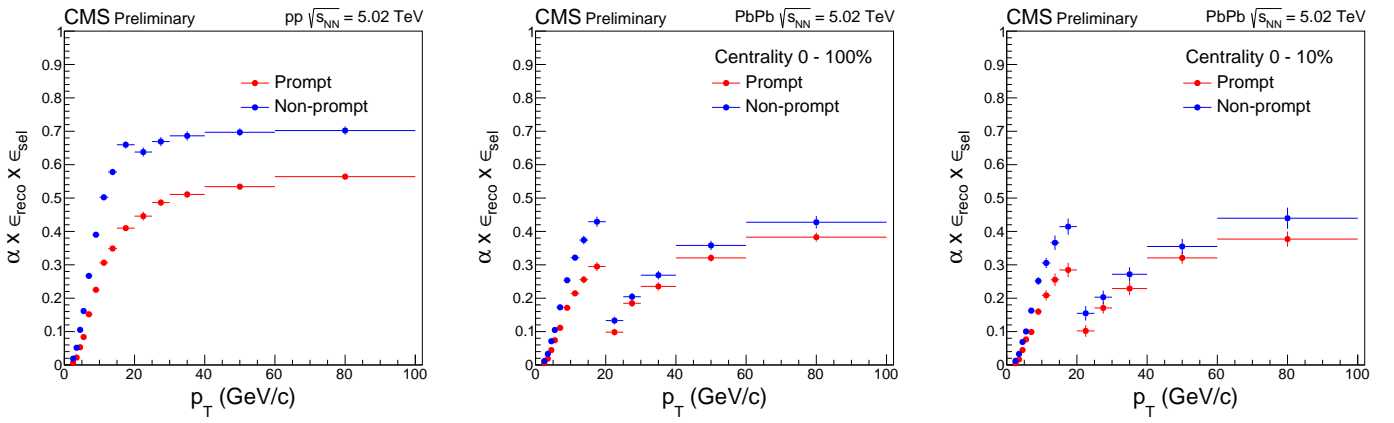


Figure 6-1: Efficiency ($\alpha \times \epsilon_{\text{reco}} \times \epsilon_{\text{sel}}$) as a function of p_T of prompt (red) and non-prompt (blue) D^0 in pp collisions (left) and Pb-Pb collisions in the inclusive centrality range (middle) and in most central events (0 – 10%) (right).

In Figure 6-1, the acceptance factors and the total efficiencies are presented as a function of p_T in both pp and Pb-Pb collisions. The results are shown for both prompt and b-hadron feed-down (non-prompt) D^0 , and the separation of these two components are discussed in Section 6.1.3. The discontinuity appearing at $p_T = 20$ GeV/c is due to the track p_T selection applied in D^0 triggers described in Section 2.3.4.

6.1.3 b-hadron Feed-down Subtraction

The number of D^0 from mass spectrum fit in data is the total number prompt D^0 (D^0 directly fragmented from charm quark) and non-prompt D^0 (D^0 from b-hadron decays). The previous component is the real signal we are interested in as a representative of open charm hadrons, and therefore the latter component is necessarily to be subtracted. In earlier similar measurements, this procedure based on theoretical calculation introduces the largest systematical uncertainty.

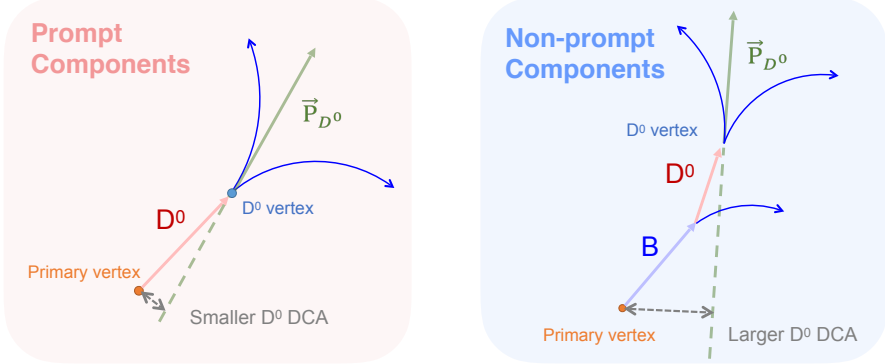


Figure 6-2: Diagram of prompt (left) and non-prompt (right) D^0 . Prompt component is defined by D^0 directly fragmented from charm quark, while non-prompt D^0 from b-hadron decays. Distance of Closest Approach (DCA) is defined by the distance between primary vertex and the direction of the momentum of D^0 . Non-prompt D^0 is featured by a large DCA due to the displacement of their parent b-hadrons, and therefore DCA is possibly used to distinguish the two components.

With the large dataset collected by CMS in 2015, a data-driven method is applied to subtract the non-prompt D^0 component dramatically reducing the systematic uncertainty. This method is inspired by the idea that the Distance of Closest Approach (DCA), whose definition is illustrated in [fig:raa.fprompt.cartoon](#), of non-prompt D^0 should be obviously larger than that of prompt D^0 . This results from the fact that the trajectory of prompt D^0 should match the primary vertex where the initial charm comes from, while this is not true for non-prompt D^0 due to displacement of the parent b-hadron. Recalling the variables defined in Section 5.2: 3D-displacement d_0 and pointing angle θ_p , D^0 DCA can be calculated by

$$l_{\text{DCA}} = d_0 \times \sin \theta_p \quad (6.1.1)$$

Practically the DCA distribution of all D^0 (including both prompt and non-prompt components) is obtained from data. The combinatorial background in each DCA bin is subtracted via sideband method. The invariant mass and sideband is presented in the left-bottom panel of Figure 6-3. The shapes of DCA distribution of prompt and non-prompt components are obtained from simulation respectively. The left-top panel of Figure 6-3 shows the DCA distributions of prompt and nonprompt D^0 obtained from MC simulations, and it clearly indicates the dramatic difference between these two components. Therefore, one can extract the relative fraction between prompt and

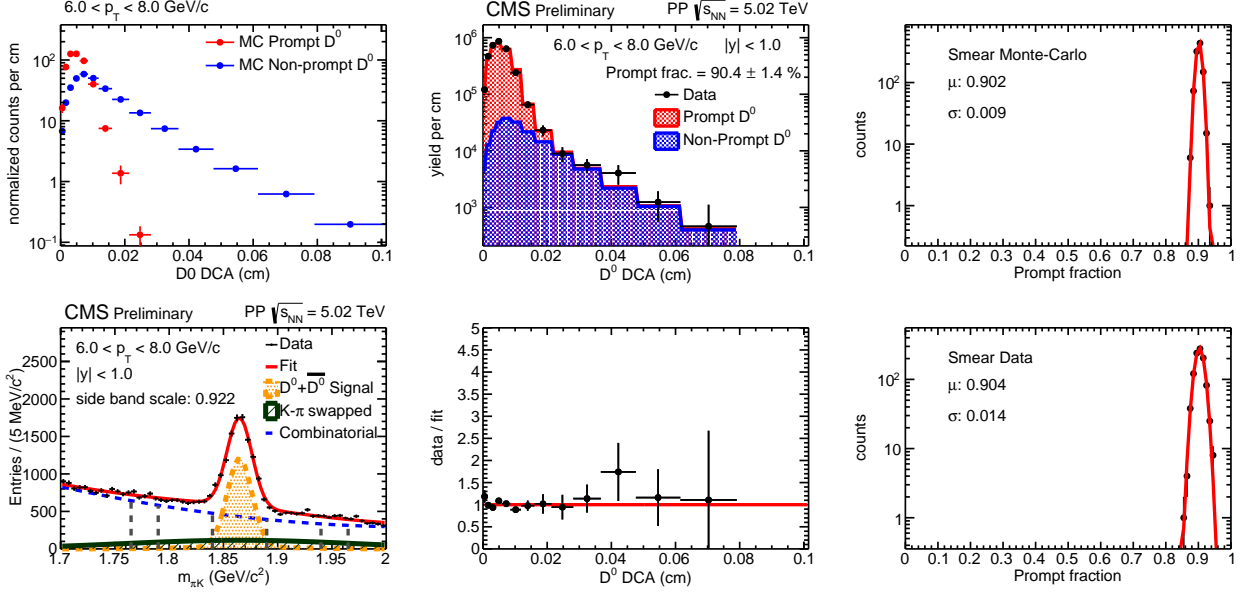


Figure 6-3: DCA distribution of prompt and nonprompt from MC simulations (left top) in pp collisions at $6 < p_T < 8 \text{ GeV}/c$; Invariant mass distributions and sideband scales (left bottom); DCA fit of data by the MC templates smeared to achieve best χ^2 probability (middle top) and the ratio of data over fit (middle bottom); Prompt fractions by randomly varying MC and data DCA distribution according to their statistic uncertainties (right top and bottom).

non-prompt component in data by fit using the template obtained from simulations. Figure 6-4 presents examples of DCA fitting performance at the same p_T range in pp and PbPb collisions. Statistic uncertainty of the prompt fraction (f_{prompt}) is estimated by randomly varying MC and data DCA distribution according to their statistic uncertainties. Specifically, for every DCA bin, when a new bin content is created according to the statistic uncertainty, accordingly a new f_{prompt} is extracted by fitting the new DCA distribution. This process was repeated by 1000 times and the width of the f_{prompt} distribution is quoted as the statistic uncertainty of f_{prompt} . The f_{prompt} distribution with MC DCA and data DCA smeared is shown in the right top and bottom panels of Figure 6-3 respectively. In this scenario the templates of DCA shape of prompt and non-prompt D⁰ are fixed from simulations. However, due to potential different resolutions, the shape obtained from MC do not necessarily describe data. To study this effect, fit using the template with different resolution is performed and we obtain a set of f_{prompt} results. Among them the one with the best performance (corresponding to the largest χ^2 probability) is picked. The systematic uncertainty of f_{prompt} is quoted by the difference between these two scenario.

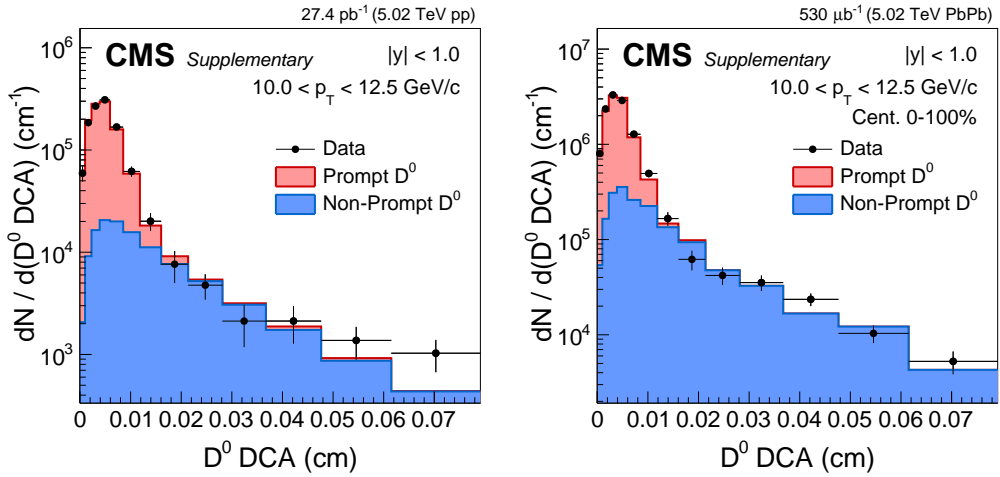


Figure 6-4: DCA distribution of inclusive D^0 in data (black circles), of prompt D^0 (red histogram) from simulations, and of non-prompt D^0 (blue histogram) from simulations at $10 < p_T^{D^0} < 12.5$ GeV/c in pp (left) and PbPb (right) collisions. As a fitting parameter, the fraction of the red histogram implies the fraction of prompt components in data.

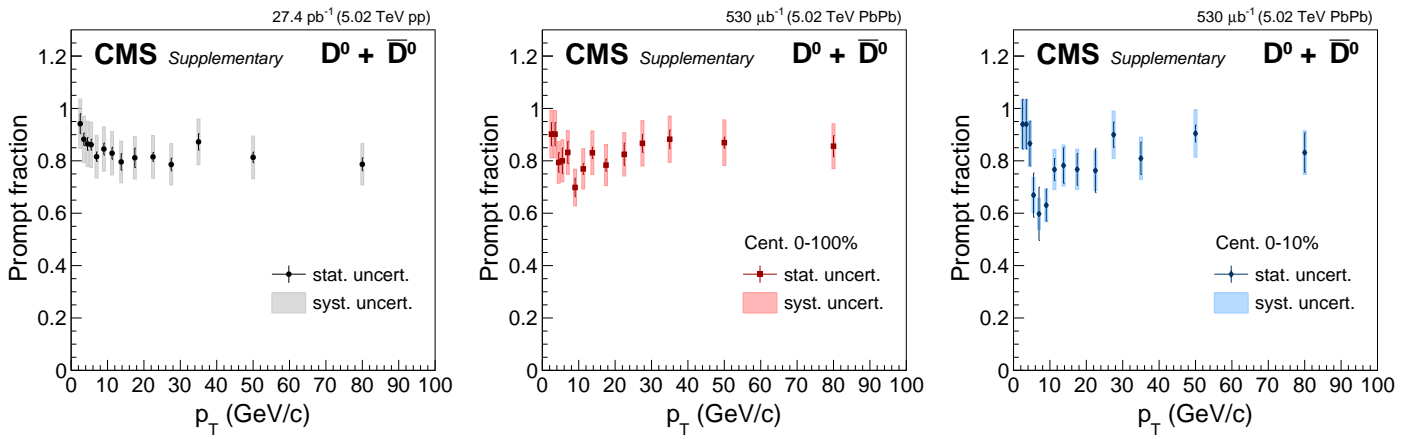


Figure 6-5: Fraction of prompt D^0 (f_{prompt}) as a function of p_T in pp events (left), PbPb events in centrality class 0 – 100% (middle), and PbPb events in centrality class 0 – 10% (right). The error bars and the boxes indicate statistic and systematic uncertainties.

This procedure is applied in each p_T range, and Figure 6-5 presents f_{prompt} as a function of p_T in both pp and PbPb collisions. The statistic and systematic uncertainties extracted according to the process described above are also shown in the same figures by the error bars and the boxes respectively. Note f_{prompt} is extracted after the selections on kinematic variables, and thus the trend of f_{prompt} strongly depends on the specific selections applied. As a comparison with the old methods and a validation of the data driven procedure of f_{prompt} estimation, the results above are compared to an estimation based on pQCD calculation (FONLL) and simulations. In particular, f_{prompt} is alternatively estimated as:

$$f_{\text{prompt}}^{\text{fonll}} = \frac{\sigma_{\text{prompt}}^{\text{fonll}} \times (\alpha \times \epsilon)_{\text{prompt}}}{\sigma_{\text{non-prompt}}^{\text{fonll}} \times (\alpha \times \epsilon)_{\text{non-prompt}} \times (R_{\text{AA}}(\text{B}^+)/R_{\text{AA}}(\text{D}^0)) + \sigma_{\text{prompt}}^{\text{fonll}} \times (\alpha \times \epsilon)_{\text{prompt}}} \quad (6.1.2)$$

where $\sigma_{\text{prompt}}^{\text{fonll}}$ and $\sigma_{\text{non-prompt}}^{\text{fonll}}$ are the production cross sections calculated by FONLL and $(\alpha \times \epsilon)_{\text{prompt}}$ and $(\alpha \times \epsilon)_{\text{non-prompt}}$ are the acceptance times efficiency factors estimated from MC. $R_{\text{AA}}(\text{B}^+)/R_{\text{AA}}(\text{D}^0)$ is the ratio of nuclear modification of B^+ over D^0 , which is only included in PbPb collision system. In the range of $8 < p_T < 50$ GeV/c, the ratio is obtained from the preliminary results of B^+ and D^0 R_{AA} measurement in PbPb collisions at 5.02 TeV by CMS collaboration, while for other p_T , ratio equal to 0.23 or 0.22 is assumed as what is done in previous measurements. In addition, results with R_{AA} ratio using non-prompt J/ψ R_{AA} measured in PbPb collisions at 2.76 TeV by CMS collaboration[132] is also obtained for comparison. Figure 6-6 shows f_{prompt} estimated by the two data-driven scenarios and by the pQCD calculation based method. This data-driven method of f_{prompt} estimation has much higher precision compared with the traditional method which requires good knowledge of R_{AA} of D and B meson.

6.2 Results

6.2.1 Prompt D^0 Cross-section in pp collisions

Measurements of D^0 production in pp collisions are a great test of pQCD and play an important role in study of hot effect in heavy-ion collisions as a baseline and a reference. The prompt D^0 p_T -differential cross section in each p_T interval in pp

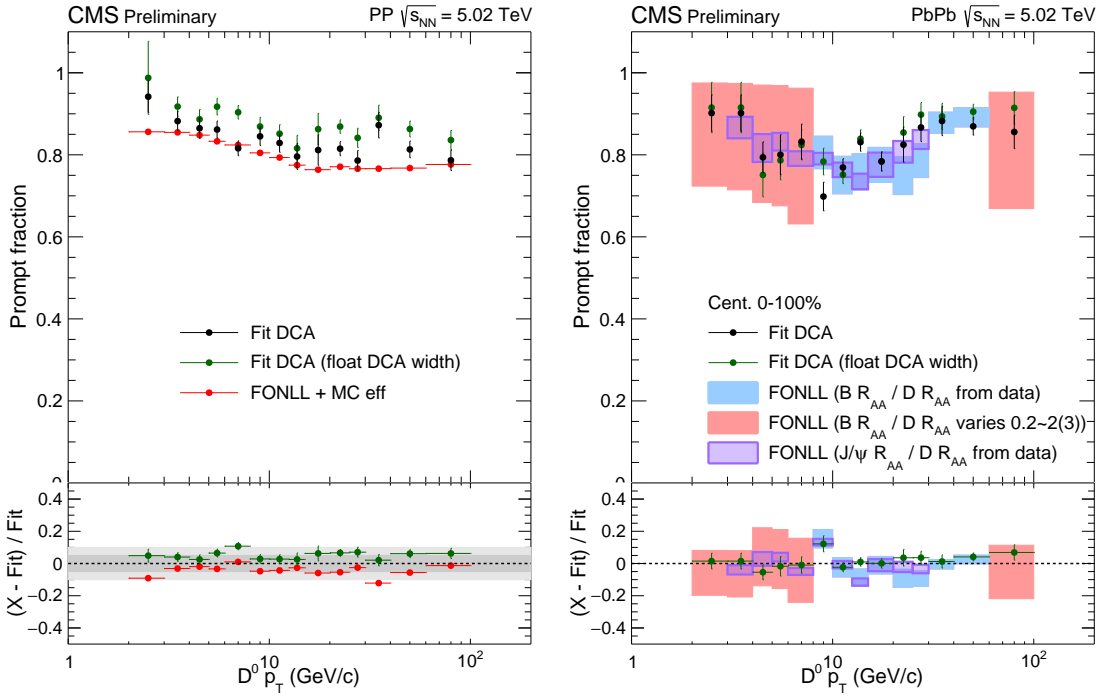


Figure 6-6: $D^0 f_{\text{prompt}}$ versus p_T via fitting data DCA with template fixed from MC (black markers), and with template floating resolution (green markers). The two panels show results in pp (left) and PbPb (right) collisions. In the left panel, $f_{\text{prompt}}^{\text{fonll}}$ obtained based on FONLL calculation is presented by red markers. In the right panel, $f_{\text{prompt}}^{\text{fonll}}$ is displayed by color shadow. The shadow cover variation of R_{AA} measured for B^+ and non-prompt J/ψ .

collisions is defined as:

$$\frac{d\sigma_{pp}^{D^0}}{dp_T} \Big|_{|y|<1} = \frac{1}{2} \frac{1}{\Delta p_T} \frac{1}{\mathcal{B} \mathcal{L}} \frac{f_{\text{prompt}} N_{pp}}{(\alpha \epsilon)_{\text{prompt}} \beta_{\text{prescale}} \epsilon_{\text{trigger}}} \Big|_{|y|<1}, \quad (6.2.1)$$

where Δp_T is the width of the p_T interval, \mathcal{B} is the branching fraction of the decay chain, \mathcal{L} is the integrated luminosity, $(\alpha \epsilon)_{\text{prompt}}$ represents the correction for acceptance and efficiency and N_{pp} is the yield of D^0 and \bar{D}^0 mesons extracted in each p_T interval. The details are discussed in Section 6.1.2 and Section 5.3. The factor 1/2 accounts for the fact that the cross section is given for the average of particles and antiparticles. The raw yields N_{pp} are corrected in order to account for the average prescale factor β_{prescale} and the efficiency $\epsilon_{\text{trigger}}$ of the trigger that was used to select events in that specific p_T interval, which is discussed in Section 2.3.4. The factor f_{prompt} is the fraction of D^0 mesons that comes directly from c quark fragmentation and is discussed in Section 6.1.3.

The p_T -differential production cross section in pp collisions measured in the interval $|y| < 1$ is presented in Figure 6-7. The result is compared to the prediction of FONLL [49] and a general-mass variable flavour number scheme (GM-VFNS) [51, 52, 53] calculation. Details of the two types of formalism are described in Section 1.3.1. FONLL calculates p_T -differential cross sections via a perturbative expansion in the strong coupling constant α_s , which includes In the FONLL calculation shown in Figure 6-7, the CTEQ6.6 parton distribution functions were considered. The central values of the predictions were obtained considering $m_c = 1.5 \text{ GeV}/c^2$, and the renormalization and factorization scales $\mu_R = \mu_F = \mu_0 = \sqrt{m^2 + p_T^2}$. The uncertainty band was evaluated varying the perturbative parameters. The quark mass is varied in the range $4.5 < m_b < 5 \text{ GeV}/c^2$, $1.3 < m_c < 1.7 \text{ GeV}/c^2$, and the renormalization μ_F and factorization scales μ_R are independently varied in the range $0.5 < \mu_F/\mu_0 < 2$ and $0.5 < \mu_R/\mu_0 < 2$ with the constraint of $0.5 < \mu_F/\mu_R < 2$. According to Figure 6-7, the CMS measurement lies close to the upper bound of the FONLL prediction and the lower bound of the GM-VFNS calculation. Also, it is surprising that GM-VFNS does not perform better than FONLL at high p_T , since the configuration is optimized by matching the zero-mass scheme at limit $m \rightarrow 0$.

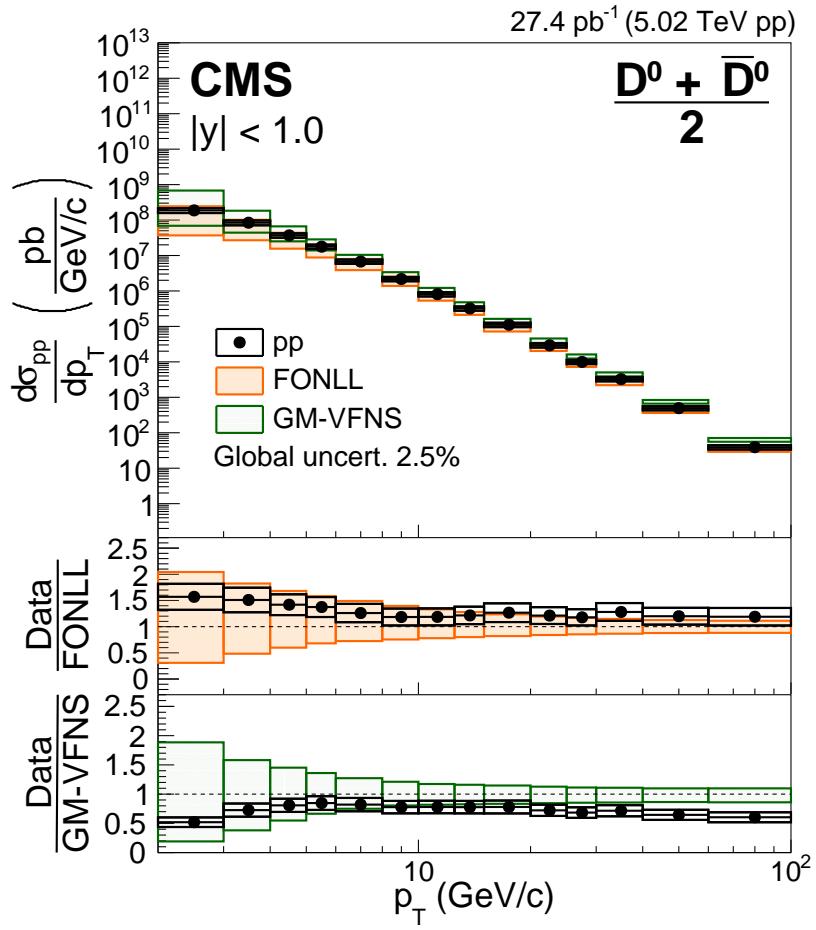


Figure 6-7: The p_T -differential production cross section of prompt D^0 mesons in pp collisions at $\sqrt{s_{NN}} = 5.02$ TeV. The vertical bars (boxes) correspond to statistical (systematic) uncertainties. The global systematic uncertainty, listed in the legend and not included in the point-to-point uncertainties, comprises the uncertainties in the integrated luminosity measurement and the D^0 meson \mathcal{B} . Results are compared to FONLL [49] (orange) and GM-VFNS [51, 52, 53] (green) calculations.

6.2.2 Prompt D⁰ Cross-section in PbPb collisions

The prompt D⁰ p_{T} -differential production yield in each p_{T} interval in PbPb collisions is defined as:

$$\frac{1}{T_{\text{AA}}} \left. \frac{\text{d}N_{\text{PbPb}}^{\text{D}^0}}{\text{d}p_{\text{T}}} \right|_{|y|<1} = \frac{1}{T_{\text{AA}}} \frac{1}{2} \frac{1}{\Delta p_{\text{T}}} \frac{1}{\mathcal{B} N_{\text{MB}}} \left. \frac{f_{\text{prompt}} N_{\text{PbPb}}}{(\alpha \epsilon)_{\text{prompt}} \beta_{\text{prescale}} \epsilon_{\text{trigger}}} \right|_{|y|<1}, \quad (6.2.2)$$

where N_{MB} is the equivalent number of Minimum-Bias events used for the analysis and T_{AA} is the nuclear overlap function [133], which is equal to the number of nucleon-nucleon (NN) binary collisions divided by the NN cross section and can be interpreted as the NN-equivalent integrated luminosity per heavy ion collision. The values of T_{AA} are 5.61 mb⁻¹ for inclusive PbPb collisions and 23.2 mb⁻¹ for central events according to the calculation using Glauber Model [11]. This scaling is applied to allow PbPb result comparable with cross section measured in pp. The other terms were defined analogously to Eq. (6.2.1). The D⁰ p_{T} -differential production yields divided by the nuclear overlap functions T_{AA} in PbPb collisions in the 0–100% and 0–10% centrality ranges are presented in Figure 6-8 and compared to the same pp cross section shown in Figure 6-7.

6.2.3 Prompt D⁰ Nuclear Modification Factor

To further present the hot effect happening in heavy-ion collisions, the nuclear modification factor (R_{AA}) is produced. R_{AA} has been defined in Eq. (1.2.2), and for D⁰ case, R_{AA} is computed as

$$R_{\text{AA}} = \frac{1}{T_{\text{AA}}} \frac{\text{d}N_{\text{PbPb}}^{\text{D}^0}}{\text{d}p_{\text{T}}} \Bigg/ \frac{\text{d}\sigma_{\text{pp}}^{\text{D}^0}}{\text{d}p_{\text{T}}} \quad (6.2.3)$$

The R_{AA} in the centrality range 0–100% is shown in the left panel of Figure 6-9 as a function of p_{T} . In the overall p_{T} range, R_{AA} is smaller than 1, indicating suppression of prompt D⁰ in a wide kinematic range and as a consequence of parton energy loss in quark gluon plasma. The R_{AA} suggests a suppression of a factor 3 to 4 at p_{T} of 6–8 GeV/c. At higher p_{T} , the suppression factor decreases to a value of about 1.3 in the p_{T} range 60–100 GeV/c. The R_{AA} for the centrality range 0–10% is presented in the right panel of Figure 6-9. The R_{AA} in central events shows a hint of stronger suppression if compared to the inclusive R_{AA} result for $p_{\text{T}} > 5$ GeV/c. This can be

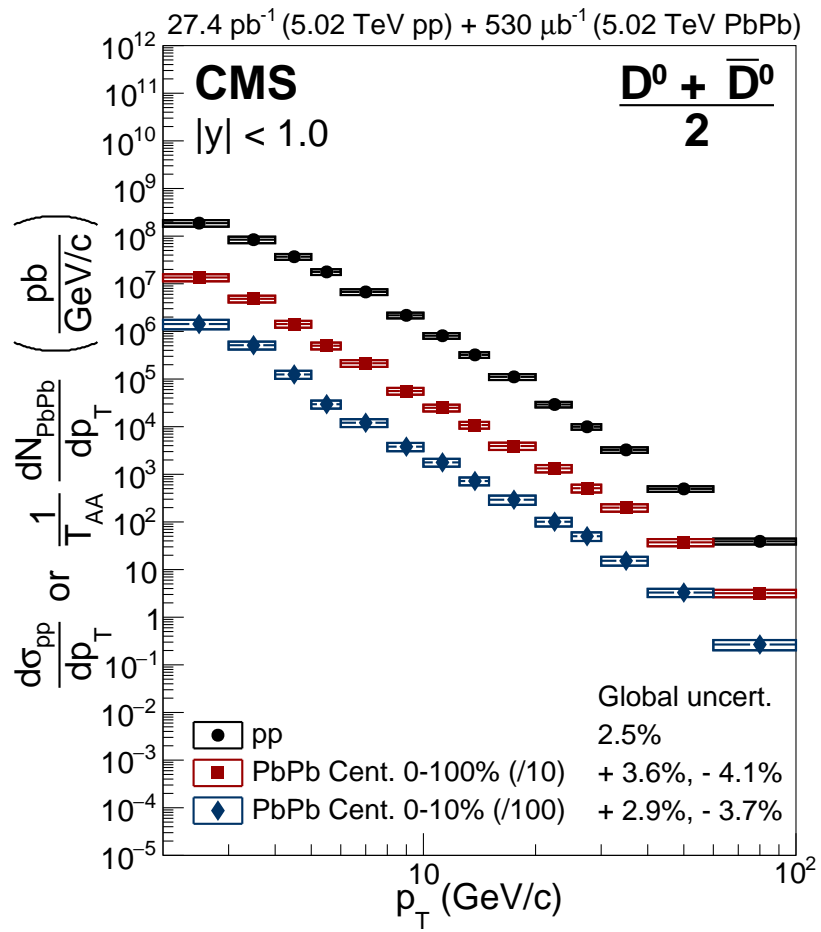


Figure 6-8: The p_T -differential production yields of D^0 mesons divided by the nuclear overlap functions T_{AA} for PbPb collisions in the 0–100% (red) and 0–10% (blue) centrality ranges compared to the pp cross sections (black) which is same with Figure 6-7.

explained by the larger medium system leading to larger path length, and a higher density of the medium in the most central events. In this comparison, the large overlap between the two results has to be considered. Indeed, roughly 40% of the D^0 candidates used in the measurement in the centrality range 0–100% are also included in the 0–10% result.

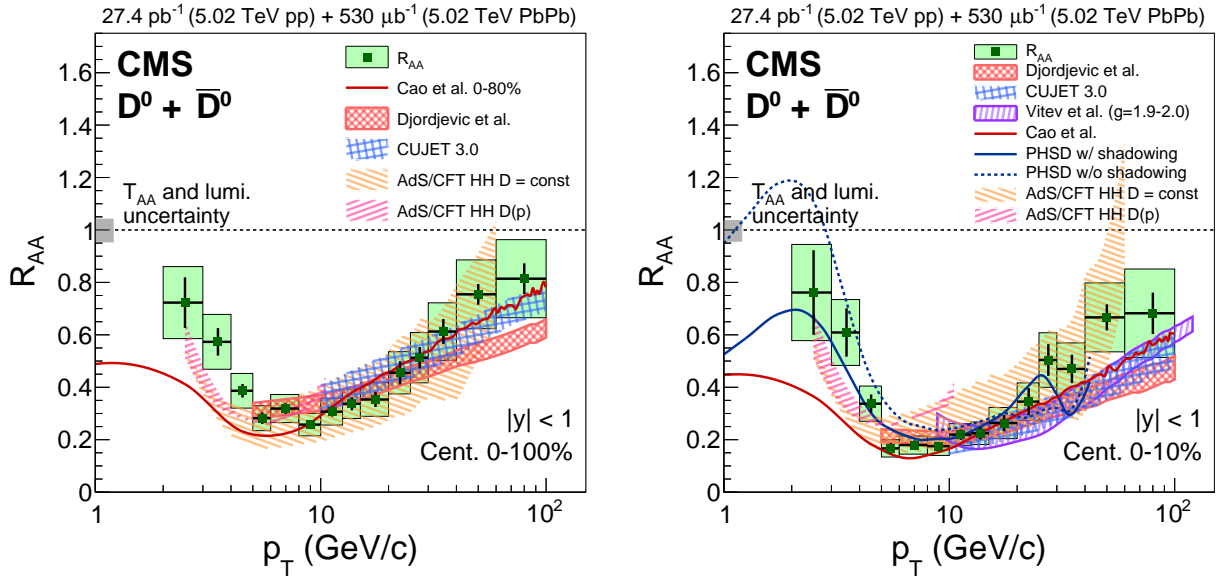


Figure 6-9: Prompt D^0 R_{AA} as a function of p_T in the centrality range 0–100% (left) and 0–10% (right). The vertical bars (boxes) correspond to statistical (systematic) uncertainties. The global systematic uncertainty, represented as a grey box at $R_{AA} = 1$, comprises the uncertainties in the integrated luminosity measurement and T_{AA} value. The prompt D^0 R_{AA} values are also compared to calculations from various theoretical models [134, 135, 136, 137, 138, 139, 140, 141, 142, 143, 144].

It is observed that the shape of R_{AA} reaches minimum at p_T of 6–8 GeV/c, and increases towards lower and higher p_T . Multiple effects contribute to this shape. First of all, the energy loss of quark as a function of p_T is reflected in both R_{AA} value and shape. Second, the production cross section shape affects R_{AA} shape independent of the energy loss. An extreme example is a unit cross section, which leads to $R_{AA} = 1$ regardless of energy loss. Third, collective flow motions may push very low- p_T parton to a higher energy that contribute to the R_{AA} shape in low- p_T region. Also, the cold-nuclear-matter (CNM) effects (e.g. (anti-) shadowing) play important role on the R_{AA} shape at low p_T . As further study of processes, measured R_{AA} is compared with various theoretical models. These models can be grouped in three types: transport models, jet models, and string models. The first group studies the heavy quarks

propagation in the evolved bulk medium, and the second group is an extension of the treatment on high- p_T jet in light quark sector to heavy-flavor sector. The last group is out of the scope of QCD framework and bases on the anti-de Sitter/comformal field theory. In Section 1.3.1, we have discussed how different models solve the diffusion coefficient, and in Table 6.3, the configurations of the components implemented by various models on market to predict $D^0 R_{AA}$ and v_2 are summarized.

Model	Ref.	Trans. Impl.	Bulk Evolution	Initial Condition	Coll. E loss	Rad. E loss	Group
UrQMD Hybrid	[68]	LV	3+1D ideal hydro	Smeared UrQMD string/energy density	✓		
TAMU	[145]	LV	2+1D ideal hydro	Smooth initial condition	✓		
SUBATECH Nantes MC@sHQ EPOS2	[146]	BM	EPOS2 3+1D ideal hydro	Fluctuating initial condition	✓	✓	Transport Models
Catania	[147]	BM	HQ interact with bulk massive quasi-particles, T-dependence of α_S is tuned to match the 1QCD EoS	-	✓	✓	
LBL-Duke Cao et al.	[140] [141]	LV	VISHNU 2+1D viscous hydro	Event-by-event fluctuating initial conditions	✓	✓	
POWLANG Torino	[148]	LV	ECHO-QGP 3+1D viscous hydro	Event-by-event fluctuating initial conditions	✓	✓	
PHSD	[142] [143]	BM	HQ interact with off-shell light quasi-particles whose masses and widths are determined to match 1QCD EoS	-	✓	✓	
Djordjevic	[134]		DGLV: variant of GLV approach including gluon radiation from multiple scattering up to 1st order in opacity		✓	✓	Jet Models
Vitev et al. SCET_G	[138] [139]		Soft Collinear Effective Theory with Glauber Gluons including quark masses (SCET _G)			✓	
CUJET3.0	[135] [136] [137]		DGLV + VISHNU 2+1D viscous hydro		✓	✓	
AdS/CFT	[144]		Model based on the anti-de Sitter/conformal field theory				String Models

Table 6.3: Summary of implement configurations of theoretical models in the current market.

(High p_T :) For D^0 meson $p_T > 20$ GeV/c, the perturbative QCD-based models roughly describe the suppression in both centrality ranges within the uncertainties. In 0–100% centrality class the transport model LBT (Cao et al.) agrees with data very well, while the two jet models, Djordjevic and CUJET3.0, suggest smaller slope than data. In the most central events (0–10%), the predictions from all pQCD models are lower than that in the experimental data. The pure jet models (Djordjevic et al. and Vitev et al.) only work at high p_T and they are found to be consistent, although the Vitev model only takes into account radiative energy loss. The AdS/CFT calculation describes data well for both the 0–100% and the 0–10% centrality classes up to 60 GeV/c, while it diverges to higher p_T and therefore a cut-off at 60 GeV/c is applied.

(Intermediate p_T :) In the intermediate p_T region ($5 < p_T < 20$ GeV/c), all the theoretical calculations describe well the R_{AA} results in both centrality intervals. **(Low p_T :**) At $p_T < 5$ GeV/c, the PHSD prediction that includes shadowing can reproduce the measurement in the 0–10% centrality region accurately. This is not surprising, although PHSD only includes collisional energy loss. On the one hand, the collisional energy loss dominates versus radiative energy loss at relatively low p_T . On the other hand, the transport coefficients and the parameters (e.g. T_c , $\tau_{\text{thermalization}}$, α_s) are inconsistent over different models, and therefore the fact that PHSD works does not mean radiative energy loss is not important. In the same low- p_T region, the calculation from LBT and that from AdS/CFT lie are lower than the experimental measurements. The AdS/CFT calculation is provided for two settings of the diffusion coefficient D of the heavy quark propagation through the medium: dependent on, and independent of the quark momentum. The calculation with constant D diverges at $p_T = 10$ GeV/c, and thus only $p_T < 10$ GeV/c is displayed. This indicates the parton energy dependence of the diffusion coefficient is crucial for the R_{AA} distribution. In the right panel of Figure 6-9, the PHSD predictions with and without including shadowing are shown, and it suggests the significant influence on $p_T < 10$ GeV/c.

Flavor-dependent energy loss is studied by comparing R_{AA} of various light-flavor and heavy-flavor hadrons. The prompt $D^0 R_{AA}$ measured in the centrality range 0–100% is compared in the left panel of Figure 6-10 to the CMS measurements of the R_{AA} of charged particles [34], B^\pm mesons [149], nonprompt D^0 [151] and nonprompt J/ψ meson [150] performed at the same energy and in the same collision system and same centrality range. Charged particle is a representative of light-flavor hadrons, while D^0 is charm representative. Beauty is studied by two strategies: exclusive and

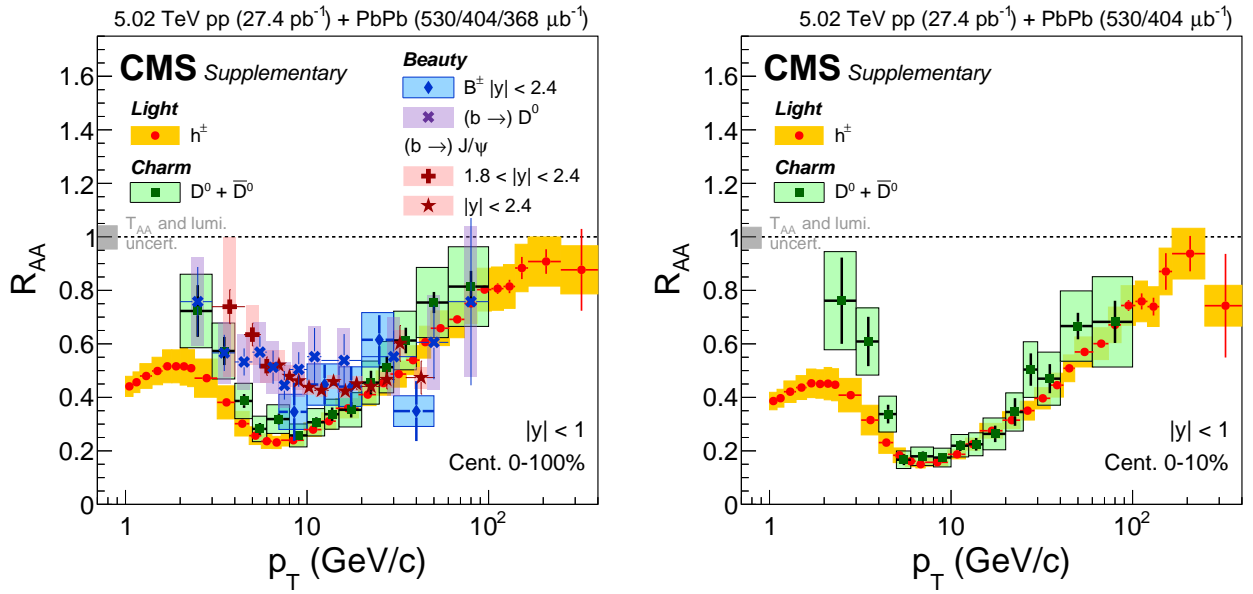


Figure 6-10: (Left) Prompt D^0 nuclear modification factor R_{AA} as a function of p_T in the centrality range 0–100% (green squares) [131] compared to the R_{AA} of charged particles (red circles with yellow boxes) [34], B^\pm mesons (blue triangles) [149], non-prompt D^0 (purple crosses) and nonprompt J/ψ meson (red crosses and stars) [150] in the same centrality range at 5.02 TeV. (Right) D^0 nuclear modification factor R_{AA} as a function of p_T in the centrality range 0–10% (green squares) [131] compared to the R_{AA} of charged particles (red circles with yellow boxes) [34] in the same centrality range. The error bars (boxes) indicate statistical (systematic) uncertainties.

inclusive measurements. CMS performs B^\pm measurements by full hadronic reconstruction in intermediate p_T region, which is called exclusive measurement for the specific B meson. b-hadrons can also be studied by measuring the daughter resonances, which is called inclusive measurements since types of parent b-hadrons are not distinguished. The systematic uncertainties between the R_{AA} measurement of the D^0 mesons, and of the light and beauty particles, are almost completely uncorrelated. The only common contribution comes from the systematic uncertainty of one track (4%), which is however negligible when compared to the total uncertainties. The D^0 meson R_{AA} values are consistent with those of charged particles for $p_T > 5 \text{ GeV}/c$. For lower p_T , a somewhat smaller suppression for D^0 mesons is observed. The R_{AA} of the B^\pm mesons, measured in the p_T range $7 - 50 \text{ GeV}/c$ and the rapidity range of $|y| < 2.4$, is also consistent with the D^0 meson measurement within the experimental uncertainties. The R_{AA} of nonprompt J/ψ , which was found to have almost no rapidity dependence [150], is shown here measured in the p_T ranges $6.5 - 50 \text{ GeV}/c$ in $|y| < 2.4$, and $3 - 6.5 \text{ GeV}/c$ in $1.8 < |y| < 2.4$. Its R_{AA} is found to be higher than the D^0 meson R_{AA} in almost the entire p_T range. In the p_T range $4 - 20 \text{ GeV}/c$ where precision is best, the R_{AA} of nonprompt D^0 is larger than that of prompt D^0 , which is consistent with nonprompt J/ψ . In the p_T region $p_T < 4 \text{ GeV}/c$ and $p_T > 20 \text{ GeV}/c$, R_{AA} of prompt D^0 is compatible with nonprompt D^0 , while the uncertainties are too large to draw conclusions. The D^0 meson R_{AA} in the centrality range 0–10% is compared in Figure 6-10 to the charged-particle R_{AA} . As observed for 0–100% PbPb events, the two results are consistent within uncertainties for $p_T > 5 \text{ GeV}/c$ and a somewhat smaller suppression for charmed mesons is observed at lower p_T . The prompt D^0 R_{AA} measured in the centrality range 0–100% is compared in Figure 6-11 to the CMS measurements of the R_{AA} of prompt J/ψ meson [150] performed at the same energy and in the same collision system and same centrality range. It indicates although charmonia (prompt J/ψ) and open-charm hadron (prompt D^0) experience dramatically different processes in the medium, for the energy and density of LHC PbPb collisions, R_{AA} of open and hidden charm mesons are similar.

As a cross-check, in Figure 6-12 prompt D^0 R_{AA} result discussed above is compared with that performed by ALICE collaboration in the centrality class 0–10% in the same collision system [43]. Note that the two measurements are performed in different rapidity range. In the p_T range $p_T < 20 \text{ GeV}/c$, the results from two collaborations are consistent, while in $p_T > 20 \text{ GeV}/c$, ALICE result has a hint of smaller R_{AA} .

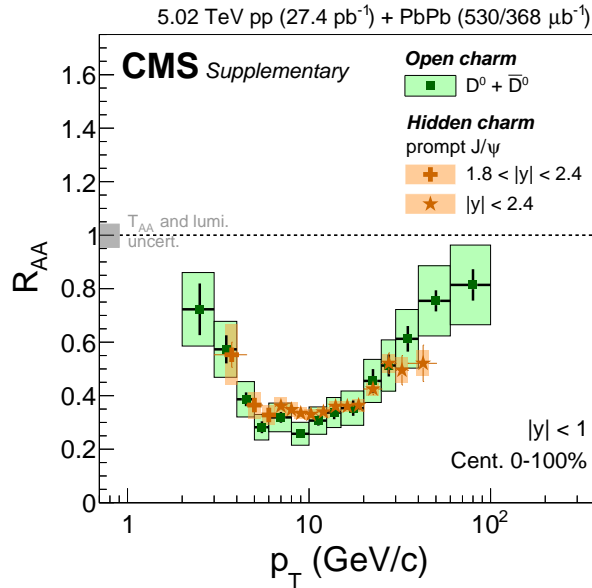


Figure 6-11: Prompt D^0 nuclear modification factor R_{AA} as a function of p_T in the centrality range 0–100% (green squares) [131] compared to the R_{AA} of prompt J/ψ meson (orange crosses and stars) [150] in the same centrality range at 5.02 TeV.

Next we take a look at the comparison between different collision systems by varying the energy and the system size. In the left panel of Figure 6-12, prompt $D^0 R_{AA}$ as a function of p_T performed by CMS collaboration in PbPb collisions at 2.76 TeV. It is consistent within the uncertainties with the measurements at 5.02 TeV in the whole p_T range showing no obvious collision energy dependence for these two energies. To compare more different collision energies, in the right panel of Figure 6-12, prompt $D^0 R_{AA}$ performed by STAR collaboration in AuAu collisions at 200 GeV [153] is shown. 200 GeV AuAu collisions yield a system with significantly smaller size, lower temperature and smaller density than the case of LHC. It is observed that R_{AA} of prompt D^0 measured are consistent within uncertainties at relatively low p_T region in the two distinct systems. However hints of different decreasing shapes of R_{AA} are implied although it is not conclusive considering the precision.

In Figure 6-13, R_{AA} of identified D^0 in 0–10% PbPb events at $\sqrt{s_{NN}} = 5.02$ TeV is compared with heavy-flavor muon R_{AA} in the similar collision system but different energy $\sqrt{s_{NN}} = 2.76$ TeV [97]. In $5 < p_T < 14$ GeV/c, heavy flavor decay muon R_{AA} is relatively flat as a function of p_T and is significantly larger than the case of D^0 . On the one hand, p_T of heavy flavor decay muons does not directly corresponds to p_T of D^0 , and the muons at a given p_T convolute the mother heavy-flavor hadrons

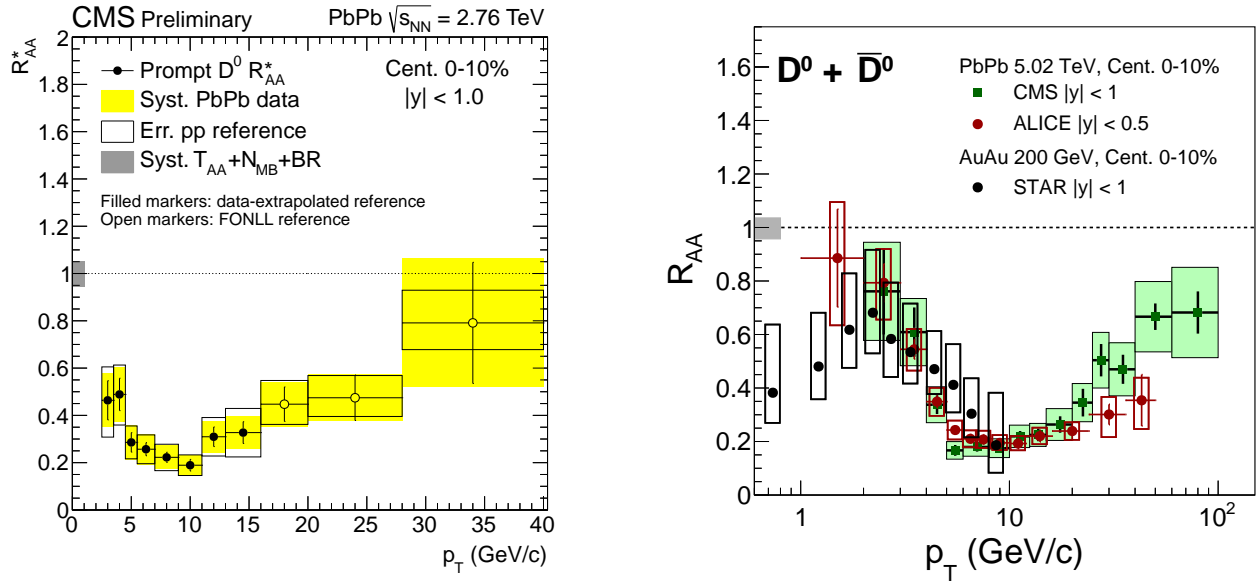


Figure 6-12: (Left) Prompt D^0 nuclear modification factor R_{AA} as a function of p_{T} in the centrality range 0–100% performed by CMS collaboration in PbPb collisions at 2.76 TeV; (Right) Prompt D^0 nuclear modification factor R_{AA} as a function of p_{T} in the centrality range 0–10% performed by CMS (green) and ALICE (red) [152] collaboration in PbPb collisions at 5.02 TeV, and by STAR collaboration (black) in AuAu collisions at 200 GeV [153].

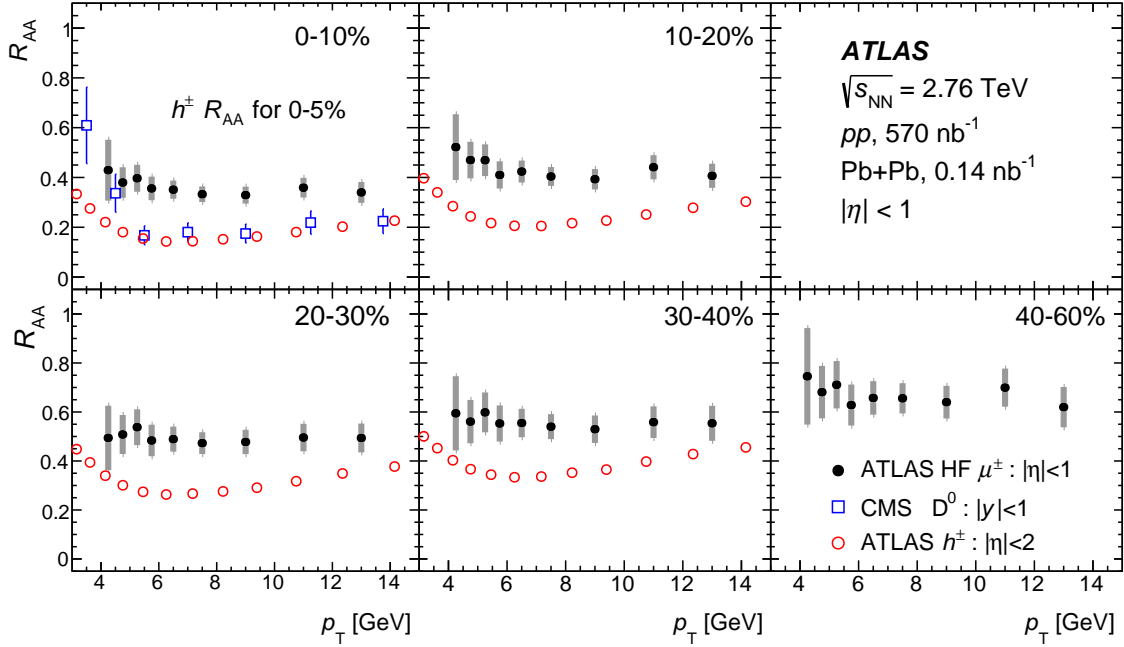


Figure 6-13: $D^0 R_{AA}$ measured in PbPb collisions at $\sqrt{s_{NN}} = 5.02$ TeV (blue) compared with heavy-flavor muon R_{AA} measured in PbPb collisions at $\sqrt{s_{NN}} = 2.76$ TeV (black) [97] as a function p_T . R_{AA} of inclusive charged particles in PbPb collisions at $\sqrt{s_{NN}} = 2.76$ TeV (red) [44] is also presented. Figure from Ref. [97].

with wide kinematic ranges. On the other hand, in Section 1.2.1 we once mentioned the measurements via leptons from heavy-flavor semileptonic decays have difficulty in extracting information from charm and beauty separately. Therefore, the difference may result from the mixture of contributions from beauty and charm. We have seen the measurements indicating that suppression of B mesons is weaker than D^0 , and $B^+ R_{AA}$ is not sensitive to p_T in intermediate p_T . Results in Figure 6-13 implies a significant contribution from the decays of b-hadrons to inclusive heavy-flavor muons measured.

6.3 Systematic Uncertainty Study

The yields are affected by several sources of systematic uncertainties arising from the signal extraction, acceptance and efficiency corrections, branching fraction, and integrated luminosity determination.

The uncertainty in the raw yield extraction is evaluated by repeating the fit procedure using different background fit functions and by forcing the widths of the Gaussian

functions that describe the signal to be equal to the values extracted in simulations to account for possible differences in the signal resolution in data and in MC. In the background variation study, an exponential plus a second-order polynomial function was considered instead of the first order polynomial one, which is used as default. The final uncertainty in the raw yield extraction is defined as the sum in quadrature of the relative differences of the signal variation and the maximum of all the background variations.

The systematic uncertainty due to the selection of the D^0 candidates is estimated by considering the differences between MC and data in the reduction of the D^0 yields obtained by applying each of the D^0 selection variables described in Section 6.1.1. The study was performed by varying selection on one variable at a time, in a range that allowed a robust signal extraction procedure and by considering the maximum relative discrepancy in the yield reduction between data and MC. The total uncertainty was the quadratic sum of the maximum relative discrepancy obtained by varying each of the three selection variables separately. The uncertainty due to the D^0 trigger efficiency is evaluated as the statistical uncertainty in the zeroth-order coefficient of the linear function used to describe the plateau of the efficiency distribution (details see Section 2.3.4). The systematic uncertainty in the hadron tracking efficiency is estimated from a comparison of two- and four-body D^0 meson decays in data and simulated samples (details see Section 4.1.2).

To evaluate the systematic uncertainty in the prompt D^0 meson fraction, the width of the DCA of MC prompt and nonprompt templates are varied in a range that covers the observed differences between the data and MC values. The systematic uncertainty was obtained in each p_T bin as the difference between the f_{prompt} value extracted from the variation that gives the best χ^2 fit to data and the nominal f_{prompt} value. To evaluate this uncertainty for the R_{AA} measurement, the widths of the template distributions are varied simultaneously in pp and PbPb. The systematic uncertainty on the f_{prompt} correction was evaluated as the spread of the ratios of fprompt in PbPb and pp to account for partial cancellations of the systematic effects in the two analyses.

The uncertainty related to the simulated p_T shape is evaluated by reweighting the simulated D^0 meson p_T distribution according to the p_T shape obtained from a FONLL prediction.

The systematic uncertainty in the cross section measurement is computed as the

sum in quadrature of the different contributions mentioned above. The global uncertainty in the pp measurement is the sum in quadrature of the systematic uncertainty in the integrated luminosity \mathcal{L} [154] and in the branching fraction \mathcal{B} (1.0%) [155]. The latter one is completely canceled for R_{AA} . The global uncertainty in the PbPb measurement is the sum in quadrature of the uncertainties in the MB selection efficiency, in the branching fraction and in the T_{AA} . For the R_{AA} results, except for explicit statement mentioned above, no other cancellation of uncertainties is assumed between the pp and PbPb results. Table 6.4 and Table 6.5 summarize the systematic uncertainties of R_{AA} from various sources in the centrality class of 0–100% and 0–10% respectively.

Minimum-Bias Data									
Source	p_T interval (GeV/c)								
	2-3	3-4	4-5	5-6	6-8	8-10	10-12.5	12.5-15	15-20
Tracking efficiency	12.0%								
Selection efficiency	5.0%								
MC p_T shape	1.3%	1.4%	1.4%	1.4%	1.4%	1.4%	1.4%	1.4%	1.4%
Signal extraction	9.5%	7.8%	4.6%	3.8%	3.4%	2.4%	2.5%	2.5%	7.6%
B feed down	10.0%	10.0%	10.0%	10.0%	10.0%	10.0%	10.0%	10.0%	10.0%
Luminosity	3.0%								
Triggered Data									
Source	p_T interval (GeV/c)								
	20-25	25-30	30-40	40-60	60-100				
Tracking efficiency	12.0%								
Selection efficiency	2.7%								
MC p_T shape	1.4%	1.4%	1.4%	1.4%	1.4%				
Signal extraction	7.4%	9.5%	7.8%	6.6%	8.7%				
B feed down	10.0%	10.0%	10.0%	10.0%	10.0%				
trigger efficiency	2.2%	2.2%	2.2%	2.2%	2.2%				
Luminosity	3.0%								

Table 6.4: Summary of relative systematic uncertainties for R_{AA} in Pb-Pb collisions at 5.02 TeV in the centrality class of 0–100%.

Minimum-Bias Data									
Source	p_T interval (GeV/c)								
	2-3	3-4	4-5	5-6	6-8	8-10	10-12.5	12.5-15	15-20
Tracking efficiency	13.0%								
Selection efficiency	8.9%								
MC p_T shape	1.3%	1.4%	1.4%	1.4%	1.4%	1.4%	1.4%	1.4%	1.4%
Signal extraction	15.2%	8.7%	6.8%	6.2%	4.8%	4.1%	4.0%	4.0%	12.6%
B feed down	10.0%	10.0%	10.0%	10.0%	10.0%	10.0%	10.0%	10.0%	10.0%
Luminosity	3.0%								
Triggered Data									
Source	p_T interval (GeV/c)								
	20-25	25-30	30-40	40-60	60-100				
Tracking efficiency	13.0%								
Selection efficiency	1.7%								
MC p_T shape	1.4%	1.4%	1.4%	1.4%	1.4%				
Signal extraction	12.2%	12.1%	12.9%	10.5%	18.2%				
B feed down	10.0%	10.0%	10.0%	10.0%	10.0%				
trigger efficiency	2.2%	2.2%	2.2%	2.2%	2.2%				
Luminosity	3.0%								

Table 6.5: Summary of relative systematic uncertainties for R_{AA} in Pb-Pb collisions at 5.02 TeV in the centrality class of 0–10%.

Chapter 7

Prompt D⁰ Azimuthal Anisotropy in Heavy-ion Collisions

In this chapter, the measurement of prompt D⁰ meson azimuthal anisotropy coefficients, v_2 and v_3 using the scalar product (SP) method in Pb-Pb collisions at a $\sqrt{s_{\text{NN}}} = 5.02$ TeV with the CMS detector is discussed. The measurement is performed in the p_{T} range of 1 to 40 GeV/c for central and midcentral collisions. Section 7.1 describes the analysis techniques utilized in this analysis. The results of prompt D⁰ meson v_2 and v_3 are discussed in Section 7.2.1 and Section 7.2.2 – this is the first measurement of D⁰ meson v_3 coefficient in heavy-ion collisions. Study of systematical uncertainties is briefly discussed in Section 6.3. This work is based on the paper Ref. [156].

7.1 Analysis Technique

7.1.1 Dataset and D⁰ Selection

The data used in this analysis are selected by a minimum bias trigger and a 30%–100% centrality trigger in Pb-Pb collisions. Details concerning these triggers can be found in Section 2.3.2. The numbers of events used in the 0%–10%, 10%–30%, and 30%–50% centrality ranges are 32×10^6 , 64×10^6 , and 151×10^6 , respectively. Since centrality distribution in minimum-bias events are flat except very peripheral events, event number is proportional to the centrality region width in 0%–30%, while there are more events in 30%–50% range due to existence of the centrality trigger.

Tracks selection criteria are similar with R_{AA} measurements, but p_{T} cut is loosen

to $p_T > 0.7$ GeV/c in this analysis to retain more signal with small transverse momentum ($p_T < 2$ GeV/c). For D^0 , one difference is that a cut on DCA (definition see Section 6.1.3) is applied as $DCA < 0.008$ cm. This selection turns out to be able to improve signal significance, and suppress influence from nonprompt D^0 and therefore reduce systematical uncertainties. Due to this difference, the optimal cut values are different from R_{AA} analysis, and they are reported in Table 7.1. The definitions of each variable can be found in Section 5.1.

p_T	θ_p	$d_0/\sigma(d_0)$	Vertex Probability
$1 < p_T < 2$ GeV/c	< 0.12	> 5.00	> 0.250
$2 < p_T < 4$ GeV/c	< 0.12	> 5.86	> 0.224
$4 < p_T < 5$ GeV/c	< 0.12	> 5.46	> 0.196
$5 < p_T < 6$ GeV/c	< 0.12	> 4.86	> 0.170
$6 < p_T < 8$ GeV/c	< 0.12	> 4.54	> 0.125
$8 < p_T < 10$ GeV/c	< 0.12	> 4.42	> 0.091
$10 < p_T < 15$ GeV/c	< 0.12	> 4.06	> 0.069
$15 < p_T < 20$ GeV/c	< 0.12	> 3.71	> 0.056
$20 < p_T < 25$ GeV/c	< 0.12	> 3.50	> 0.054
$25 < p_T < 40$ GeV/c	< 0.12	> 3.00	> 0.050

Table 7.1: The selection criteria on D^0 candidates in different p_T intervals applied in prompt $D^0 v_n$ analysis.

7.1.2 Event Plane

The “event-plane” is determined event-by-event and contains both the beam direction and the azimuthal direction of maximum particle density or, in alternative definitions, maximum transverse momentum or maximum transverse energy flow. It is defined empirically and, because of fluctuations in the positions of participant nucleons, it is not guaranteed to contain the impact parameter vector for any given event. Indeed, the participant fluctuations can lead to significant contributions of odd harmonics that would otherwise be strongly suppressed by the symmetry of a smooth lenticular-shaped region. For flow measurements based on the event plane, we are interested in determining the relative strength of particle flow outwards from the waist of the interaction region to that along the elongated dimension. Event planes can be defined separately with respect to each harmonic order and the azimuthal-flow asymmetry can be characterized by coefficients corresponding to Fourier components built on the event-plane order. Since the asymmetry that we are attempting to characterize is

also what allows us to define an experimental event plane, it is important to avoid autocorrelation effects where a given particle, or its decay products, is used for both the asymmetry measurement and the event-plane determination. This is usually done by requiring a gap in pseudorapidity between the particles used to establish the event plane and those used to determine the flow coefficients.

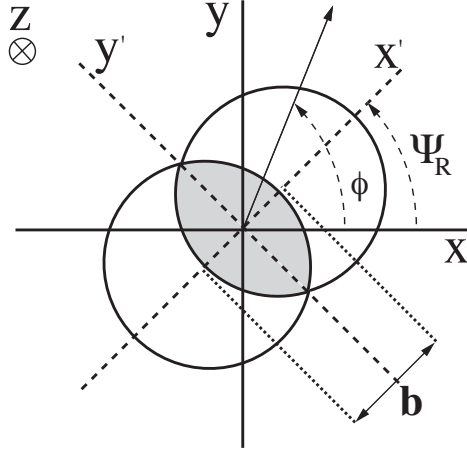


Figure 7-1: Definition of the coordinate system.

The azimuthal dependence of the particle yield can be written in terms of an harmonic expansion with [157]

$$E \frac{d^3N}{dp} = \frac{1}{2\pi} \frac{d^2N}{p_T dp_T dy} \left(1 + \sum_{n=1}^{\infty} 2v_n \cos[n(\phi - \Psi)] \right) \quad (7.1.1)$$

where ϕ , E and p_T are the particle's azimuthal angle, energy, and transverse momentum, respectively. If the impact-parameter direction is known, the reference angle Ψ can be taken as the azimuthal angle of the reaction plane Ψ_R as defined by the beam and impact parameter directions (see Figure 7-1). In analyzing an experimental distribution, the azimuthal dependence is expressed in terms of experimentally deduced event-plane angles $\Psi_{m,EP}$. These angles are defined for different harmonics and correspond to the maximum flow vector for the harmonic. The event-plane angles can be expressed in terms of Q-vectors. For perfect detector response, the Q-vector is

defined by

$$\begin{aligned}\vec{Q}_m = (Q_{mx}, Q_{my}) &= \left(\left| \vec{Q}_m \right| \cos(m\Psi_m), \left| \vec{Q}_m \right| \sin(m\Psi_m) \right) \\ &= \left(\sum_{i=1}^M w_i \cos(m\phi_i), \sum_{i=1}^M w_i \sin(m\phi_i) \right),\end{aligned}\quad (7.1.2)$$

where M is the sub-event multiplicity, w_i are weighting factors, and the corresponding event-plane angles are given as

$$\Psi_m = \frac{1}{m} \tan^{-1} \left(\frac{Q_{my}}{Q_{mx}} \right). \quad (7.1.3)$$

Different weights w_i are possible. For example, $w_i = 1$ for flow of the number of particle, $w_i = p_T(i)$ for the transverse momentum flow, and $w_i = E_T(i)$ for transverse energy flow. Since the $v_n(p_T)$ coefficients increase with p_T up to ≈ 3 GeV, the choice of either p_T or E_T weighting generally results in a better event-plane resolution than a simple particle weighting. Expressed in terms of the event-plane angle corresponding to harmonic m , the expansion of the azimuthal behavior becomes

$$\frac{dN}{d(\phi - \Psi_m)} \propto 1 + \sum_{k=1}^{\infty} 2v_{km}^{\text{obs}} \{ \Psi_m \} \cos [km(\phi - \Psi_m)]. \quad (7.1.4)$$

where dN is the differential of an observable N , such as the number of charged particles emitted into a differential azimuthal angular range $d(\phi - \Psi_m)$, $n = km$, and the dependence of v_n^{obs} on the event-plane harmonic m is explicitly noted. The event-plane harmonic m can take any integer value greater than or equal to 1. Generally, when higher-order event planes are considered ($m > 2$), only the $k = 1, n = m$ term is found to be needed. For $m > 1$, it will not be possible to describe the correlations possible with Eq. (7.1.1) corresponding to $n < m$. In the current study of the PbPb system, only the $n = m$ terms with $n = 2$ and 3 are considered.

In CMS it is possible to define event planes using either the tracker or the electromagnetic and hadronic calorimeters. To achieve the best event-plane resolutions, p_T weighting is used for the tracker planes and E_T weighting for the calorimeters. Notice that for the m^{th} -order event plane,

$$-\frac{\pi}{m} \leq \Psi'_m < \frac{\pi}{m}. \quad (7.1.5)$$

The randomness of the impact parameter direction should result in Ψ'_m having a flat angular distribution. However, asymmetries that arise from the detector acceptance and other effects correlated with the laboratory system can lead to structure in this distribution and, hence, affect the subsequent v_n analysis. Several different techniques have been developed to deal with these asymmetries. Here we follow a two-step process where the event plane is first “recentered” and subsequently “flattened” [158]. The “flattening” procedure to correct the event-plane angle for non-uniform acceptance effects has been shown in previous CMS analyses to correct for these effects within the statistical significance of the measurements. However, both PHENIX and ATLAS have reported azimuthal asymmetry results using a two-step correction process, with a recentering correction applied before subsequent flattening. The current analysis follows this two-step procedure.

When averaged over many events, the averages of $Q_{m,x}$ and $Q_{m,y}$ are expected to separately equal zero. Recentering involves correcting the observed values to assure this expectation is met, so the \vec{Q}_m vectors of Eq. (7.1.2) become

$$\vec{Q}_m = \left(\sum_i^M w_i \cos(m\phi_i) - \left\langle \sum_i^M w_i \cos(m\phi_i) \right\rangle, \sum_i^M w_i \sin(m\phi_i) - \left\langle \sum_i^M w_i \sin(m\phi_i) \right\rangle \right), \quad (7.1.6)$$

which can be expressed as an imaginary number. The corresponding event-plane angles are then given by

$$\Psi'_m = \frac{1}{m} \tan^{-1} \left\{ \frac{\sum_{i=1}^M w_i \sin(m\phi_i) - \left\langle \sum_{i=1}^M w_i \sin(m\phi_i) \right\rangle}{\sum_{i=1}^M w_i \cos(m\phi_i) - \left\langle \sum_{i=1}^M w_i \cos(m\phi_i) \right\rangle} \right\} \quad (7.1.7)$$

where $\langle \rangle$ indicates the average over all events within the same centrality class and range of vertex locations. The randomness of the impact parameter direction should result in Ψ_m having a flat angular distribution. However, asymmetries that arise from the detector acceptance and other effects correlated with the laboratory system can lead to structure in this distribution and, hence, affect the subsequent v_n analysis. Several different techniques have been developed to deal with these asymmetries. For previous CMS analysis we have used a procedure where the “raw” event-plane angle

Ψ'_m is “flattened” to become Ψ_m using the transformation [158]:

$$\Psi_m = \Psi'_m \left(1 + \sum_{j=1}^{j_{\max}} \frac{2}{jm} (-\langle \sin(jm\Psi'_m) \rangle \cos(jm\Psi'_m) + \langle \cos(jm\Psi'_m) \rangle \sin(jm\Psi'_m)) \right). \quad (7.1.8)$$

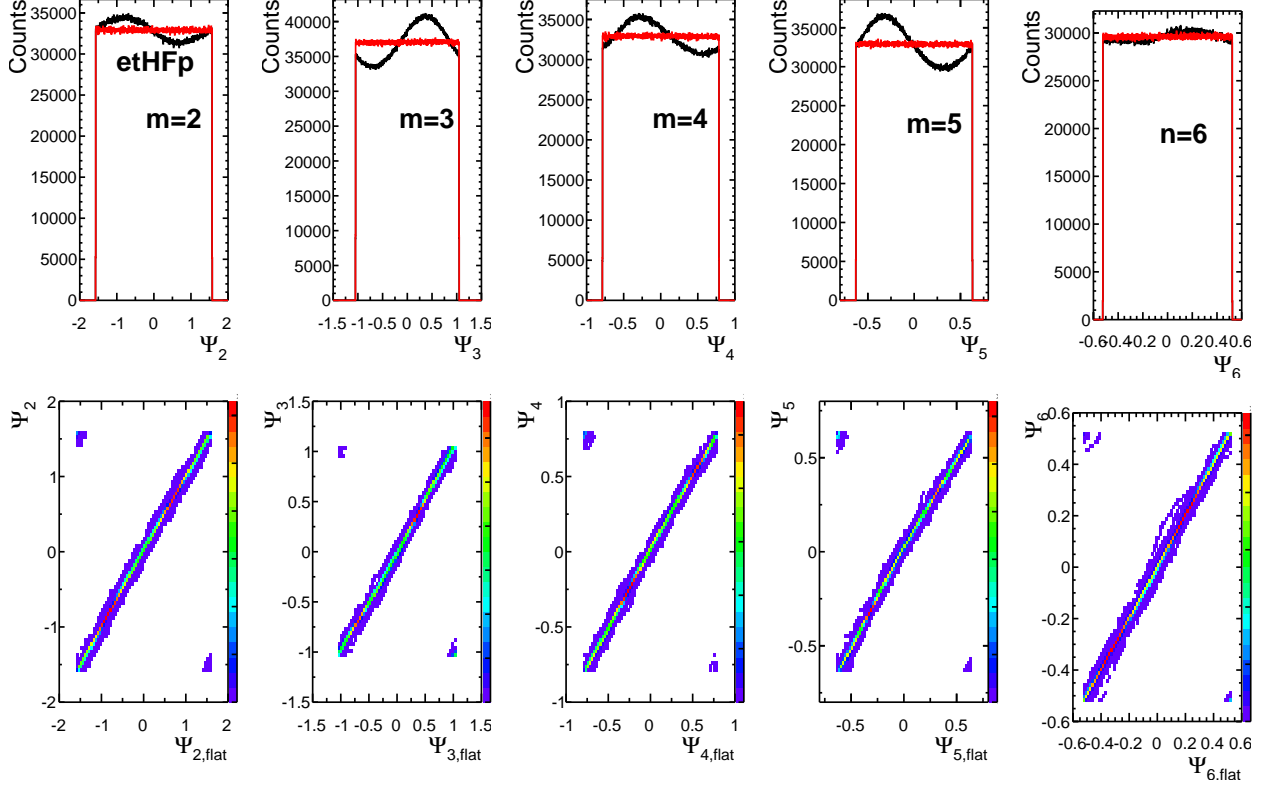


Figure 7-2: (Top) Event-plane angle distributions for HF^+ before (black curves) and after (red curves) flattening for harmonics $n = 2, 3, 4, 5, 6$. (Bottom) Correlations of before and after event-plane angles.

The flattening procedure, the result of which is illustrated in Figure 7-2, largely eliminates the influence of the detector acceptance on the obtained v_n values, although the acceptance will influence the statistical uncertainty found for these values. The effect of flattening is to shift slightly the deduced event-plane angles to correct for the azimuthal asymmetry. A larger value of the flattening order, j_{\max} , will “flatten” narrower angular structures, without necessarily improving the v_n results since the event-plane angle resolution places a limit on how well an angle can be determined. The current analysis sets $j_{\max} = 9$. Considering the same event planes shown in the top panels of Figure 7-2 by the black histograms, the bottom panels show the “flattened” event angles with respect to the angles obtained before applying the

flattening procedure. Even with the very large asymmetry observed before flattening, the shift in individual angles is found to be relatively small. In particular, the shift is small compared to the experimental resolution of the corresponding event-plane angle.

In the current analysis, the recentering operation is applied before a final event plane flattening. Figure 7-3 shows the $n = 2$ event-plane angles found for the two HF detectors. The top panels are the “raw” results without either recentering or flattening. The middle panels show the angles after recentering is applied. Finally, the bottom panel shows the final event plane angles after both recentering and flattening is done.

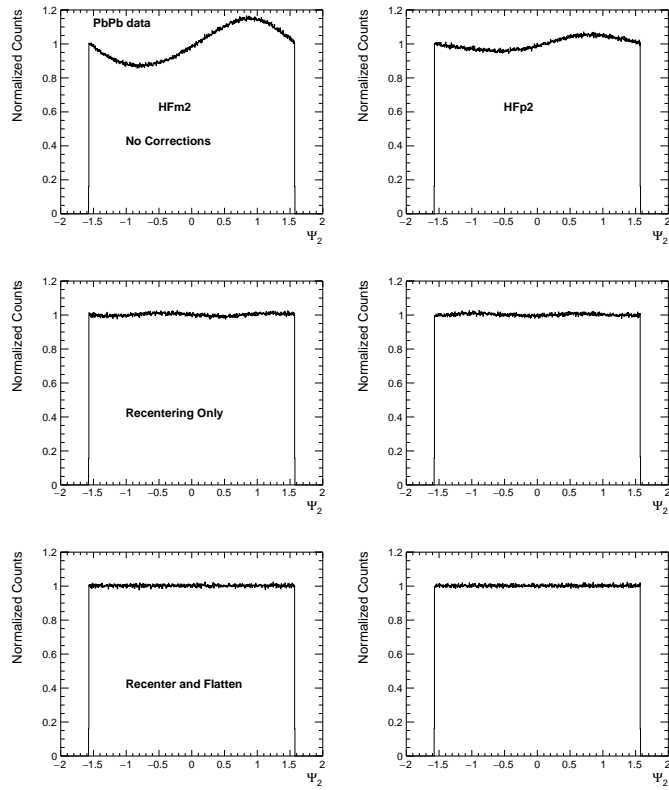


Figure 7-3: Event-plane angle distributions for HF^- and HF^+ before corrections (top panels), after flattening (middle panels) and after both recentering and flattening corrections are applied. The results are for the $n = 2$ harmonic.

To achieve the largest pseudorapidity gap possible, elliptic flow ($m = 2$) and triangular flow ($m = 3$) event planes are defined using calorimeter data, with the HF_m^- planes covering the pseudorapidity range of $-5 \leq \eta < -3$ and HF_m^+ planes covering the range $3 \leq \eta < 5$. The η gap between D^0 candidates and correlated event

planes is guaranteed to be big than 3.0 to avoid non-flow effect. Another event plane using tracker data with $-0.75 \leq \eta < 0.75$ was also defined and used in the three-sub-event technique for determining the resolution corrections, R_n , for the HF_m^- , HF_m^+ .

$$R_n = \sqrt{\frac{\left\langle \frac{Q_{nA}}{|Q_{nA}|} \frac{Q_{nB}^*}{|Q_{nB}|} \right\rangle \left\langle \frac{Q_{nA}}{|Q_{nA}|} \frac{Q_{nC}^*}{|Q_{nC}|} \right\rangle}{\left\langle \frac{Q_{nB}}{|Q_{nB}|} \frac{Q_{nC}^*}{|Q_{nC}|} \right\rangle}} \quad (7.1.9)$$

7.1.3 v_n Determination

Scalar Product Method

To determine the actual v_n coefficients, the current analysis uses the scalar product method that was first introduced by the STAR collaboration in a study of elliptic flow in AuAu collisions at $\sqrt{s_{NN}} = 130$ GeV [159]. Recently, Luzum and Ollitrault have argued that it is better to present experimental results for the v_n harmonics using this method than using the “traditional” event plane method [160] since the scalar-product method unambiguously leads to the RMS value of the flow coefficients, whereas the “traditional” method leads to a value between the mean and RMS depending on how well the event-planes can be determined. Expressed in term of the Q -vectors,

$$v_n \{SP\} \equiv \frac{\langle Q_n Q_{nA}^* \rangle}{\sqrt{\frac{\langle Q_{nA} Q_{nB}^* \rangle \langle Q_{nA} Q_{nC}^* \rangle}{\langle Q_{nB} Q_{nC}^* \rangle}}}. \quad (7.1.10)$$

In this analysis, the subscript A and B refer to event planes defined using calorimeter data, with the HF_n^- planes covering the pseudorapidity range of $-5 \leq \eta < -3$ and HF_n^+ planes covering the range $3 \leq \eta < 5$, respectively. The subscript C refers to event plane defined with tracker data with $-0.75 \leq \eta < 0.75$. The Q_n vector is computed from D^0 candidates. The event planes B and C effectively correct for the finite resolution of the A event plane that results from finite particle multiplicities and detector effects. The averages $\langle Q_{nA} Q_{nB}^* \rangle$, $\langle Q_{nA} Q_{nC}^* \rangle$ and $\langle Q_{nB} Q_{nC}^* \rangle$ are taken over all events, while the average $\langle Q_n Q_{nA}^* \rangle$ is over all D^0 candidates in all events. To avoid the autocorrelation effects, the η gap between D^0 candidates and the correlated event plane A is required to be at least 3 units. Thus HF_n^- planes are used as event plane A and HF_n^+ planes are used as event plane B for D^0 candidates from the positive η region, and vice versa.

After v_n of each D^0 candidates is calculated with Eq. (7.1.10), to extract v_n of D^0 signal (v_n^S), a simultaneous fit on mass spectrum and v_n as function of invariant mass is performed. The mass spectrum fit function is composed of three components: a third order polynomial to model the combinatorial background ($B(m_{\text{inv}})$), two Gaussian with same mean but different widths for D^0 signal ($S(m_{\text{inv}})$), and an additional Gaussian function to describe the invariant mass shape of D^0 candidates with incorrect mass assignment from the exchange of pion and kaon designation ($SW(m_{\text{inv}})$). The widths of $SW(m_{\text{inv}})$ is fixed according to MC simulations. Also the ratio between the yields of $SW(m_{\text{inv}})$ and $S(m_{\text{inv}})$ is fixed to the value extracted in simulations. The average v_n of all D^0 candidates as a function of invariant mass, $v_n^{S+B}(m_{\text{inv}})$, is fitted with Eq. (7.1.11) and Eq. (7.1.12).

$$v_n^{S+B}(m_{\text{inv}}) = \alpha(m_{\text{inv}})v_n^S + (1 - \alpha(m_{\text{inv}}))v_n^B(m_{\text{inv}}) \quad (7.1.11)$$

$$\alpha(m_{\text{inv}}) = [S(m_{\text{inv}}) + SW(m_{\text{inv}})] / [S(m_{\text{inv}}) + SW(m_{\text{inv}}) + B(m_{\text{inv}})] \quad (7.1.12)$$

$v_n^B(m_{\text{inv}})$ is the v_n of background D^0 candidates and is modeled as a linear function of invariant mass. $\alpha(m_{\text{inv}})$ is the D^0 signal fraction as a function of invariant mass, which is from mass spectrum fit function. The K- π swapped component is included in signal fraction because these candidates are from real D^0 and should have same v_n value with real D^0 signal.

Figure 7-4 shows an example of a simultaneous fit to the mass spectrum and $v_2^{S+B}(m_{\text{inv}})$ in the p_T interval 4–5 GeV/c for the centrality class 10–30%.

The D^0 signal in data is a mixture of prompt and nonprompt D^0 components, thus the v_n^S is a combination of the v_n coefficients of prompt D^0 (v_n^{prompt}) and nonprompt D^0 ($v_n^{\text{nonprompt}}$) components,

$$v_n^S = f_{\text{prompt}}v_n^{\text{prompt}} + (1 - f_{\text{prompt}})v_n^{\text{nonprompt}}, \quad (7.1.13)$$

where f_{prompt} is the fraction of prompt D^0 mesons. Besides the measurement of v_n of D^0 mesons with all analysis selections applied (v_n^S), the v_n of D^0 mesons obtained by removing the $\text{DCA} < 0.008$ cm requirement (v_n^{S*}) and the corresponding prompt D^0 fraction (f_{prompt}^*) are also measured. The prompt D^0 fractions are evaluated from data by fitting the DCA distribution using the probability distribution functions for prompt and nonprompt D^0 derived from the PYTHIA + HYDJET simulations. The DCA distributions of the D^0 signal in data are obtained with fits to mass spectra in

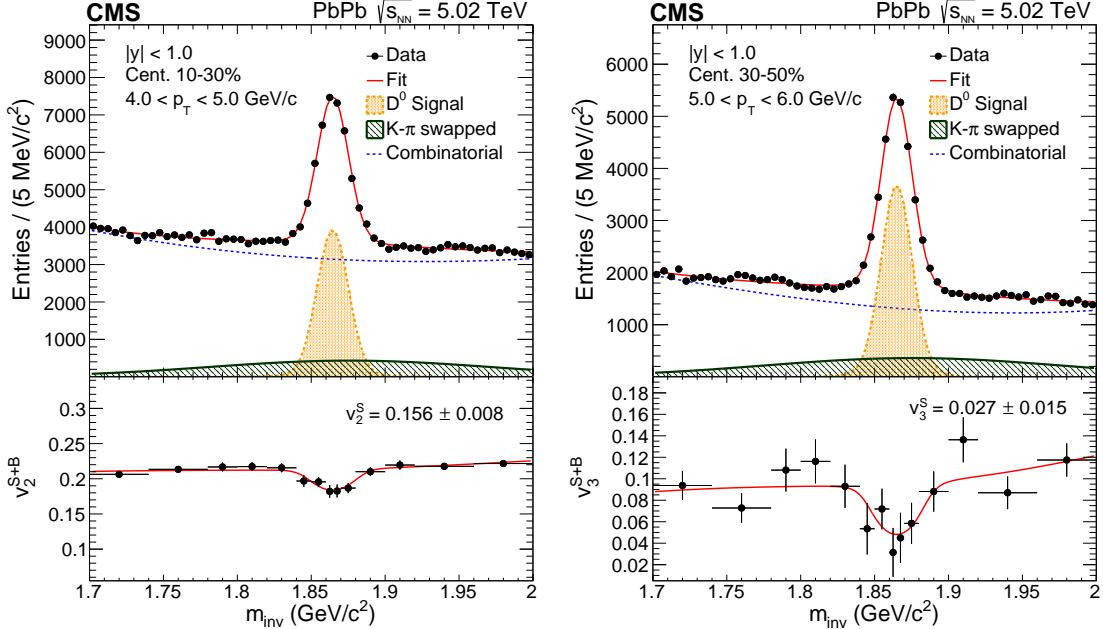


Figure 7-4: (Left) Simultaneous fit to the invariant mass spectrum and $v_2^{S+B}(m_{\text{inv}})$ in the p_T interval 4–5 GeV/c in PbPb collisions in the centrality class 10–30%. (Right) Simultaneous fit to the invariant mass spectrum and $v_3^{S+B}(m_{\text{inv}})$ in the p_T interval 5–6 GeV/c in PbPb collisions in the centrality class 30–50%.

bins of DCA. This is similar with the exercise in R_{AA} (see Section 6.1.3), while the cut on DCA leads to different treatments. The discrimination between prompt and nonprompt D^0 mesons lies mainly in the large DCA region, thus the fit is performed on the entire range. The f_{prompt} and f_{prompt}^* are then evaluated from the fit, and their values as a function of p_T are presented in Figure 7-5. It is found that the $\text{DCA} < 0.008 \text{ cm}$ requirement can suppress the fraction of nonprompt D^0 mesons by approximately 50%. The f_{prompt} ranges between 75 and 95%, depending on p_T and centrality. The v_n^{prompt} can then be expressed as:

$$v_n^{\text{prompt}} = v_n^S + \frac{1 - f_{\text{prompt}}}{f_{\text{prompt}} - f_{\text{prompt}}^*} (v_n^S - v_n^{S*}). \quad (7.1.14)$$

The second term, $\frac{1 - f_{\text{prompt}}}{f_{\text{prompt}} - f_{\text{prompt}}^*} (v_n^S - v_n^{S*})$, is a correction factor to account for the remaining nonprompt D^0 mesons after all analysis selections. Taking the uncertainties in f_{prompt} and f_{prompt}^* into account, the second term on the right of Eq. (7.1.14) is found to lie approximately between –0.02 and +0.02. In this analysis, the v_n^S values are kept as the central values of the measured prompt D^0 meson v_n , while the second term of Eq. (7.1.14) is taken as a source of systematic uncertainty.

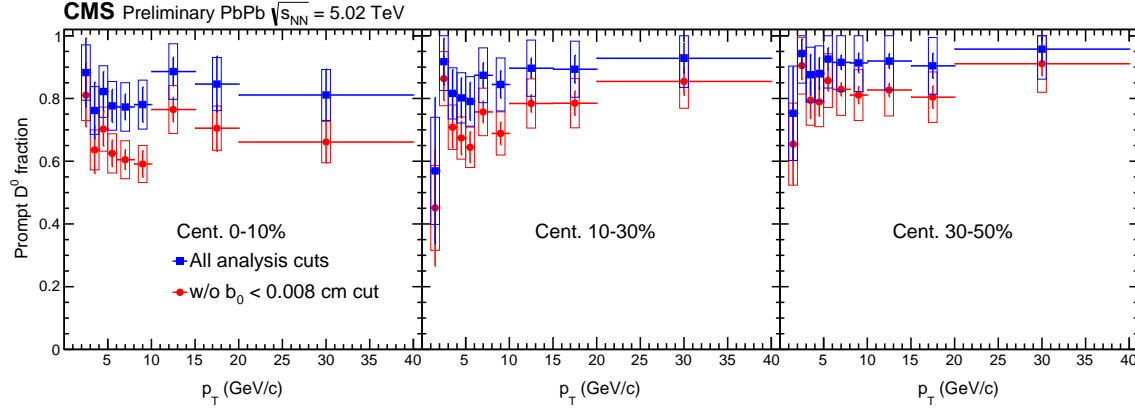


Figure 7-5: Prompt D^0 fraction with (blue) and without (red) for centrality 0–10% (left), 10–30% (middle) and 30–50% (right).

$\Delta\phi$ Method

The azimuthal dependence of the particle yield can be written in terms of an harmonic expansion with Eq. (7.1.1), thus another method to measure $D^0 v_n$ is to divide the D^0 candidates into several $\Delta\phi$ bins and get the raw D^0 yield in each $\Delta\phi$ bin. In principle, this is the same with traditional event plane method. Luzum and Ollitrault have argued that it would be better to present experimental results using scalar product method than using the traditional event plane method [160]. Their argument is that that the results of the event plane method depend on the value of the resolution correction given by Eq. (7.1.9), with

$$v_n \{\text{EP}\} \xrightarrow[\text{highres.}]{M} \langle v_n \rangle \quad (7.1.15)$$

and

$$v_n \{\text{EP}\} \xrightarrow[\text{lowres.}]{M} \sqrt{\langle v_n^2 \rangle}. \quad (7.1.16)$$

With the scalar product method one has

$$v_n \{\text{SP}\} \equiv \sqrt{\langle v_n^2 \rangle}. \quad (7.1.17)$$

Studies in Ref. [160] suggests how the mean and RMS values are expected to differ for PbPb collisions at 2.76 TeV. This is one of the main reasons that we use scalar product method as the main analysis method while $\Delta\phi$ bins method is used as cross check. Figure 7-6 shows an example of mass spectrum fit in $\Delta\phi$ bins. Then v_n^{obs} can

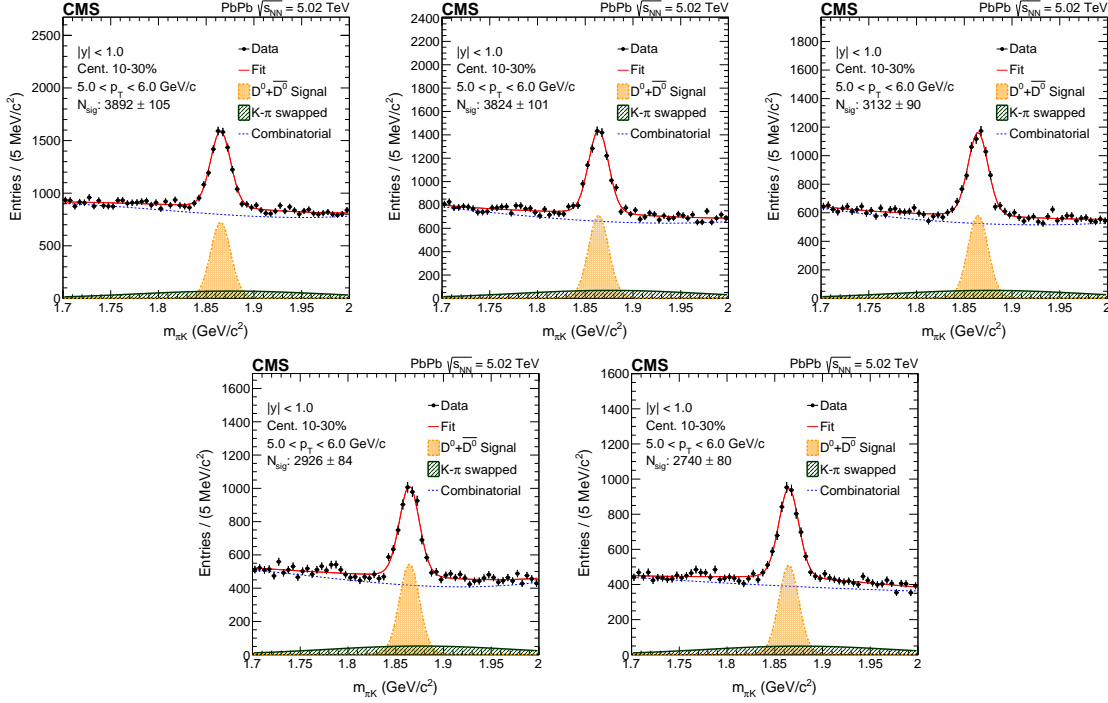


Figure 7-6: D^0 mass spectrum fit in $\Delta\phi$ bins for v_2 in p_T 5 – 6 GeV/c in PbPb collisions in the centrality range 10 – 30%.

be extracted with a fit on the $d^2N/(dp_T d\Delta\phi)$ distribution with Eq. (7.1.18), where N_0 and v_n^{obs} are free parameters. $D^0 v_n$ is the v_n^{obs} corrected by event plane resolution R_n , which is showed in Eq. (7.1.19).

$$N_0 + 2v_n^{\text{obs}} \cos(n\Delta\phi) \quad (7.1.18)$$

$$v_n = \frac{v_n^{\text{obs}}}{R_n} \quad (7.1.19)$$

Figure 7-7 shows $d^2N/(dp_T d\Delta\phi)$ distribution and fit for v_2 in p_T range 5 – 6 GeV/c in PbPb collisions in the centrality range 10 – 30%. And the v_n^{obs} values are showed in the figures.

7.1.4 Acceptance and Efficiency

Different with production measurements, v_n is not supposed to be sensitive to efficiency, considering the detector is with azimuthal isotropy. Also, the measurement is performed in bins of p_T which suppresses the influence of p_T dependence on efficiencies. To evaluate the effect from different efficiencies resulting from different p_T ,

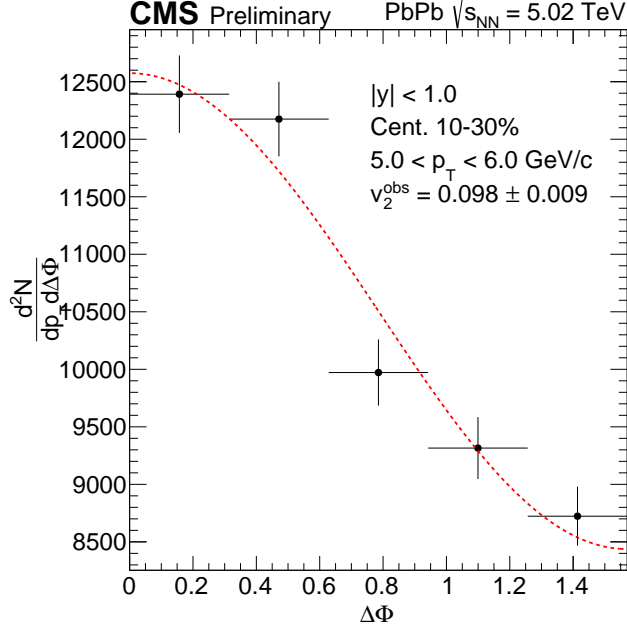


Figure 7-7: Fit for v_2 on $d^2N/(dp_T d\Delta\phi)$ in p_T $5 - 6$ GeV/c in PbPb collisions in the centrality range $10 - 30\%$.

D^0 acceptance, reconstruction efficiency and selection efficiency are studied in simulations. Figure 7-8 presents the efficiency of D^0 as a function of p_T . v_n is extracted with D^0 candidates corrected by the efficiency according to their p_T , and the results are compared with the nominal one. The discrepancy is found to be indeed small unsurprisingly, and is considered as systematical uncertainties.

7.2 Results

7.2.1 Prompt D^0 v_2 in PbPb Collisions

Figure 7-9 shows prompt D^0 v_2 coefficient at midrapidity ($|y| < 1$) as a function of p_T from scalar product (SP) method and $\Delta\phi$ bins method in the centrality range $0 - 10\%$, $10 - 30\%$ and $30 - 50\%$. Though there are some differences between values from SP method and $\Delta\phi$ bins method in some p_T bins, the results from the two methods are overall pretty consistent within uncertainties. The prompt D^0 meson v_2 coefficient increase with p_T to significant positive values in the low- p_T region, and then decrease for higher p_T . Therefore, the shape of v_2 as a function of p_T is featured by a distinct peak at $2 - 4$ GeV/c . The apparent non-zero v_2 at low p_T suggests

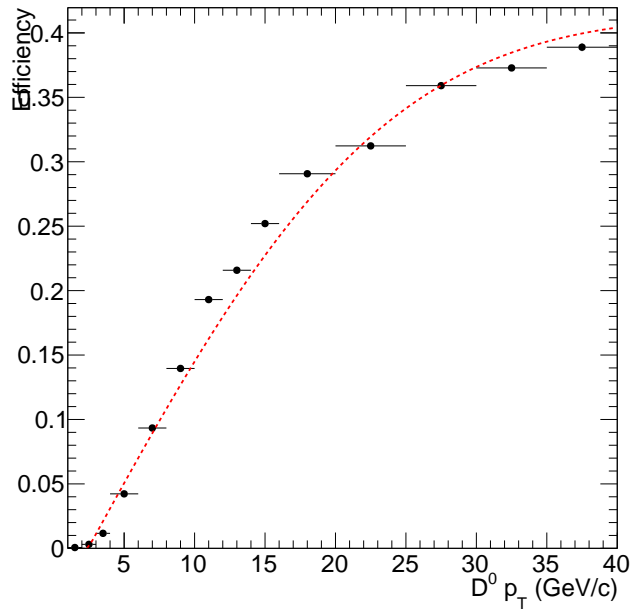


Figure 7-8: D^0 efficiency as a function of p_T .

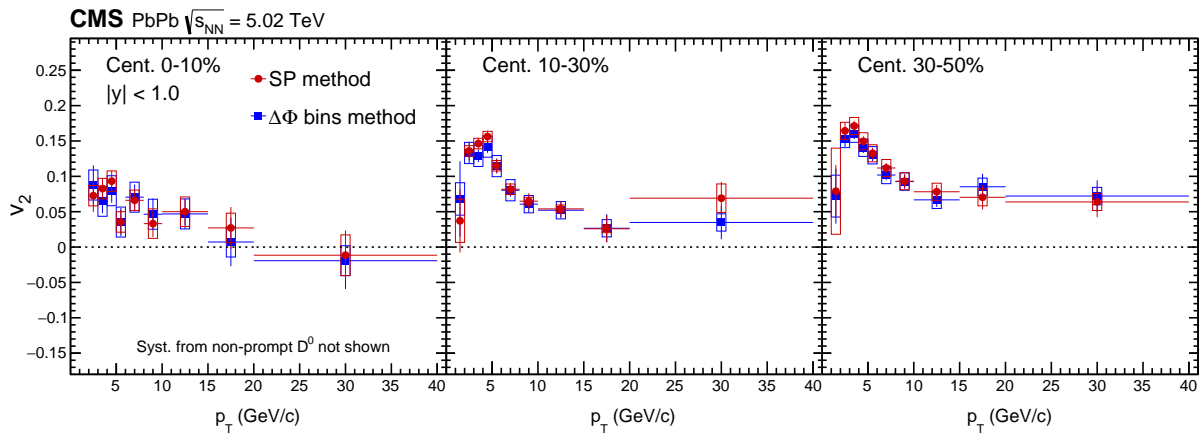


Figure 7-9: Prompt $D^0 v_2$ coefficient at midrapidity ($|y| < 1$) as a function of p_T from scalar product (SP) method (red) and $\Delta\phi$ bins method (blue) in PbPb collisions in the centrality range 0 – 10% (left), 10 – 30% (middle) and 30 – 50% (right).

that D^0 mesons still take part in collective motion with the medium, while v_2 at high p_T results from the path length dependence of energy loss. The v_2 values are larger for peripheral events compared with more central events, which is consistent with an increasing elliptical eccentricity with decreasing centrality [161]. Figure 7-10 shows

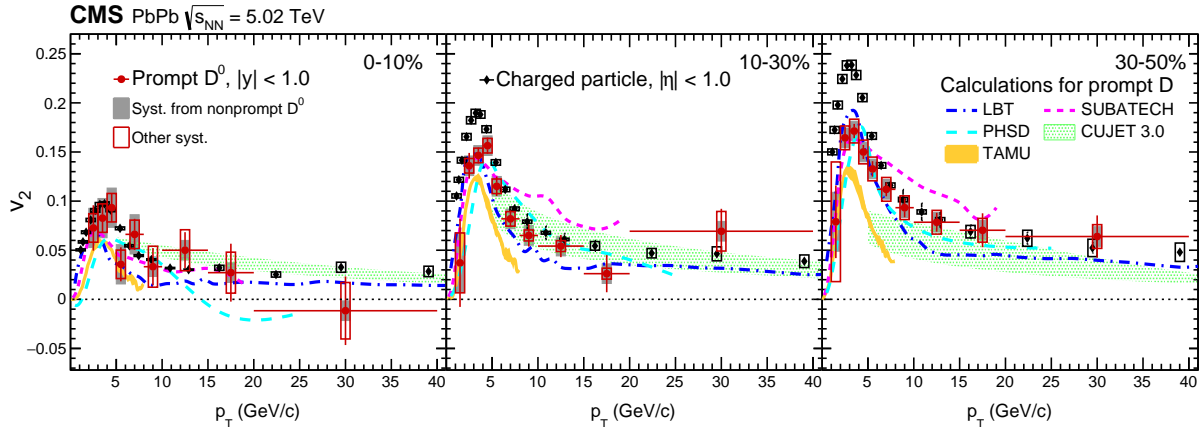


Figure 7-10: Prompt D^0 (red) and charged particle (black) v_2 coefficient at midrapidity ($|y| < 1$) as a function of p_T in PbPb collisions in the centrality range $0 - 10\%$ (left), $10 - 30\%$ (middle) and $30 - 50\%$ (right). The vertical bars represent statistical uncertainties, grey bands represent systematic uncertainties from nonprompt D^0 mesons and open boxes represent other systematic uncertainties. Various theoretical calculations for prompt D^0 meson v_2 coefficient [140, 146, 143, 145, 135] are also plotted for comparison.

prompt D^0 v_2 coefficient as a function of p_T same as shown in Figure 7-9 compared with charged particles [162] (dominated by light flavor hadrons) at same rapidity range and centrality ranges. Compared to those of charged particles, the D^0 meson v_2 coefficients exhibit a similar p_T dependence and similar centrality dependence. For $p_T < 6 \text{ GeV}/c$, the magnitudes of D^0 meson v_2 coefficients are smaller than those for charged particles in the centrality classes $10 - 30\%$ and $30 - 50\%$. Further study may determine whether it is a pure mass ordering or whether other effects play important roles, such as the degree of charm quark thermalization, coalescence, and the path length dependence of energy loss. In the centrality range $0 - 10\%$, v_2 coefficients of D^0 are consistent with charged particles within uncertainties. For $p_T > 6 \text{ GeV}/c$, the D^0 meson v_2 values remain positive, suggesting a path length dependence of the charm quark energy loss. In this p_T region, The prompt D^0 meson v_2 values are consistent with those of charged particles, suggesting that the path length dependence of charm quark energy loss is similar to that of light quarks. This is consistent with

the observation that R_{AA} of prompt D^0 agree with that of charged particles. As a

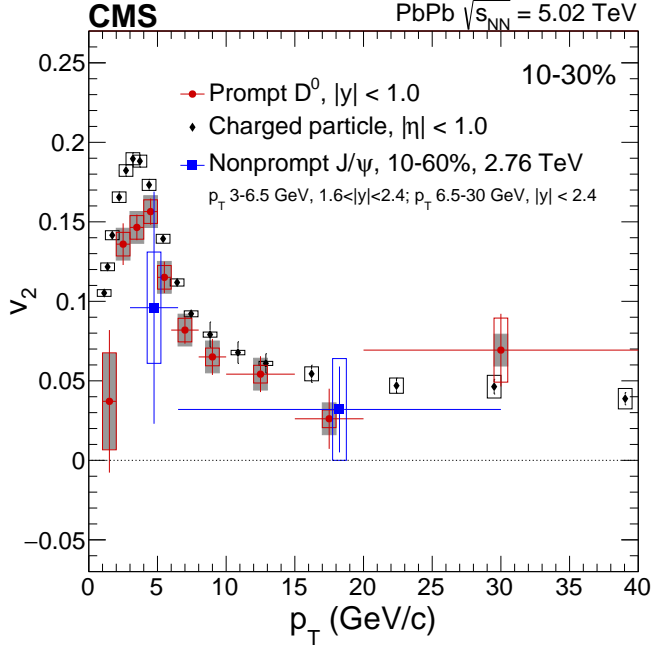


Figure 7-11: Prompt D^0 (red), charged particle (black) and nonprompt J/ψ (blue) v_2 coefficient as a function of p_T in PbPb collisions. D^0 and charged particles are measured in $|y| < 1$ in PbPb collisions at 5.02 TeV in the centrality range 10 – 30%, while nonprompt J/ψ is measured in $|y| < 2.4$ ($1.6 < |y| < 2.4$ for different p_T ranges) in PbPb collisions at 2.76 TeV in the centrality range 10 – 60%.

further study of flavor dependence of v_n , Figure 7-11 compares v_2 of charged particles, prompt D^0 and nonprompt J/ψ in mid-centrality. Nonprompt J/ψ as a representative of beauty hadron, has a hint of smaller v_2 at low p_T , despite large uncertainties.

Figure 7-10 also compares calculations from theoretical models [140, 146, 143, 145, 135] to the prompt D^0 meson v_2 experimental results. The details of implementation configurations of each theoretical model are reported in Table 6.3. The calculations from LBT [140], CUJET 3.0 [135], and SUBATECH [146] include collisional and radiative energy losses, while those from TAMU [145] and PHSD [143] include only collisional energy loss. For $p_T < 6 \text{ GeV}/c^2$, LBT, SUBATECH, TAMU, and PHSD can qualitatively describe the shapes of the measured v_2 , while the TAMU model underestimates the v_2 values. This may suggest that the heavy quark potential in the TAMU model needs to be tuned [163] or that the addition of radiative energy loss is needed. In the calculations from LBT, SUBATECH, TAMU, and PHSD, the charm quarks have acquired significant elliptic flow through the interactions with the medium constituents, and the coalescence mechanism is incorporated. Without

including the interactions between charm quarks and the medium, these models will significantly underestimate the data [140, 146, 143, 145]. Thus, the fact that the calculated v_n values are close to or even lower than the measured results suggests that the charm quarks take part in the collective motion of the system. Whether and how well the D^0 anisotropy can be described by hydrodynamics and thermalization requires further investigation. For $p_T > 6$ GeV/c, PHSD and CUJET can generally describe the v_2 results. LBT and SUBATECH predict lower and higher v_2 values than in data, respectively, indicating that improvements of the energy loss mechanisms in the two models are necessary.

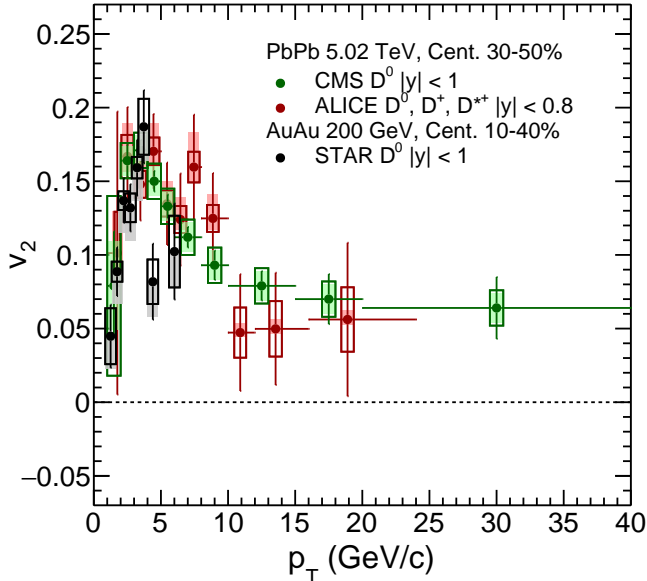


Figure 7-12: Prompt D^0 v_2 coefficient as a function of p_T performed by CMS collaboration (green) at $|y| < 1$ and by ALICE collaboration [164] (red) at $|y| < 0.8$ in PbPb collisions at 5.02 TeV in the centrality range 30 – 50% and by STAR collaboration (black) at $|y| < 1$ in AuAu collisions at 200 GeV in the centrality range 10 – 30% [165]. The vertical bars represent statistical uncertainties, shadow bands represent systematic uncertainties from nonprompt D^0 mesons and open boxes represent other systematic uncertainties.

Similar with Section 6, the measured results discussed above are compared with other experiments. In Figure 7-12, prompt $D^0 v_2$ measured by ALICE collaboration in the same system, and that measured by STAR collaboration in AuAu collisions at 200 GeV are presented. The results among the three experiments are consistent with

each other within uncertainties.

7.2.2 Prompt $D^0 v_3$ in PbPb Collisions

Distinct from that v_2 is due to the overlap shape of the two ions, v_3 results from initial fluctuations which are not yet understood well. Figure 7-13 shows prompt $D^0 v_3$ coefficient at midrapidity ($|y| < 1$) as a function of p_T from scalar product (SP) method and $\Delta\phi$ bins method in the centrality range 0 – 10%, 10 – 30% and 30 – 50%. Similar with v_2 , the results from the two methods are overall pretty consistent within uncertainties. Despite limit of statistical uncertainties, the prompt

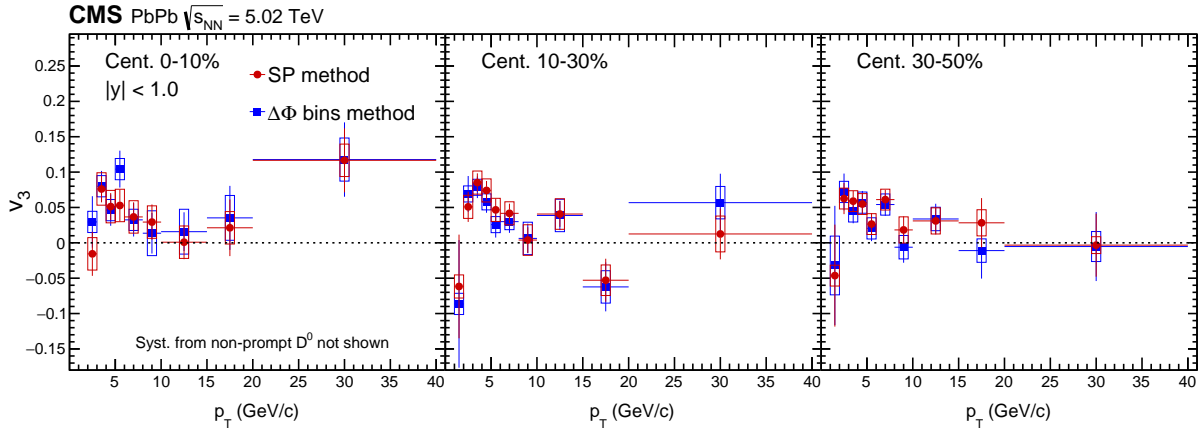


Figure 7-13: Prompt $D^0 v_3$ coefficient at midrapidity ($|y| < 1$) as a function of p_T from scalar product (SP) method (red) and $\Delta\phi$ bins method (blue) in PbPb collisions in the centrality range 0 – 10% (left), 10 – 30% (middle) and 30 – 50% (right).

D^0 meson v_3 coefficient has trend increasing with p_T to significant positive values in the low- p_T region, and then decrease for higher p_T . The non-zero v_3 shows that the final state of D^0 can reflect the initial fluctuations. Different with significant centrality dependence of v_2 , the v_3 coefficient shows little centrality dependence. This is consistent with an approximately constant triangularity stemming from geometry fluctuations [166]. Figure 7-14 shows prompt $D^0 v_3$ coefficient as a function of p_T same as shown in Figure 7-13 compared with charged particles [162] (dominated by light flavor hadrons) at same rapidity range and centrality ranges. Compared to those of charged particles, the D^0 meson v_3 coefficients exhibit a similar p_T dependence and similar centrality dependence. Generally prompt $D^0 v_3$ coefficient is a bit smaller than that of charged particles at low p_T in all centrality classes. However, there is no flavor dependence as obvious as v_2 in peripheral events.

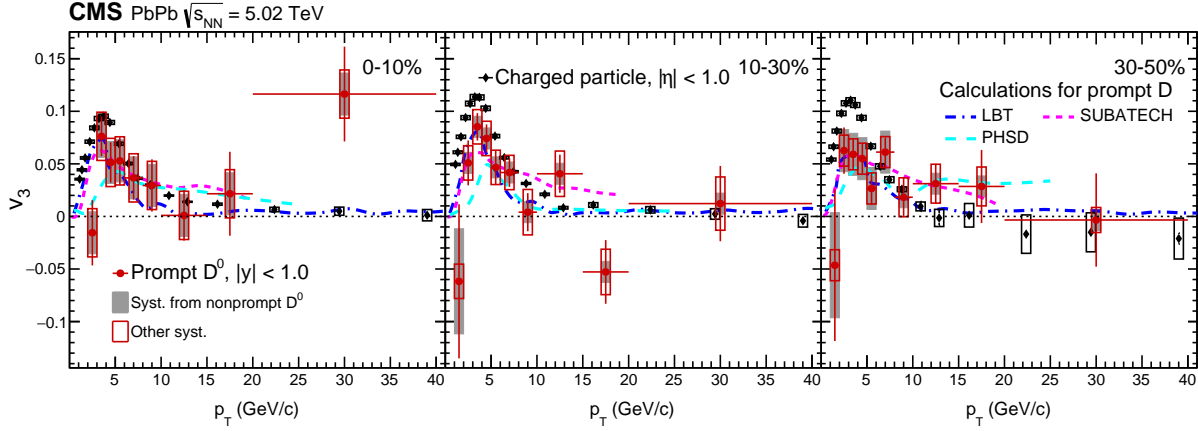


Figure 7-14: Prompt D^0 (red) and charged particle (black) v_3 coefficient at midrapidity ($|y| < 1$) as a function of p_T in PbPb collisions in the centrality range $0 - 10\%$ (left), $10 - 30\%$ (middle) and $30 - 50\%$ (right). The vertical bars represent statistical uncertainties, grey bands represent systematic uncertainties from nonprompt D^0 mesons and open boxes represent other systematic uncertainties. Various theoretical calculations for prompt D^0 meson v_3 coefficient [140, 146, 143] are also plotted for comparison.

Figure 7-14 also compares calculations from theoretical models [140, 146, 143] to the prompt D^0 meson v_3 experimental results. The calculations are described in Section 7.2.1. Note initial-state fluctuations [167] are included in the calculations from LBT, SUBATECH, and PHSD; thus calculations for the v_3 coefficient are only available from these three models. The calculations from LBT and SUBATECH are in reasonable agreement with the v_3 results, while the PHSD calculations are systematically below the measured v_3 for centrality class $10 - 30\%$.

7.3 Systematic Uncertainty Study

Apart from the systematic uncertainties from D^0 acceptance and efficiency in Section 7.1.4 and the remaining nonprompt D^0 mesons discussed in Section 7.1.3, other sources of systematic uncertainty in this analysis include the background mass probability distribution function (PDF), the track selections, and the background v_n PDF. The systematic uncertainties from the background mass PDF are evaluated by the variations of v_n while changing the background mass PDF to a second-order polynomial or an exponential function. The track selections are also varied and systematic uncertainties from track selections are assigned based on the variations of v_n . Specif-

ically, the cut on the relative p_T error is changed to $< 30\%$ from $< 10\%$, and the cuts on number of hit and on χ^2 are removed. v_2 and v_3 with the loose track selections are compared with default values, and the discrepancy is accounted for in systematic uncertainties. The systematic uncertainties from the background v_n PDF are evaluated by changing $v_n^B(m_{\text{inv}})$ to a second-order polynomial function of the invariant mass. The effects from few-particle correlations are also studied by varying the η gap and are found to be negligible.

Centrality and Source (GeV/c)	Invariant mass (SP) method				$\Delta\phi$ bins method			
	1-2	2-8	8-20	20-40	1-2	2-8	8-20	20-40
Centrality 0-10%								
Bkg mass PDF variation	-	0.001	0.001	0.001	-	0.005	0.005	0.005
Efficiency correction	-	0.003	0.003	0.005	-	0.005	0.005	0.005
Track cuts variation	-	0.01	0.02	0.02	-	0.02	0.02	0.02
Bkg v_n PDF	-	0.01	0.005	0.02	-	-	-	-
Non-prompt D ⁰	-	0.02	0.01	0.01	-	0.02	0.01	0.01
Centrality 10-30%								
Bkg mass PDF variation	0.001	0.001	0.001	0.001	0.005	0.005	0.005	0.005
Efficiency correction	0.002	0.002	0.002	0.002	0.01	0.01	0.005	0.005
Track cuts variation	0.005	0.005	0.005	0.02	0.02	0.01	0.01	0.01
Bkg v_n PDF	0.03	0.005	0.001	0.001	-	-	-	-
Non-prompt D ⁰	0.03	0.01	0.01	0.01	0.03	0.01	0.01	0.01
Centrality 30-50%								
Bkg mass PDF variation	0.001	0.001	0.001	0.001	0.015	0.005	0.005	0.005
Efficiency correction	0.003	0.003	0.003	0.003	0.005	0.005	0.005	0.005
Track cuts variation	0.01	0.01	0.01	0.01	0.025	0.01	0.01	0.01
Bkg v_n PDF	0.06	0.006	0.006	0.006	-	-	-	-
Non-prompt D ⁰	0.03	0.01	0.01	0.01	0.03	0.01	0.01	0.01

Table 7.2: Summary of systematic uncertainties for v_2 . Absolute uncertainties are assigned.

Summaries of systematic uncertainties for v_2 and v_3 are reported in Table 7.2 and Table 7.3 respectively.

Centrality and Source (GeV/c)	Invariant mass (SP) method				$\Delta\phi$ bins method			
	1-2 GeV/c	2-8	8-20	20-40	1-2	2-8	8-20	20-40
Centrality 0-10%								
Bkg mass PDF variation	-	0.001	0.001	0.001	-	0.005	0.002	0.002
Efficiency correction	-	0.005	0.005	0.005	-	0.01	0.01	0.005
Track cuts variation	-	0.02	0.02	0.02	-	0.01	0.03	0.03
Bkg v_n PDF	-	0.01	0.01	0.01	-	-	-	-
Non-prompt D ⁰	-	0.02	0.02	0.02	-	0.02	0.02	0.02
Centrality 10-30%								
Bkg mass PDF variation	0.001	0.001	0.001	0.001	0.01	0.002	0.01	0.01
Efficiency correction	0.004	0.004	0.004	0.004	0.005	0.005	0.005	0.005
Track cuts variation	0.015	0.015	0.015	0.015	0.01	0.01	0.02	0.02
Bkg v_n PDF	0.005	0.005	0.015	0.02	-	-	-	-
Non-prompt D ⁰	0.05	0.01	0.01	0.01	0.05	0.01	0.01	0.01
Centrality 30-50%								
Bkg mass PDF variation	0.001	0.001	0.001	0.001	0.005	0.005	0.005	0.005
Efficiency correction	0.004	0.004	0.004	0.004	0.01	0.01	0.005	0.005
Track cuts variation	0.01	0.01	0.01	0.005	0.04	0.01	0.015	0.02
Bkg v_n PDF	0.01	0.01	0.015	0.01	-	-	-	-
Non-prompt D ⁰	0.05	0.02	0.01	0.01	0.05	0.02	0.01	0.01

Table 7.3: Summary of systematic uncertainties for v_3 . Absolute uncertainties are assigned.

Chapter 8

D⁰ Jet Angular Correlation

Modifications of the energy and structure of jets are observed in heavy-ion collisions, compared to proton-proton collisions assuming that no or negligible amount of QGP is formed. These modifications can be related, via theoretical models, to the thermodynamic and transport properties of the medium. Apart from the inclusive jet quenching, another prominent phenomenon observed is the enhanced production of low transverse momentum (p_T) hadrons at large angles with respect to the final-state jet axis. This phenomenon is observed as modifications of the jet fragmentation [168, 169, 170], the jet radial profile and energy flow [171, 172, 173]. Figure 8-1 shows the nuclear modification of jet shape measured in PbPb collisions at $\sqrt{s_{NN}} = 5.02$ TeV. Jet shape is characterized by the particle radial distribution as a function of the angle distance with respect to the jet axis weighted by the particle p_T . It suggests enhancement of soft particles at large angle, which indicates the particles tend to be farther away from jet axis in heavy-ion collisions. Interpretations of those experimental results include medium-induced gluon radiation, modification of jet splitting functions, and medium response to the hard scattered partons [174, 175, 176, 177, 178]. Since the heavy quark masses are larger than the typical QGP temperature scale produced in LHC, one gains insights into the origin of the enhanced production of low p_T charged particles in jets by the studies of heavy flavor mesons associated with jets. In addition, measurements of the heavy flavor meson production in jets could provide new information about heavy flavor jet fragmentation in both pp and PbPb collisions. Finally, it is believed angular correlation is a more sensitive observable to diffusion and energy loss mechanisms of heavy quarks [57, 179, 180]. The left panel of Figure 8-2 presents the D meson R_{AA} as a function of p_T in central PbPb events at

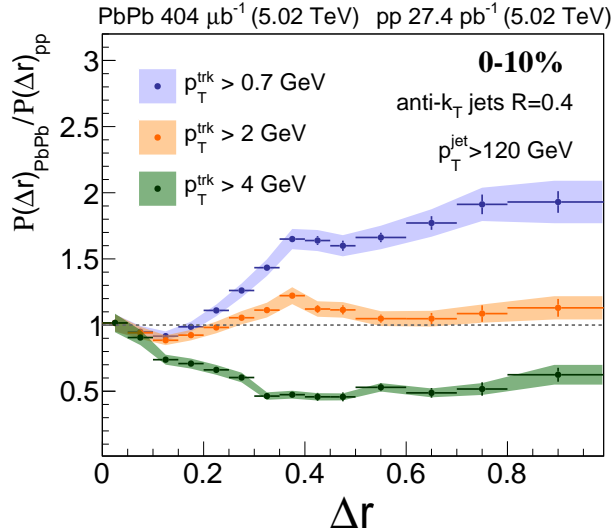


Figure 8-1: The ratio of the radial jet momentum distribution $P(\Delta r)$ of jets between PbPb and pp collisions at $\sqrt{s_{NN}} = 5.02$ TeV for the indicated intervals of p_T^{trk} shown for the 0-10% (most central) bin. Figure from Ref. [172]

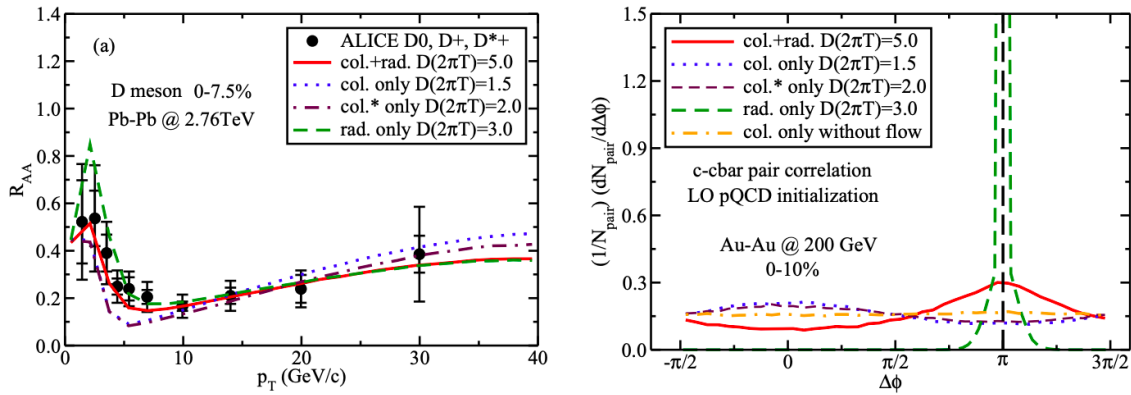


Figure 8-2: (Left) D meson nuclear modification factor R_{AA} in central Pb-Pb collisions. (Right) Theoretical calculations of angular correlations of $c\bar{c}$ pairs in central Au-Au collisions. For both observables different diffusion coefficients and different energy-loss mechanisms are employed for comparison. Figure from Ref. [179].

$\sqrt{s_{\text{NN}}} = 2.76$ TeV. Predictions are also presented with a given theoretical model utilizing different diffusion coefficients and different energy-loss mechanisms. We can see various configurations lead to similar calculation results with decent description of measurements. However, in the right panel of Figure 8-2, calculations are presented for angular correlations of $c\bar{c}$ pairs. For this observable, different configurations are clearly distinguished. Therefore, angular correlation measurements between heavy flavor meson and jets could be used to constrain parton energy loss mechanisms and to measure heavy quark diffusion inside the medium, complementary to the measurements of inclusive heavy flavor meson R_{AA} , heavy flavor meson azimuthal anisotropy, and heavy flavor tagged jets. Specifically the correlation between D^0 mesons and jet axes is studied with the CMS detector to study the diffusion of charm quarks with respect to the dominant energy flow.

In this section, the measurement of the radial distributions of D^0 mesons in jets in PbPb and pp collisions with the CMS detector is presented. The observable is the normalized angular distribution of the D^0 meson with respect to the jet axis, defined as

$$\frac{1}{N_{\text{JD}}} \frac{dN_{\text{JD}}}{dr} = \frac{1}{N_{\text{JD}} \Delta r} \frac{N_{\text{JD}}|_{\Delta r}}{(\alpha \times \epsilon)} \quad (8.0.1)$$

where

$$r = \sqrt{(\Delta\phi_{\text{JD}})^2 + (\Delta\eta_{\text{JD}})^2} \quad (8.0.2)$$

is defined by the differences in pseudorapidity ($\Delta\eta_{\text{JD}}$) and in azimuth ($\Delta\phi_{\text{JD}}$) of the D^0 from the jet axis, and Δr is the width of the r interval. The quantity $\alpha \times \epsilon$ represents the acceptance times efficiency, $N_{\text{JD}}|_{\Delta r}$ is the number of signal D^0 in the Δr interval, and N_{JD} is the integral of the distribution in the r region from 0 to 0.3, the distance parameter used for jet reconstruction. Section 8.1 describes analysis techniques employed in this analysis, while in Section 8.3 systematic uncertainty studies are discussed. The results are shown in Section 8.2

8.1 Analysis Techniques

8.1.1 Analysis Procedure

The pp (PbPb) dataset used for this analysis corresponds to an integrated luminosity of 27.4 pb^{-1} ($404 \mu\text{b}^{-1}$). High- p_T jet events were selected by the HLT algorithms described in Section 2.3.3 with p_T^{jet} threshold $60 \text{ GeV}/c$.

8.1.2 D^0 Selection

p_T of D^0 mesons measured in this analysis is higher than that applied in R_{AA} and v_n due to since low- p_T D^0 are strongly suppressed by the existence of high- p_T jet recalling fragmentation functions. Also, as measurement of angular correlation, we used D^0 in a wider rapidity range to $|y| < 2$. Therefore, track quality selections are similar with R_{AA} and v_n analysis, while track p_T ($p_T > 2$ GeV/c) and rapidity ($|\eta| < 2$) selections are different. The selection criteria on kinematic variables to suppress combinatorial backgrounds are obtained by cut optimization (see Section 5.2) in different p_T and r ranges. The resulting cut values obtained from cut optimization are summarized

	p_T	r	θ_p	$d_0/\sigma(d_0)$	Vertex Probability	
pp						
	$4 < p_T < 20$ GeV/c	0-0.05	< 0.020	> 4.00	> 0.05	
	$4 < p_T < 20$ GeV/c	0.05-0.1	< 0.039	> 3.26	> 0.05	
	$4 < p_T < 20$ GeV/c	0.1-0.3	< 0.046	> 3.23	> 0.05	
	$4 < p_T < 20$ GeV/c	0.3-0.5	< 0.046	> 3.23	> 0.05	
	> 20 GeV/c	0-0.05	< 0.037	> 2.86	> 0.05	
	> 20 GeV/c	0.05-0.1	< 0.037	> 2.86	> 0.05	
	> 20 GeV/c	0.1-0.3	< 0.039	> 2.34	> 0.05	
	> 20 GeV/c	0.3-0.5	< 0.039	> 2.34	> 0.05	
PbPb						
	$4 < p_T < 20$ GeV/c	0-0.05	< 0.040	> 4.44	> 0.05	
	$4 < p_T < 20$ GeV/c	0.05-0.1	< 0.040	> 4.44	> 0.05	
	$4 < p_T < 20$ GeV/c	0.1-0.3	< 0.043	> 4.34	> 0.05	
	$4 < p_T < 20$ GeV/c	0.3-0.5	< 0.043	> 4.34	> 0.05	
	> 20 GeV/c	0-0.05	< 0.038	> 2.68	> 0.05	
	> 20 GeV/c	0.05-0.1	< 0.038	> 2.68	> 0.05	
	> 20 GeV/c	0.1-0.3	< 0.107	> 2.08	> 0.05	
	> 20 GeV/c	0.3-0.5	< 0.107	> 2.08	> 0.05	

Table 8.1: Summary table of the optimal selections on D^0 .

in Table 8.1. These selections lead to decent signal significance in all p_T and r bins, and Figure 8-3 presents examples of invariant mass distributions after optimal cuts. Yield extraction follows the scenario described in Section 5.3.

8.1.3 Jet Selection and Correction

The general description of jet reconstruction in CMS is documented in Section 4.2. Specifically for this analysis jets reconstructed by particle-flow (PF) algorithms with

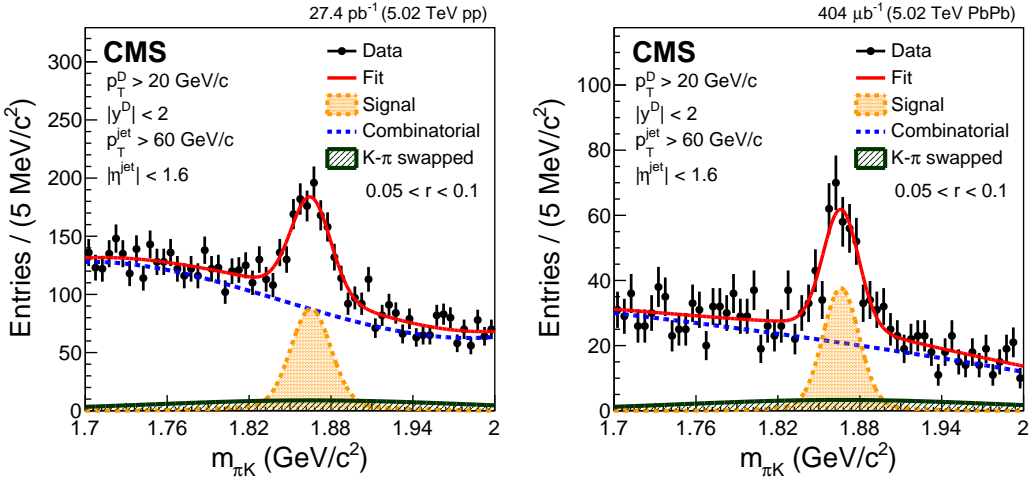


Figure 8-3: Invariant mass distributions after optimal cuts for D^0 candidates with $p_T^D > 20 \text{ GeV}/c$ and $0.05 < r < 0.1$ in pp (left) and Pb-Pb (right) collisions.

a distance parameter $R = 0.3$ are chosen. A smaller distance parameter is applied to minimize the effects of the underlying event fluctuations. Rapidity selection of $|\eta^{\text{jet}}| < 1.6$ is determined to obtain good resolutions. To obtain decent statistics of D^0 at both low p_T and high p_T , jets with corrected $p_T^{\text{jet}} > 60 \text{ GeV}/c$ are selected for this analysis. It is mentioned in Section 4.2 that jet energy corrections for inclusive jets have been applied to derive the true energy of jets from the reconstructed one. To account for potential difference between inclusive jets and jets with D^0 mesons, a residual energy correction is studied in D^0 signal PYTHIA and PYTHIA + HYDJET Monte-Carlo simulations. The global strategy for residual jet energy correction is as follows:

(1) Jet energy scale

- The jet energy scale as a function of the generated jet p_T is estimated as the average of the distribution of $p_T^{\text{reco}}/p_T^{\text{gen}}$ in bins of the jet generated p_T — $\mu_{p_T^{\text{reco}}/p_T^{\text{gen}}}(p_T^{\text{gen}})$.
- The aforementioned average ratio $\mu_{p_T^{\text{reco}}/p_T^{\text{gen}}}$ is also estimated as a function of the reconstructed jet p_T , and a correction map $f(p_T^{\text{reco}}) = \mu_{p_T^{\text{reco}}/p_T^{\text{gen}}}(p_T^{\text{reco}})$ is created to correlate the average reconstructed p_T with the average generated p_T .
- For each jet in data, the corresponding generated (true) jet p_T is estimated using the correction map $p_T^{\text{gen}} = f(p_T^{\text{reco}})$. The jet energy correction $\mu_{p_T^{\text{reco}}/p_T^{\text{gen}}}(p_T^{\text{gen}})$ is subsequently applied according to the generated p_T obtained above.

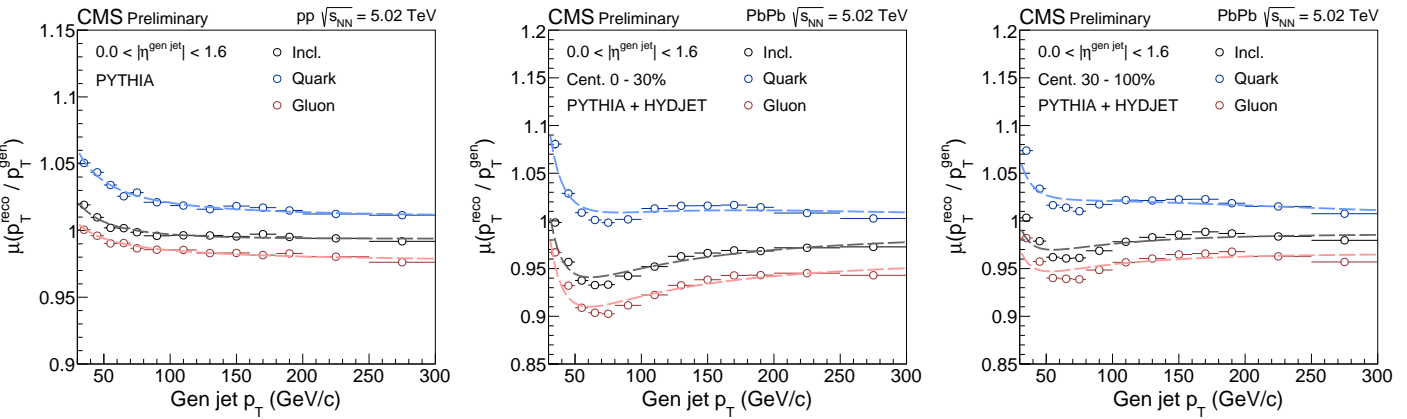


Figure 8-4: Jet transverse momentum response for quark, gluon, and inclusive jets as a function of generated jet p_T in PYTHIA and in different event collision centrality intervals in PYTHIA + HYDJET after the jet energy correction for inclusive jet.

Jet energy scale $\mu_{p_T^{\text{reco}}/p_T^{\text{gen}}}$ derived in PYTHIA and PYTHIA + HYDJET is presented in Figure 8-4 as a function of generated jet p_T . Due to unknown gluon-quark ratio in PbPb collisions, jet energy scales derived from jets with D^0 signal and pure quark/gluon jets are presented. This will be taken into account as systematical uncertainties. After applying residual jet energy scale following the procedures above, deviation between p_T^{reco} and p_T^{gen} is below 2% in the whole p_T range for pp and PbPb. To study the possible influence of jet fragmentation on the jet energy scale, fragmentation-dependent corrections are derived. The main motivation for this approach is that the performance of the calorimeters is expected to be significantly better in the presence of a jet with hard fragmentation. This is a consequence of the fact that jets with softer fragmentation produce a larger amount of low- p_T particles, which deposit, on average, a smaller amount of energy in the calorimeter. The response of the calorimeter for low- p_T particles is typically worse than for high- p_T particles. The procedures for this study is similar with (1).

(2) Jet energy scale with fragmentation dependence

- The mean of the ratio $\mu_{p_T^{\text{reco}}/p_T^{\text{gen}}}$ is studied as a function of the number of jet constituents (n_{CS}) with $p_T > 2 \text{ GeV}/c$. This exercise is performed in different reconstructed jet p_T since we are specifically interested in the reconstruction bias in presence of jets with soft fragmentation. In pp collisions, the number of jet constituents is simply the number of particle flow objects clustered in the given jet, while in PbPb collisions, it is the same quantity, but is calculated after

applying background subtraction. As shown in Figure 8-5, $\mu_{p_T^{\text{reco}}/p_T^{\text{gen}}}(p_T^{\text{reco}}, n_{\text{CS}})$ decreases almost linearly as a function of n_{CS} . Therefore, a linear fit is performed to model this dependence.

- Then a correction depending on both p_T^{reco} and n_{CS} is applied and the average p_T^{gen} is derived to given reconstructed jets.
- Finally the standard jet energy correction procedure is applied according to $\mu_{p_T^{\text{reco}}/p_T^{\text{gen}}}(p_T^{\text{gen}})$.

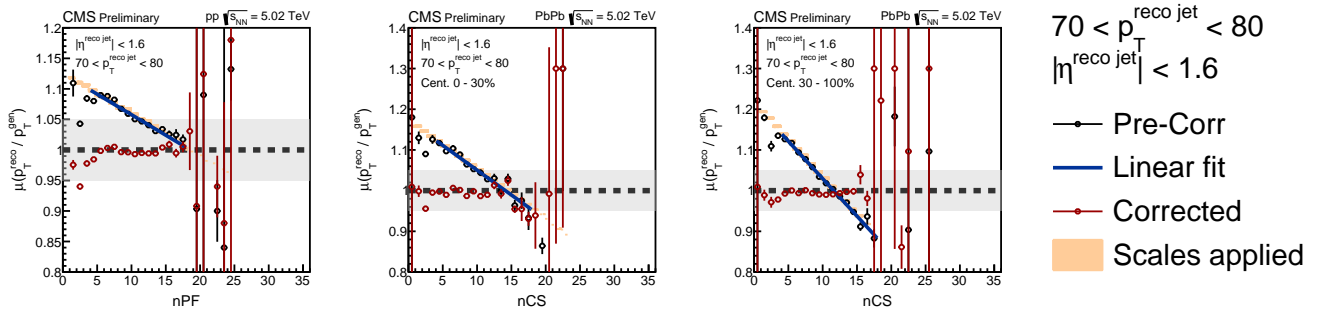


Figure 8-5: Averaged p_T ratio $\mu_{p_T^{\text{reco}}/p_T^{\text{gen}}}$ as a function of n_{CS} for jets with $70 < p_T^{\text{reco}} < 80$ GeV/c (black markers) for pp collisions (left) and PbPb collisions at centrality class of 0 – 30% (middle) and 30 – 100% (right). A linear fitting (blue line) and the same quantity after correction (red markers) are also shown.

In addition, jet energy and angular resolution is studied to take care of discrepancy between data and simulations.

(3) Jet energy and angular resolution

- The jet energy resolution is estimated as the width of the Gaussian fits of the distribution of $p_T^{\text{reco}}/p_T^{\text{gen}}$ in bins of generated jet p_T , and is then parameterized by

$$\sigma(p_T^{\text{gen}}) = \sqrt{C^2 + \frac{S^2}{p_T^{\text{gen}}} + \frac{N^2}{(p_T^{\text{gen}})^2}} \quad (8.1.1)$$

- The η angular resolution is estimated as a function of generated jet p_T as the width of the distribution of $\eta^{\text{reco}} - \eta^{\text{gen}}$. The same procedure is applied to estimate the ϕ angular resolution.
- In MC, the gen p_T is smeared according to the jet energy resolution. The η and ϕ of the generated jets are then smeared according to the value of the angular resolution corresponding to the smeared value of generated jet p_T .

- The correction factor that accounts for the jet energy resolutions and the η and ϕ angular resolutions is obtained by taking the ratio between the dN/dr distributions after and before all the smearings are applied.

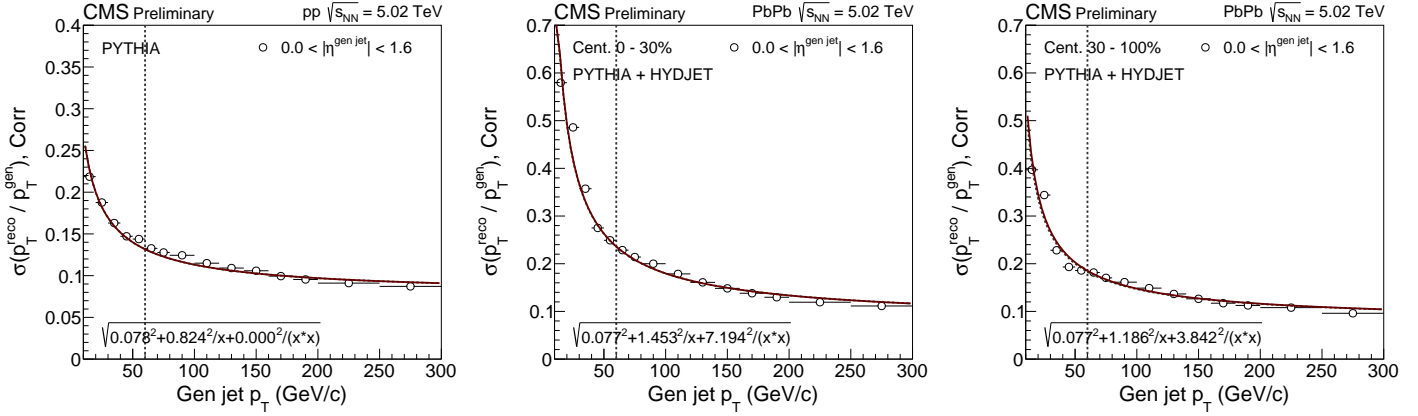


Figure 8-6: p_T -dependence of the jet energy resolution after correction from PYTHIA (left) and from PYTHIA + HYDGET at centrality class of 0–30% (middle) and 30–100% (right).

In Figure 8-6 the jet energy resolution of reconstructed jets with respect to generated jets in PYTHIA and PYTHIA + HYDGET samples is presented.

8.1.4 Jet Background Subtraction

To clarify the observable, we want to measure the radial distribution r between D^0 and jets produced in the same hard scattering. The fact that we measure D -jet pairs produced in the same hard scattering does not mean that the D^0 and the jet come necessarily from the same parton shower. For example, in the case of a $c - \bar{c}$ pair produced in a gluon splitting process, the same D^0 produced in one of the two c -jets can be associated to both the jets due to the fact that the radius of the jets is 0.3 but we consider correlations up to $r = 0.5$.

In our measurement, the main source of background is coming from D^0 -jet pairs that are created due to the presence of uncorrelated hard scatterings or fake objects. Indeed, in one PbPb event where a correlated D^0 -jet pair is produced, one can create other background correlations by combining the signal jet or the signal D^0 with a D^0 or a jet which are not correlated to the hard scattering under study (Figure 8-7). These uncorrelated objects are conventionally underlying event (UE) jets or D^0 mesons. In the case of jets, the definition of jet_{UE} includes jets not correlated from D^0 and

fake jets. The definition of D_{UE}^0 includes only D^0 mesons not correlated since we already remove the contamination of fake D^0 with the signal extraction procedure. To summarize, in a PbPb event that includes a genuine produced D^0 -jet pairs we will have the following contributions:

$$\{jet, D\}_{\text{all}} = \{jet_{\text{signal}}, D_{\text{signal}}\} + \{jet_{\text{signal}}, D_{\text{UE}}\} + \{jet_{\text{UE}}, D_{\text{signal}}\} + \{jet_{\text{UE}}, D_{\text{UE}}\} \quad (8.1.2)$$

where $\{jet_{\text{signal}}, D_{\text{signal}}\}$ are the correlated signal pairs, $\{jet_{\text{signal}}, D_{\text{UE}}\}$ are the pairs produced by combining the signal jet with a UE D^0 , $\{jet_{\text{UE}}, D_{\text{signal}}\}$ by combining a signal D^0 with a UE jet and $\{jet_{\text{UE}}, D_{\text{UE}}\}$ by combining a UE D^0 with a UE jet.

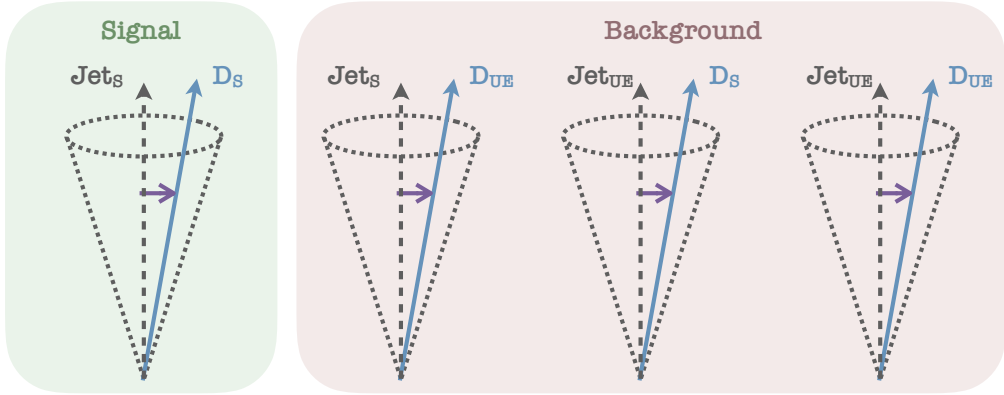


Figure 8-7: Signal event of a genuine correlation of D -jet compared to the background events due to the presence of at least one object (jet or D^0) coming from the underlying event.

Mixed Event Subtraction

The uncorrelated component due to the presence of correlations with the objects generated in the underlying event can be removed by mixing events coming from the jet triggered sample with Minimum-Bias (MB) events since the MB events provides a realistic representation of that underlying event. In particular, the mixed event techniques proceeds as follow:

- For each trigger event, one has to find one or more MB events that present the same global characteristics (centrality, vertex position and event plane). This is required in order to match events that present similar properties in term of event geometry, multiplicity, reconstruction efficiency etc. In this analysis 100

bins in centrality, 30 bins in z-position of the primary vertex (from -15 to 15 cm) and 16 bins in event plane are considered.

- Three ingredients are produced by performing the analysis by correlating *i*. jets from the MB sample with D^0 from the triggered sample, *ii*. jets from the triggered sample with D^0 with the MB samples and finally *iii*. D^0 and jets from the same MB samples.
- The contribution of the signal component can be isolated by properly combining the three ingredients above.

Below in Eq. (8.1.3) one can find the contributions expected in each of the mixed sample for this analysis.

$$\begin{aligned}
 \{jet_{\text{TRG}}, D_{\text{TRG}}\} &= \{jet_{\text{signal}}, D_{\text{signal}}\} + \{jet_{\text{signal}}, D_{\text{UE}}\} + \{jet_{\text{UE}}, D_{\text{signal}}\} + \{jet_{\text{UE}}, D_{\text{UE}}\} \\
 \{jet_{\text{TRG}}, D_{\text{MB}}\} &= \{jet_{\text{signal}}, D_{\text{UE}}\} + \{jet_{\text{UE}}, D_{\text{UE}}\} \\
 \{jet_{\text{MB}}, D_{\text{TRG}}\} &= \{jet_{\text{UE}}, D_{\text{signal}}\} + \{jet_{\text{UE}}, D_{\text{UE}}\} \\
 \{jet_{\text{MB}}, D_{\text{MB}}\} &= \{jet_{\text{UE}}, D_{\text{UE}}\}
 \end{aligned} \tag{8.1.3}$$

Therefore, the true signal component can be

$$\begin{aligned}
 \{jet_{\text{signal}}, D_{\text{signal}}\} &= \{jet_{\text{TRG}}, D_{\text{TRG}}\} \\
 &\quad - \{jet_{\text{TRG}}, D_{\text{MB}}\} - \{jet_{\text{MB}}, D_{\text{TRG}}\} + \{jet_{\text{MB}}, D_{\text{MB}}\}
 \end{aligned} \tag{8.1.4}$$

The closure of this subtraction machinery is tested with simulation productions. Figure 8-8 presents r distribution of D^0 with $4 < p_T^D < 20$ GeV/c in before background subtraction, the background contributions subtracted, and the result after background subtraction with event mixing methods. For D^0 -jet correlation, the background contribution is very small compared with signals.

η -reflection subtraction

The background subtraction study was also performed using the η -reflection method. In the η -reflection method, the contribution of the underlying event (UE) is estimated by measuring the correlation between the real D^0 and an “artificial” jet that is created by reflecting the real jet with respect to the η -axis as shown int the left panel of

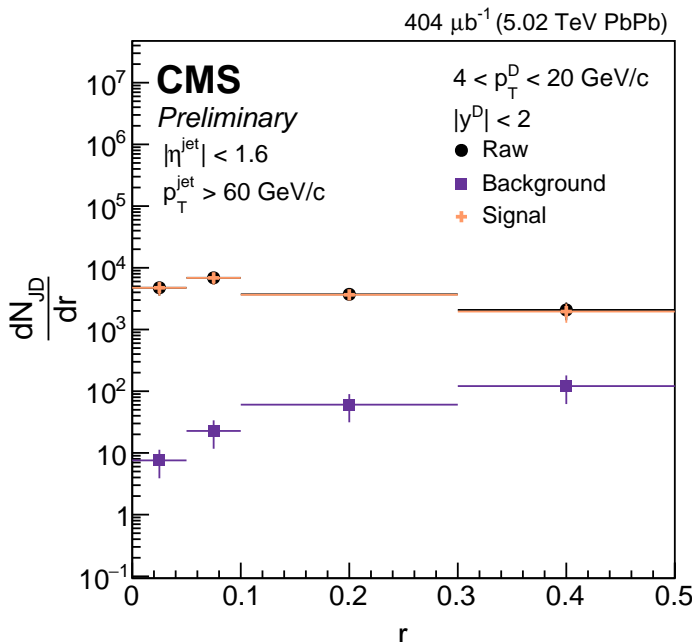


Figure 8-8: r distribution of D^0 with $4 < p_T^D < 20$ GeV/c in PbPb collisions before background subtraction (black), the background contributions subtracted (Purple), and the result after background subtraction (orange) with event mixing methods.

Figure 8-9. Practically, the standard analysis of r correlation is made by considering every time all the real D^0 and all the reflected jets. The subtracted r result is obtained by subtracting this distribution from the one obtained with the original jet directions. This procedure is expected to remove the contribution of uncorrelated D^0 -jet pairs coming from the presence of D^0 and jet coming from other hard scattering but also to the contribution of fake jets (as described before, fake D^0 are not expected to contribute to our background due to the signal extraction procedure). This is true under the assumption that in the reflected cone no D^0 mesons or jets can be produced starting from the same hard scattering, which is characterized by a back to back direction. The analyses that use the η -reflection method, indeed, typically reduce the η range of the jets to $|\eta| > 0.3$ when using jets of radii of 0.3 in order to reduce the possibility of subtracting the contribution of the same jet. However, this selection does not completely exclude the possibility of oversubtracting the contribution of uncorrelated pairs for $r > 0.3$. This is mainly due to the fact that jets in heavy-ion collisions are typically wider than $R = 0.3$. For this reason, a sizable difference between the subtracted results with the mixed event technique and the η -reflection method might be in principle expected. The mixed event result should be in general

considered as the preferred subtraction method especially in that interval.

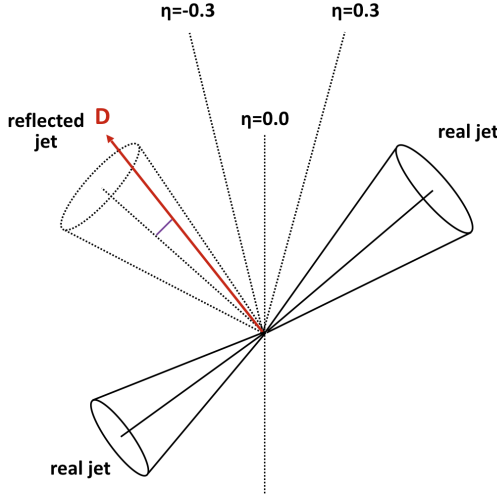


Figure 8-9: Genuine type of uncorrelated event that enters the η -reflection subtraction and therefore it is statistically subtracted with this procedure.

8.2 Results

8.2.1 D^0 Radial Distribution in jets in pp and PbPb Collisions

Figure 8-10 shows the measured D^0 radial profiles in pp and PbPb collisions, and the measurement is performed for low- p_T D^0 ($4 < p_T^D < 20$ GeV/c) and high- p_T D^0 ($p_T^D > 20$ GeV/c) separately. For a preliminary comparison, the shapes of D^0 radial distributions are similar in pp and PbPb for both D^0 p_T bins. At low p_T ($4 < p_T^D < 20$ GeV/c), the shape of measured spectrum is relatively flat and reaches a maximum at $0.05 < r < 0.1$. At high p_T ($p_T^D > 20$ GeV/c), the measured spectra in pp and PbPb collisions fall rapidly as a function of r . These features are similar to what was observed in inclusive jet-hadron correlation functions [172]. The results are compared to predictions from the PYTHIA 8 event generator in Figure 8-11. For D^0 with $4 < p_T^D < 20$ GeV/c, the observation that the distribution reaches a maximum at $0.05 < r < 0.1$ is consistent with the prediction from PYTHIA 8 for pp events. However, spectra from PYTHIA are slightly wider than the pp data. The pp spectrum of D^0 with $p_T^D > 20$ GeV/c is quantitatively consistent with the the PYTHIA 8 prediction. To measure the modification of the radial profile, a ratio of PbPb to pp spectra is also

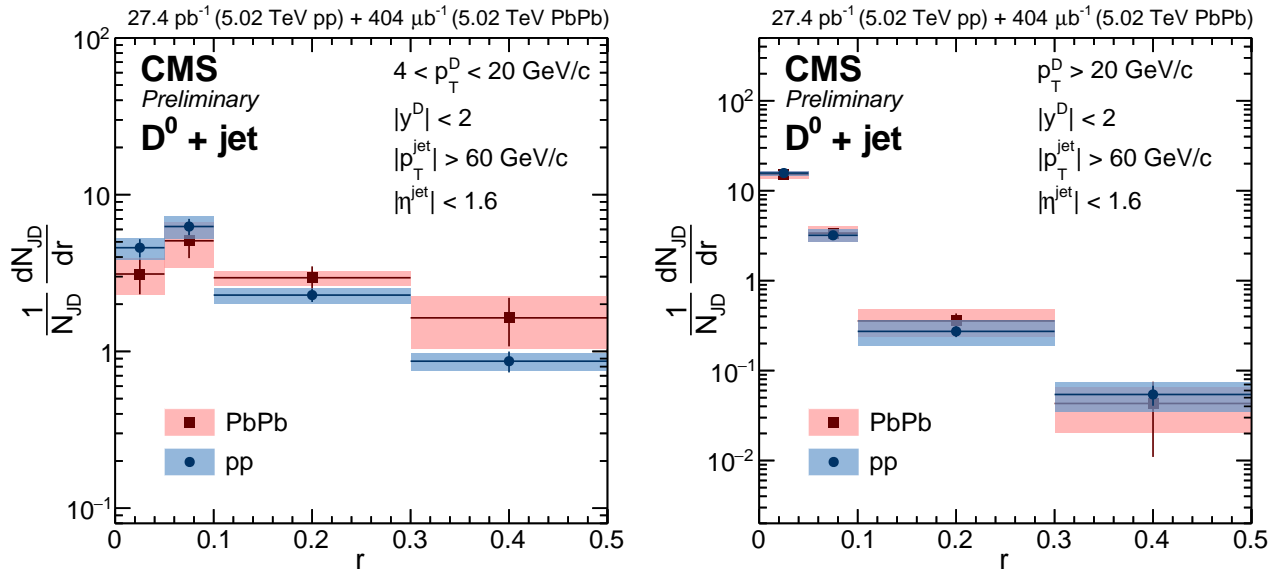


Figure 8-10: Distributions of D^0 mesons in jets as a function of the distance from the jet axis for jets of $p_T^{\text{jet}} > 60 \text{ GeV}/c$ and $|\eta^{\text{jet}}| < 1.6$ measured in pp and PbPb collisions at $\sqrt{s_{\text{NN}}} = 5.02 \text{ TeV}$. The measurement is performed in the $D^0 p_T^D$ range $4 - 20 \text{ GeV}/c$ (left) and for $p_T^D > 20 \text{ GeV}/c$ (right). Each spectrum is normalized to its integral in the region $0 < r < 0.3$. The vertical bars (boxes) correspond to statistical (systematic) uncertainties.

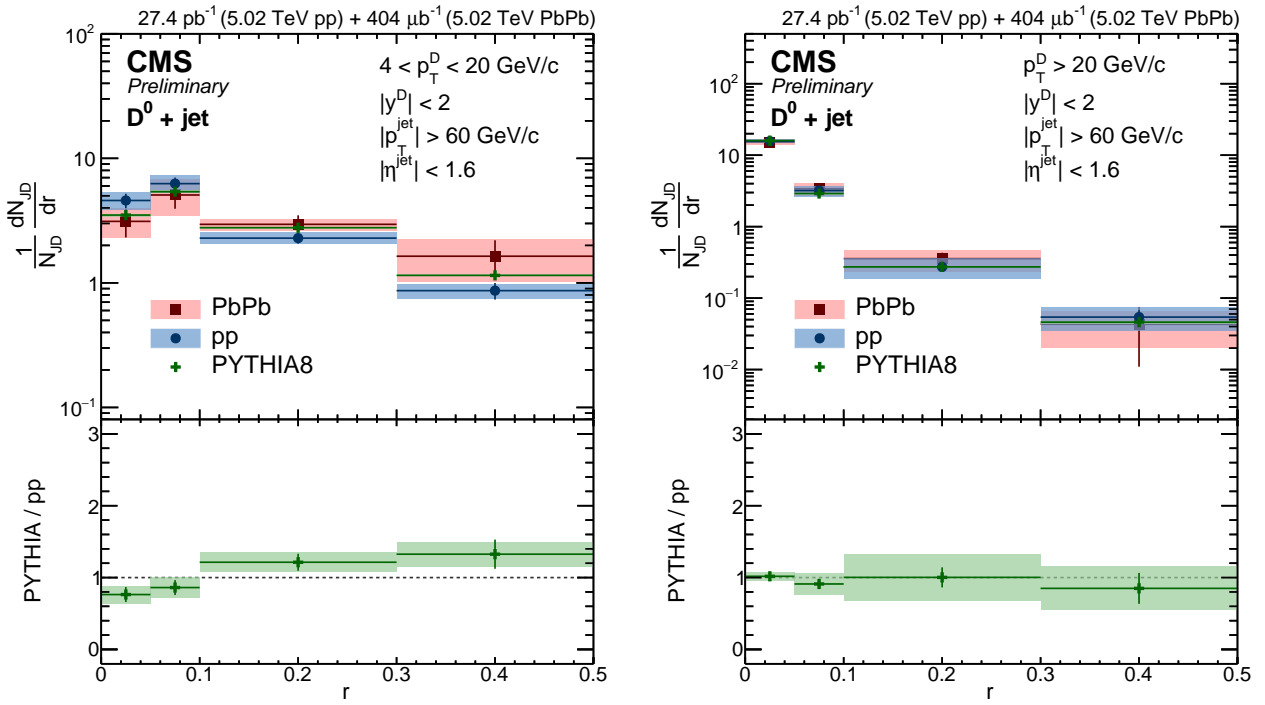


Figure 8-11: Distributions of D^0 mesons in jets as a function of the distance from the jet axis for jets of $p_T^{\text{jet}} > 60 \text{ GeV}/c$ and $|\eta^{\text{jet}}| < 1.6$ measured in pp and PbPb collisions at $\sqrt{s_{\text{NN}}} = 5.02 \text{ TeV}$. The predictions from the PYTHIA 8 event generator are also superimposed, and in the bottom panel the ratios of the D^0 radial distributions of pp over PYTHIA 8 predictions are presented.

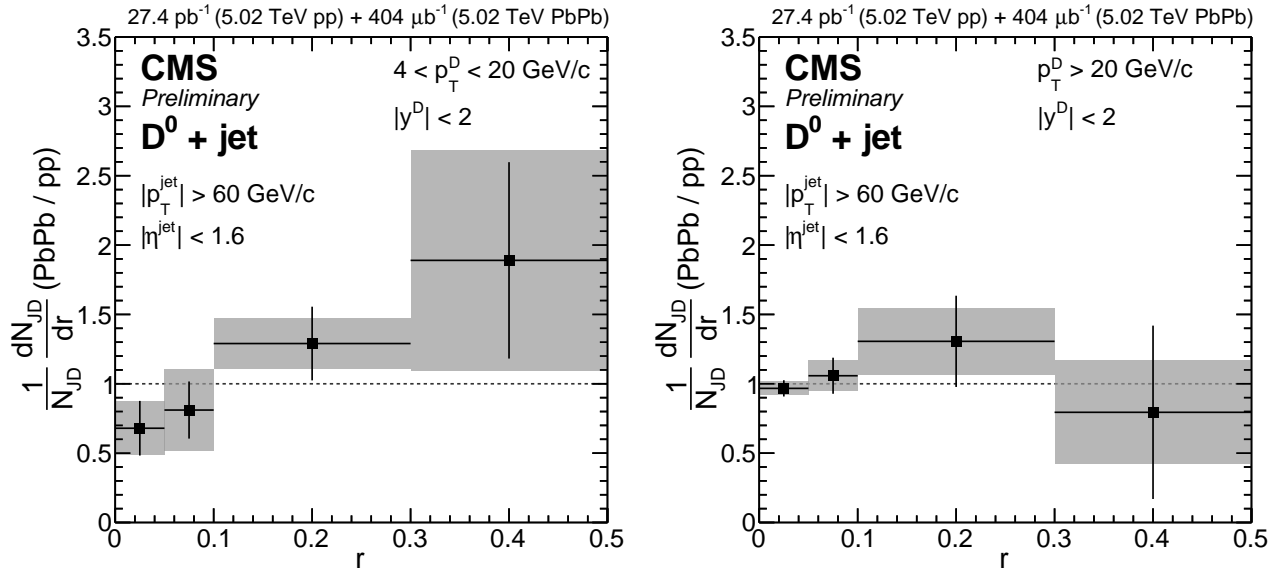


Figure 8-12: The ratios of the D^0 radial distributions of PbPb to pp in the D^0 p_T^D range $4 - 20 \text{ GeV}/c$ (left) and for $p_T^D > 20 \text{ GeV}/c$ (right).

presented in Figure 8-12. This ratio increases as a function of r at $4 < p_T^D < 20 \text{ GeV}/c$. This result indicates that D^0 mesons at low p_T are farther away from the jet axis in PbPb compared to pp collisions. The ratio of PbPb to pp is consistent with unity within uncertainties for $D^0 p_T^D > 20 \text{ GeV}/c$, which shows that the modification of the radial profile of high- p_T D^0 mesons is small. These features in spectra ratios at low and high p_T^D are qualitatively different from charged particle radial distributions with respect to the jet axis measured in similar transverse momentum ranges [172].

8.3 Systematic Uncertainty Study

Several sources of systematic uncertainty are considered for the D^0 yield extraction and the jet reconstruction which are studied in bins of p_T^D and r . The uncertainty in the raw yield extraction is evaluated by repeating the fit procedure using different background and signal fit functions and by varying the widths of the Gaussian functions that describe the D^0 signal according to differences between data and MC. In the signal variation study, the sum of three Gaussian functions with the same mean but different widths is considered, while in the background variation study, a second-order polynomial function is used. This functional form provides a good description of the combinatorial background according to same-sign studies. The systematic uncertainty due to the selection of the D^0 meson candidates is estimated by considering the differences between MC and data in the reduction of the D^0 yields obtained by applying each of the D^0 selection variables. The study is performed by varying one selection at a time in a range that allowed a robust signal extraction procedure and by considering the maximum relative discrepancy in the yield reduction between data and MC. The total uncertainty is the quadratic sum of the maximum relative discrepancy obtained by varying each of the three selection variables separately. The systematic uncertainties for the jets used in the analysis include components for the uncertainty in jet energy scale (JES) and jet energy resolution (JER). The systematic uncertainty pertaining to JES is estimated by varying the p_T^{jet} by 2.8% (in both pp and PbPb results), which represents the sum in quadrature of the observed data-MC differences (2%) and the non-closure (i.e. deviation from unity) in MC, when comparing reconstructed (detector level) jets versus truth (generator level) jets smeared by the known detector and reconstruction effects. An additional uncertainty is added to account for the different detector response to quark versus gluon jets. The assigned

uncertainty represents the maximum difference from the nominal results, when applying JES corrections obtained with a pure-gluon sample or a pure-quark sample. The systematic uncertainty for the JER is estimated by varying by 15% the p_T^{jet} energy resolution to account for an imperfect description of the fluctuations of the UE event in MC simulations. The variation considered is estimated by studying the effects of these fluctuations using two different methods: the random cone technique [181, 182] and the embedding procedure. The random cone method consists of reconstructing many jets in a zero bias event, clustering particles in randomly placed cones in the entire (η, ϕ) space. When the method is applied in events with no contribution from hard scatterings, as it is the case for zero-bias events, the standard deviation of the distribution of the jet p_T obtained with this procedure can be indeed used to estimate the magnitude of the UE fluctuations. Also, the systematic uncertainties from trigger bias is estimated by the difference between the result with trigger efficiency corrected and the nominal result. Finally, since a bin-by-bin correction is applied for the non-closure between reconstructed and generated jets smeared by the resolution extracted from simulation, the magnitude of the correction is quoted as the systematic uncertainties for resolution unfolding. Systematic uncertainties from all sources are summarized in Table 8.2 and Table 8.3.

Source	r			
	0-0.05	0.05-0.10	0.10-0.30	0.30-0.50
$4 < p_T^D < 20 \text{ GeV}/c$				
Signal extraction	4.5%	4.8%	3.1%	2.6%
Selection efficiency	3.6%			
Jet energy scale	6.8%	15.2%	7.7%	10.3%
Jet energy resolution	3.0%	0.3%	1.2%	1.3%
Trigger efficiency	1.1%	1.8%	1.8%	1.6%
Non-closure	12.7%	1.3%	6.1%	6.4%
$p_T^D > 20 \text{ GeV}/c$				
Signal extraction	3.8%	3.7%	3.8%	5.4%
Selection efficiency	3.6%			
Jet energy scale	1.6%	7.2%	9.6%	17.5%
Jet energy resolution	0.4%	1.2%	2.5%	0.8%
Trigger efficiency	0.3%	0.6%	2.7%	1.3%
Non-closure	4.4%	14.3%	30.1%	30.7%

Table 8.2: Summary of relative systematic uncertainties in pp collision.

Source	r			
	0-0.05	0.05-0.10	0.10-0.30	0.30-0.50
$4 < p_T^D < 20 \text{ GeV}/c$				
Signal extraction	4.9%	5.2%	4.8%	7.7%
Selection efficiency	3.5%			
Jet energy scale	24.3%	31.5%	8.1%	35.8%
Jet energy resolution	5.6%	1.3%	2.9%	3.7%
Trigger efficiency	7.4%	6.2%	0.7%	14.5%
Non-closure	6.2%	3.2%	0.7%	1.1%
$p_T^D > 20 \text{ GeV}/c$				
Signal extraction	5.9%	5.0%	8.2%	1.4%
Selection efficiency	2.7%			
Jet energy scale	1.8%	5.0%	11.5%	41.8%
Jet energy resolution	0.6%	0.7%	4.9%	1.8%
Trigger efficiency	0.8%	1.6%	4.8%	8.5%
Non-closure	6.3%	17.8%	30.1%	31.5%

Table 8.3: Summary of relative systematic uncertainties in PbPb collision.

Chapter 9

Conclusions

9.1 Discussions

So far we have seen the whole story of D^0 fate in heavy-ion collisions studied with CMS detectors. Recall in Section 1.3.1 we describe the expected dynamics of heavy quarks in heavy-ion collisions, and it is time to summarize what we have learned from experiments. We will see how our measurements discussed in this thesis provide insights of the interaction between charm quarks and the medium in heavy-ion collisions and the properties of quark gluon plasma. Also, we will try to answer the questions raised at the end of Section 1.3.2.

PRODUCTION As the charm quark mass is larger than the typical temperature of the medium created in current heavy-ion collisions $m_c \gg T$, the charm quarks mainly emerge via the initial hard scatterings. Since the charm quark mass is also larger than the QCD scale $m_c \gg \Lambda_{\text{QCD}}$, the initial production can be calculated with pQCD even down to zero p_T . This is tested by the measurement of p_T -differential cross section of prompt D^0 in proton-proton collisions. The D^0 production spectrum measured by CMS detectors in proton-proton collisions is compared with pQCD calculations with two configurations over a wide kinematic range $2 < p_T < 100$ GeV/c. FONLL calculates p_T -differential cross section via a perturbative expansion in the strong coupling constant α_s and performs an exact treatment up to next leading order (α_s^3), while GM-VFNS absorbs the large logarithmic terms into parton distribution functions and fragmentation functions, and determine parameters by matching massless scheme at limit $m \rightarrow 0$. FONLL and GM-VFNS can both reasonably predict data within uncertainties. However, the data measurement is close to the upper bound of the FONLL

prediction and the lower bound of the GM-VFNS calculation, and at high p_T region data agree better with FONLL than GM-VFNS. On the other hand, the production in proton-proton collisions is not equivalent to the initial production in ion-ion collisions as the modification of parton distribution function in a nucleus have to be taken into account. Figure 9-1 shows theoretical predictions of $D^0 R_{AA}$ and v_2 in PbPb collisions

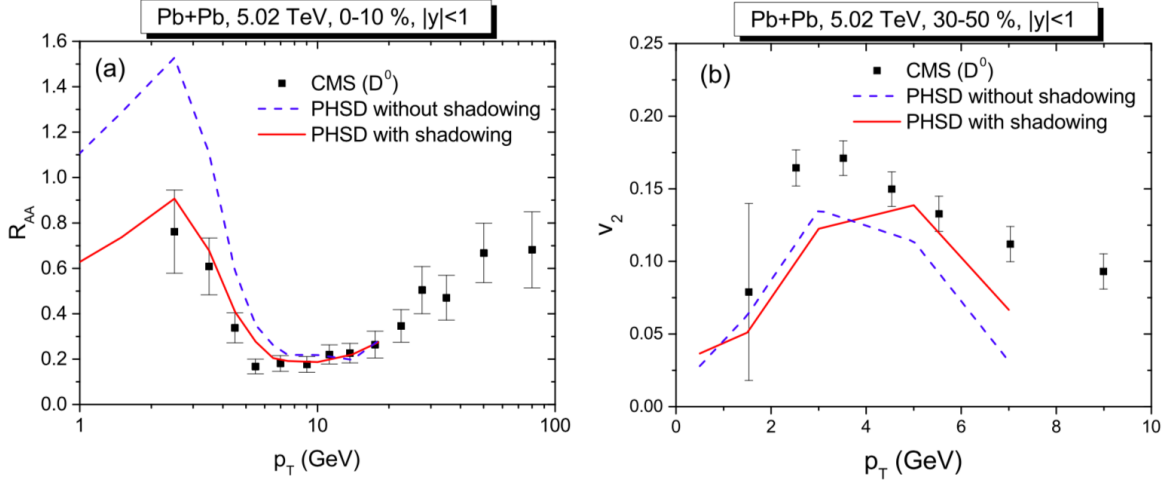


Figure 9-1: D^0 nuclear modification factor R_{AA} (left) and elliptic flow coefficient v_2 (right) as a function of p_T in PbPb collisions at $\sqrt{s_{NN}} = 5.02$ TeV in the centrality class of 0–10% and 30–50% respectively from PHSD with (solid line) and without (dashed line) shadowing effects. Figure from Ref. [183].

at $\sqrt{s_{NN}} = 5.02$ TeV from PHSD [183]. The calculation results are presented with and without EPS09 [81] shadowing effects measured by solid lines and dashed lines respectively. It suggests that including shadowing effect significantly suppress R_{AA} at low p_T . We have seen in Figure 1-11, the partons carrying small energy fraction of the nucleon are suppressed in nuclei compared with free nucleon. At high-energy collisions, the charm quarks with small p_T are mainly produced via quarks and gluons with small x , and therefore, low- p_T D^0 production may be suppressed. The calculation is compared with experimental measurements and it indicates that accounting for nPDF is necessary when studying heavy flavor production in heavy-ion collisions. At the same time, v_2 of D^0 is less affected by shadowing effects, while the peak shifts a bit.

DIFFUSION The fact that the charm quark mass is larger than the temperature of the medium suggests that the diffusion of charm quarks can be treated as Brownian

motion. Therefore, the diffusion can be studied by the Fokker-Planck equation

$$\frac{\partial}{\partial t} f_Q(t, \mathbf{p}) = \frac{\partial}{\partial p_i} \left[A_i(\mathbf{p}) f_Q(t, \mathbf{p}) + \frac{\partial}{\partial p_j} (B_{ij}(\mathbf{p}) f_Q(t, \mathbf{p})) \right] \quad (9.1.1)$$

and the complicated behaviors can be parameterized by simple transport coefficients. Specifically, the heavy-quark spatial diffusion coefficient D_s in the QGP is related to the relaxation (equilibrium) time of heavy quarks $\tau_Q = \frac{m_Q}{T} D_s$, where m_Q is the quark mass and T is the medium temperature. Apart from the recipe based on the Fokker-Planck equation, there are also models in the market based on energy loss extended from light-flavor sector and models based on string theory. The diffusion behavior of charm quarks is studied by the measurement of prompt $D^0 R_{AA}$ and v_n in heavy-ion collisions especially at low- p_T region. The experimental measurements show non-zero v_2 of prompt D^0 at $1 < p_T < 40$ GeV/c in multiple centrality classes, and larger v_2 is observed at peripheral events compared with the most central events. As p_T increases, v_2 increases first and decreases which leads to maximum v_2 at p_T around 3–5 GeV/c. The prompt $D^0 v_2$ is smaller than that of charged particles at low p_T , and the difference increases from the case in central events to that in peripheral events. The property of prompt $D^0 v_3$ is similar to v_2 but suggests no significant dependence on centrality classes.

In Figure 9-2, calculations of prompt $D^0 R_{AA}$, v_2 and v_3 as a function of p_T in PbPb collisions using Monte Carlo D-And-B MODular simulation code (DAB-mod) [185] are compared with the measurements. The simulations employ a parametric energy loss model [26] and a Fokker-Planck-equation-based model with two parameterizations for both. For the energy loss model, the parameterization is defined by $dE/dx = -f(T, \nu_Q)\Gamma_{\text{flow}}$, where T and Γ_{flow} are local temperature and a flow factor respectively, and the latter accounts for the Lorentz boost. Two parameterizations are applied $-f(T, \nu_Q) = \alpha$ and $f(T, \nu_Q) = \xi T^2$, where α and ξ are free parameters. For Langevin model, two diffusion coefficients are employed. “M&T” (Moore & Teaney) uses spatial diffusion coefficient $D_s = k_{\text{M\&A}}$ derived with pQCD+HTL, while “G&A” (Gossiaux & Aichelin) applies drag coefficient $\Gamma = k_{\text{G\&A}} A(T, p)$ derived with QCD+HTL using running coupling and optimized gluon propagator. The transport model (energy loss model) works better at low (high) p_T , and relative low decoupling temperature leads to a better agreement with data.

Besides examining the change of the observable (R_{AA} , v_n) by varying the parameters, it is more inspiring that the transport coefficients can be directly extracted

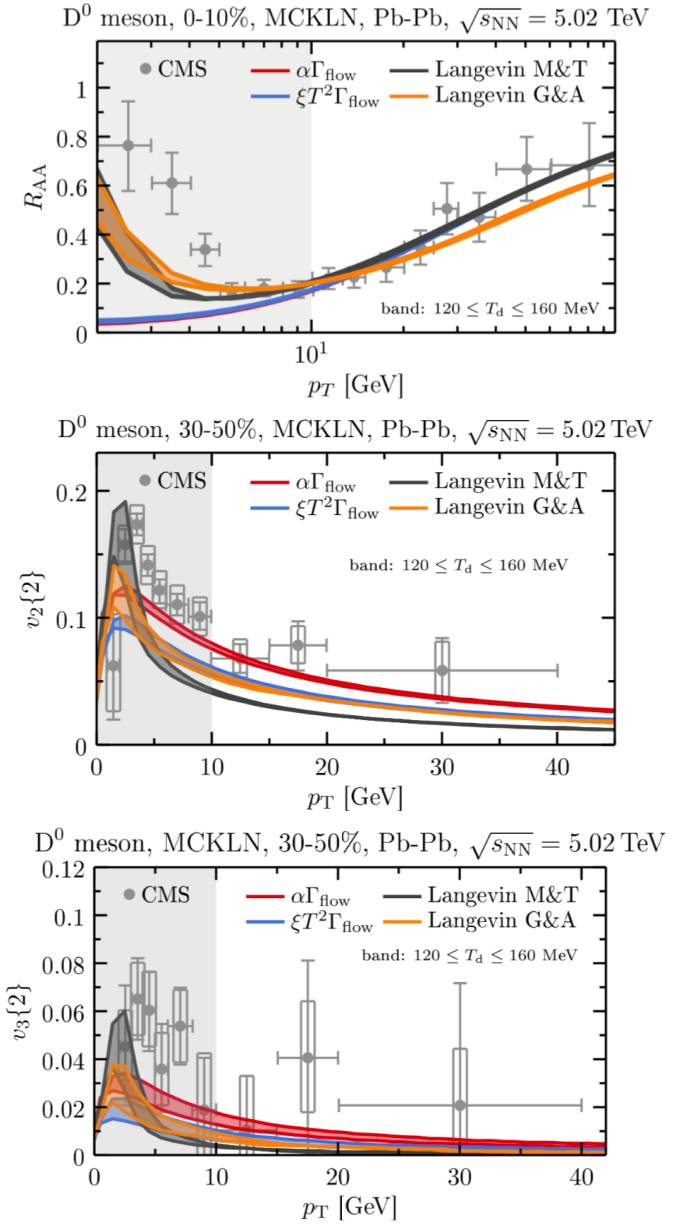


Figure 9-2: Calculations of D⁰ nuclear modification factor R_{AA} (up), elliptic flow v_2 (middle) and triangle flow v_3 (bottom) as a function of p_T in PbPb collisions at $\sqrt{s_{\text{NN}}} = 5.02 \text{ TeV}$ under different configurations; The simulations apply both energy loss model ($\alpha\Gamma_{\text{flow}}$, $\xi T^2\Gamma_{\text{flow}}$) and Langevin-based model (M&T, G&A) with two sets of parameters for both. The bands are obtained by varying decoupling temperature $120 < T_d < 160 \text{ MeV}$. Figures from Ref. [184].

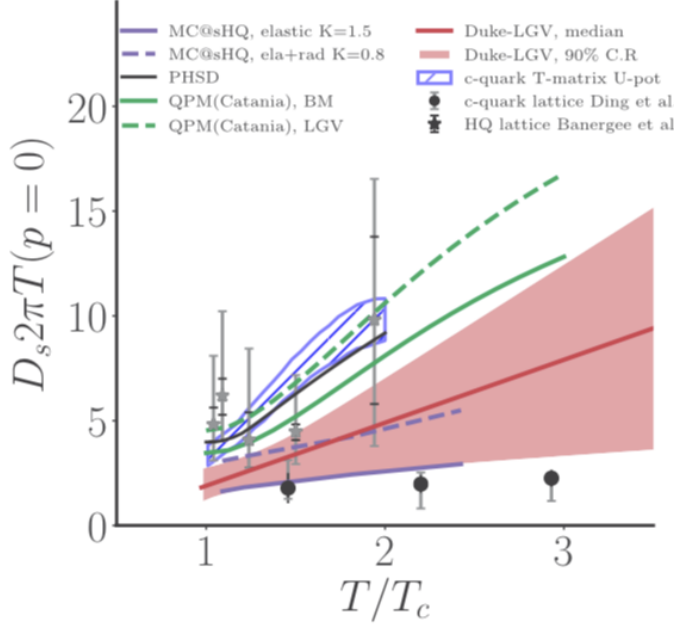


Figure 9-3: Comparison of the heavy quark dimensionless spatial diffusion coefficient at zero momentum $D_s 2\pi T$ ($p = 0$) versus temperature across multiple approaches. Figure from Ref. [186].

with constrained by various measurements of R_{AA} and v_n of D^0 . Figure 9-3 presents the heavy quark dimensionless spatial diffusion coefficients from Duke group [186], MC@sHQ [187], PHSD [64], Catania group [65], T-matrix method [67], and the lattice QCD calculations [188, 189]. The temperature dependence of $D_s 2\pi T$ is close to linear relationship with positive slope at $p = 0$ for all models. Around $T \sim T_c$, the values of $D_s 2\pi T$ ($p = 0$) from different models are all within the range of 1 – 5, although the underlying mechanisms are rather different. At higher temperature, $D_s 2\pi T$ ($p = 0$) values are more sensitive to models, while the result from Duke group indicates lower precision at higher temperature constrained by data. The current extracted D_s values described here are consistent with Lattice QCD calculations and Ads-CFT based calculations, while the calculation based on leading-order pQCD turns out to be wrong [190]. In addition, compared with R_{AA} and v_n the observable of correlation is believed to be more sensitive to the mechanisms and the transport coefficients. Radial distributions of D^0 with respect to the jet axis are measured in both proton-proton and PbPb collisions. At $4 < p_T < 20$ GeV/c, a hint of wider distribution of D^0 is implied in PbPb collisions than pp collisions. At $p_T > 20$ GeV/c, there is no obvious modification on radial profile of D^0 in PbPb collisions. These studies reflect the diffusion of charm quarks with respect to the direction of main energy flow.

ENERGY LOSS It is expected that charm quarks lose energy in the medium. In the frame of pQCD, the energy loss is due to elastic collisions and medium induced gluon radiations. In light-flavor sector, jet quenching is studied at very high p_T where radiative energy loss dominates. However in the case of charm quarks, due to their large energy, it is feasible to reach low p_T and study the contributions from both mechanisms. In addition, the kinematic effect “dead cone effect” predicts a negative correlation between the radiative energy loss and the mass of the partons. This motivates the study of flavor dependence of R_{AA} in heavy-ion collisions. According to the measurements, R_{AA} of prompt D^0 is smaller than 1 over a wide kinematic range $2 < p_T < 100$ GeV/c in PbPb collisions, indicating numerous suppression of charm quarks resulting from energy loss. R_{AA} of prompt D^0 suggests a strongest suppression of a factor of $3 - 4$ at $6 < p_T < 8$ GeV/c, and R_{AA} increases towards lower and higher p_T . It is observed that R_{AA} in the most central events is smaller than the case of inclusive events, which implies the medium density dependence of energy loss. At $p_T > 5$ GeV/c, $D^0 R_{AA}$ is consistent with that of charged particles and B^+ , while at low p_T ($2 < p_T < 5$ GeV/c) there is a hint that R_{AA} of D^0 is larger than the charged particles. R_{AA} of J/ψ from b-hadron decays is found to be larger than that of D^0 at $p_T < 20$ GeV/c, while at higher p_T their R_{AA} are consistent. Nonprompt D^0 performs a similar behavior to nonprompt J/ψ , but is measured in a wider p_T range. The R_{AA} of nonprompt D^0 is larger than that of prompt D^0 in the p_T range $4 - 20$ GeV/c, while at $2 < p_T < 4$ GeV/c and $p_T > 20$ GeV/c they are consistent within uncertainties. On the other hand, v_n at high p_T results from the path length dependence of energy loss. The measurements at high p_T show non-zero v_2 of prompt D^0 and v_2 has smaller dependence on p_T in $10 < p_T < 40$ GeV/c, while at high- p_T , prompt $D^0 v_3$ is consistent with zero within uncertainties. Also, no significant difference of v_2 or v_3 between charged particles and prompt D^0 is observed at high p_T .

Similar with D_s , we can define another transport coefficients for high p_T , the momentum diffusion coefficient \hat{q} . Within specific framework, \hat{q} can be related to the radiative intensity spectra as $\hat{q} = 2m_D^2/\lambda$ where m_D and λ are the Debye mass and mean-free-path respectively. Figure 9-4 presents the heavy quark dimensionless momentum diffusion coefficients from Duke group [186], LBT model [140], the JET collaboration [178] and calculation in leading-order pQCD. The results the first three models are roughly comparable, while the leading-order pQCD calculation is signif-

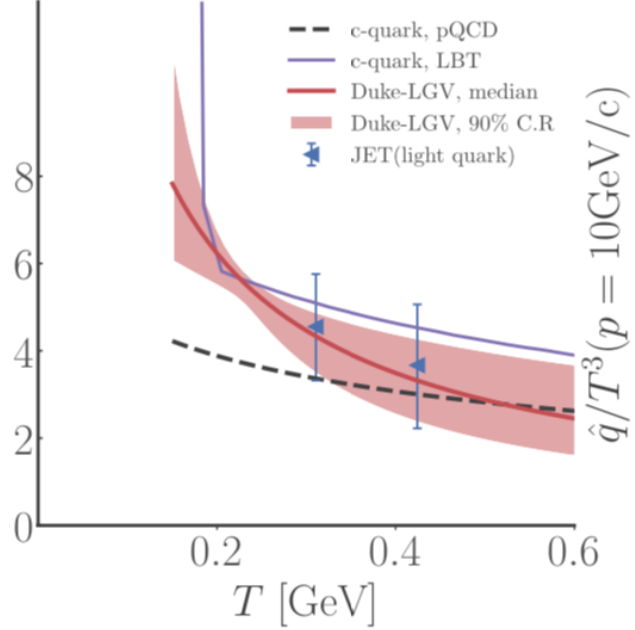


Figure 9-4: Comparison of the heavy quark dimensionless momentum diffusion coefficient at $p = 10$ GeV (\hat{q}/T^3 ($p = 10$ GeV)) versus temperature across multiple approaches. Figure from Ref. [186].

icantly smaller at lower temperature. However, it should be emphasized that the meaning of \hat{q} is quite model dependent. When study particle energy loss in QGP, the medium is generally treated in average sense. In addition, energetic particle passing through quark gluon plasma may result in chromo-electromagnetic field fluctuations in the medium. This response from medium causes the particle to gain energy with collisions. This effect is studied in [191] for , and Figure 9-5 presents the simulations of R_{AA} with and without taking into account the fluctuations. The effect enhances R_{AA} at low p_T due to energy gained by the fluctuations.

HADRONIZATION The hadronization process of partons into mesons and baryons turns out to be an important ingredient to understand the final states of heavy-flavor hadrons seen in experiments. The hadronization mechanism is found to play an important role in the resulting observables. In heavy-ion collisions, in addition to the fragmentation process, recombination with the partons in the medium also contributes to the production of hadrons. Figure 9-6 displays the effects of recombination on various observables. Prompt $D^0 R_{AA}$ and v_2 is calculated using DAB-mod code [185] under the case of fragmentation only and the case accounting for coalescence, and the calculation is compared with the measurements performed by CMS detectors. For R_{AA} , coalescence significantly enhance the production of D^0 at low p_T and indicates

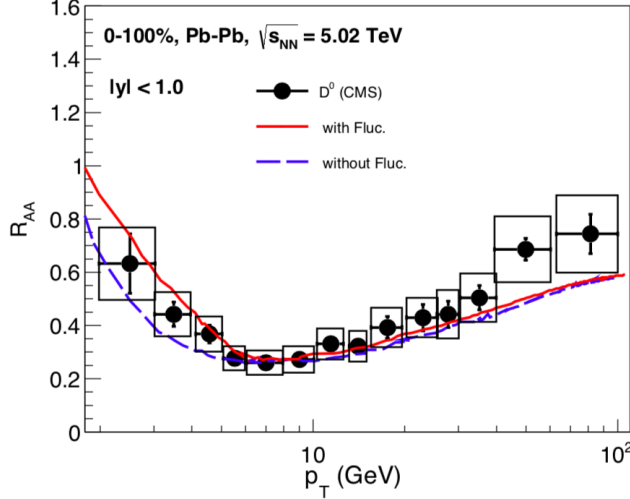


Figure 9-5: Langevin simulation of D^0 nuclear modification factor R_{AA} as a function of p_T in PbPb collisions at $\sqrt{s_{NN}} = 5.02$ TeV in the centrality class of 0–100% from with (solid line) and without (dashed line) the chromo-electromagnetic field fluctuations. Figure from Ref. [191].

that coalescence is necessarily taken into account. For flow coefficients, coalescence leads the flow bump to higher p_T , which results in being closer to data measurements. To look into the effect of hadronization, Figure 9-7 presents the calculations of v_2 and R_{AA} of D mesons and charm quark separately from POWLANG [192]. It suggests that the hadronization process significantly enhances elliptic flow and pushes the peak of R_{AA} and v_2 (flow bump) to higher p_T . Two sets of transport coefficients are applied derived from weak-coupling HTL and non-perturbative lattice-QCD respectively. It is found that v_2 with the two transport coefficients are dramatically different at the quark level. The case from lQCD leads to a larger (smaller) v_2 than the case from HTL at low (high) p_T . However, after hadronization the predictions for D mesons with different coefficients are rather reasonable compared with data.

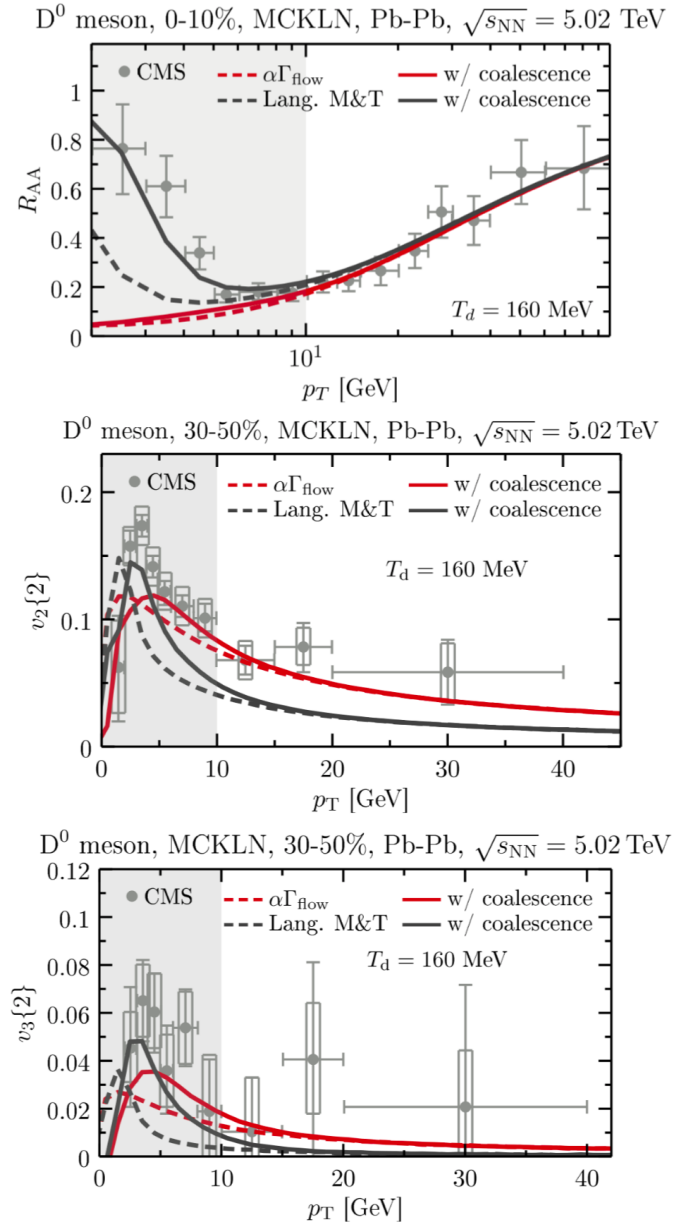


Figure 9-6: Calculations of D⁰ nuclear modification factor R_{AA} (up), elliptic flow v_2 (middle) and triangle flow v_3 (bottom) as a function of p_T in PbPb collisions at $\sqrt{s_{\text{NN}}} = 5.02 \text{ TeV}$ with solid line) and without (dashed line) coalescence hadronization on top of fragmentation taken into account. Figures from Ref. [184].

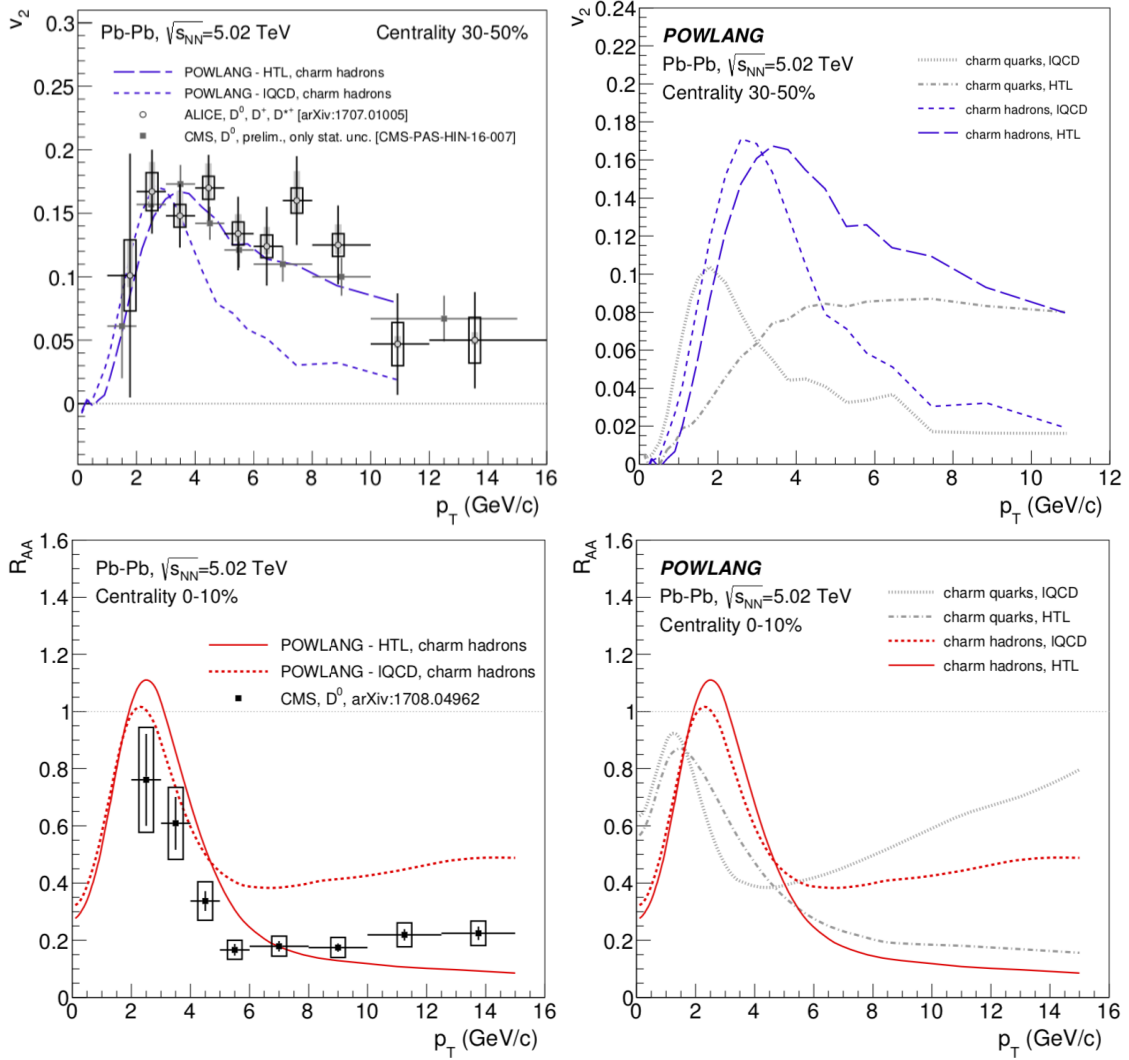


Figure 9-7: v_2 (top) and R_{AA} (bottom) calculated from POWLANG for D mesons and charm quark in PbPb collisions at $\sqrt{s_{NN}} = 5.02$ TeV in the centrality class of 30–50%. Two sets of transport coefficients are applied. Figure from Ref. [192].

9.2 Outlook

In 2018 LHC conducted the last heavy-ion collisions for run 2, and afterwards LHC will launch the Long Shutdown 2 when hardware is upgraded on the collider and the detectors. These are prepared for the so-called “High-Luminosity LHC” (HL-LHC) era that is scheduled to start in Run 4 in the second half of the 2020s. During HL-LHC period, the proposed accumulated luminosity that CMS records reaches 13 nb^{-1} for Pb-Pb collisions, 2 pb^{-1} for p-Pb collisions, and $650 \mu\text{b}^{-1}$ for pp reference. Specifically for open heavy flavors, this will open a new precision era for the observable we have discussed in this thesis, and will also make new and more differential observable accessible for the first time. Focusing on CMS detectors, the upgrades that will benefit heavy-flavor measurements most will be the improvement on the trackers, the trigger system and the data transferring system. The upgraded inner tracker will cover a large acceptance up to $|\eta| < 4$, which makes precise forward measurements possible in CMS. The improved L1 (up to 750 kHz) and DAQ rate (up to 60 GB/s) will allow more sophisticated triggers and record a larger number of minimum-bias triggered events. In addition, a MIP Timing Detector with a radius of 1.16 m and a time resolution of $\simeq 30 \text{ ps}$ is proposed to implement in LHC run 4 and beyond. The MIP Timing Detector could provide, in conjunction with other detectors, proton, pion and kaon separation in the interval $0.7 < p_T < 2 \text{ GeV}/c$ in $|\eta| < 1.5$.

To estimate quantitatively the prospective precision HL-LHC can achieve, we produced the projected performance for several observables of D^0 mesons [193]. The left panel of Figure 9-8 shows the projected performance of R_{AA} of several particles carrying different flavors in Pb-Pb collisions with integrated luminosity $\mathcal{L}_{\text{in}} = 10 \text{ nb}^{-1}$. The central values of the R_{AA} for charged particles and nonprompt J/ψ are taken from [34] and [150], respectively. In the $p_T > 2 \text{ GeV}/c$ interval, the $D^0 R_{AA}$ values are taken from [131] and the spectrum is smoothed using a polynomial fit on the existing measurements. In the $p_T < 2 \text{ GeV}/c$ region, the central values of $D^0 R_{AA}$ are taken from [64]. Finally, the B^+ center values are obtained from predictions in [134]. The systematical uncertainties are scaled down to account for the increased integrated luminosity in the HL-LHC era, with a minimum of 2.5% per charged track. We can see the measurements with high precision can be performed from low to high p_T (0.5–200 GeV/c) for D^0 , and flavor hierarchy can be clearly distinguished under such precision. The right panel of Figure 9-8 shows the expected performance of v_2 of charged particles and D^0 with 1.5 billion minimum-bias PbPb events corresponding

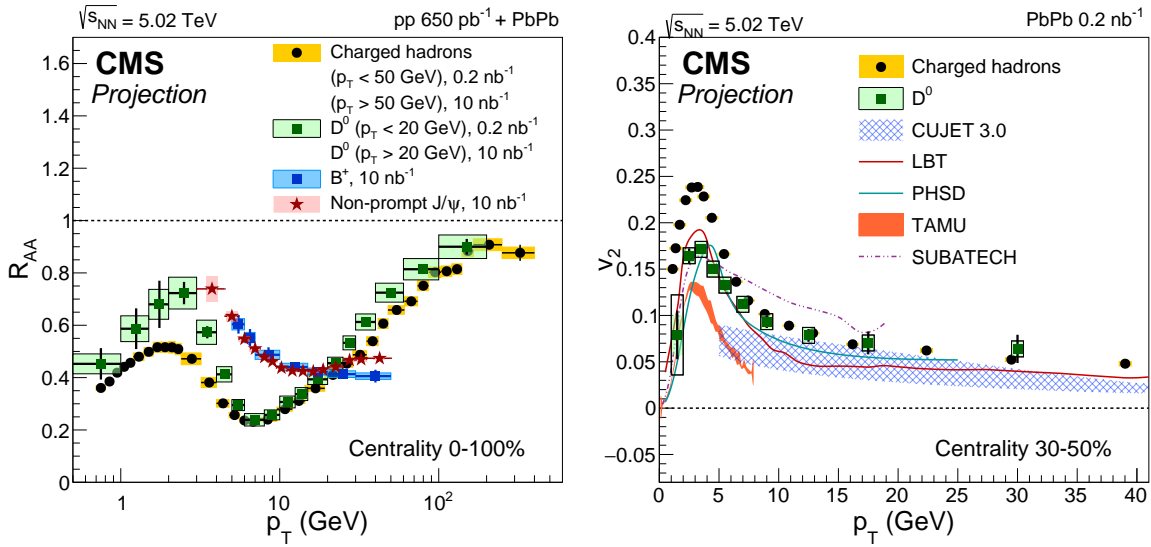


Figure 9-8: (Left) Projected performance of nuclear modification factors of charged particles, D^0 , B^+ and non-prompt J/ψ in CMS in Pb-Pb collisions for $\mathcal{L}_{\text{int}} = 10 \text{ nb}^{-1}$; (Right) Projected v_2 of charged particles and D^0 with the expected statistics of minimum-bias event $\mathcal{L}_{\text{int}} = 0.2 \text{ nb}^{-1}$ compared to theoretical predictions of $D^0 v_2$.

to $\mathcal{L}_{\text{int}} = 0.2 \text{ nb}^{-1}$. The central values are taken from [24] and [156] and smoothed with a polynomial fit. The systematic uncertainties are scaled down to account for the increased luminosity in the HL-LHC era. Note the proposed minimum-bias event statistics are dramatically under estimated, and Pb-Pb run data taking in 2018 has already collected 5 billion minimum-bias events. The new precise data will be able to constrain various components of the theoretical models to determine the heavy quark diffusion coefficient in QGP, and to reveal the possible flavor dependence of the parton energy loss. Currently the several models that can reasonably describe the single charm hadron R_{AA} and v_n data, the diffusion coefficient (D_s) varies significantly and is to be determined. Higher statistics in LH-LHC era will be able to constrain the heavy quark diffusion coefficient in the QGP medium to a more precise level, and potentially distinguish different mechanisms. Figure 9-9 shows the constraint power of experimental measurements of R_{AA} and v_n on the heavy quark diffusion coefficient $2\pi T D_s$ from two different transport models (Fokker-Plank transport model on the left [65], and an improved Langevin framework on the right [186]). The left panel presents a normalized χ^2 as a function of spatial diffusion coefficient constant by comparing the model's calculation on D meson R_{AA} in PbPb collisions at $\sqrt{s_{\text{NN}}} = 5.02 \text{ TeV}$ in a single centrality (7 observation in total). With $\chi^2_{R_{AA}}/\text{n.d.f}$ around 1.5 (corresponding to 85% confidence), one could see that by reducing the current

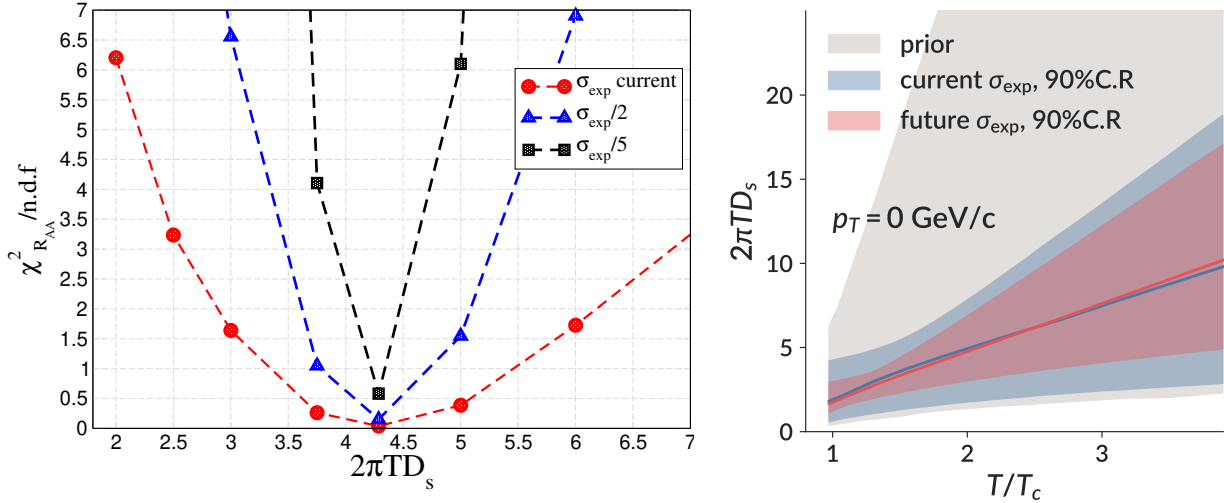


Figure 9-9: (Left) Normalized χ^2 as a function of spatial diffusion coefficient ($2\pi TD_s$) under different experimental precision from an Fokker-Plank transport model; (Right) Coefficient range (90% credibility region) in the phase plane of $2\pi TD_s$ vs T/T_c under different experimental precision, estimated by a model-to-data Bayesian analysis using an improved Langevin framework.

experimental uncertainty to 50%, the uncertainty for the estimation $2\pi TD_s$ would be reduced almost to 50%. The right panel presents the diffusion coefficient as a function of temperature, which is estimated by a state-of-the-art Bayesian calibration on D-meson R_{AA} and v_2 in PbPb 5.02 TeV for different centrality classes. Figure 9-10 shows the projection for the radial distribution of D^0 mesons in Pb-Pb collisions divided by the distribution in pp collisions. With the precision achievable with the high-luminosity data, one would be able to measure precisely the effect of heavy-quark in-medium energy loss and the redistribution of the energy at large angle with respect to the jet axis. This is expected to provide new constraints on in-medium energy loss calculations. By comparing the quantity measured for D^0 with the one obtained for charged particles, it will be possible to assess the relevance of medium response phenomena, which can induce modification of the jet shape at large angles and are expected to be less relevant for heavy quarks due to their large masses.

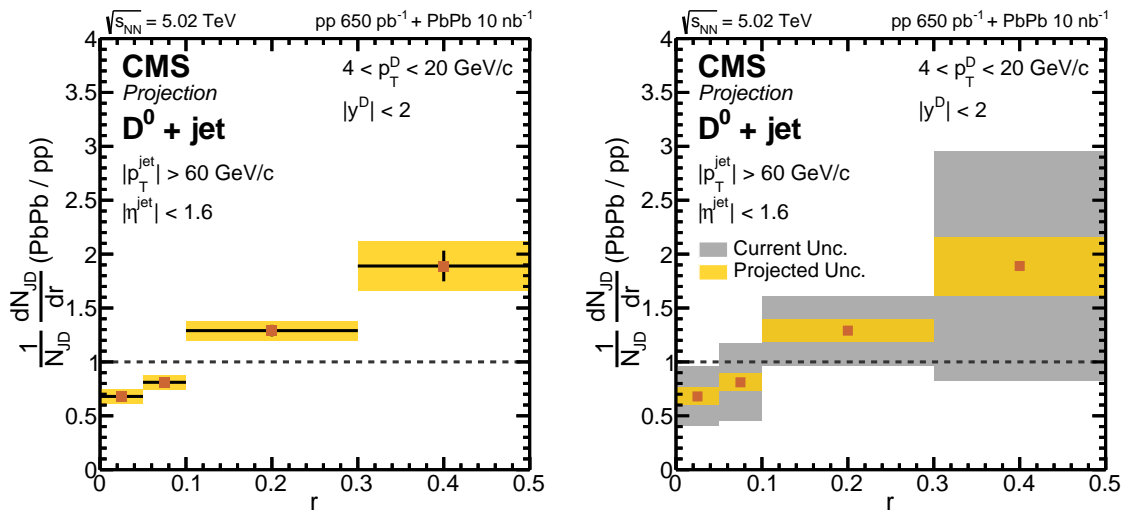


Figure 9-10: Projection for the radial distribution of D^0 mesons in jets as a function of the distance from the jet axis for jets of $p_T > 60 \text{ GeV}/c$ in Pb-Pb collisions divided by the distribution in pp collisions with integrated luminosity $\mathcal{L}_{\text{int}}^{\text{PbPb}} = 10 \text{ nb}^{-1}$ and $\mathcal{L}_{\text{int}}^{\text{pp}} = 650 \text{ pb}^{-1}$.

Bibliography

- [1] S. Bethke, “ α_s 2016”, *Nuclear and Particle Physics Proceedings*, vol. 282-284: (2017) pp. 149 , ISSN 2405-6014, DOI: [10.1016/j.nuclphysbps.2016.12.028](https://doi.org/10.1016/j.nuclphysbps.2016.12.028).
- [2] H. Caines, “The Search for Critical Behavior and Other Features of the QCD Phase Diagram Current Status and Future Prospects”, *Nuclear Physics A*, vol. 967: (2017) pp. 121 , ISSN 0375-9474, DOI: [10.1016/j.nuclphysa.2017.05.116](https://doi.org/10.1016/j.nuclphysa.2017.05.116).
- [3] D. Bailin *et al.*, “Superfluidity and superconductivity in relativistic fermion systems”, *Physics Reports*, vol. 107 (6): (1984) pp. 325 , ISSN 0370-1573, DOI: [10.1016/0370-1573\(84\)90145-5](https://doi.org/10.1016/0370-1573(84)90145-5).
- [4] M. Baldo; *et al.*, “Neutron stars and the transition to color superconducting quark matter”, *Physics Letters B*, vol. 562 (3): (2003) pp. 153 , ISSN 0370-2693, DOI: [10.1016/S0370-2693\(03\)00556-2](https://doi.org/10.1016/S0370-2693(03)00556-2).
- [5] K. G. Wilson, “Confinement of quarks”, *Phys. Rev. D*, vol. 10: (1974) pp. 2445, DOI: [10.1103/PhysRevD.10.2445](https://doi.org/10.1103/PhysRevD.10.2445).
- [6] HotQCD Collaboration, A. Bazavov; *et al.*, “Equation of state in (2 + 1)-flavor QCD”, *Phys. Rev. D*, vol. 90: (2014) p. 094503, DOI: [10.1103/PhysRevD.90.094503](https://doi.org/10.1103/PhysRevD.90.094503).
- [7] E. Follana; *et al.*, “Highly improved staggered quarks on the lattice with applications to charm physics”, *Phys. Rev. D*, vol. 75: (2007) p. 054502, DOI: [10.1103/PhysRevD.75.054502](https://doi.org/10.1103/PhysRevD.75.054502).
- [8] M. H. Thoma, “Strongly coupled plasmas in high-energy physics”, *IEEE Transactions on Plasma Science*, vol. 32 (2): (2004) pp. 738, ISSN 0093-3813, DOI: [10.1109/TPS.2004.826106](https://doi.org/10.1109/TPS.2004.826106).

- [9] V. G. Bornyakov; *et al.*, “New approach to canonical partition functions computation in $N_f = 2$ lattice QCD at finite baryon density”, *Phys. Rev. D*, vol. 95: (2017) p. 094506, DOI: [10.1103/PhysRevD.95.094506](https://doi.org/10.1103/PhysRevD.95.094506).
- [10] P. Sorensen, “Elliptic Flow: A Study of Space-Momentum Correlations In Relativistic Nuclear Collisions”, *Quark-gluon plasma 4* (R. C. Hwa *et al.*, eds.), pp. 323–374 (2010), DOI: [10.1142/9789814293297_0006](https://doi.org/10.1142/9789814293297_0006), arXiv:[0905.0174](https://arxiv.org/abs/0905.0174).
- [11] M. L. Miller; *et al.*, “Glauber Modeling in High-Energy Nuclear Collisions”, *Annual Review of Nuclear and Particle Science*, vol. 57 (1): (2007) pp. 205, DOI: [10.1146/annurev.nucl.57.090506.123020](https://doi.org/10.1146/annurev.nucl.57.090506.123020).
- [12] ATLAS Collaboration, “Measurement of Z Boson Production in Pb-Pb Collisions at $\sqrt{s_{NN}}=2.76$ TeV with the ATLAS Detector”, *Phys. Rev. Lett.*, vol. 110: (2013) p. 022301, DOI: [10.1103/PhysRevLett.110.022301](https://doi.org/10.1103/PhysRevLett.110.022301).
- [13] ATLAS Collaboration, “Measurement of the production and lepton charge asymmetry of W bosons in Pb+Pb collisions at $\sqrt{s_{NN}} = 2.76$ TeV with the ATLAS detector”, *The European Physical Journal C*, vol. 75 (1): (2015) p. 23, ISSN 1434-6052, DOI: [10.1140/epjc/s10052-014-3231-6](https://doi.org/10.1140/epjc/s10052-014-3231-6).
- [14] CMS Collaboration, “Study of Z Boson Production in PbPb Collisions at $\sqrt{s_{NN}} = 2.76$ TeV”, *Phys. Rev. Lett.*, vol. 106: (2011) p. 212301, DOI: [10.1103/PhysRevLett.106.212301](https://doi.org/10.1103/PhysRevLett.106.212301).
- [15] CMS Collaboration, “Study of W boson production in PbPb and pp collisions at $\sqrt{s_{NN}} = 2.76$ TeV”, *Physics Letters B*, vol. 715 (1): (2012) pp. 66 , ISSN 0370-2693, DOI: [10.1016/j.physletb.2012.07.025](https://doi.org/10.1016/j.physletb.2012.07.025).
- [16] CMS Collaboration, “Measurement of isolated photon production in pp and PbPb collisions at $\sqrt{s_{NN}} = 2.76$ TeV”, *Physics Letters B*, vol. 710 (2): (2012) pp. 256 , ISSN 0370-2693, DOI: [10.1016/j.physletb.2012.02.077](https://doi.org/10.1016/j.physletb.2012.02.077).
- [17] CMS Collaboration, “Dependence on pseudorapidity and on centrality of charged hadron production in PbPb collisions at $\sqrt{s_{NN}} = 2.76$ TeV”, *Journal of High Energy Physics*, vol. 2011 (8): (2011) p. 141, ISSN 1029-8479, DOI: [10.1007/JHEP08\(2011\)141](https://doi.org/10.1007/JHEP08(2011)141).

- [18] ALICE Collaboration, “Centrality Dependence of the Charged-Particle Multiplicity Density at Midrapidity in Pb-Pb Collisions at $\sqrt{s_{NN}} = 2.76$ TeV”, *Phys. Rev. Lett.*, vol. 106: (2011) p. 032301, DOI: [10.1103/PhysRevLett.106.032301](https://doi.org/10.1103/PhysRevLett.106.032301).
- [19] ALICE Collaboration, “Centrality and pseudorapidity dependence of the charged-particle multiplicity density in Xe-Xe collisions at $\sqrt{s_{NN}} = 5.44$ TeV”, *Physics Letters B*, vol. 790: (2019) pp. 35 , ISSN 0370-2693, DOI: [10.1016/j.physletb.2018.12.048](https://doi.org/10.1016/j.physletb.2018.12.048).
- [20] ALICE Collaboration, “Centrality Dependence of the Charged-Particle Multiplicity Density at Midrapidity in Pb-Pb Collisions at $\sqrt{s_{NN}} = 5.02$ TeV”, *Phys. Rev. Lett.*, vol. 116: (2016) p. 222302, DOI: [10.1103/PhysRevLett.116.222302](https://doi.org/10.1103/PhysRevLett.116.222302).
- [21] B. e. a. Alver, “Charged-particle multiplicity and pseudorapidity distributions measured with the PHOBOS detector in Au + Au, Cu + Cu, d + Au, and p + p collisions at ultrarelativistic energies”, *Phys. Rev. C*, vol. 83: (2011) p. 024913, DOI: [10.1103/PhysRevC.83.024913](https://doi.org/10.1103/PhysRevC.83.024913).
- [22] BRAHMS Collaboration, “Rapidity and centrality dependence of particle production for identified hadrons in Cu+Cu collisions at $\sqrt{s_{NN}} = 200$ GeV”, (2016), [arXiv:1602.01183](https://arxiv.org/abs/1602.01183).
- [23] CMS Collaboration, “Measurement of the Pseudorapidity and Centrality Dependence of the Transverse Energy Density in Pb-Pb Collisions at $\sqrt{s_{NN}} = 2.76$ TeV”, *Phys. Rev. Lett.*, vol. 109: (2012) p. 152303, DOI: [10.1103/PhysRevLett.109.152303](https://doi.org/10.1103/PhysRevLett.109.152303).
- [24] CMS Collaboration, “Azimuthal anisotropy of charged particles with transverse momentum up to 100 GeV/c in PbPb collisions at $\sqrt{s_{NN}} = 5.02$ TeV”, *Physics Letters B*, vol. 776: (2018) pp. 195 , ISSN 0370-2693, DOI: [10.1016/j.physletb.2017.11.041](https://doi.org/10.1016/j.physletb.2017.11.041).
- [25] J. Xu; *et al.*, “Bridging soft-hard transport properties of quark-gluon plasmas with CUJET3.0”, *Journal of High Energy Physics*, vol. 2016 (2): (2016) p. 169, ISSN 1029-8479, DOI: [10.1007/JHEP02\(2016\)169](https://doi.org/10.1007/JHEP02(2016)169).

- [26] J. Noronha-Hostler; *et al.*, “Cumulants and nonlinear response of high p_T harmonic flow at $\sqrt{s_{NN}} = 5.02$ TeV”, *Phys. Rev. C*, vol. 95: (2017) p. 044901, DOI: [10.1103/PhysRevC.95.044901](https://doi.org/10.1103/PhysRevC.95.044901).
- [27] H. Song; *et al.*, “Elliptic flow in $\sqrt{s} = 200$ GeV Au+Au collisions and $\sqrt{s} = 2.76$ TeV Pb+Pb collisions: Insights from viscous hydrodynamics+hadron cascade hybrid model”, *Phys. Rev. C*, vol. 83: (2011) p. 054912, DOI: [10.1103/PhysRevC.83.054912](https://doi.org/10.1103/PhysRevC.83.054912).
- [28] P. K. Kovtun; *et al.*, “Viscosity in Strongly Interacting Quantum Field Theories from Black Hole Physics”, *Phys. Rev. Lett.*, vol. 94: (2005) p. 111601, DOI: [10.1103/PhysRevLett.94.111601](https://doi.org/10.1103/PhysRevLett.94.111601).
- [29] STAR Collaboration, “Centrality dependence of charged hadron and strange hadron elliptic flow from $\sqrt{s_{NN}} = 200$ GeV Au+Au collisions”, *Phys. Rev. C*, vol. 77: (2008) p. 054901, DOI: [10.1103/PhysRevC.77.054901](https://doi.org/10.1103/PhysRevC.77.054901).
- [30] ALICE Collaboration, “Elliptic Flow of Charged Particles in Pb-Pb Collisions at $\sqrt{s_{NN}} = 2.76$ TeV”, *Phys. Rev. Lett.*, vol. 105: (2010) p. 252302, DOI: [10.1103/PhysRevLett.105.252302](https://doi.org/10.1103/PhysRevLett.105.252302).
- [31] H. Song; *et al.*, “Viscous QCD matter in a hybrid hydrodynamic+Boltzmann approach”, *Phys. Rev. C*, vol. 83: (2011) p. 024912, DOI: [10.1103/PhysRevC.83.024912](https://doi.org/10.1103/PhysRevC.83.024912).
- [32] H.-J. Drescher *et al.*, “Eccentricity fluctuations from the color glass condensate in ultrarelativistic heavy ion collisions”, *Phys. Rev. C*, vol. 76: (2007) p. 041903, DOI: [10.1103/PhysRevC.76.041903](https://doi.org/10.1103/PhysRevC.76.041903).
- [33] T. Hirano *et al.*, “Eccentricity fluctuation effects on elliptic flow in relativistic heavy ion collisions”, *Phys. Rev. C*, vol. 79: (2009) p. 064904, DOI: [10.1103/PhysRevC.79.064904](https://doi.org/10.1103/PhysRevC.79.064904).
- [34] CMS Collaboration, “Charged-particle nuclear modification factors in PbPb and pPb collisions at $\sqrt{s_{NN}} = 5.02$ TeV”, *Journal of High Energy Physics*, vol. 2017 (4): (2017) p. 39, ISSN 1029-8479, DOI: [10.1007/JHEP04\(2017\)039](https://doi.org/10.1007/JHEP04(2017)039).
- [35] “Nuclear effects on the transverse momentum spectra of charged particles in pPb collisions at $\sqrt{s_{NN}} = 5.02$ TeV”, *The European Physical Journal*

nal C, vol. 75 (5): (2015) p. 237, ISSN 1434-6052, DOI: [10.1140/epjc/s10052-015-3435-4](https://doi.org/10.1140/epjc/s10052-015-3435-4).

- [36] CMS Collaboration, “Study of high-pT charged particle suppression in PbPb compared to pp collisions at $\sqrt{s_{\text{NN}}} = 2.76 \text{ TeV}$ ”, *The European Physical Journal C*, vol. 72 (3): (2012) p. 1945, ISSN 1434-6052, DOI: [10.1140/epjc/s10052-012-1945-x](https://doi.org/10.1140/epjc/s10052-012-1945-x).
- [37] CMS Collaboration, “Charged-particle nuclear modification factors in XeXe collisions at $\sqrt{s_{\text{NN}}} = 5.44 \text{ TeV}$ ”, *Journal of High Energy Physics*, vol. 2018 (10): (2018) p. 138, DOI: [10.1007/JHEP10\(2018\)138](https://doi.org/10.1007/JHEP10(2018)138).
- [38] I. Arsene; *et al.*, “Quark-gluon plasma and color glass condensate at RHIC? The perspective from the BRAHMS experiment”, *Nuclear Physics A*, vol. 757 (1): (2005) pp. 1 , ISSN 0375-9474, DOI: [10.1016/j.nuclphysa.2005.02.130](https://doi.org/10.1016/j.nuclphysa.2005.02.130).
- [39] B. Back; *et al.*, “The PHOBOS perspective on discoveries at RHIC”, *Nuclear Physics A*, vol. 757 (1): (2005) pp. 28 , ISSN 0375-9474, DOI: [10.1016/j.nuclphysa.2005.03.084](https://doi.org/10.1016/j.nuclphysa.2005.03.084).
- [40] STAR Collaboration, “Experimental and theoretical challenges in the search for the quark-gluon plasma: The STAR Collaboration’s critical assessment of the evidence from RHIC collisions”, *Nuclear Physics A*, vol. 757 (1): (2005) pp. 102 , ISSN 0375-9474, DOI: [10.1016/j.nuclphysa.2005.03.085](https://doi.org/10.1016/j.nuclphysa.2005.03.085).
- [41] PHENIX Collaboration, “Formation of dense partonic matter in relativistic nucleus-nucleus collisions at RHIC: Experimental evaluation by the PHENIX Collaboration”, *Nuclear Physics A*, vol. 757 (1): (2005) pp. 184 , ISSN 0375-9474, DOI: [10.1016/j.nuclphysa.2005.03.086](https://doi.org/10.1016/j.nuclphysa.2005.03.086).
- [42] ALICE Collaboration, “Centrality dependence of charged particle production at large transverse momentum in Pb-Pb collisions at $\sqrt{s_{\text{NN}}} = 2.76 \text{ TeV}$ ”, *Physics Letters B*, vol. 720 (1): (2013) pp. 52 , ISSN 0370-2693, DOI: [10.1016/j.physletb.2013.01.051](https://doi.org/10.1016/j.physletb.2013.01.051).
- [43] ALICE Collaboration, “Transverse momentum spectra and nuclear modification factors of charged particles in pp, p-Pb and Pb-Pb collisions at the LHC”, *Journal of High Energy Physics*, vol. 2018 (11): (2018) p. 13, ISSN 1029-8479, DOI: [10.1007/JHEP11\(2018\)013](https://doi.org/10.1007/JHEP11(2018)013).

- [44] ATLAS Collaboration, “Measurement of charged-particle spectra in Pb+Pb collisions at $\sqrt{s_{NN}} = 2.76$ TeV with the ATLAS detector at the LHC”, *Journal of High Energy Physics*, vol. 2015 (9): (2015) p. 50, DOI: [10.1007/JHEP09\(2015\)050](https://doi.org/10.1007/JHEP09(2015)050).
- [45] CMS Collaboration, “Observation and studies of jet quenching in PbPb collisions at $\sqrt{s_{NN}} = 2.76$ TeV”, *Phys. Rev. C*, vol. 84: (2011) p. 024906, DOI: [10.1103/PhysRevC.84.024906](https://doi.org/10.1103/PhysRevC.84.024906).
- [46] CMS Collaboration, “Study of jet quenching with isolated-photon+jet correlations in PbPb and pp collisions at $\sqrt{s_{NN}} = 5.02$ TeV”, *Physics Letters B*, vol. 785: (2018) pp. 14 , ISSN 0370-2693, DOI: [10.1016/j.physletb.2018.07.061](https://doi.org/10.1016/j.physletb.2018.07.061).
- [47] K. J. Eskola; *et al.*, “EPPS16: nuclear parton distributions with LHC data”, *The European Physical Journal C*, vol. 77 (3): (2017) p. 163, ISSN 1434-6052, DOI: [10.1140/epjc/s10052-017-4725-9](https://doi.org/10.1140/epjc/s10052-017-4725-9).
- [48] N. Armesto, “Nuclear shadowing”, *Journal of Physics G: Nuclear and Particle Physics*, vol. 32 (11): (2006) pp. R367, DOI: [10.1088/0954-3899/32/11/r01](https://doi.org/10.1088/0954-3899/32/11/r01).
- [49] M. Cacciari; *et al.*, “The pT spectrum in heavy-flavour hadroproduction”, *Journal of High Energy Physics*, vol. 1998 (05): (1998) pp. 007, DOI: [10.1088/1126-6708/1998/05/007](https://doi.org/10.1088/1126-6708/1998/05/007).
- [50] M. Cacciari; *et al.*, “Theoretical predictions for charm and bottom production at the LHC”, *Journal of High Energy Physics*, vol. 2012 (10): (2012) p. 137, ISSN 1029-8479, DOI: [10.1007/JHEP10\(2012\)137](https://doi.org/10.1007/JHEP10(2012)137).
- [51] B. A. Kniehl; *et al.*, “Inclusive $D^{*\pm}$ production in $p\bar{p}$ collisions with massive charm quarks”, *Phys. Rev. D*, vol. 71: (2005) p. 014018, DOI: [10.1103/PhysRevD.71.014018](https://doi.org/10.1103/PhysRevD.71.014018).
- [52] B. A. Kniehl; *et al.*, “Collinear subtractions in hadroproduction of heavy quarks”, *The European Physical Journal C - Particles and Fields*, vol. 41 (2): (2005) pp. 199, ISSN 1434-6052, DOI: [10.1140/epjc/s2005-02200-7](https://doi.org/10.1140/epjc/s2005-02200-7).
- [53] B. A. Kniehl; *et al.*, “Inclusive charmed-meson production at the CERN LHC”, *The European Physical Journal C*, vol. 72 (7): (2012) p. 2082, ISSN 1434-6052, DOI: [10.1140/epjc/s10052-012-2082-2](https://doi.org/10.1140/epjc/s10052-012-2082-2).

- [54] R. Rapp *et al.*, “Heavy Quarks in the Quark-Gluon Plasma”, *Quark-Gluon Plasma 4*, pp. 111–206, DOI: [10.1142/9789814293297_0003](https://doi.org/10.1142/9789814293297_0003), arXiv:0903.1096.
- [55] B. Svetitsky, “Diffusion of charmed quarks in the quark-gluon plasma”, *Phys. Rev. D*, vol. 37: (1988) pp. 2484, DOI: [10.1103/PhysRevD.37.2484](https://doi.org/10.1103/PhysRevD.37.2484).
- [56] W. M. Alberico; *et al.*, “Heavy-flavour spectra in high-energy nucleus–nucleus collisions”, *The European Physical Journal C*, vol. 71 (6): (2011) p. 1666, ISSN 1434-6052, DOI: [10.1140/epjc/s10052-011-1666-6](https://doi.org/10.1140/epjc/s10052-011-1666-6).
- [57] M. Nahrgang; *et al.*, “Azimuthal correlations of heavy quarks in Pb + Pb collisions at $\sqrt{s} = 2.76$ TeV at the CERN Large Hadron Collider”, *Phys. Rev. C*, vol. 90: (2014) p. 024907, DOI: [10.1103/PhysRevC.90.024907](https://doi.org/10.1103/PhysRevC.90.024907).
- [58] P. B. Gossiaux; *et al.*, “Tomography of quark gluon plasma at energies available at the BNL Relativistic Heavy Ion Collider (RHIC) and the CERN Large Hadron Collider (LHC)”, *Phys. Rev. C*, vol. 79: (2009) p. 044906, DOI: [10.1103/PhysRevC.79.044906](https://doi.org/10.1103/PhysRevC.79.044906).
- [59] J. Aichelin; *et al.*, “Gluon radiation by heavy quarks at intermediate energies”, *Phys. Rev. D*, vol. 89: (2014) p. 074018, DOI: [10.1103/PhysRevD.89.074018](https://doi.org/10.1103/PhysRevD.89.074018).
- [60] J. Uphoff; *et al.*, “Open heavy flavor in Pb + Pb collisions at $s=2.76\text{TeV}$ within a transport model”, *Physics Letters B*, vol. 717 (4): (2012) pp. 430 , ISSN 0370-2693, DOI: [10.1016/j.physletb.2012.09.069](https://doi.org/10.1016/j.physletb.2012.09.069).
- [61] J. Uphoff; *et al.*, “Elliptic flow and energy loss of heavy quarks in ultrarelativistic heavy ion collisions”, *Phys. Rev. C*, vol. 84: (2011) p. 024908, DOI: [10.1103/PhysRevC.84.024908](https://doi.org/10.1103/PhysRevC.84.024908).
- [62] E. Bratkovskaya; *et al.*, “Parton–Hadron-String Dynamics at relativistic collider energies”, *Nuclear Physics A*, vol. 856 (1): (2011) pp. 162 , ISSN 0375-9474, DOI: [10.1016/j.nuclphysa.2011.03.003](https://doi.org/10.1016/j.nuclphysa.2011.03.003).
- [63] T. Song; *et al.*, “Tomography of the quark-gluon plasma by charm quarks”, *Phys. Rev. C*, vol. 92: (2015) p. 014910, DOI: [10.1103/PhysRevC.92.014910](https://doi.org/10.1103/PhysRevC.92.014910).

- [64] T. Song; *et al.*, “Charm production in Pb + Pb collisions at energies available at the CERN Large Hadron Collider”, *Phys. Rev. C*, vol. 93: (2016) p. 034906, DOI: [10.1103/PhysRevC.93.034906](https://doi.org/10.1103/PhysRevC.93.034906).
- [65] F. Scardina; *et al.*, “Estimating the charm quark diffusion coefficient and thermalization time from D meson spectra at energies available at the BNL Relativistic Heavy Ion Collider and the CERN Large Hadron Collider”, *Phys. Rev. C*, vol. 96: (2017) p. 044905, DOI: [10.1103/PhysRevC.96.044905](https://doi.org/10.1103/PhysRevC.96.044905).
- [66] L. Ravagli *et al.*, “Quark coalescence based on a transport equation”, *Physics Letters B*, vol. 655 (3): (2007) pp. 126 , ISSN 0370-2693, DOI: [10.1016/j.physletb.2007.07.043](https://doi.org/10.1016/j.physletb.2007.07.043).
- [67] F. Riek *et al.*, “Quarkonia and heavy-quark relaxation times in the quark-gluon plasma”, *Phys. Rev. C*, vol. 82: (2010) p. 035201, DOI: [10.1103/PhysRevC.82.035201](https://doi.org/10.1103/PhysRevC.82.035201).
- [68] T. Lang; *et al.*, “Heavy quark transport in heavy ion collisions at energies available at the BNL Relativistic Heavy Ion Collider and at the CERN Large Hadron Collider within the UrQMD hybrid model”, *Phys. Rev. C*, vol. 93: (2016) p. 014901, DOI: [10.1103/PhysRevC.93.014901](https://doi.org/10.1103/PhysRevC.93.014901).
- [69] H. van Hees *et al.*, “Thermalization of heavy quarks in the quark-gluon plasma”, *Phys. Rev. C*, vol. 71: (2005) p. 034907, DOI: [10.1103/PhysRevC.71.034907](https://doi.org/10.1103/PhysRevC.71.034907).
- [70] J. Casalderrey-Solana *et al.*, “Heavy quark diffusion in strongly coupled $\mathcal{N} = 4$ Yang-Mills theory”, *Phys. Rev. D*, vol. 74: (2006) p. 085012, DOI: [10.1103/PhysRevD.74.085012](https://doi.org/10.1103/PhysRevD.74.085012).
- [71] Y. Dokshitzer *et al.*, “Heavy-quark colorimetry of QCD matter”, *Physics Letters B*, vol. 519 (3): (2001) pp. 199 , ISSN 0370-2693, DOI: [10.1016/S0370-2693\(01\)01130-3](https://doi.org/10.1016/S0370-2693(01)01130-3).
- [72] S. S. Gubser, “Drag force in AdS/CFT”, *Phys. Rev. D*, vol. 74: (2006) p. 126005, DOI: [10.1103/PhysRevD.74.126005](https://doi.org/10.1103/PhysRevD.74.126005).
- [73] V. Greco; *et al.*, “Parton Coalescence and the Antiproton/Pion Anomaly at RHIC”, *Phys. Rev. Lett.*, vol. 90: (2003) p. 202302, DOI: [10.1103/PhysRevLett.90.202302](https://doi.org/10.1103/PhysRevLett.90.202302).

- [74] PHENIX Collaboration, K. Adcox; *et al.*, “Measurement of Single Electrons and Implications for Charm Production in $Au + Au$ Collisions at $\sqrt{s_{NN}} = 130\text{GeV}$ ”, *Phys. Rev. Lett.*, vol. 88: (2002) p. 192303, DOI: [10.1103/PhysRevLett.88.192303](https://doi.org/10.1103/PhysRevLett.88.192303).
- [75] ALICE Collaboration, “Measurement of electrons from semileptonic heavy-flavor hadron decays in pp collisions at $\sqrt{s}=7\text{ TeV}$ ”, *Phys. Rev. D*, vol. 86: (2012) p. 112007, DOI: [10.1103/PhysRevD.86.112007](https://doi.org/10.1103/PhysRevD.86.112007).
- [76] ATLAS Collaboration, “Measurements of the electron and muon inclusive cross-sections in proton-proton collisions at $\sqrt{s} = 7\text{ TeV}$ with the ATLAS detector”, *Physics Letters B*, vol. 707 (5): (2012) pp. 438 , ISSN 0370-2693, DOI: [10.1016/j.physletb.2011.12.054](https://doi.org/10.1016/j.physletb.2011.12.054).
- [77] ALICE Collaboration, “Measurement of the production of high-pT electrons from heavy-flavour hadron decays in $Pb-Pb$ collisions at $\sqrt{s_{NN}} = 2.76\text{ TeV}$ ”, *Physics Letters B*, vol. 771: (2017) pp. 467 , ISSN 0370-2693, DOI: [10.1016/j.physletb.2017.05.060](https://doi.org/10.1016/j.physletb.2017.05.060).
- [78] “Multiple scattering effects on heavy meson production in $p+A$ collisions at backward rapidity”, *Physics Letters B*, vol. 740: (2015) pp. 23 , ISSN 0370-2693, DOI: [10.1016/j.physletb.2014.11.024](https://doi.org/10.1016/j.physletb.2014.11.024).
- [79] R. Sharma; *et al.*, “Light-cone wave function approach to open heavy flavor dynamics in QCD matter”, *Phys. Rev. C*, vol. 80: (2009) p. 054902, DOI: [10.1103/PhysRevC.80.054902](https://doi.org/10.1103/PhysRevC.80.054902).
- [80] A. M. Sickles, “Possible evidence for radial flow of heavy mesons in $d+Au$ collisions”, *Physics Letters B*, vol. 731: (2014) pp. 51 , ISSN 0370-2693, DOI: [10.1016/j.physletb.2014.02.013](https://doi.org/10.1016/j.physletb.2014.02.013).
- [81] K. Eskola; *et al.*, “EPS09 — A new generation of NLO and LO nuclear parton distribution functions”, *Journal of High Energy Physics*, vol. 2009 (04): (2009) pp. 065, DOI: [10.1088/1126-6708/2009/04/065](https://doi.org/10.1088/1126-6708/2009/04/065).
- [82] PHENIX Collaboration, A. Adare; *et al.*, “Energy Loss and Flow of Heavy Quarks in $Au + Au$ Collisions at $\sqrt{s_{NN}} = 200\text{ GeV}$ ”, *Phys. Rev. Lett.*, vol. 98: (2007) p. 172301, DOI: [10.1103/PhysRevLett.98.172301](https://doi.org/10.1103/PhysRevLett.98.172301).

- [83] PHENIX Collaboration, A. Adare; *et al.*, “Heavy-quark production in $p + p$ and energy loss and flow of heavy quarks in Au + Au collisions at $\sqrt{s_{NN}} = 200$ GeV”, *Phys. Rev. C*, vol. 84: (2011) p. 044905, DOI: [10.1103/PhysRevC.84.044905](https://doi.org/10.1103/PhysRevC.84.044905).
- [84] PHENIX Collaboration, A. Adare; *et al.*, “Nuclear-modification factor for open-heavy-flavor production at forward rapidity in Cu+Cu collisions at $\sqrt{s_{NN}} = 200$ GeV”, *Phys. Rev. C*, vol. 86: (2012) p. 024909, DOI: [10.1103/PhysRevC.86.024909](https://doi.org/10.1103/PhysRevC.86.024909).
- [85] STAR Collaboration, B. I. Abelev; *et al.*, “Transverse Momentum and Centrality Dependence of High- p_T Nonphotonic Electron Suppression in Au + Au Collisions at $\sqrt{s_{NN}} = 200$ GeV”, *Phys. Rev. Lett.*, vol. 98: (2007) p. 192301, DOI: [10.1103/PhysRevLett.98.192301](https://doi.org/10.1103/PhysRevLett.98.192301).
- [86] STAR Collaboration, A. Adare; *et al.*, “Heavy-quark production and elliptic flow in Au+Au collisions at $\sqrt{s_{NN}} = 62.4$ GeV”, (2014), [arXiv:1405.3301](https://arxiv.org/abs/1405.3301).
- [87] STAR Collaboration, L. Adamczyk; *et al.*, “Elliptic flow of electrons from heavy-flavor hadron decays in Au + Au collisions at $\sqrt{s_{NN}} = 200$, 62.4, and 39 GeV”, *Phys. Rev. C*, vol. 95: (2017) p. 034907, DOI: [10.1103/PhysRevC.95.034907](https://doi.org/10.1103/PhysRevC.95.034907).
- [88] ALICE Collaboration, “Measurements of low-pT electrons from semileptonic heavy-flavour hadron decays at mid-rapidity in pp and Pb-Pb collisions at $\sqrt{s_{NN}} = 2.76$ TeV”, *Journal of High Energy Physics*, vol. 2018 (10): (2018) p. 61, DOI: [10.1007/JHEP10\(2018\)061](https://doi.org/10.1007/JHEP10(2018)061).
- [89] ALICE Collaboration, “Measurement of electrons from beauty-hadron decays in p-Pb collisions at $\sqrt{s_{NN}} = 5.02$ TeV and Pb-Pb collisions at $\sqrt{s_{NN}} = 2.76$ TeV”, *Journal of High Energy Physics*, vol. 2017 (7): (2017) p. 52, ISSN 1029-8479, DOI: [10.1007/JHEP07\(2017\)052](https://doi.org/10.1007/JHEP07(2017)052).
- [90] ALICE Collaboration, “Elliptic flow of electrons from heavy-flavour hadron decays at mid-rapidity in Pb-Pb collisions at $\sqrt{s_{NN}} = 2.76$ TeV”, *Journal of High Energy Physics*, vol. 2016 (9): (2016) p. 28, ISSN 1029-8479, DOI: [10.1007/JHEP09\(2016\)028](https://doi.org/10.1007/JHEP09(2016)028).

- [91] ALICE Collaboration, “Production of Muons from Heavy Flavor Decays at Forward Rapidity in pp and Pb-Pb Collisions at $\sqrt{s_{NN}}=2.76$ TeV”, *Phys. Rev. Lett.*, vol. 109: (2012) p. 112301, DOI: [10.1103/PhysRevLett.109.112301](https://doi.org/10.1103/PhysRevLett.109.112301).
- [92] ALICE Collaboration, “Elliptic flow of muons from heavy-flavour hadron decays at forward rapidity in Pb-Pb collisions at $\sqrt{s_{NN}} = 2.76$ TeV”, *Physics Letters B*, vol. 753: (2016) pp. 41 , ISSN 0370-2693, DOI: [10.1016/j.physletb.2015.11.059](https://doi.org/10.1016/j.physletb.2015.11.059).
- [93] ALICE Collaboration, “Heavy-flavour decay electrons RAA in PbPb at 5.02 TeV”, (2019), accessed: 2019-04-10, URL: <http://alice-figure.web.cern.ch/node/10196>.
- [94] ALICE Collaboration, “Heavy-flavour hadron decay electron v2 in Pb-Pb collisions at 5.02 TeV”, (2019), accessed: 2019-04-10, URL: <http://alice-figure.web.cern.ch/node/11094>.
- [95] ALICE Collaboration, “Electrons from heavy-flavour hadron decays at mid-rapidity and low transverse momenta in Xe-Xe collisions at $\sqrt{s_{NN}} = 5.44$ TeV”, (2019), accessed: 2019-04-10, URL: <http://alice-figure.web.cern.ch/node/12971>.
- [96] ALICE Collaboration, “Production of heavy-flavour decay muons at forward rapidity in Xe-Xe collisions at $\sqrt{s_{NN}} = 5.44$ TeV with ALICE”, (2019), accessed: 2019-04-10, URL: <http://alice-figure.web.cern.ch/node/13561>.
- [97] ATLAS Collaboration, “Measurement of the suppression and azimuthal anisotropy of muons from heavy-flavor decays in Pb+Pb collisions at $\sqrt{s_{NN}} = 2.76$ TeV with the ATLAS detector”, *Phys. Rev. C*, vol. 98: (2018) p. 044905, DOI: [10.1103/PhysRevC.98.044905](https://doi.org/10.1103/PhysRevC.98.044905).
- [98] PHENIX Collaboration, A. Adare; *et al.*, “Cold-Nuclear-Matter Effects on Heavy-Quark Production at Forward and Backward Rapidity in $d + \text{Au}$ Collisions at $\sqrt{s_{NN}} = 200$ GeV”, *Phys. Rev. Lett.*, vol. 112: (2014) p. 252301, DOI: [10.1103/PhysRevLett.112.252301](https://doi.org/10.1103/PhysRevLett.112.252301).
- [99] ALICE Collaboration, “Measurement of electrons from heavy-flavour hadron decays in p-Pb collisions at $\sqrt{s_{NN}} = 5.02$ TeV”, *Physics Letters B*, vol. 754: (2016) pp. 81 , ISSN 0370-2693, DOI: [10.1016/j.physletb.2015.12.067](https://doi.org/10.1016/j.physletb.2015.12.067).

- [100] ALICE Collaboration, “Azimuthal Anisotropy of Heavy-Flavor Decay Electrons in p -Pb Collisions at $\sqrt{s_{NN}} = 5.02$ TeV”, *Phys. Rev. Lett.*, vol. 122: (2019) p. 072301, DOI: [10.1103/PhysRevLett.122.072301](https://doi.org/10.1103/PhysRevLett.122.072301).
- [101] ALICE Collaboration, “Production of muons from heavy-flavour hadron decays in p-Pb collisions at $\sqrt{s_{NN}} = 5.02$ TeV”, *Physics Letters B*, vol. 770: (2017) pp. 459 , ISSN 0370-2693, DOI: [10.1016/j.physletb.2017.03.049](https://doi.org/10.1016/j.physletb.2017.03.049).
- [102] CMS Collaboration, “The CMS experiment at the CERN LHC”, *Journal of Instrumentation*, vol. 3 (08): (2008) pp. S08004, DOI: [10.1088/1748-0221/3/08/s08004](https://doi.org/10.1088/1748-0221/3/08/s08004).
- [103] ATLAS Collaboration, “The ATLAS Experiment at the CERN Large Hadron Collider”, *Journal of Instrumentation*, vol. 3 (08): (2008) pp. S08003, DOI: [10.1088/1748-0221/3/08/s08003](https://doi.org/10.1088/1748-0221/3/08/s08003).
- [104] ALICE Collaboration, “The ALICE experiment at the CERN LHC”, *Journal of Instrumentation*, vol. 3 (08): (2008) pp. S08002, DOI: [10.1088/1748-0221/3/08/s08002](https://doi.org/10.1088/1748-0221/3/08/s08002).
- [105] LHCb Collaboration, “The LHCb Detector at the LHC”, *Journal of Instrumentation*, vol. 3 (08): (2008) pp. S08005, DOI: [10.1088/1748-0221/3/08/s08005](https://doi.org/10.1088/1748-0221/3/08/s08005).
- [106] CMS Collaboration, “CMS detector design”, (2011), accessed: 2019-04-10, URL: <http://cms.web.cern.ch/news/cms-detector-design>.
- [107] CMS Collaboration, “The CMS trigger system”, *Journal of Instrumentation*, vol. 12 (01): (2017) pp. P01020, DOI: [10.1088/1748-0221/12/01/p01020](https://doi.org/10.1088/1748-0221/12/01/p01020).
- [108] T. Sjöstrand; et al., “An introduction to PYTHIA 8.2”, *Computer Physics Communications*, vol. 191: (2015) pp. 159 , ISSN 0010-4655, DOI: [10.1016/j.cpc.2015.01.024](https://doi.org/10.1016/j.cpc.2015.01.024).
- [109] “Event generator tunes obtained from underlying event and multiparton scattering measurements”, *The European Physical Journal C*, vol. 76 (3): (2016) p. 155, ISSN 1434-6052, DOI: [10.1140/epjc/s10052-016-3988-x](https://doi.org/10.1140/epjc/s10052-016-3988-x).

- [110] CDF Collaboration, T. Aaltonen; *et al.*, “Study of the energy dependence of the underlying event in proton-antiproton collisions”, *Phys. Rev. D*, vol. 92: (2015) p. 092009, DOI: [10.1103/PhysRevD.92.092009](https://doi.org/10.1103/PhysRevD.92.092009).
- [111] “Measurement of the Underlying Event Activity at the LHC at 7 TeV and Comparison with 0.9 TeV”, *Tech. Rep. CMS-PAS-FSQ-12-020*, CERN, Geneva (2012), URL: <https://cds.cern.ch/record/1478982>.
- [112] D. J. Lange, “The EvtGen particle decay simulation package”, *Nuclear Instruments and Methods in Physics Research Section A: Accelerators, Spectrometers, Detectors and Associated Equipment*, vol. 462 (1): (2001) pp. 152 , ISSN 0168-9002, DOI: [10.1016/S0168-9002\(01\)00089-4](https://doi.org/10.1016/S0168-9002(01)00089-4).
- [113] E. Barberio; *et al.*, “Photos – a universal Monte Carlo for QED radiative corrections in decays”, *Computer Physics Communications*, vol. 66 (1): (1991) pp. 115 , ISSN 0010-4655, DOI: [10.1016/0010-4655\(91\)90012-A](https://doi.org/10.1016/0010-4655(91)90012-A).
- [114] S. Agostinelli; *et al.*, “Geant4—a simulation toolkit”, *Nuclear Instruments and Methods in Physics Research Section A: Accelerators, Spectrometers, Detectors and Associated Equipment*, vol. 506 (3): (2003) pp. 250 , ISSN 0168-9002, DOI: [10.1016/S0168-9002\(03\)01368-8](https://doi.org/10.1016/S0168-9002(03)01368-8).
- [115] I. P. Lokhtin *et al.*, “A model of jet quenching in ultrarelativistic heavy ion collisions and high- pT hadron spectra at RHIC”, *The European Physical Journal C - Particles and Fields*, vol. 45 (1): (2006) pp. 211, ISSN 1434-6052, DOI: [10.1140/epjc/s2005-02426-3](https://doi.org/10.1140/epjc/s2005-02426-3).
- [116] “Description and performance of track and primary-vertex reconstruction with the CMS tracker”, *JINST*, vol. 9 (10): (2014) p. P10009, DOI: [10.1088/1748-0221/9/10/P10009](https://doi.org/10.1088/1748-0221/9/10/P10009), arXiv:[1405.6569](https://arxiv.org/abs/1405.6569).
- [117] M. Swartz, “CMS pixel simulations”, *Nuclear Instruments and Methods in Physics Research Section A: Accelerators, Spectrometers, Detectors and Associated Equipment*, vol. 511 (1): (2003) pp. 88 , ISSN 0168-9002, DOI: [10.1016/S0168-9002\(03\)01757-1](https://doi.org/10.1016/S0168-9002(03)01757-1).
- [118] M. Swartz; *et al.*, “Observation, modeling, and temperature dependence of doubly peaked electric fields in irradiated silicon pixel sensors”, *Nuclear Instruments and Methods in Physics Research Section A: Accelerators, Spectrometers, Detectors and Associated Equipment*, vol. 511 (1): (2003) pp. 88 , ISSN 0168-9002, DOI: [10.1016/S0168-9002\(03\)01757-1](https://doi.org/10.1016/S0168-9002(03)01757-1).

ments and Methods in Physics Research Section A: Accelerators, Spectrometers, Detectors and Associated Equipment, vol. 565 (1): (2006) pp. 212 , ISSN 0168-9002, DOI: [10.1016/j.nima.2006.05.002](https://doi.org/10.1016/j.nima.2006.05.002).

- [119] P. Billoir, “Progressive track recognition with a Kalman-like fitting procedure”, *Computer Physics Communications*, vol. 57 (1): (1989) pp. 390 , ISSN 0010-4655, DOI: [https://doi.org/10.1016/0010-4655\(89\)90249-X](https://doi.org/10.1016/0010-4655(89)90249-X).
- [120] P. Billoir *et al.*, “Simultaneous pattern recognition and track fitting by the Kalman filtering method”, *Nuclear Instruments and Methods in Physics Research Section A: Accelerators, Spectrometers, Detectors and Associated Equipment*, vol. 294 (1): (1990) pp. 219 , ISSN 0168-9002, DOI: [https://doi.org/10.1016/0168-9002\(90\)91835-Y](https://doi.org/10.1016/0168-9002(90)91835-Y).
- [121] R. Mankel, “A concurrent track evolution algorithm for pattern recognition in the HERA-B main tracking system”, *Nuclear Instruments and Methods in Physics Research Section A: Accelerators, Spectrometers, Detectors and Associated Equipment*, vol. 395 (2): (1997) pp. 169 , ISSN 0168-9002, DOI: [https://doi.org/10.1016/S0168-9002\(97\)00705-5](https://doi.org/10.1016/S0168-9002(97)00705-5).
- [122] R. FrĂČĂŠhwirth, “Application of Kalman filtering to track and vertex fitting”, *Nuclear Instruments and Methods in Physics Research Section A: Accelerators, Spectrometers, Detectors and Associated Equipment*, vol. 262 (2): (1987) pp. 444 , ISSN 0168-9002, DOI: [https://doi.org/10.1016/0168-9002\(87\)90887-4](https://doi.org/10.1016/0168-9002(87)90887-4).
- [123] M. Cacciari; *et al.*, “FastJet user manual”, *The European Physical Journal C*, vol. 72 (3): (2012) p. 1896, ISSN 1434-6052, DOI: [10.1140/epjc/s10052-012-1896-2](https://doi.org/10.1140/epjc/s10052-012-1896-2).
- [124] “Particle-Flow Event Reconstruction in CMS and Performance for Jets, Taus, and MET”, *Tech. Rep. CMS-PAS-PFT-09-001*, CERN, Geneva (2009), URL: <https://cds.cern.ch/record/1194487>.
- [125] “Commissioning of the Particle-Flow reconstruction in Minimum-Bias and Jet Events from pp Collisions at 7 TeV”, *Tech. Rep. CMS-PAS-PFT-10-002*, CERN, Geneva (2010), URL: <http://cds.cern.ch/record/1279341>.

- [126] M. Cacciari; *et al.*, “The catchment area of jets”, *Journal of High Energy Physics*, vol. 2008 (04): (2008) pp. 005, DOI: [10.1088/1126-6708/2008/04/005](https://doi.org/10.1088/1126-6708/2008/04/005).
- [127] O. Kodolova; *et al.*, “The performance of the jet identification and reconstruction in heavy ions collisions with CMS detector”, *The European Physical Journal C*, vol. 50 (1): (2007) pp. 117, ISSN 1434-6052, DOI: [10.1140/epjc/s10052-007-0223-9](https://doi.org/10.1140/epjc/s10052-007-0223-9).
- [128] Particle Data Group, M. Tanabashi; *et al.*, “Review of Particle Physics”, *Phys. Rev. D*, vol. 98: (2018) p. 030001, DOI: [10.1103/PhysRevD.98.030001](https://doi.org/10.1103/PhysRevD.98.030001).
- [129] M. Lisovyi; *et al.*, “Combined analysis of charm-quark fragmentation-fraction measurements”, *The European Physical Journal C*, vol. 76 (7): (2016) p. 397, ISSN 1434-6052, DOI: [10.1140/epjc/s10052-016-4246-y](https://doi.org/10.1140/epjc/s10052-016-4246-y).
- [130] H. Voss; *et al.*, “TMVA, the Toolkit for Multivariate Data Analysis with ROOT”, *XIth International Workshop on Advanced Computing and Analysis Techniques in Physics Research (ACAT)* (2007) p. 40, [arXiv:physics/0703039](https://arxiv.org/abs/physics/0703039).
- [131] CMS Collaboration, “Nuclear modification factor of D0 mesons in PbPb collisions at $\sqrt{s_{\text{NN}}} = 5.02 \text{ TeV}$ ”, *Physics Letters B*, vol. 782: (2018) pp. 474 , ISSN 0370-2693, DOI: [10.1016/j.physletb.2018.05.074](https://doi.org/10.1016/j.physletb.2018.05.074).
- [132] CMS Collaboration, “Suppression and azimuthal anisotropy of prompt and nonprompt J/ψ production in PbPb collisions at $\sqrt{s_{\text{NN}}} = 2.76 \text{ TeV}$ ”, *The European Physical Journal C*, vol. 77 (4): (2017) p. 252, DOI: [10.1140/epjc/s10052-017-4781-1](https://doi.org/10.1140/epjc/s10052-017-4781-1).
- [133] M. L. Miller; *et al.*, “Glauber modeling in high energy nuclear collisions”, *Ann. Rev. Nucl. Part. Sci.*, vol. 57: (2007) p. 205, DOI: [10.1146/annurev.nucl.57.090506.123020](https://doi.org/10.1146/annurev.nucl.57.090506.123020), [arXiv:nucl-ex/0701025](https://arxiv.org/abs/nucl-ex/0701025).
- [134] M. Djordjevic *et al.*, “Predictions of heavy-flavor suppression at 5.1 TeV Pb+Pb collisions at the CERN Large Hadron Collider”, *Phys. Rev. C*, vol. 92: (2015) p. 024918, DOI: [10.1103/PhysRevC.92.024918](https://doi.org/10.1103/PhysRevC.92.024918), [arXiv:1505.04316](https://arxiv.org/abs/1505.04316).

- [135] J. Xu; *et al.*, “Bridging soft-hard transport properties of quark-gluon plasmas with CUJET3.0”, *JHEP*, vol. 02: (2016) p. 169, DOI: [10.1007/JHEP02\(2016\)169](https://doi.org/10.1007/JHEP02(2016)169), [arXiv:1508.00552](https://arxiv.org/abs/1508.00552).
- [136] J. Xu; *et al.*, “Azimuthal jet flavor tomography with CUJET2.0 of nuclear collisions at RHIC and LHC”, *JHEP*, vol. 08: (2014) p. 063, DOI: [10.1007/JHEP08\(2014\)063](https://doi.org/10.1007/JHEP08(2014)063), [arXiv:1402.2956](https://arxiv.org/abs/1402.2956).
- [137] J. Xu; *et al.*, “Consistency of Perfect Fluidity and Jet Quenching in Semi-Quark-Gluon Monopole Plasmas”, *Chin. Phys. Lett.*, vol. 32: (2015) p. 092501, DOI: [10.1088/0256-307X/32/9/092501](https://doi.org/10.1088/0256-307X/32/9/092501), [arXiv:1411.3673](https://arxiv.org/abs/1411.3673).
- [138] Z.-B. Kang; *et al.*, “Jet quenching phenomenology from soft-collinear effective theory with Glauber gluons”, *Phys. Rev. Lett.*, vol. 114: (2015) p. 092002, DOI: [10.1103/PhysRevLett.114.092002](https://doi.org/10.1103/PhysRevLett.114.092002), [arXiv:1405.2612](https://arxiv.org/abs/1405.2612).
- [139] Y.-T. Chien; *et al.*, “Jet quenching from QCD evolution”, *Phys. Rev. D*, vol. 93: (2016) p. 074030, DOI: [10.1103/PhysRevD.93.074030](https://doi.org/10.1103/PhysRevD.93.074030), [arXiv:1509.02936](https://arxiv.org/abs/1509.02936).
- [140] S. Cao; *et al.*, “Linearized Boltzmann transport model for jet propagation in the quark-gluon plasma: Heavy quark evolution”, *Phys. Rev. C*, vol. 94: (2016) p. 014909, DOI: [10.1103/PhysRevC.94.014909](https://doi.org/10.1103/PhysRevC.94.014909), [arXiv:1605.06447](https://arxiv.org/abs/1605.06447).
- [141] S. Cao; *et al.*, “Heavy and light flavor jet quenching at RHIC and LHC energies”, *Physics Letters B*, vol. 777: (2018) pp. 255 , ISSN 0370-2693, DOI: [10.1016/j.physletb.2017.12.023](https://doi.org/10.1016/j.physletb.2017.12.023).
- [142] T. Song; *et al.*, “Tomography of the quark-gluon-plasma by charm quarks”, *Phys. Rev. C*, vol. 92: (2015) p. 014910, DOI: [10.1103/PhysRevC.92.014910](https://doi.org/10.1103/PhysRevC.92.014910), [arXiv:1503.03039](https://arxiv.org/abs/1503.03039).
- [143] T. Song; *et al.*, “Charm production in Pb + Pb collisions at energies available at the CERN Large Hadron Collider”, *Phys. Rev. C*, vol. 93: (2016) p. 034906, DOI: [10.1103/PhysRevC.93.034906](https://doi.org/10.1103/PhysRevC.93.034906), [arXiv:1512.00891](https://arxiv.org/abs/1512.00891).
- [144] W. A. Horowitz, “Fluctuating heavy quark energy loss in a strongly coupled quark-gluon plasma”, *Phys. Rev. D*, vol. 91: (2015) p. 085019, DOI: [10.1103/PhysRevD.91.085019](https://doi.org/10.1103/PhysRevD.91.085019), [arXiv:1501.04693](https://arxiv.org/abs/1501.04693).

- [145] M. He; *et al.*, “Heavy flavor at the large hadron collider in a strong coupling approach”, *Phys. Lett. B*, vol. 735: (2014) p. 445, DOI: [10.1016/j.physletb.2014.05.050](https://doi.org/10.1016/j.physletb.2014.05.050), [arXiv:1401.3817](https://arxiv.org/abs/1401.3817).
- [146] M. Nahrgang; *et al.*, “Elliptic and triangular flow of heavy flavor in heavy-ion collisions”, *Phys. Rev. C*, vol. 91: (2015) p. 014904, DOI: [10.1103/PhysRevC.91.014904](https://doi.org/10.1103/PhysRevC.91.014904), [arXiv:1410.5396](https://arxiv.org/abs/1410.5396).
- [147] S. K. Das; *et al.*, “Toward a solution to the RAA and v2 puzzle for heavy quarks”, *Physics Letters B*, vol. 747: (2015) pp. 260 , ISSN 0370-2693, DOI: [10.1016/j.physletb.2015.06.003](https://doi.org/10.1016/j.physletb.2015.06.003).
- [148] A. Beraudo; *et al.*, “Heavy flavors in heavy-ion collisions: quenching, flow and correlations”, *The European Physical Journal C*, vol. 75 (3): (2015) p. 121, ISSN 1434-6052, DOI: [10.1140/epjc/s10052-015-3336-6](https://doi.org/10.1140/epjc/s10052-015-3336-6).
- [149] CMS Collaboration, “Measurement of the B^\pm Meson Nuclear Modification Factor in Pb-Pb Collisions at $\sqrt{s_{NN}} = 5.02$ TeV”, *Phys. Rev. Lett.*, vol. 119: (2017) p. 152301, DOI: [10.1103/PhysRevLett.119.152301](https://doi.org/10.1103/PhysRevLett.119.152301).
- [150] CMS Collaboration, “Measurement of prompt and nonprompt charmonium suppression in PbPb collisions at 5.02 TeV”, *The European Physical Journal C*, vol. 78 (6): (2018) p. 509, DOI: [10.1140/epjc/s10052-018-5950-6](https://doi.org/10.1140/epjc/s10052-018-5950-6).
- [151] CMS Collaboration, “Studies of beauty suppression via nonprompt D^0 mesons in PbPb collisions at $\sqrt{s_{NN}} = 5.02$ TeV”, (2018), [arXiv:1810.11102](https://arxiv.org/abs/1810.11102).
- [152] ALICE Collaboration, “Measurement of D^0 , D^+ , D_s^* and D_s^+ production in Pb-Pb collisions at $\sqrt{s_{NN}} = 5.02$ TeV”, *Journal of High Energy Physics*, vol. 2018 (10): (2018) p. 174, ISSN 1029-8479, DOI: [10.1007/JHEP10\(2018\)174](https://doi.org/10.1007/JHEP10(2018)174).
- [153] STAR Collaboration, “Centrality and transverse momentum dependence of D^0 -meson production at mid-rapidity in Au + Au collisions at $\sqrt{s_{NN}} = 200$ GeV”, *Phys. Rev. C*, vol. 99: (2019) p. 034908, DOI: [10.1103/PhysRevC.99.034908](https://doi.org/10.1103/PhysRevC.99.034908).
- [154] “CMS Luminosity Calibration for the pp Reference Run at $\sqrt{s} = 5.02$ TeV”, *Tech. Rep. CMS-PAS-LUM-16-001*, CERN, Geneva (2016), URL: <https://cds.cern.ch/record/2235781>.

- [155] K. Olive, “Review of Particle Physics”, *Chinese Physics C*, vol. 40 (10): (2016) p. 100001, DOI: [10.1088/1674-1137/40/10/100001](https://doi.org/10.1088/1674-1137/40/10/100001).
- [156] CMS Collaboration, “Measurement of Prompt D^0 Meson Azimuthal Anisotropy in Pb-Pb Collisions at $\sqrt{s_{NN}} = 5.02$ TeV”, *Phys. Rev. Lett.*, vol. 120: (2018) p. 202301, DOI: [10.1103/PhysRevLett.120.202301](https://doi.org/10.1103/PhysRevLett.120.202301).
- [157] A. M. Poskanzer *et al.*, “Methods for analyzing anisotropic flow in relativistic nuclear collisions”, *Phys. Rev. C*, vol. 58: (1998) p. 1671, DOI: [10.1103/PhysRevC.58.1671](https://doi.org/10.1103/PhysRevC.58.1671), arXiv:[nucl-ex/9805001](https://arxiv.org/abs/nucl-ex/9805001).
- [158] Collaboration E877, J. Barrette *et al.*, “Proton and pion production relative to the reaction plane in Au + Au collisions at 11-A-GeV/c”, *Phys. Rev.*, vol. C56: (1997) pp. 3254, DOI: [10.1103/PhysRevC.56.3254](https://doi.org/10.1103/PhysRevC.56.3254), arXiv:[nucl-ex/9707002](https://arxiv.org/abs/nucl-ex/9707002).
- [159] Collaboration STAR, C. Adler *et al.*, “Elliptic flow from two and four particle correlations in Au+Au collisions at $s(\text{NN})^{**}(1/2) = 130\text{-GeV}$ ”, *Phys. Rev.*, vol. C66: (2002) p. 034904, DOI: [10.1103/PhysRevC.66.034904](https://doi.org/10.1103/PhysRevC.66.034904), arXiv:[nucl-ex/0206001](https://arxiv.org/abs/nucl-ex/0206001).
- [160] M. Luzum *et al.*, “Eliminating experimental bias in anisotropic-flow measurements of high-energy nuclear collisions”, *Phys. Rev.*, vol. C87 (4): (2013) p. 044907, DOI: [10.1103/PhysRevC.87.044907](https://doi.org/10.1103/PhysRevC.87.044907), arXiv:[1209.2323](https://arxiv.org/abs/1209.2323).
- [161] Collaboration CMS, S. Chatrchyan *et al.*, “Measurement of the elliptic anisotropy of charged particles produced in PbPb collisions at $\sqrt{s_{NN}} = 2.76$ TeV”, *Phys. Rev. C*, vol. 87: (2013) p. 014902, DOI: [10.1103/PhysRevC.87.014902](https://doi.org/10.1103/PhysRevC.87.014902), arXiv:[1204.1409](https://arxiv.org/abs/1204.1409).
- [162] Collaboration CMS, A. M. Sirunyan *et al.*, “Azimuthal anisotropy of charged particles with transverse momentum up to 100 GeV/ c in PbPb collisions at $\sqrt{s_{NN}} = 5.02$ TeV”, *Phys. Lett. B*, vol. 776: (2018) p. 195, DOI: [10.1016/j.physletb.2017.11.041](https://doi.org/10.1016/j.physletb.2017.11.041), arXiv:[1702.00630](https://arxiv.org/abs/1702.00630).
- [163] S. Y. F. Liu *et al.*, “An in-medium heavy-quark potential from the $Q\bar{Q}$ free energy”, *Nucl. Phys. A*, vol. 941: (2015) p. 179, DOI: [10.1016/j.nuclphysa.2015.07.001](https://doi.org/10.1016/j.nuclphysa.2015.07.001), arXiv:[1501.07892](https://arxiv.org/abs/1501.07892).

- [164] ALICE Collaboration, “ D -Meson Azimuthal Anisotropy in Midcentral Pb-Pb Collisions at $\sqrt{s_{NN}} = 5.02$ TeV”, *Phys. Rev. Lett.*, vol. 120: (2018) p. 102301, DOI: [10.1103/PhysRevLett.120.102301](https://doi.org/10.1103/PhysRevLett.120.102301).
- [165] STAR Collaboration, “Measurement of D^0 Azimuthal Anisotropy at Midrapidity in Au + Au Collisions at $\sqrt{s_{NN}} = 200$ GeV”, *Phys. Rev. Lett.*, vol. 118: (2017) p. 212301, DOI: [10.1103/PhysRevLett.118.212301](https://doi.org/10.1103/PhysRevLett.118.212301).
- [166] Collaboration CMS, S. Chatrchyan *et al.*, “Measurement of higher-order harmonic azimuthal anisotropy in PbPb collisions at $\sqrt{s_{NN}} = 2.76$ TeV”, *Phys. Rev. C*, vol. 89: (2014) p. 044906, DOI: [10.1103/PhysRevC.89.044906](https://doi.org/10.1103/PhysRevC.89.044906), [arXiv:1310.8651](https://arxiv.org/abs/1310.8651).
- [167] B. Alver *et al.*, “Collision geometry fluctuations and triangular flow in heavy-ion collisions”, *Phys. Rev. C*, vol. 81: (2010) p. 054905, DOI: [10.1103/PhysRevC.82.039903](https://doi.org/10.1103/PhysRevC.82.039903), [arXiv:1003.0194](https://arxiv.org/abs/1003.0194).
- [168] Collaboration CMS, S. Chatrchyan *et al.*, “Measurement of jet fragmentation in PbPb and pp collisions at $\sqrt{s_{NN}} = 2.76$ TeV”, *Phys. Rev. C*, vol. 90: (2014) p. 024908, DOI: [10.1103/PhysRevC.90.024908](https://doi.org/10.1103/PhysRevC.90.024908), [arXiv:1406.0932](https://arxiv.org/abs/1406.0932).
- [169] ATLAS Collaboration, M. Aaboud *et al.*, “Measurement of jet fragmentation in Pb+Pb and pp collisions at $\sqrt{s_{NN}} = 2.76$ TeV with the ATLAS detector at the LHC”, *Eur. Phys. J. C*, vol. 77: (2017) p. 379, DOI: [10.1140/epjc/s10052-017-4915-5](https://doi.org/10.1140/epjc/s10052-017-4915-5), [arXiv:1702.00674](https://arxiv.org/abs/1702.00674).
- [170] Collaboration CMS, A. M. Sirunyan *et al.*, “Observation of medium induced modifications of jet fragmentation in PbPb collisions using isolated-photon-tagged jets”, [arXiv:1801.04895](https://arxiv.org/abs/1801.04895).
- [171] Collaboration CMS, S. Chatrchyan *et al.*, “Modification of jet shapes in PbPb collisions at $\sqrt{s_{NN}} = 2.76$ TeV”, *Phys. Lett. B*, vol. 730: (2014) p. 243, DOI: [10.1016/j.physletb.2014.01.042](https://doi.org/10.1016/j.physletb.2014.01.042), [arXiv:1310.0878](https://arxiv.org/abs/1310.0878).
- [172] Collaboration CMS, A. M. Sirunyan *et al.*, “Jet properties in PbPb and pp collisions at $\sqrt{s_{NN}} = 5.02$ TeV”, *JHEP*, vol. 05: (2018) p. 006, DOI: [10.1007/JHEP05\(2018\)006](https://doi.org/10.1007/JHEP05(2018)006), [arXiv:1803.00042](https://arxiv.org/abs/1803.00042).

- [173] Collaboration CMS, V. Khachatryan *et al.*, “Measurement of transverse momentum relative to dijet systems in PbPb and pp collisions at $\sqrt{s_{\text{NN}}} = 2.76$ TeV”, *JHEP*, vol. 01: (2016) p. 006, DOI: [10.1007/JHEP01\(2016\)006](https://doi.org/10.1007/JHEP01(2016)006), arXiv:[1509.09029](https://arxiv.org/abs/1509.09029).
- [174] J. Casalderrey-Solana *et al.*, “Introductory lectures on jet quenching in heavy ion collisions”, *Acta Phys. Polon. B*, vol. 38: (2007) p. 3731, arXiv:[0712.3443](https://arxiv.org/abs/0712.3443).
- [175] D. d’Enterria, “Jet quenching”, vol. 23: Relativistic Heavy Ion Physics: (2010) p. 99, DOI: [10.1007/978-3-642-01539-7_16](https://doi.org/10.1007/978-3-642-01539-7_16), arXiv:[0902.2011](https://arxiv.org/abs/0902.2011).
- [176] U. A. Wiedemann, “Jet quenching in heavy ion collisions”, *Landolt-Bornstein*, p. 521, DOI: [10.1007/978-3-642-01539-7_17](https://doi.org/10.1007/978-3-642-01539-7_17), arXiv:[0908.2306](https://arxiv.org/abs/0908.2306).
- [177] A. Majumder *et al.*, “The Theory and Phenomenology of Perturbative QCD Based Jet Quenching”, *Prog. Part. Nucl. Phys.*, vol. 66: (2011) p. 41, DOI: [10.1016/j.ppnp.2010.09.001](https://doi.org/10.1016/j.ppnp.2010.09.001), arXiv:[1002.2206](https://arxiv.org/abs/1002.2206).
- [178] JET Collaboration, K. M. Burke; *et al.*, “Extracting the jet transport coefficient from jet quenching in high-energy heavy-ion collisions”, *Phys. Rev. C*, vol. 90: (2014) p. 014909, DOI: [10.1103/PhysRevC.90.014909](https://doi.org/10.1103/PhysRevC.90.014909).
- [179] S. Cao; *et al.*, “Modeling of heavy-flavor pair correlations in Au-Au collisions at 200A GeV at the BNL Relativistic Heavy Ion Collider”, *Phys. Rev. C*, vol. 92 (5): (2015) p. 054909, DOI: [10.1103/PhysRevC.92.054909](https://doi.org/10.1103/PhysRevC.92.054909), arXiv:[1505.01869](https://arxiv.org/abs/1505.01869).
- [180] R. Hambrock *et al.*, “AdS/CFT predictions for azimuthal and momentum correlations of $b\bar{b}$ pairs in heavy ion collisions”, *Nucl. Part. Phys. Proc.*, vol. 289-290: (2017) p. 233, DOI: [10.1016/j.nuclphysbps.2017.05.052](https://doi.org/10.1016/j.nuclphysbps.2017.05.052), arXiv:[1703.05845](https://arxiv.org/abs/1703.05845).
- [181] CMS Collaboration, “Jet energy scale and resolution in the CMS experiment in pp collisions at 8 TeV”, *Journal of Instrumentation*, vol. 12 (02): (2017) pp. P02014, DOI: [10.1088/1748-0221/12/02/p02014](https://doi.org/10.1088/1748-0221/12/02/p02014).
- [182] CMS Collaboration, “Measurement of inclusive jet cross sections in pp and PbPb collisions at $\sqrt{s_{\text{NN}}} = 2.76$ TeV”, *Phys. Rev. C*, vol. 96: (2017) p. 015202, DOI: [10.1103/PhysRevC.96.015202](https://doi.org/10.1103/PhysRevC.96.015202).

- [183] T. Song; *et al.*, “Open charm and dileptons from relativistic heavy-ion collisions”, *Phys. Rev. C*, vol. 97: (2018) p. 064907, DOI: [10.1103/PhysRevC.97.064907](https://doi.org/10.1103/PhysRevC.97.064907).
- [184] R. Katz; *et al.*, “Heavy-flavor dynamics in event-by-event viscous hydrodynamic backgrounds”, (2019), [arXiv:1812.08009](https://arxiv.org/abs/1812.08009).
- [185] C. A. G. Prado; *et al.*, “Event-by-event correlations between soft hadrons and D^0 mesons in 5.02 TeV PbPb collisions at the CERN Large Hadron Collider”, *Phys. Rev. C*, vol. 96: (2017) p. 064903, DOI: [10.1103/PhysRevC.96.064903](https://doi.org/10.1103/PhysRevC.96.064903).
- [186] Y. Xu; *et al.*, “Data-driven analysis for the temperature and momentum dependence of the heavy-quark diffusion coefficient in relativistic heavy-ion collisions”, *Phys. Rev. C*, vol. 97: (2018) p. 014907, DOI: [10.1103/PhysRevC.97.014907](https://doi.org/10.1103/PhysRevC.97.014907).
- [187] P. B. Gossiaux *et al.*, “Toward an understanding of the single electron data measured at the BNL Relativistic Heavy Ion Collider (RHIC)”, *Phys. Rev. C*, vol. 78: (2008) p. 014904, DOI: [10.1103/PhysRevC.78.014904](https://doi.org/10.1103/PhysRevC.78.014904).
- [188] H.-T. Ding; *et al.*, “Charmonium properties in hot quenched lattice QCD”, *Phys. Rev. D*, vol. 86: (2012) p. 014509, DOI: [10.1103/PhysRevD.86.014509](https://doi.org/10.1103/PhysRevD.86.014509).
- [189] D. Banerjee; *et al.*, “Heavy quark momentum diffusion coefficient from lattice QCD”, *Phys. Rev. D*, vol. 85: (2012) p. 014510, DOI: [10.1103/PhysRevD.85.014510](https://doi.org/10.1103/PhysRevD.85.014510).
- [190] X. Dong; *et al.*, “Open Heavy-Flavor Production in Heavy-Ion Collisions”, (2019), [arXiv:1903.07709](https://arxiv.org/abs/1903.07709).
- [191] A. I. Sheikh *et al.*, “Heavy flavour Langevin diffusion with the chromo-electromagnetic field fluctuations in the quark-gluon plasma”, (2019), [arXiv:1902.02477](https://arxiv.org/abs/1902.02477).
- [192] A. Beraudo; *et al.*, “Development of heavy-flavour flow-harmonics in high-energy nuclear collisions”, *Journal of High Energy Physics*, vol. 2018 (2): (2018) p. 43, ISSN 1029-8479, DOI: [10.1007/JHEP02\(2018\)043](https://doi.org/10.1007/JHEP02(2018)043).

- [193] Z. Citron; *et al.*, “Future physics opportunities for high-density QCD at the LHC with heavy-ion and proton beams”, *Tech. rep.*, CERN, Geneva (2018), URL: <http://cds.cern.ch/record/2650176>, arXiv:1812.06772.